Author: Jitrin Chaiprapa

Thesis title: New Supramolecular Liquid Crystal Structures in Wedge-Shaped Molecules

Qualification: PhD

New Supramolecular Liquid Crystal Structures in Wedge-Shaped Molecules

Jitrin Chaiprapa

Supervised by Professor Goran Ungar
and Dr Xiangbing Zeng

A thesis submitted for the degree of Doctor of Philosophy
Department of Materials Science and Engineering
University of Sheffield

January 2012

Abstract

The main subject of this thesis is structure determination of self-assembled wedge-shaped liquid crystal-forming molecules. The main part of the work involves 3,4,5-trialkoxygallate alkali metal salts. These salts, with two short and one long alkyl chains, are studied in search for close packed micellar phases, which have never been observed before in thermotropic liquid crystals. The molecular structures of these compounds were designed on the basis of the theoretical prediction of volume filling of Voronoi polyhedra of close-packed structures. The idea is that the longer alkyl chain in the molecule would help fill the octahedral interstices, furthest points from the centers of surrounding micelles, in a structure of close packed spheres. To fill the octahedral interstices even better, various proportions of n-paraffin C_nH_{2n+2}, where n= 15, 17, 19, are also added to these dendrons. For comparison, 3,4,5-tridodecyloxygallates are also studied with varying proportions of added $C_{19}H_{40}$. Small-angle X-ray diffraction (SAXD) experiments have been carried out to identify the phase structures at different temperatures. It is found that neither of the pure compounds yields a close-packed structure, and it is only in the mixtures of Na or Rb salts with added $C_{19}H_{40}$ which the hexagonal close-packed (HCP) phase is obtained. The first order phase transition from the hexagonal columnar phase to another hexagonal columnar phase is also observed in pure compounds of Na salts and their mixtures with added $C_{19}H_{40}$ whereas the hexagonal columnar superlattice is also obtained from the mixtures of Li salt and n-alkane C_nH_{2n+2} (n=15, 17). The phase diagrams of the binary systems are constructed, to understand the principles of close-packed structure formation in self-assembled tapered mesogens and dendrimers.

The second subject of this thesis is structure determination of wedge-shaped liquid crystal molecules of hybrid dendrons of methyl 3,4-(4′-alkoxy biphenylmethyl-4-yloxy) benzoate, with different lengths of alkyl chains. The molecular structure of these dendrons is a combination of molecular structures of previously studied benzyl ether based dendrons and biphenyl methyl ether based dendrons. Using SAXD, it is found that these dendrons yield wiggly lamellar phases, as well as hexagonal columnar phases consisting of core-shell supramolecular columns. The core-shell structure is confirmed by the good results of the intensity fitting between experimental intensities and intensities calculated from geometric models, as well as by reconstructing electron density maps and performing molecular dynamics simulations.

Acknowledgements

First of all, I am deeply grateful to my supervisors Prof. Goran Ungar and Dr Xiangbing Zeng for giving a great support to me to complete this thesis. They have devoted a great deal of thought, time, and patience to my thesis. Also, I would like to thank you Dr Feng Liu for giving a good support and some advice for my works. I would remain grateful to them.

I wish to acknowledge my collaborators from the University of Hull, Prof. George Mehl and Dr Liliana Cseh, for providing materials for me. Without them, this thesis would not have been possible. I am also greatly indebted to Royal Thai government for the full scholarship for my study here in the United Kingdom. I would like to express my appreciation to my mother. She has given me inspiration, encouragement and kindness. Last but not least, I would like to thank my friends in Polymers and Liquid crystals research group at the University of Sheffield for their moral support and help.

Contents

Abstract ii
Acknowledgements iii

Chapter 1 Liquid Crystals 1

1.1 Introduction 1
1.2 General types of liquid crystals 1
    1.2.1 Molecular structures of liquid crystals 2
    1.2.2 Phase structures in liquid crystals 2
1.3 Dendrimeric liquid crystals 3
1.4 Literature review 5
1.5 Objective of the project 9
References 10

Chapter 2 X-ray Diffraction 16

2.1 Introduction 16
2.2 X-ray diffraction 16
2.3 Bragg's law 17
2.4 Reciprocal lattice 18
2.5 Ewald sphere 19
2.6 SAXS and WAXS 21
2.7 Powder diffractions 22
2.8 Indexing diffraction pattern 23
2.9 Electron density reconstruction 24
References 25

Chapter 3 Apparatus and Data Reduction 26

3.1 Introduction 26
3.2 Synchrotron radiation source 26
3.3 Apparatus 29

3.3.1 Station 2.1 29

3.3.2 Station 6.2 30

3.4 Experimental procedures 31

3.5 Data reduction 32

3.5.1 Data reduction for 1-D data 32

3.5.1.1 Data normalization 32

3.5.1.2 Detector response correction 33

3.5.1.3 Empty capillary subtraction 33

3.5.1.4 Calibration: creating a q-axis 33

3.5.1.5 Lorentz correction 35

3.5.2 Data reduction for 2-D data 35

3.5.3 Debye - Waller factor 36

References 37

Chapter 4 Hexagonal Close Packed structure in the Binary Mixtures of Alkali Metal (Na, Rb) Salts of Trialkoxygallates and n-Paraffin $C_{19}H_{40}$ 38

4.1 Introduction 38

4.2 Voronoi polyhedron 40

4.3 Radial distribution of volume of voronoi polyhedron 42

4.4 The studied materials: alkali metal (Na, Rb) salts of 3,4,5-trialkoxygallates and their binary mixtures with added n-paraffin (12-12-18M+m%$C_{19}H_{40}$ and 12-12-12M+m%$C_{19}H_{40}$ where M=Na, Rb and m=0, 5, 10, 15, 30) 44

4.5 Experimental Results and Discussion 45

4.5.1 SAXS results and phase indentification 45

4.5.2 The first order Col_h-Col_h transition 71

4.5.3 Characterisation of unit cell and corresponding supramolecular building objects 75

4.5.4 Binary phase diagrams 79

4.5.5 Electron density reconstruction 84

4.5.6 Location of Rb^+ ions 87

4.6 Conclusion 91

References 92

Chapter 5 Hexagonal Columnar Superlattice in the Binary Mixtures of Li salt of 3,4,5-Trialkoxygallate and n-Paraffins C_nH_{2n+2} (n=15, 17) 96

5.1 Introduction 96
5.2 The materials studied: Li salt of 3,4,5-trialkoxygallate and its binary mixtures with added n-paraffins (12-12-18Li+m%C_nH_{2n+2} where m=0, 5, 10, 15, 30 and n=15, 17) 97
5.3 Experimental Results and Discussion 97
  5.3.1 SAXS results and phase identification 97
  5.3.2 Characterisation of unit cell and corresponding supramolecular building object 108
  5.3.3 Electron density reconstruction 111
  5.3.4 Determination of the number of 12-12-18Li and C_nH_{2n+2} (n=15, 30) molecules in supramolecular columns in the superlattice 119
  5.3.5 The Col_h-Col_s phase transition 123
  5.3.6 Molecular dynamics simulation 124
5.4 Conclusion 125
References 126

Chapter 6 Core-Shell Supramolecular Cylindrical Columns and Wiggled-Like Layer Structure of Methyl 3,4-(-Alkoxy Biphenylmethyl-4-Yloxy) Benzoate 128

6.1 Introduction 128
6.2 The materials studied: methyl 3,4-(4′-alkoxy biphenylmethyl-4-yloxy) benzoate with different alkyl chain lengths (Bn where n=12, 14, 16, 18) 129
6.3 Experimental Results and Discussion 130
  6.3.1 SAXS results and phase identification 130
  6.3.2 Wiggly lamellar phase 135
  6.3.3 Bilayer hexagonal columnar phase 137

6.3.4 Simulation of the powder x-ray diffraction data 140
6.3.5 Electron density reconstruction 143
6.3.6 Molecular dynamics simulation 149
6.4 Conclusion 150
References 150

Summary 154

Future works 156

Appendices

Appendix 1: DSC data for 12-12-18M+m%$C_{19}H_{40}$ and 12-12-12M+m%$C_{19}H_{40}$ where M=Na, Rb and m=0, 5, 10, 15, 30 157
Appendix 2: Measured d-spacings of diffraction peaks and unit cell parameters for various lattices formed by 12-12-18M+m%$C_{19}H_{40}$ and 12-12-12M+m%$C_{19}H_{40}$ where M=Na, Rb and m=0, 15 160
Appendix 3: Electron density maps with different phase combinations for the HCP lattice of 12-12-12M+15%$C_{19}H_{40}$ where M=Na and Rb 168
Appendix 4: Equation for calculating the volume fraction of the aliphatic content in 12-12-12M+m%$C_{19}H_{40}$ where M=Na and Rb 177
Appendix 5: Measured d-spacings of diffraction peaks and unit cell parameters for various lattices formed by 12-12-18Li+m%C_nH_{2n+2} where m=0, 15, 30 and n=15, 17 181
Appendix 6: Electron density maps and electron density contours with different phase combinations for the hexagonal columnar superlattice of 12-12-18Li+30%$C_{15}H_{32}$, 12-12-18Li+15%$C_{17}H_{36}$, and 12-12-18Li+30%$C_{17}H_{40}$ 187
Appendix 7: DSC data for Bn where n=12, 14, 16, 18 191
Appendix 8: Measured d-spacings of diffraction peaks and unit cell parameters for various lattices formed by Bn where n=12, 14, 16, 18 196

Chapter 1

Liquid Crystals

1.1 Introduction

A liquid crystal[1,2] is a substance that shows a phase of matter lying between a crystalline solid and liquid. The molecules in the liquid crystalline phase are free to move like those in the liquid phase, but they tend to remain oriented themselves in a certain direction, which is called the *director* and represented by the vector $\vec{n}$ as shown in Figure 1-1. Nonetheless, the orientation order of molecules in the liquid crystalline phase is not as perfect as that in a crystalline phase. Liquid crystalline compounds may possess more than one liquid crystalline phase as a result of different degrees of positional and orientational orders of molecules. The liquid crystalline phases are also called *mesophases* and the molecules possessing liquid crystalline properties are also called *mesogens*.

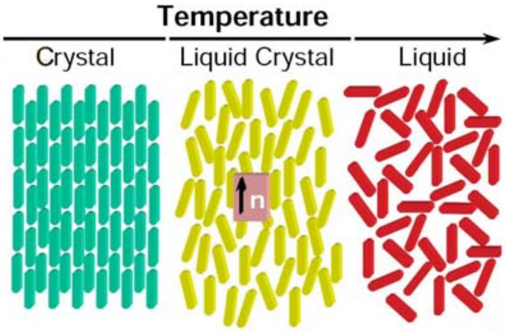

Figure 1-1 Diagram of the arrangement of molecules in the crystalline, liquid crystalline, and isotropic liquid phases[3].

1.2 General Types of Liquid Crystals

Liquid crystals (LCs) can be categorized into two types: thermotropic and lyotropic LCs. Thermotropic LCs are formed by pure mesogens and exhibit a phase transition as the temperature is changed. Lyotropic LCs are obtained from amphiphiles, e. g. surfactants, dissolving in the solvents. The amphiphile solution possesses the liquid crystalline properties in a certain concentration range of amphiphiles. When the concentration of amphiphiles is changed, the phase transition will be observed. Since all my studies are to explore new structures in thermotropic LCs, only thermotropic LCs are therefore concentrated on.

1.2.1 Molecular structures of liquid crystals

Thermotropic LCs can be classified according to the molecular shape of mesogens.

Calamitic LCs are formed by rod-like molecules (see Figure 1-2a) and they are considered as the classical LCs.

Discotic LCs are obtained from disc-like molecules (see Figure 1-2b) and they are also considered as the conventional LCs.

Samidic LCs are obtained from lath-like (board-like) molecules.

Polymeric LCs are a class of materials which possess the properties of polymers and those of liquid crystals. This type of LCs is obtained from incorporating the mesogens into the polymer chains. Polymeric LCs can be categorized into low-molecular-weight LCs, main-chain polymeric LCs, side-chain polymeric LCs, and segmented-chain polymeric LCs. The last three types are classified according to the placement position of mesogens incorporated into the main chains

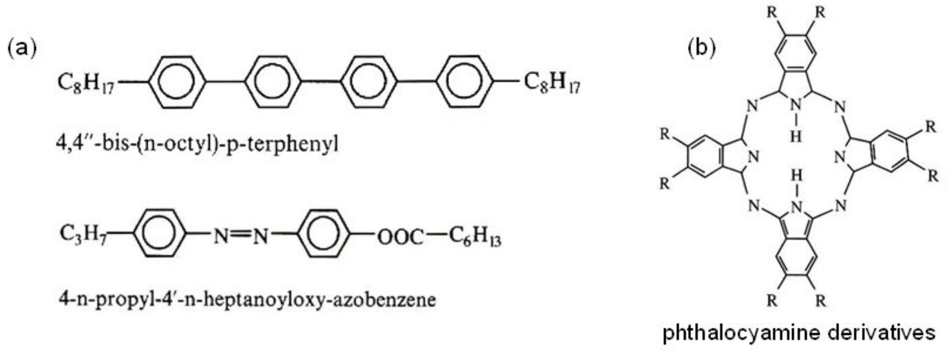

Figure 1-2 (a) Rod-like mesogens (b) Disc-like mesogens[1].

1.2.2 Phase structures in liquid crystals

Under the changing of temperatures, the molecules in thermotropic liquid crystal materials will arrange themselves into different phase structures. Each phase is classified by the amount of positional and orientational orders of molecules.

Nematic phase is the simplest liquid crystalline phase because the molecules do not have the positional order but they possess the orientational order such that most of molecules tend to point to one direction (see Figure 1-3a).

Cholesteric phase or chiral nematic phase is obtained from chiral molecules. This phase was first observed in cholesterol derivatives and has been observed in other compounds later. Figure 1-3b shows the arrangement of rod-like molecules in the chiral nematic phase that the director twists round in a helical fashion.

Smectic phase is characterised by the layer-like structure of mesogens. Smectic phase is also classified according to the arrangement of molecules inside the layers. In smectic A phase (Figure 1-3c), for example, within a particular layer of molecules the mesogens are parallel, on an average, to the others. Their long axes are perpendicular to the layer plane. However, if the long axis of messogens is tilted with respect to the layer normal, this characteristic of the layer-like structure of mesogens is termed smectic C phase (see Figure 1-3d). With more order than that of smectic A and C phases, other smectic phases are named and designated with sequential letter B, F, G…M according to the chronological sequence of their discovery. In a similar way to chiral nematic phase, many chiral compounds can form smectic phases of different types. For example, smectic C^* phase (see Figure 1-3e) is formed by the stacking up of layers of molecules, each of which has a different tilt angle of the director. The director rotates from layer to layer which leads to the formation of helix.

1.3 Dendrimeric Liquid Crystals

Dendrimeric liquid crystals are novel liquid crystals obtained from dendrimers. Dendrimer is generally considered as a highly branched polymer for which the new branches of repetitive units are added step-by-step (i.e. generation) to each existing branch until a symmetrical branched structure is created (see Figure 1-4a and 4b). Instead of getting the dendrimer from one highly branched macromolecule, dendrimers can be also obtained from the self-assembling of dendrons (tree-like molecules), as shown in Figure 1-4c and d, which is considered as one branch arm of dendrimer. This type of dendrimers is called *supramolecular dendrimers* because it derives from the non-covalent interactions occurring in the self-assembling process of dendrons.

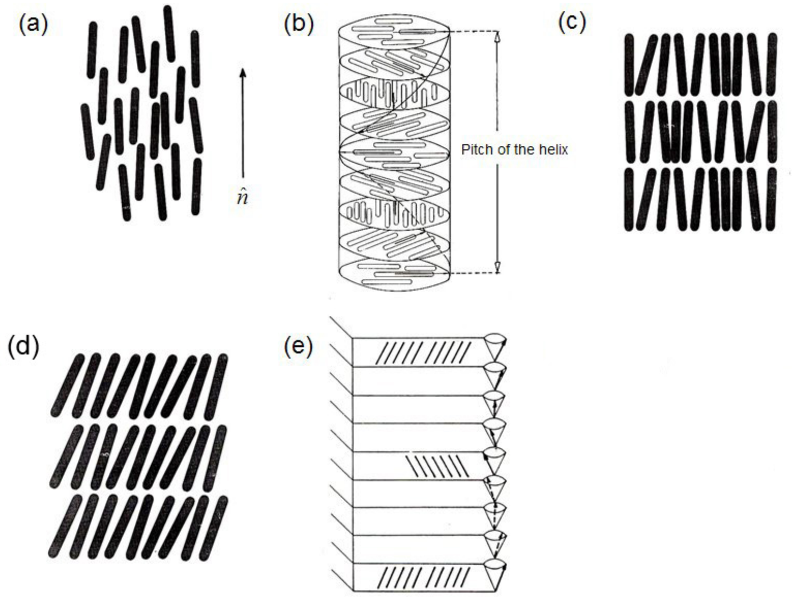

Figure 1-3 Liquid crystalline phases: (a) Nematic phase (b) Cholesteric phase (c) Smectic A phase (d) Smectic C phase (e) Smectic C* phase[4].

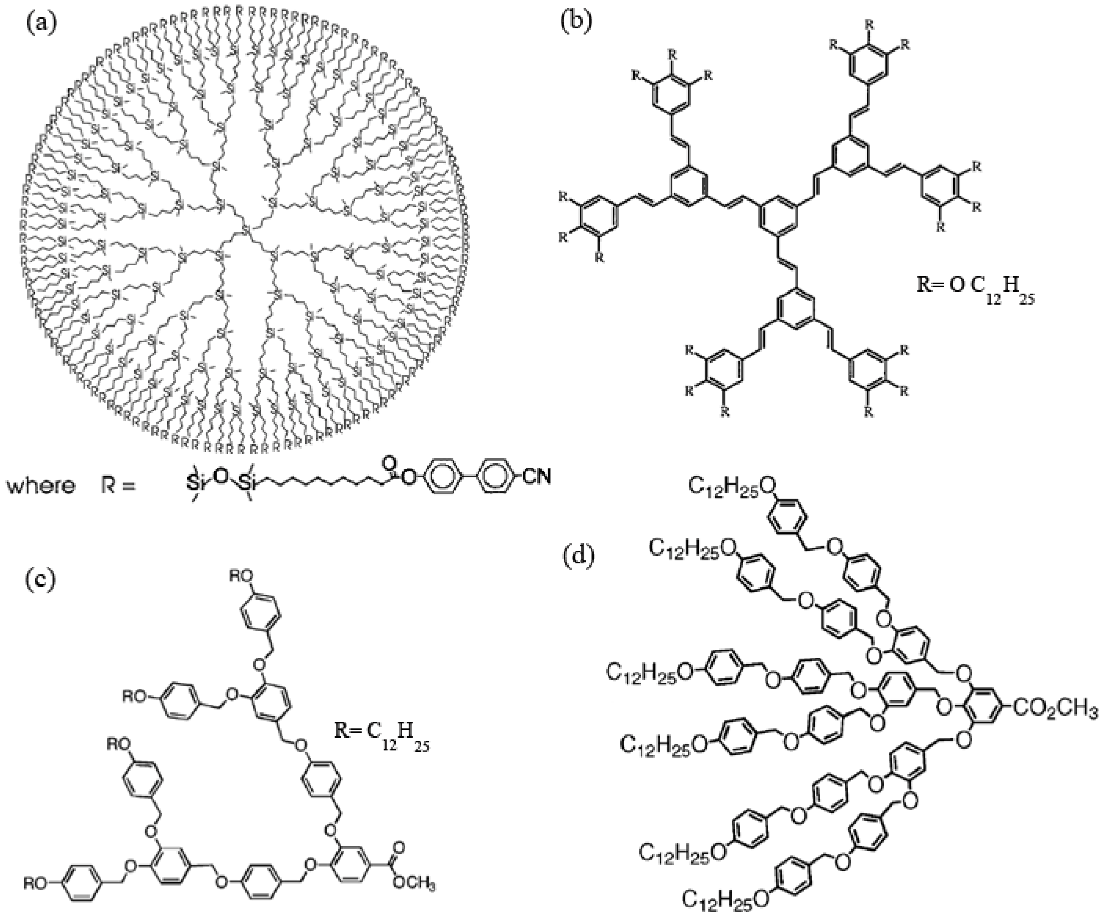

Figure 1-4 Examples of (a,b) liquid crystalline dendrimers[5,6] and (c,d) dendrons[7].

Like other mesogens possessing the liquid crystalline properties, dendrons and dendrimers are composed of two main parts, i.e. the aromatic and the aliphatic parts. The aromatic part is a rigid part whose stiffness is caused by the steric hindrance and resonance. This part of dendrimers plays an important role for forming the lattice structure. The aliphatic part is a flexible part which provides for independent movement of the molecules to facilitate proper alignment and cause the liquid crystalline properties. Next section will show that dendrimers and dendrons have influence in thermotropic LCs since they yield the novel phases and novel structures which these structures never obtained from the conventional shapes of mesogens.

1.4 Literature Review

This section is a brief overview of the discovery of novel mesophases and new modes of assembly of dendrons (tree-like molecules) and supramolecular dendrimers regarded as novel-shaped mesogens. Thermotropic LC phases recently discovered in self-assembling dendrons and supramolecular dendrimers can be categorised into three main types: 1D lamellar smectic, 2D columnar, and 3D globular phases. The schematic in Figure 1-5a illustrates the ways of self-arranging of dendrons in the 1D lamellar smectic phase whereas the schematics in Figure 1-5b and Figure 1-5c show the self-assembling of dendrons and self-organisation of corresponding supramolecular objects into 2D columnar and 3D globular phases respectively. In Figure 1-5a, the dendrons arrange themselves in the interdigitated way to form a layer. The layers of dendrons stack up each other and the lamellar structure is then formed. Within the layers, if the dendrons are oriented along the layer normal, the lamellar smectic A phase will be obtained whereas the tilting of dendrons with respect to the layer normal leads to the lamellar smectic C phase. Figure 1-5b shows another mode of the self-assembling of dendrons which leads to the formation of the columnar mesophases. The dendrons with small number of branching units (low-generation dendrons) have a tapered wedge shape. The tapered wedge-shaped dendrons are self-assembled into a supramolecular disc. The discs stack up each other and the supramolecular column is then formed. Then, the columns are self-organised into 2-D lattice. Figure 1-5c shows the self-assembling of high-generation dendrons having a conical shape which leads to the formation of the 3D globular mesophases. The conical-shaped dendrons are self-assembled into a supramolecular sphere. Then, the spheres are packed into 3-D lattice.

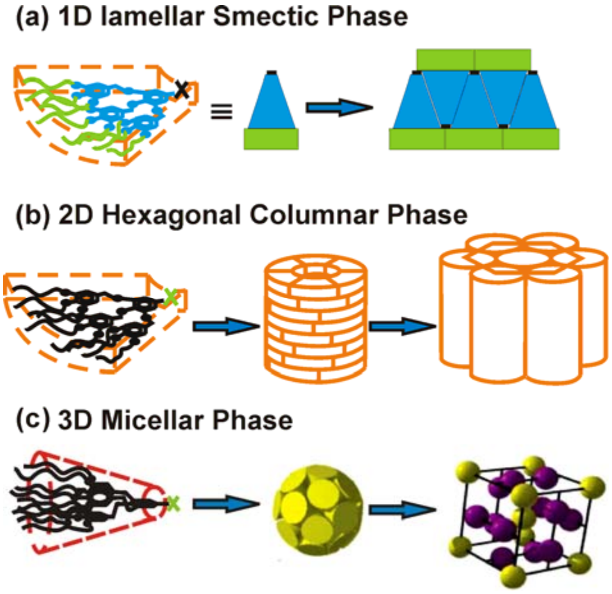

Figure 1-5 The formation of (a) 1D lamellar smectic, (b) 2D hexagonal columnar, and (c) 3D micellar phases of dendrons[8].

According to the recent reports of structural determination in self-assembling dendrons and supramolecular dendrimers, the lamellar smectic A phases with different interlayer structures, i.e. modular bilayer structure smectic A[7,9], non-modular bilayer structures smectic A[9-14], have been reported. For the 2D columnar phases, the hexagonal columnar phase with $p6mm$ symmetry[7,9-13] is the most prevalent in self-assembling dendrons and supramolecular dendrimers whereas the simple rectangular columnar lattice with $p2mm$ symmetry[7,9,11,12] and the centred rectangular columnar lattice with $c2mm$ symmetry[7,9,11,12] were also found. The 2D columnar phases were originally obtained from the self-organisation of cylindrical inverse micellar supramolecular columns. However, with the new designs of dendritic structures of self-assembling dendrons and dendrimers, the *p6mm* hexagonal columnar phase was also obtained from the self-organisation of helical supramolecular columns[11,12,14], helical[15-17] and nonhelical[18-19] pyramidal supramolecular columns. With the help of wide angle X-ray scattering technique, it was additionally found that some self-assembling dendrons and dendrimers also gave supramolecular helical columns with the intracolumnar order[14-17,20], thereby obtaining 2D columnar phases possessing the intracolumnar order of supramolecular helical columns. The attaching of dendrons to dipeptide backbones also affords supramolecular helical porous columns[21-28] self-organised into hexagonal columnar, simple rectangular columnar, centred rectangular columnar lattices with and without intracolumnar order of helical pores. Most of supramolecular columns obtained from self-assembling dendrons or dendrimers are nonhollow singly segregated aliphatic-aromatic columns[7,9-12,15,17,29-42] whereas hollow singly segregated aliphatic-aromatic[11,12,43], hollow and nonhollow doubly segregated aliphatic-aromatic-aliphatic supramolecular columns[43] were rarely obtained from self-assembling dendrons. The formation of the bilayer structure of supramolecular columns was correlated with the decrease of solid angle of dendrons, thereby requiring the much higher number of dendrons to form supramolecular columns. The formation of doubly segregated aliphatic-aromatic-aliphatic columns by the large number of dendrons is to reduce the size of the hole or to fill the empty space at the centre of columns by the alkyl parts of dendrons. This will reduce the energy penalty of system. The self-assembly of dendrons into doubly segregated aliphatic-aromatic-aliphatic columns is considered as the new mode of self-assembly of dendrons in thermotropic LCs. Recently, the novel 3D simple orthorhombic columnar lattice with $P222_1$[20] and *Pmna*[44] symmetry were also obtained from the 3-fold symmetric dendrimers and the deconstruction strategy-based dendrons respectively. In addition, such dendrons and dendrimers also afforded the 3D hexagonal columnar superlattice[20,44] formed by closely packing of undulated supramolecular columns, whereas the 2D hexagonal columnar superlattices were obtained from twin-tapered dendrons[45,46] playing as side groups of polymers. Figure 1-6 illustrates different ways of self-assembling of dendrons and crown-like dendrimers into different fashions of supramolecular columns which are self-organised into hexagonal columnar lattice.

For the 3D globular phases, the cubic phase with $Pm\overline{3}n$ symmetry was first observed in the benzyl ether type dendrons[42] and also found later in other self-assembling dendrons[9-12,47]. The body centred cubic (BCC) phase with $Im\overline{3}m$ symmetry[10,48,49], which are less prevalent than the cubic $Pm\overline{3}n$ phase, was the second cubic phase found in thermotropic LCs. The tetragonal phase with $P4_2/mnm$ symmetry[50] and the liquid quasicrystal[51] (LQC) with dodecagonal (i.e. 12-fold

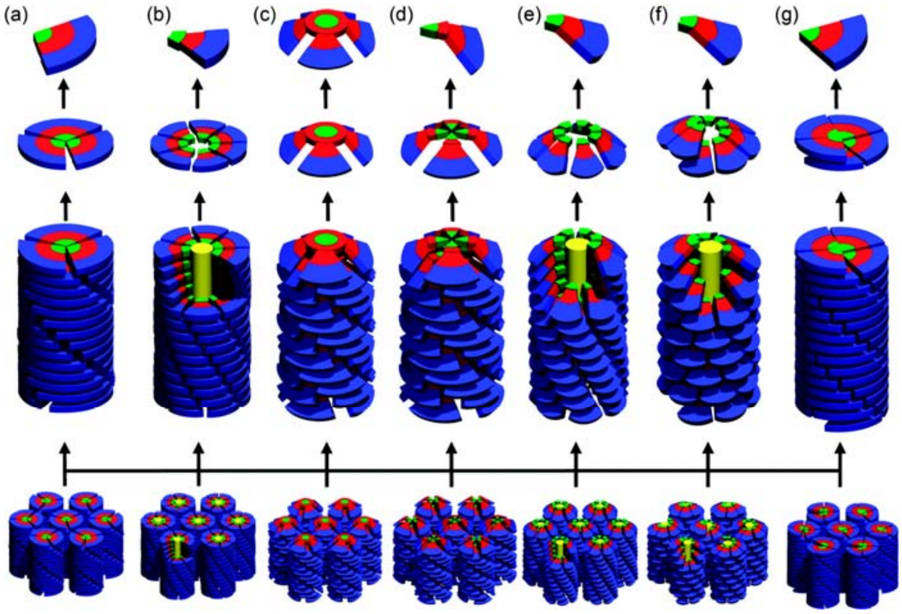

Figure 1-6 The formation of *p6mm* hexagonal columnar lattice by various fashions of supramolecular discs and corresponding supramolecular columns: (a,b) flat (c,d,e) pyramidal (f, g) helicene-like helical supramolecular discs[17].

rotation) symmetry, which were rarely observed in self-assembling dendrons and dendrimers, have been recently discovered. All these 3D globular phases mentioned above were originally obtained from the self-organisation of inverse micelle-like supramolecular objects, thereby being called the 3D micellar phases. However, with the new designs of dendritic structures of dendrons and dendrimers and new strategy of synthesising dendronized materials to attain dendritic structures which were never obtained from the convergent and divergent methods, such 3D globular phases are not limited to the self-organisation of micelle-like supramolecular spheres, but they can be also obtained from the self-organisation of supramolecular assemblies with polyhedral shape or supramolecular objects with the internal helical order. Recently, many studies reported that the cubic $Pm\overline{3}n$ phase was also obtained from the self-organisation of hollow spherical supramolecular objects[14,52], helical nonhollow spherical supramolecular objects[16,53], and vesicular interdigitated supramolecular assemblies with polyhedral shape[14,43]. The tetragonal $P4_2/mnm$[16,53] and the LQC[16] phases were also obtained from the self-organisation of helical nonhollow spherical supramolecular objects. In addition, the bicontinuous cubic $Ia\overline{3}d$ and the triply continuous $Im\overline{3}m$ (type1) phases, which were never observed in any previously studied dendrons and dendrimers, but observed in phasmidic molecules[54,55], were also obtained from dendrons with fluorinated alkyl tails[56] and dendrons synthesized by the deconstruction method[44] as a new strategy of synthesising new libraries of self-assembling dendrons. The schematic diagram in Figure 1-7 shows the routes of forming 1D lamellar smectic A, 2D columnar and 3D globular as well as bicontinuous cubic $Ia\bar{3}d$ phases of dendrons and dendrimers which were synthesized in Percec's group.

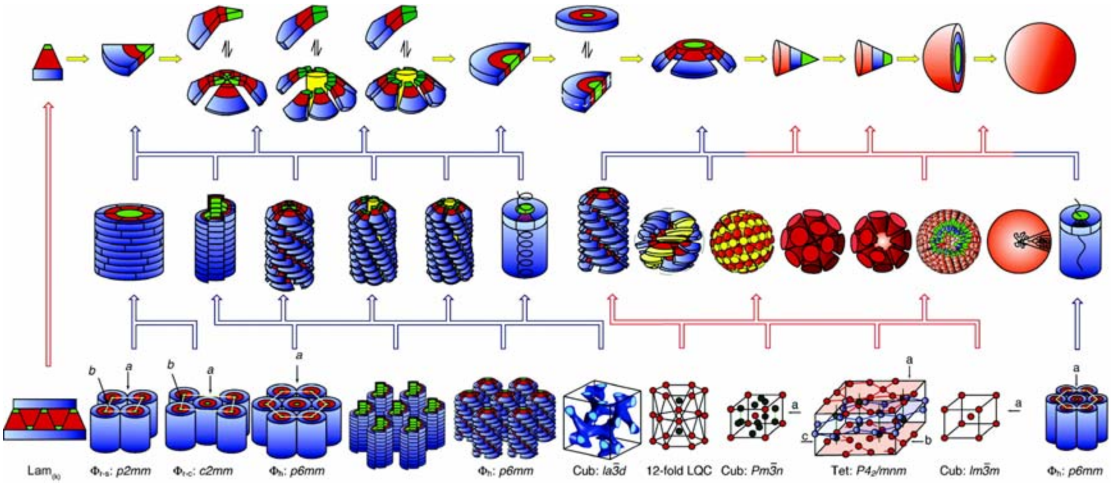

Figure 1-7 The routes of forming various 2D columnar and 3D globular lattices as well as 3D bicontinuous cubic $Ia\bar{3}d$ phase of tapered wedge-shaped dendrons, conical dendrons, semi- and full- sphere dendrons, and crown-like dendrimers[14].

1.5 Objective of the Project

The aim of my PhD project is to study new liquid crystal (LC) phases created by self-assembly of wedge-shaped tree-like liquid crystal-forming molecules. The new molecular structures of these molecules were designed on the basis of the theoretical prediction of achieving undiscovered structures and the previous works of our research group exploring various 2-D columnar and 3-D micellar phases in thermotropic liquid crystals. The phase structures of these molecules at different temperatures are determined by using small angle X-ray scattering (SAXS) and wide angle X-ray scattering (WAXS) methods, together with the information of differential scanning calorimetry (DSC) data. The simulation of powder X-ray data and the recreation of electron density maps are performed to help understand how molecules are self-assembled into supramolecular structures. The structures obtained from self-assembly of molecules are confirmed by running the molecular dynamic simulations. With these study results, studied wedge-shaped dendrons serve as models of a larger class of materials, the so called dendrimers.

References

[1] P. J. Collings, "Liquid crystals: nature's delicate phase of matter", 2nd ed., Princeton N.J., Oxford: Princeton University Press, 2002.

[2] I. W. Hamley, "Introduction to soft matter: polymers, colloids, amphiphiles and liquid crystals", Chichester: Wiley, 2000.

[3] B. J. He and J. S. Maxwell, "Liquid Crystal lecture slides", University of Wisconsin-Madison, Internships in Public Science Education, Spring 2004.

[4] H. Stegemeyer, "Liquid crystals", Darmstadt: New York: Steinkopff; Springer, 1994.

[5] H. Meier and M. Lehmann, "Stilbenoid dendrimers", Angew. Chem. Int. Ed., 1998, 37, 643-645.

[6] S. A. Ponomarenko, N. I. Boiko, V. P. Shibaev, and S. N. Magonov, "Atomic force microscopy study of structural organization of carbosilane liquid crystalline dendrimer", Langmuir, 2000, 16, 5487-5493.

[7] V. Percec, C. M. Mitchell, W. D. Cho, S. Uchida, M. Glodde, G. Ungar, X. B. Xeng et al., "Designing libraries of first generation AB_3 and AB_2 self-assembling dendrons via the primary structure generated from combinations of $(AB)_y$–AB_3 and $(AB)_y$–AB_2 building blocks", J. Am. Chem. Soc., 2004, 126, 6078-6094.

[8] V. Percec, W. D. Cho, P. E. Mosier, G. Ungar and D. J. P. Yeardley, "Structural analysis of cylindrical and spherical supramolecular dendrimers quantifies the concept of monodendron shape control by generation number", J. Am. Chem. Soc., 1998, 120, 11061–11070.

[9] V. Percec, C. M. Mitchell, W. D. Cho, S. Uchida, M. Glodde, G. Ungar, X. B. Xeng et al., "Designing libraries of first generation AB_3 and AB_2 self-assembling dendrons via the primary structure generated from combinations of $(AB)_y$–AB_3 and $(AB)_y$–AB_2 building blocks", J. Am. Chem. Soc., 2004, 126, 6078-6094.

[10] V. Percec, W.D. Cho, G. Ungar and D.J.P. Yeadly, “Synthesis and structural analysis of two constitutional isomeric libraries of AB_2-based monodendrons and supramolecular dendrimers”, J. Am. Chem. Soc., 2001, 123, 1302-1315.

[11] V. Percec, M. Peterca, M. J. Sienkowska, M. A. Ilies, E. Aqad, J. Smidrkal, and P. A. Heiney, “Synthesis and retrostructural analysis of libraries of AB_3 and constitutional isomeric AB_2 phenylpropyl ether-based supramolecular dendrimers”, J. Am. Chem. Soc., 2006, 128, 3324-3334.

[12] V. Percec, M. N. Holerca, S. Nummellin, J. J. Morrison, M. Glodde, J. Smidrkal, M. Peterca, B. M. Rosen, S. Uchida, V. S. K. Balagurusamy, M. J. Sienkowska, and P. A. Heiney, “Exploring and expanding the structural diversity of self-assembling dendrons through combinations of AB, constitutional isomeric AB_2, and AB_3 biphenyl-4-methyl ether building blocks”, Chem. Eur. J. 2006, 12, 6216-6241.

[13] V. Percec, J. Smidrkal, M. Peterca, C. M. Mitchell, S. Nummellin, A. E. Dulcey, M. J. Sienkowska, and P. A. Heiney, “Self-assembling phenylpropyl ether dendronized helical polyphenylacetylenes”, Chem. Eur. J., 2007, 13, 3989-4007.

[14] B. M. Rosen, D. A. Wilson, C. J. Wilson, M. Peterca, B. C. Won, C. H. Huang, L. R. Lipski, X. B. Zeng, G. Ungar, P. A. Heiney, and V. Percec, “Predicting the structure of supramolecular dendrimers via the analysis of libraries of AB_3 and constitutional isomeric AB_2 biphenylpropyl ether self-assembling dendrons”, J. Am. Chem. Soc., 2009, 131, 17500–17521.

[15] V. Percec, B. C. Won, M. Peterca, and P. A. Heiney, “Expanding the structural diversity of self-assembling dendrons and supramolecular dendrimers via complex building blocks”, J. Am. Chem. Soc., 2007, 129, 11265-11278.

[16] V. Percec, M. R. Imam, M. Peterca, D. A. Wilson, R. Graf, H. W. Spiess, V. S. K. Balagurusamy and P. A. Heiney, “Self-assembly of dendronized triphenylenes into helical pyramidal columns and chiral spheres”, J. Am. Chem. Soc., 2009, 131, 7662–7677.

[17] M. Peterca, V. Percec, M. R. Imam, P. Leonawat, K. Morimitsu, and P. A. Heiney, “Molecular structure of helical supramolecular dendrimers”, J. Am. Chem. Soc., 2008, 130, 14840-14852.

[18] V. Percec, M. Glodde, G. Johansson, V.S.K. Balagurusamy and P.A. Heiney, “Transformation of a spherical suprmaolecular dendrimer into a pyramidal

columnar supramolecular dendrimer mediated by the fluorophobic effect", Angew. Chem. Int. Ed., 2003, 42, 4338-4342.

[19] V. Percec, M. R. Imam, T. K. Bera, V. S. K. Balagurusamy, M. Peterca and P. A. Heiney, "Self-assembly of semifluorinated Janus-dendritic benzamides into bilayered pyramidal columns", Angew. Chem. Int. Ed., 2005, 44, 4739-4745.

[20] M. Peterca, M. R. Imam, C. H. Ahn, V. S. K. Balagurusamy, D. A. Wilson, B. M. Rosen, and V. Percec, "Transfer, amplification, and inversion of helical chirality mediated by concerted interactions of C_3-supramolecular dendrimers", J. Am. Chem. Soc., 2011, 133, 2311–2328.

[21] V. Percec, A. E. Dulcey, M. Peterca, M. Ilies, S. Nummelin, M. J. Sienkowska, and P. A. Heiney, "Principles of self-assembly of helical pores from dendritic dipeptides", Proc. Nat. Acad. Sci. U.S.A., 2006, 103, 2518-2523.

[22] V. Percec, A. E. Dulcey, V. S. K. Balagurusamy, Y. Miura, J. Smidrkal, M. Peterca, S. Nummelin, U. Edlund, S. D. Hudson, P. A. Heiney, H. Duan, S. N. Maganov, and S. A. Vinogradov, "Self-assembly of amphiphilic dendritic dipeptides into helical pores", Nature, 2004, 430, 764-768.

[23] V. Percec, A. S. E. Dulcey, M. Peterca, M. Ilies, J. Ladislaw, B. M. Rosen, U. Edlund, and P. A. Heiney, "The internal structure of helical pores self-assembled from dendritic dipeptides is stereochemically programmed and allosterically regulated", Angew. Chem. Int. Ed ., 2005, 44, 6516-6521.

[24] V. Percec, A. Dulcey, M. Peterca, M. Ilies, Y. Miura, U. Edlund, and P. A. Heiney, "Helical porous protein mimics self-assembled from amphiphilic dendritic dipeptides", Aust. J. Chem., 2005, 58, 472-482.

[25] V. Percec, A. E. Dulcey, M. Peterca, M. Ilies, M. J. Sienkowska, and P. A. Heiney, "Programming the internal structure and stability of helical pores self-assembled from dendritic dipeptides via the protective groups of the peptide", J. Am. Chem. Soc., 2005, 127, 17902-17909.

[26] M. Peterca, V. Percec, A. E. Dulcey, S. Nummelin, S. Korey, M. Ilies, and P. A. Heiney, "Self-assembly, structural, and retrostructural analysis of dendritic dipeptide pores undergoing reversible circular to elliptical shape change", J. Am. Chem. Soc., 2006, 128, 6713-6720.

[27] V. Percec, A. E. Dulcey, M. Peterca, P. Adelman, R. Samant, V. S. K. Balagurusamy, and P. A. Heiney, "Helical pores self-assembled from homochiral

dendritic dipeptides based on L-Tyr and nonpolar alpha-amino acids", J. Am. Chem. Soc., 2007, 129, 5992-6002.

[28] M. S. Kaucher, M. Peterca, A. E. Dulcey, A. J. Kim, S. A. Vinogradov, D. A. Hammer, P. A. Heiney, and V. Percec, "Selective transport of water mediated by porous dendritic dipeptides", J. Am. Chem. Soc., 2007, 129, 11698-11699.

[29] B. M. Rosen, C. J. Wilson, D. A. Wilson, M. Peterca, M. R. Imam, and V. Percec, "Dendron-mediated self-assembly, disassembly, and self-organization of complex systems", Chem. Rev., 2009, 109, 6275-6540.

[30] J. K. Kim, M. K. Hong, J. H. Ahn, and M. Lee, "Liquid-crystalline assembly from rigid wedge–flexible coil diblock molecules", Angew. Chem. Int. Ed., 2005, 44, 328–332.

[31] E. R. Zubarev, M. U. Pralle, E. D. Sone, and S. I. Stupp, "Self-assembly of dendron rodcoil molecules into nanoribbons", J. Am. Chem. Soc., 2001, 123, 4105-4106.

[32] N. Sakai, Y. Kamikawa, M. Nishii, T. Matsuoka, T. Kato, and S. Matile, "Dendritic folate rosettes as ion channels in lipid bilayers", J. Am. Chem. Soc., 2006, 128, 2218-2219.

[33] X. Zhang, Z. Chen, and F. Wurthner, "Morphology Control of Fluorescent Nanoaggregates by Co-Self-Assembly of Wedge- and Dumbbell-Shaped Amphiphilic Perylene Bisimides", J. Am. Chem. Soc., 2007, 129, 4886-4887.

[34] L. Gehringer, C. Bourgogne, D. Guillon, and B. Donnio, "Liquid-crystalline octopus dendrimers: block molecules with unusual mesophase morphologies", J. Am. Chem. Soc., 2004, 126, 3856-3867.

[35] A. G. Cook, U. Baumeister, and C. Tschierske, "Supramolecular dendrimers: unusual mesophases of ionic liquid crystals derived from protonation of DAB dendrimers with facial amphiphilic carboxylic acids", J. Mater. Chem., 2005, 15, 1708-1721.

[36] I. Bury, B. Heinrich, C. Bourgogne, D. Guillon, and B. Donnio, "Supramolecular self-organization of "Janus-like" diblock codendrimers: synthesis, thermal behaviour, and phase modeling", Chem. Eur. J., 2006, 12, 8396-8413.

[37] M. Lee, Y. S. Jeong, B. K. Cho, N. K. Oh, and W. C. Zin, "Self-assembly of molecular dumbbells into organized bundles with tunable size", Chem. Eur. J., 2002, 8, 876-883.

[38] B. K. Cho, A. Jain, S. M. Gruner, and U. Wiesner, “Mesophase structure-mechanical and ionic transport correlations in extended amphiphilic dendrons”, Science, 2004, 305, 1598–1601.

[39] D. R. Dukeson, G. Ungar, V. S. K. Balagurusamy, V. Percec, G. A. Johansson, and M. Glodde, “Application of isomorphous replacement in the structure determination of a cubic liquid crystal phase and location of counterions”, J. Am. Chem. Soc., 2003, 125, 15974-15980.

[40] V. Percec, M. Peterca, Y. Tsuda, B. M. Rosen, S. Uchida, M. R. Imam, G. Ungar, and P. A. Heiney, “Elucidating the structure of the cubic phase of supramolecular dendrimers through the modification of their aliphatic to aromatic volume ratio”, Chem. Eur. J., 2009, 15, 8994–9004.

[41] V. Percec, J. G. Rudick, M. Peterca, M. E. Yurchenko, J. Smidrkal, and P. A. Heiney, “Supramolecular structural diversity among first-generation hybrid dendrimers and twin dendrons”, Chem. Eur. J., 2008, 14, 3355-3362.

[42] V. S. K. Balagurusamy, G. Ungar, V. Percec and J. Johansson, “Rational design of the first spherical supramolecular dendrimers self-organised in a novel thermotropic cubic liquid-crystalline phase and the determination of their shape by X-ray analysis”, J. Am. Chem. Soc., 1997, 119, 1539-1555.

[43] M. Peterca, M. R. Imam, P. Leowanawat, B. M. Rosen, D. A. Wilson, C. J. Wilson, X. B. Zeng, G. Ungar, P. A. Heiney, and V. Percec, “Self-assembly of hybrid dendrons into doubly segregated supramolecular polyhedral columns and vesicles”, J. Am. Chem. Soc., 2010, 132, 11288-1305.

[44] B. M. Rosen, M. Peterca, C. Huang, X. B. Zeng, G. Ungar, and V. Percec, “Deconstruction as a strategy for the design of libraries of self-assembling dendrons”, Angew. Chem. Int. Ed., 2010, 49, 7002 –7005.

[45] V. Percec, C. H. Ahn, T. K. Bera, G. Ungar, and D. J. P. Yeardley, “Coassembly of a hexagonal columnar liquid crystalline superlattice from polymer(s) coated with a three-cylindrical bundle supramolecular dendrimer”, Chem. Eur. J., 1999, 5, 1070-1083.

[46] V. Percec, T. K. Bera, M. Glodde, Q. Y. Fu, V.S.K. Balagurusamy, and P. A. Heiney, “Hierarchical self-assembly, coassembly, and self-organization of novel liquid crystalline lattices and superlattices from a twin-tapered dendritic benzamide and its four-cylinder-bundle supramolecular polymer”, Chem. Eur. J., 2003, 9, 921-935.

[47] S. D. Hudson, H. T. Jung, V. Percec, W. D. Cho, G. Johansson, G. Ungar and V. S. K. Balagurusamy, “Direct visualization of individual cylindrical and spherical supramolecular dendrimers”, Science, 1997, 278, 449-452.

[48] D. J. P. Yeardley, G. Ungar, V. Percec, M. N. Holerca and G. Johansson, “Spherical supramolecular minidendrimers self organized in an inverse micellar-like thermotropic body-centered cubic liquid crystalline phase”, J. Am. Chem. Soc., 2000**,** 122, 1684-1689.

[49] H. Duan, S. D. Hudson, G. Ungar, M. N. Holerca and V. Percec, “Definitive support by transmission electron microscopy, electron diffraction, and electron density maps for the formation of a BCC lattice from poly{n-[3,4,5-tris(n-dodecan-l-yloxy)benzoyl]ethyleneimine}”, Chem. Eur. J., 2001, 7, 4134-4141.

[50] G. Ungar, Y. S. Liu, X. B. Zeng, V. Percec and W. D. Cho, “Giant supramolecular liquid crystal lattice”, Science, 2003, 299, 1208-1211.

[51] X. B. Zeng, G. Ungar, Y. S. Liu, V. Percec, S. E. Dulcey, and J. K. Hobbs, “Supramolecular dendritic liquid quasicrystals”, Nature, 2004, 428, 157-160.

[52] V. Percec, M. Peterca, A. E. Dulcey, M. R. Imam, S. D. Hudson, S. Nummelin, P. Adelman, and P. A. Heiney, “Hollow spherical supramolecular dendrimers”, J. Am. Chem. Soc., 2008, 130, 13079-13094.

[53] V. Percec, M. R. Imam, M. Peterca, D. A. Wilson, and P. A. Heiney, “Self-assembly of dendritic crowns into chiral supramolecular spheres”, J. Am. Chem. Soc., 2009, 131, 1294-1304.

[54] X. B. Zeng, L. Cseh, G. H. Mehl, and G. Ungar, “Testing the triple network structure of the cubic $Im\bar{3}m$ (I) phase by isomorphous replacement and model refinement”, J. Mater. Chem., 2008, 18, 2953-2961.

[55] X. Zeng, G. Ungar, M. Imperor-Clerc, “A triple-network tricontinuous cubic liquid crystal”, Nat. Mater., 2005, 4, 562-567.

[56] S. N. Chvalun, M. A. Shcherbina, A. N. Yakunin, J. Blackwell and V. Percec, “Structure of gyroid mesophase formed by monodendrons with fluorinated alkyl tails”, Polym. Sci., Ser. A, 2007, 49, 158–167.

Chapter 2

X-ray Diffraction

2.1 Introduction

X-ray diffraction is a versatile technique. For example, it is used to determine the structures of materials, analyse the phase composition of powders, measure stress of materials, etc. In my work, X-ray diffraction is the main method used to investigate the structures of the studied materials. Therefore, the application of X-ray diffraction in the structural determination is discussed here. In this chapter, the fundamental principle of X-ray diffraction and Bragg’s law are explained first. Then, the reciprocal lattice and a geometrical tool called Ewald sphere, which is used to explain the geometrical condition of diffraction in reciprocal space, are explained. Small angle X-ray scattering (SAXS) and wide angle X-ray scattering (WAXS), which are techniques of X-ray diffraction, are described in the next section. The derivation of diffraction pattern of powder materials, indexing powder diffraction pattern and recreating electron density maps are explained consecutively in the last three sections in this chapter.

2.2 X-ray Diffraction

X-ray diffraction is the process when X-rays pass through crystals and are scattered by the electrons of the atoms. X-rays are electromagnetic waves. The scattering process of X-rays is regarded as the emission of coherent secondary waves from the electrons of the atoms when they are excited and resonate with the frequency of periodically changing electric field of X-rays. The outgoing waves will superimpose and the outcome of interference depends on amplitude, wavelength and relative phase of waves. If waves have the same wavelength, amplitude and phase at the starting point of propagation and propagate at the same distance, such waves are still in phase and the addition of waves will yield the resultant waveform having the maximum amplitude from the summation of amplitude of each wave. This is known as constructive interference. Conversely, if such waves propagate at a different distance, they are out of phase. So, the amplitude of the resultant waveform will be less than that of the resultant waveform in case of constructive interference. The simplest example for understanding of the latter case is of the superimposition of two waves having the same wavelength and amplitude. If two waves are 180° out of phase, the amplitude of the resultant waveform will be zero. This case is known as destructive interference

2.3 Bragg's Law

Bragg's law is the geometrical conditions of scattering of X-rays which produce the maximum intensity of diffraction peaks. Figure 2-1 demonstrates the scattering of X-rays caused by regularly spaced rows of atoms. X-rays are incident on atoms with the angle of incidence θ and are scattered in all directions. The maximum intensity of diffraction peaks (i.e. Bragg peaks) will be obtained only if the angle of incidence and the angle of scattering of X-rays are equal and the path difference between any two rays, e.g. rays $1K1'$ and $2L2'$, is a multiple of X-ray wavelength. According to Figure 2-1, the path difference for rays $1K1'$ and $2L2'$ is

$$ML + LN = d\,sin\theta + d\,sin\theta = 2d\,sin\theta \tag{2-1}$$

The maximum intensity of diffraction peaks will be obtained only if the path difference between those two rays is a multiple of wavelength

$$2d_{hkl}\sin\theta_B = n\lambda \tag{2-2}$$

where θ_B is the Bragg angle,

d_{hkl} is the interplanar spacing of (*hkl*) plane,

and n is the integer number.

Equation (2-2) is commonly known as Bragg's equation.

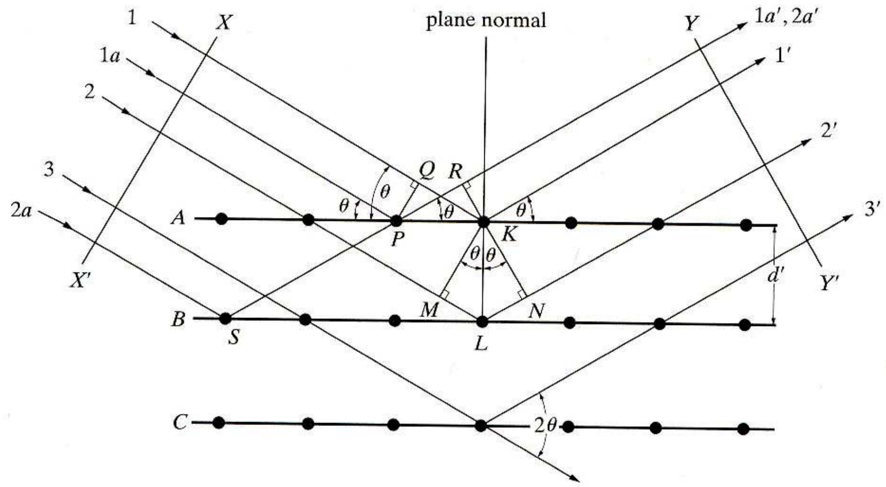

Figure 2-1 Diffraction of X-rays by a crystal[1].

2.4 Reciprocal Lattice

The reciprocal lattice is an array of imaginary points, each of which represents a plane in the real lattice space in a crystal. Reciprocal-lattice concept is the thinking of sets of planes in terms of their normals instead of two dimensional planes. The construction of the reciprocal lattice is demonstrated in Figure 2-2. The origin of the reciprocal lattice space coincides with that of the real lattice space. For a given (*hkl*) plane in the real space, a line of the length $1/d_{hkl}$ is drawn perpendicular to that (*hkl*) plane. Then, a point is created at the end of that line and this is the reciprocal lattice point corresponding to that plane. With a number of planes in the real lattice space, the corresponding reciprocal lattice points will be created and these points will form the reciprocal lattice. With the construction of the reciprocal lattice, a relationship between the reciprocal axes, i.e. $\vec{a}^*$, $\vec{b}^*$, and $\vec{c}^*$, and the real axes, $\vec{a}$, $\vec{b}$, and $\vec{c}$, will be obtained as follows:

$$\begin{array}{lll} \vec{a}^*.\vec{a}=1 & \vec{a}^*.\vec{b}=0 & \vec{a}^*.\vec{c}=0 \\ \vec{b}^*.\vec{a}=0 & \vec{b}^*.\vec{b}=1 & \vec{b}^*.\vec{c}=0 \\ \vec{c}^*.\vec{a}=0 & \vec{c}^*.\vec{b}=0 & \vec{c}^*.\vec{c}=1 \end{array} \tag{2-3}$$

Therefore, a reciprocal lattice vector $\vec{s}_{hkl}$ pointing to a reciprocal lattice point of the (*hkl*) plane can be written in vector notation.

$$\vec{s}_{hkl} = h\vec{a}^* + k\vec{b}^* + l\vec{c}^* \tag{2-4}$$

The reciprocal space is also considered as the momentum space which a reciprocal lattice vector is the momentum difference of incoming and diffracted X rays. The concept of the reciprocal lattice is useful in the interpretation of X-ray diffraction patterns since diffraction patterns are considered as the Fourier transform of the electron density from the real space to the reciprocal space. Therefore, the determination of reciprocal lattice vectors will tell us the positions of atoms in a crystal or the positions of molecules in the studied materials.

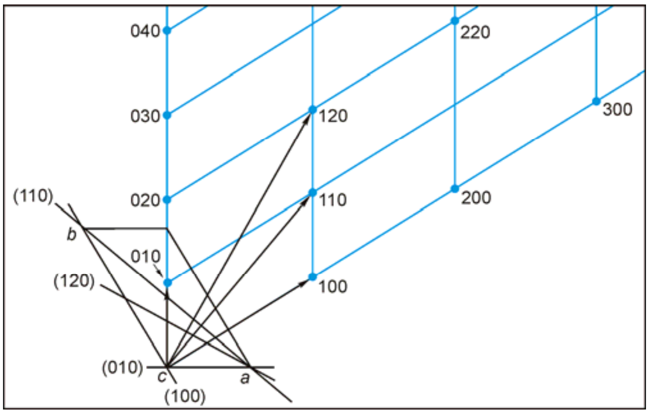

Figure 2-2 A unit cell of a monoclinic crystal looking along [001] zone (black) and the corresponding reciprocal lattice (blue)[2].

2.5 Ewald Sphere

The geometrical conditions for X-ray diffraction in real space were described in section 2.3. In reciprocal space, a useful geometric tool, known as *Ewald sphere* or *sphere of reflection*, derived from Bragg's equation, is used to portray the diffraction. According to Eq. (2-2), when any order reflections can be considered as a first-order (n=1) reflection of real or fictitious planes, Bragg equation can be rearranged to

$$\sin\theta_B = \frac{1/d_{hkl}}{2/\lambda}. \tag{2-5}$$

It is known that any triangle which is inscribed in a circle and has a hypotenuse as the diameter of circle is a right triangle. Therefore, according to Eq. (2-5) a right triangle can be obtained from drawing a triangle whose one leg equals to $1/d_{hkl}$ and inscribing in a circle (or a sphere in 3D) of diameter $2/\lambda$, (see Figure 2-3a). With the concept of reciprocal lattice, Figure 2-3a can be interpreted in the following way. When a beam of X-rays is incident on the plane (*hkl*), the diffraction will occur if and only if the reciprocal lattice point P_{hkl}, representing plane (*hkl*), lies on that circle (or a sphere in 3D) and the diffracted beam will pass through that point. In three dimensions, this sphere is known as Ewald sphere.

Powder diffraction patterns can be presented by one dimensional intensity plots showing the intensities and the q_{hkl} values, i.e. $q_{hkl} = 2\pi / d_{hkl}$, of Debye rings in diffraction patterns. q_{hkl} is the magnitude of a reciprocal lattice vector $\vec{q}_{hkl}$ in q-reciprocal space. $\vec{q}_{hkl}$ is equivalent to $\vec{s}_{hkl}$, that the latter is expressed in Eq. (2-4). They are just different by the factor 2π which come from different definitions of reciprocal lattice vectors defined by physicists, i.e. $e^{i\vec{q}.\vec{r}} = 1$, and by crystallographers, i.e. $e^{2\pi i\vec{s}.\vec{r}} = 1$, where $\vec{r}$ is the position vector of the lattice point in real space. According to Figure 2-3b, incident and diffracted X-rays are represented by wave vectors $\vec{k}_i$ and $\vec{k}_f$ respectively. $\vec{q}_{hkl} = \vec{k}_f - \vec{k}_i$ is considered as the momentum transfer occurring in the crystal, that the momentum transfer can be expressed in wavenumber units in reciprocal length, i.e. $q = k_f - k_i$. q can be also expressed in Bragg angle according to Eq. (2-6)

$$q = \frac{4\pi \sin\theta}{\lambda} \tag{2-6}$$

or

$$q = \frac{2\pi}{d} \tag{2-7}$$

Using q-values rather than using $2\theta_B$ values to present the positions of diffraction peaks is useful since q does not depend on the type of radiation and wavelength used. Therefore, the diffraction results obtained from the different methods and different types of radiation can be compared.

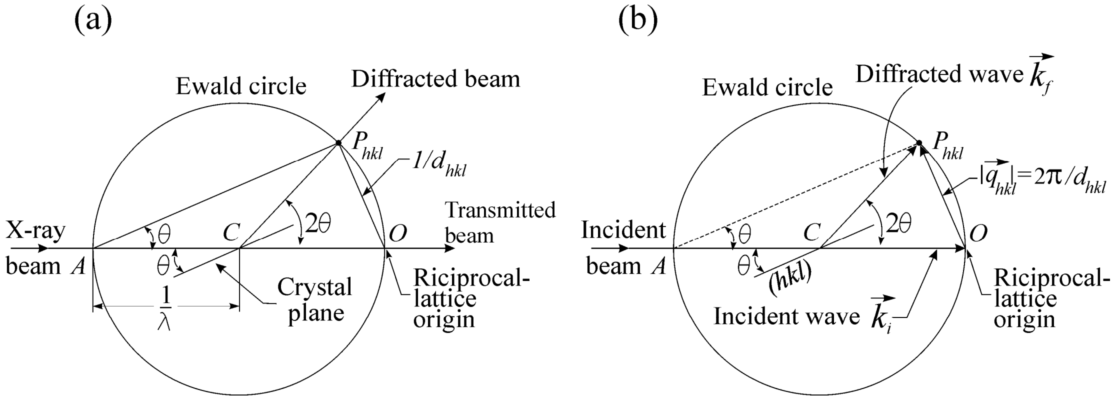

Figure 2-3 (a) Geometrical conditions for diffraction in reciprocal space[2] (b) The scattering vector $\vec{q}$ in q-reciprocal space.

2.6 SAXS and WAXS

Small angle X-ray scattering (SAXS) and wide angle X-ray scattering (WAXS) are techniques for studying the structures of materials. The basic idea of these techniques is based on a reciprocity between the scattering angle and the variation in electron density in the studied materials. Scattering of X-rays at small angle, i.e. $2\theta_B < 10^{\circ}$, is resulted from the inhomogenieties of electron density of the order larger than interatomic distance, and vice versa. This can be understood from considering Ewald sphere in Figure 2-3a. Very small q values (i.e. very big interplanar d-spacing), when compared to the radius of Ewald sphere of $1/\lambda$, correspond to very small scattering angle $2\theta_B$. For example, if a monochromatic beam of X-rays at wavelength 1.5401 Å, i.e. Cu Kα1, is used to determine the structures of materials, the scattered X-rays collected in a range of $2\theta_B$ of 0.7° - 7°, i.e. q range of 0.1-0.5 Å^{-1}, come from the inhomogenieties of electron density in a range of 13-126 Å. In this study, SAXS is used to determine the 2-D and 3-D periodic lattice structures obtained from the self-organisation of supramolecular objects (see Figure 2-4) whose diameters are of the order of 35-50 Å and the size of corresponding unit cells are of the order of 40-80 Å.

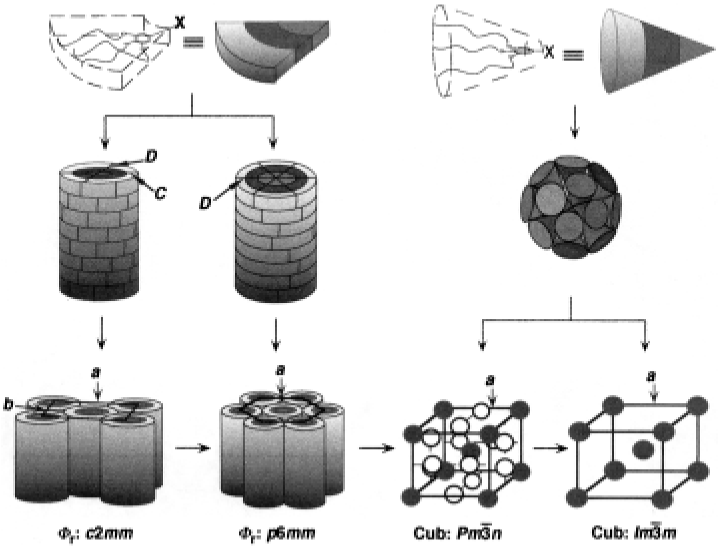

Figure 2-4 Schematic representation of forming 2D and 3D supramolecular structures from self-asembling of dendrons and self-organisaton of corresponding supramolecular objects[3].

2.7 Powder Diffractions

According to Figure 2-3b, if a crystal plane P_{hkl} assumes all possible orientations, the scattering vector $\vec{q}$ will form a sphere whose radius is $2\pi / d_{hkl}$. The tilting of crystal planes to all possible orientations is equivalent to crystal planes in powder materials having all possible orientations. Therefore, for powder materials reciprocal space consists of many spheres, each of which is shared by crystal planes having the same interplanar spacing. When these spheres intersect the Ewald sphere (see Figure 2-5a), diffraction rings will be obtained. Figure 2-5b shows the diffraction rings of powder material recorded by an area detector. For powder materials, a 1D profile, i.e. the plot of intensity vs q, is normally presented and it can be obtained from 2D data by performing radial integration.

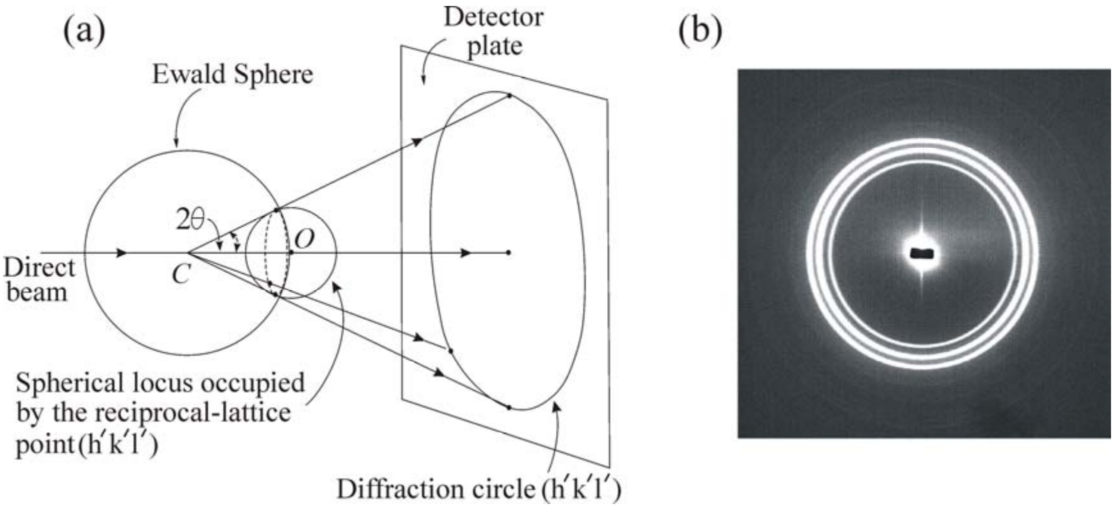

Figure 2-5 (a) The derivation of a Debye ring[4]. (b) Diffraction pattern of powder sample recorded by area detector at station 2.1, SRS Daresbury Laboratory.

2.8 Indexing Diffraction Pattern

Indexing diffraction pattern is the preliminary procedure for the structural determination of studied materials. The different characteristics of diffraction patterns are resulted from different arrangements of atoms or molecules to various structures. Indexing diffraction pattern can be done manually or by using computer softwares. For manually indexing diffraction pattern, the first thing to do is to measure q value of each reflection. Next step is to take the square of ratios of q values in order to find out which crystal system the structure of the studied materials belongs to. If the square of ratios of q values is in sequence 1, 2, 3, 4 and so on, the obtained structure falls into a cubic system. If the square of ratios of q values is in sequence 1, 3, 4, 7, etc, the obtained structure belongs to a hexagonal system. Identifying a crystal system by taking the square of ratios of q values takes the advantage of having small number of principal crystallographic parameters of high symmetry systems. This also helps a lot in guessing the Miller indices (*hkl*) of each diffraction peak. After a crystal system of materials is assumed, the Miller indices (*hkl*) of each diffraction peak will be guessed by trial and error. Guessing (*hkl*) indices of diffraction peaks always starts from the first few peaks with the lowest h, k, l values. With q values and guessed h, k, l indices of first few peaks, a^*, b^*, and c^* are determined by using Eq. (2-8). With a^*, b^*, and c^* obtained from guessing h, k, l indices of the first few peaks, the q values of higher diffraction orders are calculated and compared to the measured ones. The procedure is repeated until a satisfactory match is found.

For low symmetry crystal systems such as triclinic, tetragonal, or orthorhombic systems, manually indexing diffraction pattern is more difficult since low symmetry crystal systems, especially triclinic system, are characterised by more principal crystallographic parameters, i.e. *a*, *b*, *c*, *α*, *β*, and *γ*. Hence, computer programs have been developed. Nonetheless, the usage of indexing programs has limitations. Therefore, manually indexing powder diffraction pattern are still necessary.

$$\begin{aligned} q_{hkl}{}^{2} &= \vec{q}_{hkl}.\vec{q}_{hkl} = (h\vec{a}^{*} + k\vec{b}^{*} + l\vec{c}^{*}) \, . \, (h\vec{a}^{*} + k\vec{b}^{*} + l\vec{c}^{*}) \\ &= h^{2}a^{*2} + k^{2}b^{*2} + l^{2}c^{*2} + 2hka^{*}b^{*}\cos\gamma^{*} + 2hla^{*}c^{*}\cos\beta^{*} + 2klb^{*}c^{*}\cos\alpha^{*} \qquad (2\text{-}8) \end{aligned}$$

where $\alpha^{*} = \mathrm{sine}^{-1}\left(\dfrac{\mathrm{V}}{\mathrm{abc}\ \sin\beta\ \sin\gamma}\right)$

$$\beta^{*} = \mathrm{sine}^{-1}\left(\frac{\mathrm{V}}{\mathrm{abc}\ \sin\alpha\ \sin\gamma}\right)$$

$$\gamma^{*} = \mathrm{sine}^{-1}\left(\frac{\mathrm{V}}{\mathrm{abc}\ \sin\alpha\ \sin\beta}\right)$$

$$\mathrm{V} = abc\ (1\text{-}\cos^{2}\alpha - \cos^{2}\beta - \cos^{2}\gamma + 2\cos\alpha\ \cos\beta\ \cos\gamma)^{1/2}.$$

2.9 Electron Density Reconstruction

Reconstructing the electron density map is an important structural analysis procedure which will elucidate how atoms or molecules are arranged. The electron density map can be obtained from performing the inverse Fourier transform of the diffraction pattern.

To recreate the electron density map, the electron density which can be expressed as a Fourier series according to Eq. (2-9) will be computed.

$$\rho(x,y,z) = \frac{1}{V}\sum_{h,k,l}\sqrt{I(h,k,l)}\exp[-\,i2\pi(hx+ky+lz) + i\phi_{h,k,l}] \qquad (2\text{-}9)$$

$\rho(x,y,z)$ is the electron density at point (x,y,z) in the unit cell. $I(h,k,l)$ and $\phi_{h,k,l}$ are the integrated intensity and the phase angle of each diffraction peak associated with the (*hkl*) indices respectively. The phase angle of each diffraction peak cannot be directly measured from the experiments, therefore causing the problem of recreating the electron density map. Luckily for crystallographers, if the structure is centrosymmetric – in other words, having an inversion centre, i.e. $\rho(x,y,z)=\rho(-x,-y,-z)$, the phase angle $\phi_{h,k,l}$ for each diffraction peak can be only either 0 or π. Therefore, Eq. (2-9) can be simplified to

$$\rho(x,y,z)=\frac{1}{V}\sum_{h,k,l}\sqrt{I(h,k,l)}\ cos\ [-\ 2\pi(hx+ky+lz)+\phi_{h,k,l}]. \qquad (2\text{-}10)$$

Using additional information about the studied system, a choice of the correct phase combination is made on the basis of the physical merits of the electron density maps and the corresponding histograms of the electron density distribution. The right choice should give a good separation between low- and high electron density regions of the histogram and a volume ratio of low- and high electron density regions of the histogram should be consistent with that of molecules calculated from the molecular model.

References

[1] B. D. Cullity and S. R. Stock, "Elements of X-ray diffraction", 3rd ed., Upper Saddle River, New Jersey: Prentice Hall, 2001.

[2] L. V. Azároff, "Elements of X-ray crystallography", New York: McGraw-Hill, 1968.

[3] V. Percec, M. N. Holerca, S. Uchida, W. D. Cho, G. Ungar, Y. S. Lee and D. J. P. Yeardley, "Exploring and expanding the three-dimensional structural diversity of supramolecular dendrimers with the aid of libraries of alkali metals of their AB_3 minidendritic carboxylates", Chem. Eur. J. 2002, 8, 1106-1117.

[4] L. E. Alexander, "X-ray diffraction methods in polymer science", New York: Wiley-Interscience, 1969.

Chapter 3

Apparatus and Data Reduction

3.1 Introduction

Synchrotron is a powerful source of X-ray radiation of outstanding versatility for academic and industrial research. For my works, the X-ray source used to carry out the experiments was the Synchrotron Radiation Source (SRS), Daresbury Laboratory. The X-ray diffraction experiments were performed at stations 2.1 and 6.2. Hence, in this chapter synchrotron radiation and its applications, especially for the field of materials science, are presented in the first section. In the following section, the apparatus at stations 2.1 and 6.2 are schematically described. The way of conducting the experiments is given in the next section, and the procedures for data reduction are explained in detail in the last part of this chapter.

3.2 Synchrotron Radiation Source

Synchrotron radiation is produced from accelerating charged particles close to the speed of light. Charged particles do not radiate power while they are in uniform motion. However, when they are accelerated, they will emit electromagnetic radiation. Electromagnetic radiation emitted from a synchrotron ranges in wavelength from 10^{-4} to 10^{-11} meters and covers the spectrum from hard X-rays, via UV, visible and into the infrared.

Synchrotron is a cyclic charged particle accelerator. It comprises three main parts, i.e. the linear accelerator (LINAC), the intermediate synchrotron (or booster synchrotron), and the main ring (or the storage ring). The charged particles mostly used to produce radiation are electrons since electrons are light particles, thereby losing a larger fraction of their energy when their trajectory is bent. Free electrons are generated by an electron gun and bunched by the buncher in short pulses (in order of tens nanoseconds) before moving to the LINAC. At LINAC, bunches of electrons are accelerated by applying microwave radio frequency fields generated from a klystron. The acceleration of bunches of electrons results from synchronising the movement of groups of electrons with the applied field in such a way that bunches of electrons always meet the crest of a wave to gain the energy from wave. This is similar to the movement of a surfer pushed by a water wave. The groups of electrons travel along a vacuum chamber to avoid losing their energy in collisions with air molecules. At the end of the LINAC, bunches of electrons are kicked by a kicker magnet into the intermediate synchrotron to boost their energy. At the booster ring, bunches of electrons circulate around the ring and obtain energy from microwaves generated from a radio frequency (RF) cavity. Their energy is increased every cycle while they circulate through the RF cavity. Meanwhile, the speed of electrons is also increased. To maintain the orbit of electrons while they are circulating and their energy and speed are being increased, two main magnets, bending magnets and quadrupole magnets, are used to control the orbit of electrons. Bending magnets (or dipole magnets) are used to turn electrons to travel along the circular path of the ring whereas quadrupole magnets are used to focus the electrons back into the ideal orbit. When the energy of electrons reaches a level where electrons can produce synchrotron light, the speed of the electrons is close to the speed of light and bunches of electrons will be injected into the storage ring to circulate for hours at constant energy to produce synchrotron radiation for users. The storage ring has the shape of a round-cornered polygon. Round corners are usually house bending magnets which bend the electron path and produce radiation. Straight sections of a ring are essentially required for putting the RF cavities to add energy to the electrons lost in the production of synchrotron radiation. In addition, quadrupole magnets are used to focus the electron beam to the ideal trajectory whereas other magnets like sextupole magnets and steering magnets are used to correct the orbit of electrons. The energy of synchrotron radiation depends on the radius of the synchrotron ring and the strength of magnetic field of the bending magnets. Hence, more powerful synchrotrons are built by having a large radius and using many powerful RF cavities to accelerate the electrons. However, building a large-radius synchrotron is very costly. To overcome the energy limitation of small-size synchrotrons, insertion devices such as wigglers and undulators are inserted into the synchrotron ring at straight sections to extract more energy from the relativistic electrons. At the bending magnets and the insertion devices, experimental stations (or beam lines) are built to transport photons to the experimental cabins where the sample are placed. Note that the above describes the operation of a basic particle accelerator[1,2]. The main parts of accelerators, especially for modern particle accelerators, may be varied according to their designs.

Synchrotron radiation has excellent properties. The spectrum of synchrotron radiation is continuous and has a wide range, covering infrared, visible, ultraviolet, and X-ray wavelengths. A particular range of energies or a fixed energy can be used and selected by the monochromator. With this property of synchrotron radiation, using energy-dispersive techniques like X-ray absorption spectroscopy (XAS) and X-ray fluorescence (XRF) the element and its local structure, bond lengths and coordination numbers in a compound, including information of neighbouring atoms, can be obtained and identified . Synchrotron radiation has a pulsed structure or a time structure since it is produced from bunches of relativistic electrons. The pulse length is typically 10 to 100 picoseconds and they are separated by 10 to 100 nanoseconds. With this property, the mechanics of time-dependence, with a time scale ranges from nanoseconds to hours, can be studied. The synchrotron beam is highly collimated since the angular divergence of the beam is very small. Hence, it is applied to lithographic patterning and structuring materials on micro- and nanoscale, commonly known as microlithography and nanolithography respectively. Synchrotron beam also has low emittance, i.e. small cross section and small solid angle. Thus, it has very high concentration of photon flux and this ensures that a high number of photons still reach the sample when placed at some distance from the radiation source. Because of having very high concentration of photons, synchrotron light is extremely bright, billions times brighter than sunlight. The intensity of synchrotron radiation can be of the order of a billion times greater than that of radiation obtained from an in-house laboratory X-ray source. Hence, the exposure time used in the experiments is short, which not only saves a lot of time but also produces a lot of data. More importantly, studies of dynamic processes or dynamic structural changes in both biological and chemical materials can be performed *in situ*. In addition, synchrotron is a clean radiation source since emission of synchrotron light takes place in ultra-high vacuum. Hence, the instrumental contamination of the sample is negligible. With these properties, the synchrotron radiation source becomes a powerful radiation source for academic and industrial research.

3.3 Apparatus

The X-ray diffraction experiments were performed at stations 2.1 and 6.2 of the synchrotron radiation source (SRS), Daresbury Laboratory. In this section, the apparatus at the station 2.1 and 6.2 are schematically described.

3.3.1 Station 2.1

At station 2.1, synchrotron radiation is generated by a 1.2 T bending magnet. According to the schematic drawing of station 2.1 in Figure 3-1, the synchrotron beam goes down along the ultra-high vacuum tube and passes through the horizontal and vertical water-cooled apertures positioned before a monochromator. Both apertures are used to limit horizontal and vertical beam acceptance. After passing two apertures, the synchrotron beam is monochromatized by a monochromator using the triangular bent Ge (111) crystal to select the energy of synchrotron beam at 8.04 keV X-rays (i.e. λ=1.54 Å). Because of using a bent crystal monochromator, the X-ray beam coming out from the monochromator is also horizontally focused. Then, the monochromatic X-ray beam passes through the first pair of vertical and horizontal slits and is vertically focused by an uncoated fused quartz mirror. Next to the focusing mirror, three pairs of slits are used to collimate the beam in the vertical and horizontal planes. Each set of slits comprises two vertical and two horizontal jaws which can be moved independently of each other. Therefore, four pairs of slits, i.e. one before the focusing mirror and three after the focusing mirror, are used to define the beam size at the sample position. Next to the fourth slit, two ionisation chambers are installed before and after the sample to observe the status of the beam. In addition, the readings from the ionisation chambers will be used later for data normalisation. After the X-ray beam hits the sample, the diffraction pattern is recorded by an area detector, whilst the direct X-ray beam passes through a semitransparent beam stopper installed to reduce the radiation damage to the detector.

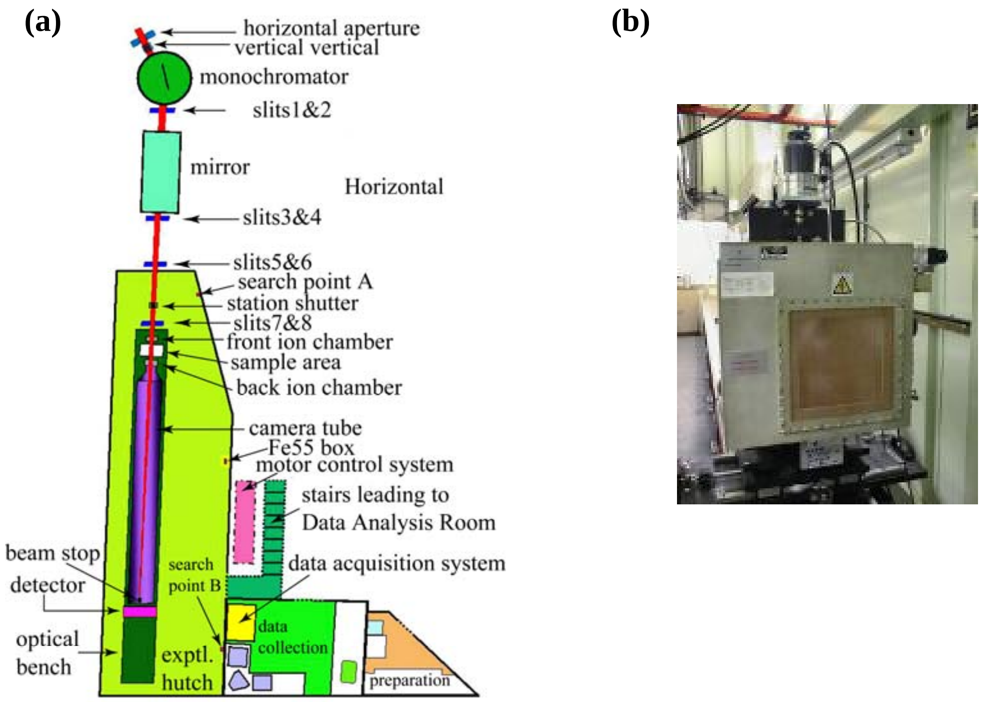

Figure 3-1 (a) Schematic representation of station 2.1- synchrotron radiation source (SRS), Daresbury[3]. (b) Area detector.

3.2.2 Station 6.2

At station 6.2, synchrotron radiation is generated from a multipole wiggler (MPW). According to the schematic drawing of the station in Figure 3-2, a water-cooled aperture is installed at the beginning of the beamline to receive the synchrotron radiation from the multipole wiggler and limit the beam size before arriving at the optical elements of the station. After passing the aperture, the synchrotron beam is collimated by the first pair of slits positioned behind the aperture. Then, the beam is focused by a plane cylindrically-bent Si/Rh mirror. At this stage, a vertically parallel beam is obtained. Next the beam is collimated by the second pair of slits before it falls onto a double crystal monochromator, using Si (111). The crystals in the monochromator have different shape. The first one is flat and is cooled with water. This one is used to select the energy of the beam, whilst the second one has the sagitally-bent shape, which is used to horizontally focus the diffracted beam coming from the first crystal. Behind the monochromator, there is a pair of slits and a second plane Si/Rh mirror which are used to collimate and vertically focus the beam respectively. Then, three pairs of silts, positioned after the second focusing mirror, are used to collimate the beam in the vertical and horizontal planes and define the beam size at the sample position. Note that the last pair of slits is placed just before the sample position. At this station, a quadrant detector and a curved 1-D wide-angle detector are used simultaneously to record the scattered X-rays at small and wide angles respectively.

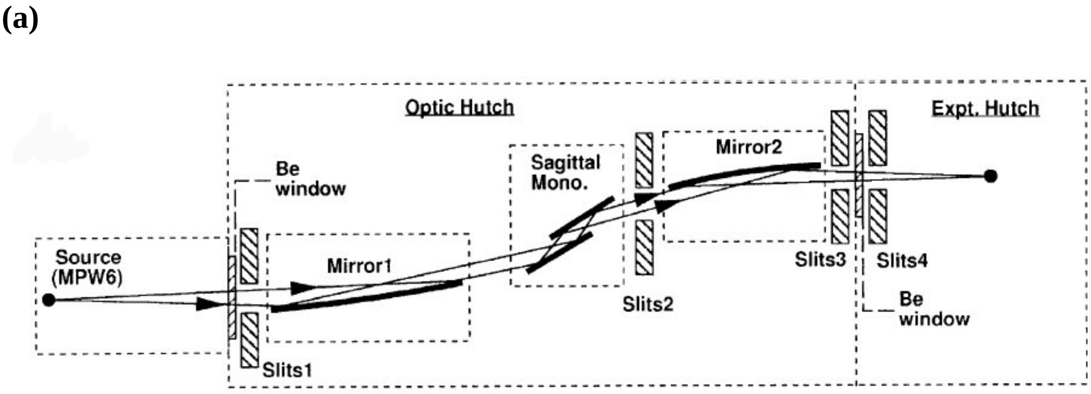

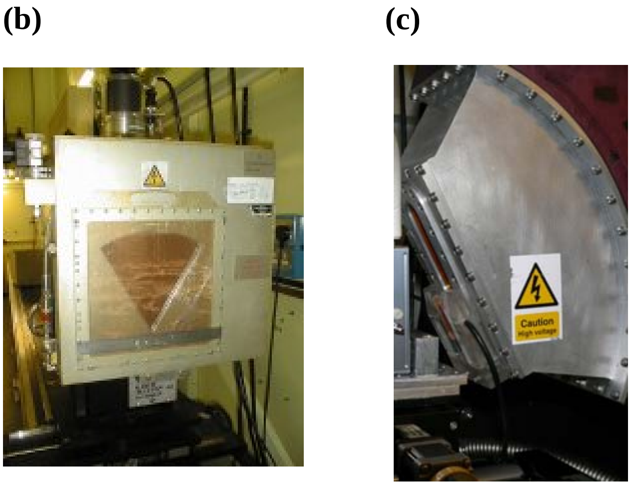

Figure 3-2 (a) Schematic drawing of optical components used at station 6.2 to focus synchrotron beam[4]. (b) A quadrant detector. (c) A curved 1-D wide-angle detector.

3.4 Experimental Procedures

1. A sample of powder material is filled into a capillary glass with a very thin glass which is cleaned with alcohol.
2. With the aid of a vacuum system, air in the capillary is pumped out (oil sealed rotary pump with a liquid nitrogen trap). Then, the end of a capillary glass is sealed by holding it over a flame.
3. The glass capillary is inserted into the sample holder on the stage to let the direct X-ray beam impinge on the sample. The direct X-ray beam is allowed

by the beam shutter controlled by software and interlock system of experimental station. The stage is heated by a heater or cooled by liquid nitrogen and the temperature is monitored and controlled by a temperature controller.

4. Guided by DSC data, the sample is heated or cooled down with constant rate in a particular range of temperatures to observe phase transitions. The sample may be heated or cooled several times to ensure that such phases really exist and can be reproduced.

3.5 Data Reduction

Before proceeding to structural analysis (see Section 2.8 and 2.9), the data has to be corrected and transformed into a practical form. The data file obtained from stations 2.1 and 6.2 is in the format of Biology Support Laboratory (BSL) program; it consists of an ASCII header file and a number of binary data files. The data in the binary data file of station 2.1 is 2-D binary image data, whereas those from station 6.2 are reduced to 1-D binary data. Although the data collected from stations 2.1 and 6.2 are in different form, the procedures for data reduction are quite similar.

3.5.1 Data Reduction for 1-D Data

3.5.1.1 Data Normalisation

Because of the different data collection time, the decay of electron current in the storage ring and the corresponding photon flux emitted, data collected at different times during the day can not be compared together. To be able to compare such data together, therefore, data have to be normalised by using the reading of the ionisation chamber placed after the sample; thereby the variation in absorption from sample to sample is also taken into account. Normalising data is done by dividing the data by the reading of the ionisation chamber, according to Eq. (3-1)

$$I_{sample}^{norm} = \frac{I_{sample}^{accum}}{I_{ion}^{accum}} \qquad (3\text{-}1)$$

where I_{sample}^{norm} = normalized intensity of data

I_{sample}^{accum} = accumulated intensity of raw data

I_{ion}^{accum} = accumulated ionisation current.

3.5.1.2 Detector Response Correction

Since the sensitivity of each element of the detector to X-ray photons is not equal ("gain variance"), the data are divided by the data of the detector response which is obtained by bombarding the detector with uniform radiation of a radioactive source like Fe55.

3.5.1.3 Empty Capillary Subtraction

Since the scattering of an X-ray beam does not only come from the sample but also originate from a capillary glass used to contain the sample, the scattering of an X-ray beam caused by the capillary glass should be removed from the experimental data by subtracting it from the data, according to Eq. (3-2). A file of scattered X-rays caused by a capillary glass can be obtained from collecting data without the sample but with the same sample environment and experimental profile. Moreover, if the data is collected for hours, the sample-environmental background, i.e. the radiation background of synchrotron, will be also included in that file, which it is also removed when doing background subtraction.

$$I_{sample}^{norm,bak\ sub} = I_{sample}^{norm} - I_{capil}^{norm} \tag{3-2}$$

where $I_{sample}^{norm,bak\ sub}$ = normalized intensity of background-removed data

I_{sample}^{norm} = normalized intensity of background-included data

I_{capil}^{norm} = normalized intensity of empty capillary glass data.

3.5.1.4 Calibration: Creating a *q*-Axis

The data obtained from the experiments contains two columns of the channel number (1024 channels) and the intensity of each channel. The channel number has to be converted to reciprocal *q*-space. To convert the channel number to the *q*-value, a standard sample, n-tetracontane ($C_{40}H_{82}$), will be used for calibration. The first step of calibration is to locate the channel number of the beam centre and the centre of each diffraction peak in the diffraction pattern of $C_{40}H_{82}$. Next, the camera length *L* is guessed in order to calculate the *q* value of each peak of $C_{40}H_{82}$, by using Eq. (3-3). Since *q*-values of diffraction peaks of $C_{40}H_{48}$ are known, *L*-value will be modified until the optimum value of *L* is obtained; all calculated q-values are close to the known *q*-values. Note that *q*-value of each peak must be measured after applying Lorentz correction (see section 3.4.5) to the intensity since applying Lorentz correction to the intensity causes the shift of the centres of peaks to a bit larger *q*-values.

$$q = \frac{4\pi}{\lambda}\sin\left(0.5\arctan(\frac{r}{L})\right) \tag{3-3}$$

where q = magnitude of scattering vector $\vec{q}$ in reciprocal space

λ = wavelength of x-rays

L = camera length from sample to detector

r = the distance, i.e. the number of channels (or the number of pixels for the case of diffraction image), from the centre of the nth peak to the beam centre.

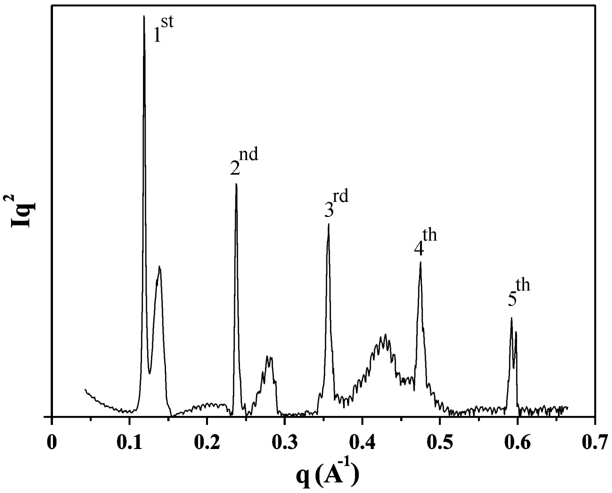

Figure 3-3 Diffraction pattern of n-tetracontane ($C_{40}H_{82}$): the interplanar d-spacing of the nth order diffraction peak is 52.8/n Å.

3.5.1.5 Lorentz Correction

Lorentz correction takes account of geometrical factors which affect the intensity of the diffracted beam. This can be understood by considering a reciprocal lattice rotating around its origin at a constant angular velocity. Under these conditions, one will see that different reciprocal lattice points spend different times in contact with the surface of the Ewald sphere; shorter reciprocal lattice vectors take more time in contact with the surface of Ewald sphere than longer reciprocal lattice vectors do. That means the density of equivalent reciprocal lattice points located on the surface of Ewald sphere at low angles is higher than that at wide angles. In powder diffraction, this is equivalent to having high and low density of crystallites diffracting at small and wide angles respectively. To normalise the density of crystallites contributing to the intensity of diffracted beam at different scattering angles, the intensity of each channel is multiplied by its corresponding q-value squared.

3.5.2 Data Reduction for 2-D Data

The procedures for data reduction for 2-D diffraction patterns of powder samples are quite similar to that of 1-D data. The program FiberFix[5] is used to perform data reduction for image data. The procedures for data reduction for 2-D binary image data start from performing data normalisation and detector response correction. Next, the intensity of scattered beam obtained from an empty capillary glass is subtracted from normalised and detector-response-corrected data. The weight factor multiplied to the data of an empty capillary glass is varied until a better result is obtained, i.e. a cleaner image. Next step is background fitting and subtraction. Although the intensity of scattered beam caused by an empty capillary glass is removed from the data, there is still sample-environmental background left. To make the image data look even cleaner, background fitting is performed and then background obtained from fitting actual background is removed from the data. After the process of background fitting and subtraction, the radial integration of intensity in clean diffraction image is performed. The next step is calibration, which is the conversion of the radius length of scanning to q-value by using Eq. (3-3). Finally, Lorentz correction is performed. By the process of data reduction, the plot of Iq^2 and q is created. Then, the structural analysis procedures are performed.

3.5.3 Debye - Waller factor

It is known that the intensities of diffraction peaks are decreased as the q value is increased. This is because the form factor is decreased at bigger Bragg angle or q value. However, one factor which also damps the intensities of Bragg reflections is thermal vibrations of atoms, which is commonly known as Debye–Waller factor (DWF)[6,7], expressed as

$$\mathrm{DWF} \;=\; \langle \exp(i\vec{q}.\vec{u}) \rangle^2 \tag{3.4}$$

where $\vec{u}(t)$ is the displacement of the atom from its equilibrium position at time t and $\vec{q}$ is a scattering vector in the reciprocal space. The symbol $\langle\ \rangle$ denotes either thermal or time averaging.

When DWF is taken into account and the j$^{\mathrm{th}}$ atoms are simply assumed as harmonic oscillators, the form factor of j$^{\mathrm{th}}$ atom can be approximated as

$$f_j \exp\left(-i\vec{q}.\,\vec{r}_j\right)\exp\left(-\frac{1}{6}\left\langle u(t)^2\right\rangle q^2\right) \tag{3.5}$$

where $u(t)$ is the displacement of the j$^{\mathrm{th}}$ atom from its equilibrium position $\vec{r}_j$.

Since the intensity of Bragg reflection is equal to the square of the structure factor, it can be written as

$$\mathrm{I} \sim f_j \exp\left(-i\vec{q}_j.\vec{r}_j\right) f_j \exp\left(i\vec{q}_j.\vec{r}_j\right)\exp\left(-\frac{1}{3}\left\langle u(t)^2\right\rangle q^2\right) = \mathrm{I}_0 \exp\left(-\frac{1}{3}\left\langle u(t)^2\right\rangle q^2\right) \tag{3.6}$$

where I_0 is the intensity from the rigid lattice.

So, a drop in the intensity of Bragg reflections arises both from the drop in the form factor and the Debye-Waller factor. If DWF is taken into account for correcting the intensities of reflections, the factor $\exp\left(\frac{1}{3}\left\langle u(t)^2\right\rangle q^2\right)$ has to be multiplied to the intensity of every diffraction peak.

References

[1] H. Winick, “Synchrotron radiation sources-A primer”, Singapore: World Scientific Publishing Company, 1995.

[2] H. Wiedeman, “Particle Accelerator Physics I: Basic Principles and linear beamdynamics”, Berlin: Springer, 2nd ed., 1999.

[3] Picture from the homepage of station 2.1- synchrotron radiation (SRS), Daresbury Laboratory: http://www.srs.ac.uk/srs/stations/station2.1.htm.

[4] C. C. Tang, C. M. Martin, D. Laundy, S. P. Thompson, G. P. Diakun, R. J. Cernik, “X-ray beam characteristics on MPW6.2 at the SRS”, Nucl. Instr. and Meth. in Phys. Res. B, 2004, 222, 659–666.

[5] F. Eakins and J. Squire, FibreFix tutorial 4: Time-resolved low-angle X-ray diffraction from muscle, May 19th 2005.

[6] B. E. Warren, “X-ray Diffraction”, Reading (Massachusetts): Addison-Wesley Publishing Company, 1969.

[7] C. Kittel, “Introduction to solid state physics”, 8th ed., Hoboken, New Jersey: Wiley, 2005.

Chapter 4

Hexagonal Close Packed structure in the Binary Mixtures of Alkali Metal (Na, Rb) salts of Trialkoxygallates and n-Paraffin $C_{19}H_{40}$

4.1 Introduction

The phase structures in thermotropic liquid crystals (LCs) have been studied by many research groups. The most common phase structures are usually obtained from mesogenic molecules having classical shapes. For example, disc-like mesogens yield hexagonal columnar structures whereas rod-like molecules give a variety of classical phases, e.g. nematic, smectic A and smectic C phases, etc. However, the advent of the concept of repetitive growth with branching of tree-like molecules called dendrimers, introduced by Buhleier et al[1] and Tomalia's group[2] and later developed by a number of organic chemists, especially Percec, leads to the revelation of undiscovered phase structures in thermotropic LCs. Even more interestingly, most of phase structures found in lyotropic systems, metals, and alloys are in common with thermotropic systems since in those systems the spherical objects packed into various lattices are treated as soft spheres.

For lyotropic systems, the packing spherical-like object is called 'micelle'. Micelles are also classified into 'direct micelles' and 'inverse micelles'[3] which refer to the relative concentration of polar or non-polar solvents with respect to the concentration of the amphiphilic molecules. For example, soap in water is a direct micellar system. Polar head groups of soap molecules are in contact with water molecules while the hydrocarbon chains turn away toward the core. Conversely, soap in oil is one of examples of the inverse micellar systems – that is, the hydrocarbon chains are in contact with oil as a solvent and polar groups turn away toward the core. It was reported that the direct micellar system of nonionic surfactant $C_{12}EO_{12}$ in water[4] yields the cubic close packed structure, commonly known as face-centred cubic (FCC, space group $Fm\overline{3}m$), the body-centred cubic (BCC, space group $Im\overline{3}m$) and the cubic $Pm\overline{3}n$ structures. The last one is also known as A15 structure. A lipid system[5] and a $C_{12}EO_8$/Water binary system[6] also yield the cubic $Pm\overline{3}n$ and the hexagonal close packed (HCP, space group $P6_3/mmc$) phases respectively. However, only two inverse micellar phases in lyotropic systems have been reported so far, i.e. the cubic $Fd\overline{3}m$ and the HCP phases. The $Fd\overline{3}m$ phase, which is more prevalent than the HCP phase, has been observed in many lipid systems[7,8]. The HCP phase[9] has recently been found in ternary lipid mixtures comprising of dioleoylphosphatidylcholine (DOP), dioleoylglycerol (DOG) and cholesterol in excess water. The cubic $Fd\overline{3}m$, the FCC, and the HCP structures are also well known in metals. The $Fd\overline{3}m$ structure is that of $MgCu_2$ Laves phase, also known as C15, whereas the FCC and the HCP structures are mostly found in pure metals.

For thermotropic LCs, the spherical objects obtained from dendrimers are portrayed as inverse micelles since they are consisted of aromatic hard core and peripheral alkyl chains. Like lyotropic systems, the BCC[10] and the $Pm\overline{3}n$ [11] structures have been also found in thermotropic systems. Interestingly, the novel structures in thermotropic LCs, i.e. a tetragonal $P4_2/mnm$ structure[12] and a liquid quasicrystal (LQC)[13] with dodecagonal symmetry, have been recently discovered. It should be noted that the BCC, $Pm\overline{3}n$ and $P4_2/mnm$ are well known structures mostly found in metals and alloys. The BCC structure is that of α-iron. The $Pm\overline{3}n$ structure is found in a series of binary transition metal alloys such as Cr_3Si or Nb_3Sn. The tetragonal $P4_2/mnm$ structure is known as σ-phase found in many alloys, such as $Fe_{46}Cr_{54}$[14]. Therefore, one can see that there are analogies between any two systems of dendrimeric systems, lyotropic systems, metals, and alloys.

However, although there are a lot of studies searching for other 3D structures in dendrimeric systems obtained from the self-assembly of conical dendrons (tree-like molecules)[10-11, 15] , the close packed structures, i.e. FCC and HCP, which are prevalent in pure metals, have never been found in any previously studied dendrimeric systems. The reason is that close packed structures are obtained from the close packing of hard spheres, whereas the micelles obtained from the dendrimers are treated as soft balls.

Theses soft balls are comprised of hard core and soft corona shells inherited from aromatic and aliphatic parts of dendrimeric molecules respectively. When these soft spheres are packed together, there will be repulsive interactions of approaching or overlapping of different coronal parts of different soft balls. Consequently, the void volume resulted from the packing of micelles is increased rather than minimized. In addition, there is a following packing frustration of close packed structures caused by the stretching of alkyl chains to reach the centres of octahedral interstices.

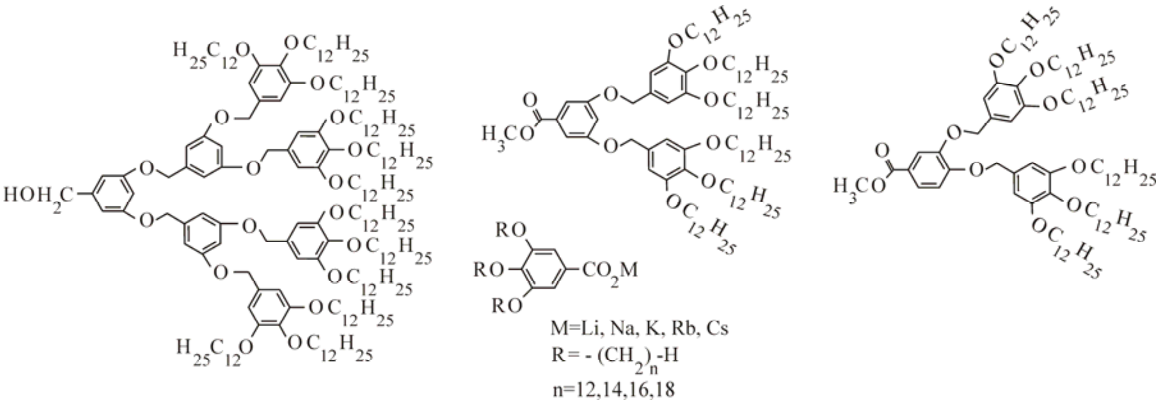

Figure 4-1 Some of previously studied dendrons yielding 3D structures, i.e. BCC, $Pm\overline{3}n$, $P4_2/mnm$, and LQC[10-13].

4.2 Voronoi Polyhedron

In order to understand why the previously studied dendrons, for example the dendrons in Figure 4-1, cannot afford the close packed structures, it is necessary to understand how the packing of spherical micelles obtained from the self-assembly of conical dendrons fills the unit cell of close packed structures. First of all, let us start with the concept of Voronoi Polyhedron that explains the nearest neighbours in 2D or 3D spaces by applying the methods introduced by Bernal[16]. To be easy to understand how to create Voronoi polyhedra in any given lattices, a given 2D lattice in Figure 4-2 is selected for demonstration. The red straight lines are drawn to connect any two lattice points. At the half way of each red line, a blue dashed line is sketched. When blue dashed lines intersect each other, a set of polyhedra is created, where the atoms, ions, polymer chain segments, or micelles are at the centers of polyhedra.

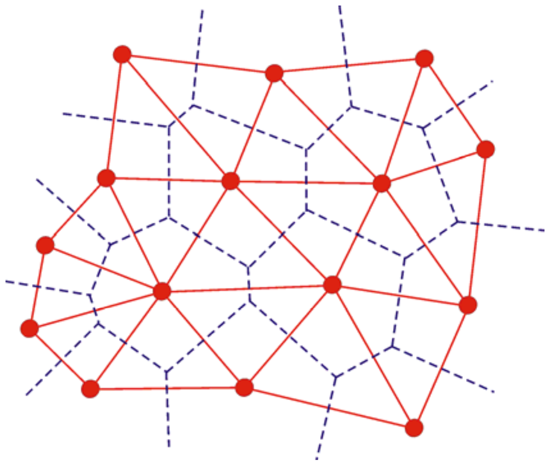

Figure 4-2 The demonstration of creating Voronoi polyhedra from non-cystalline structure.

Figure 4-2 is also a good example demonstrating that some lattices have more than one type of polyhedron whereas some lattices may need only one type of polyhedron to fill. For example, the BCC and the FCC lattices can be filled with only one type of polyhedron - that is, a truncated octahedron for BCC lattice and a rhombic dodecahedron for FCC lattice. The $Pm\overline{3}n$ cubic unit cell contains two pentagonal dodecahedron and six tetrakaidecahedron[17]. The $P4_2/mnm$ tetragonal unit cell contains ten pentagonal dodecahedron, sixteen tetrakaidecahedron, and four pentakaidecahedron[12]. Dodecahedron has twelve facets which means that a micelle located at the centre of dodecahedron is surrounded by other twelve micelles (coordination number (CN) =12). Tetrakaidecahedron (CN=14) has twelve pentagonal and two hexagonal facets. Like tetrakaidecahedron, pentakaidecahedron (CN=15) has twelve pentagonal and three hexagonal facets. All mentioned Voronoi polyhedra of the BCC, FCC, $Pm\overline{3}n$, and $P4_2/mnm$ lattices are shown in Figure 4-3.

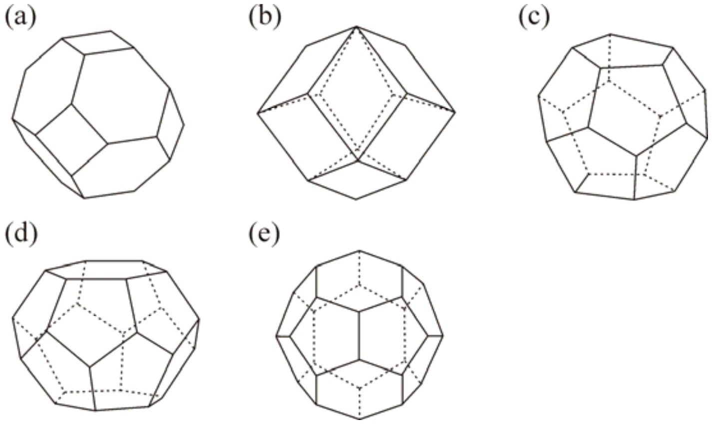

Figure 4-3 Different Voronoi polyhedra: (a) truncated octahedron (b) rhombic dodecahedron (c) pentagonal dodecahedron (d) tetrakaidecahedron (e) pentakaidecahedron.

4.3 Radial Distribution of Volume of Voronoi Polyhedron

To explain why the close packed structures are not obtained from some of previously studied dendrons in Figure 4-1, the average radial distribution of the volume dV/dr of Voronoi polyhedron of the FCC lattice was studied and compared to dV/dr of Voronoi polyhedron of the BCC, $Pm\overline{3}n,$ and $P4_2/mnm$ lattices[12]. To understand the distribution curves as shown in Figure 4-4, let us imagine that there are spheres with radius r where the centre of each sphere is located at the centre of each polyhedron. When these spheres grow simultaneously, the average volume of Voronoi cells which is contained within spheres is increased. However, when the spheres firstly hit the walls of polyhedra, which is represented by a vertical tick, and protrude from the facets of their own Voronoi cells, the averaged changing rate of Voronoi volume starts decreasing and goes to zero when all Voronoi cells are covered by its own sphere. Note that the beginning of the dV/dr curves, whose the acute apex is $r=0,$ is ignored to show in Figure 4-4 since all these curves coincide with each other, thereby not having significant difference among them. According to the results of calculation in Figure 4-4, the radial distribution curve of FCC structure has a higher peak than that of other structures. The r distance where the spheres firstly hit the facets of the polyhedron is also the farthest. It means that the FCC structure has more space to fill than the other structures have. In addition, a longer tail of radial distribution curve of FCC structure indicates that one has to go further to reach the vertices of polyhedron of FCC lattice.

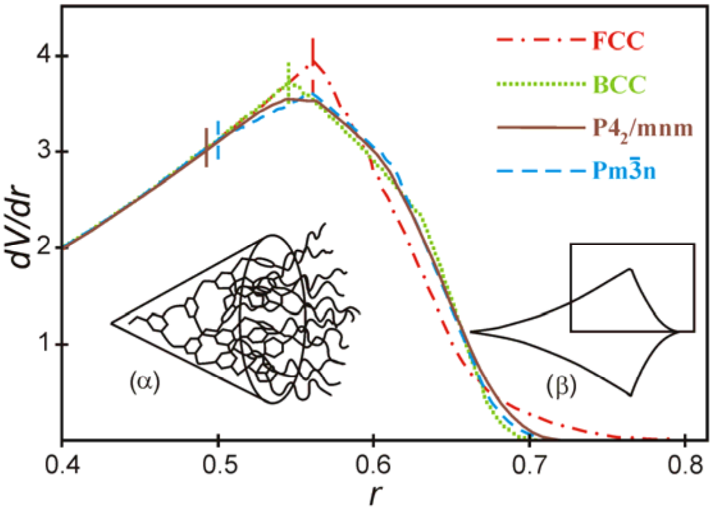

Figure 4-4 Radial distribution of the volume dV/dr of Voronoi polyhedron of BCC, FCC, $P4_2/mnm$ and $Pm\overline{3}n$ lattices[12].

The radial distribution curve dV/dr of the FCC is thought as the ideal shape of dendron that would fill the Voronoi polyhedron of the FCC lattice perfectly. Thus, the molecular shape of the conical dendron is then related to the radial distribution curve dV/dr of the FCC. First, the conical molecule (inset α in Figure 4-4) is rolled out flat in the direction perpendicular to the cone axis, which looks like a hyperbolic fan as schematically drawn in the inset β in Figure 4-4. Next, only the important region of the unrolled dendron (the rectangle in inset β) is focused on and is compared to the shape of the dV/dr curve. Now, it can be seen that the shapes of some of previously studied dendrons in Figure 4-1 is quite similar to the shapes of ideal dendrons for BCC, $Pm\overline{3}n$, and $P4_2/mnm$ lattices, but, by contrast, they are quite different from the ideal dendron for FCC. The shape of the ideal dendron of FCC is less curved than that of other lattices. More importantly, it has a longer tail. In this study, Ungar[12] suggested that to achieve the close packed structures the dendron should have a short branch on one of the first carbons of the alkyl tail and should include a small fraction of extra-long tails to fill the tail of dV/dr curve of FCC.

4.4 The studied materials: Alkali salts of 3,4,5-trialkoxygallates and their binary mixtures with added n-nonadecane (12-12-18M+m%$C_{19}H_{40}$ and 12-12-12M +m%$C_{19}H_{40}$ where M=Na, Rb and m=0, 5, 10, 15, 30)

In this work based on the previous study of the average radial distribution of Voronoi volume dV/dr of FCC lattice[12], we attempt to achieve the close packed structures by modifying previously studied dendrons of 3,4,5-tridodecyloxygallate alkali metal salts[15b] (12-12-12M where M=Na and Rb, Figure 4-5). Thus, one of the C12 chains is replaced with a C18 chain to produce 12-12-18M salt (see Figure 4-6a). Again, the idea is that the longer alkyl chain in the molecule would help fill the octahedral interstices, furthest points from the centers of surrounding micelles represented by a longer tail of red curve than others in Figure 4-4, in a structure of close packed structures. This longer alkyl chain also helps reduce the frustration of stretching of alkyl chains to fill octahedral interstices. To fill the octahedral interstices even better, various proportions of an n-paraffin $C_{19}H_{40}$ are added to 12-12-18M (Figure 4-6b). For comparison, the binary mixtures of 12-12-12M and varying proportions of $C_{19}H_{40}$ are also studied (Figure 4-6c).

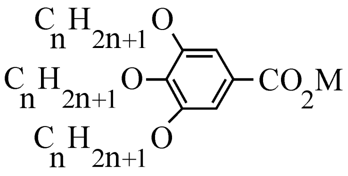

n-n-nM

n=12, 14, 16, 18.
M=Na, Rb

Figure 4-5 3,4,5-trialkoxygallate alkali metal salts with all same alkyl chain lengths.

(a) 12-12-18M

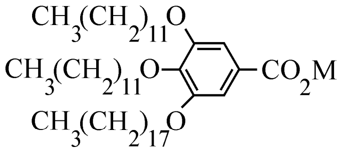

(b) 12-12-18M + m%C_{19}

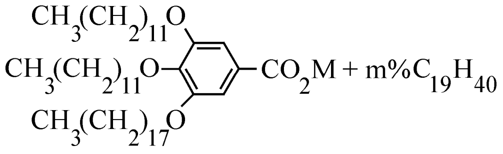

(c) 12-12-12M + m%C_{19}

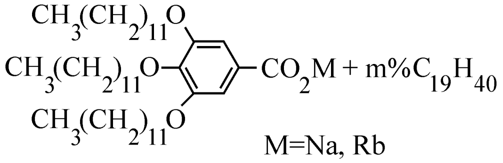

M=Na, Rb

m=5, 10, 15, 30

Figure 4-6 (a) Our dendron candidates and (b) their binary mixtures with added $C_{19}H_{40}$. (c) The binary mixtures of previously studied dendrons 12-12-12M and $C_{19}H_{40}$.

4.5 Experimental Results and Discussion

4.5.1 SAXS results and phase identification

The supramolecular structures of all alkali metal salts and their mixtures with added $C_{19}H_{40}$ were determined by a combination of differential scanning calorimetry (DSC) and small angle X-ray diffraction experiments. The DSC is used for determining how many phases are in the studied materials and what the transition temperature from one phase to another would be seen. In addition, it also tells us about the range of temperatures of a particular phase. However, the DSC cannot identify the phase structures of studied materials. Hence, the X-ray diffraction is then exploited for phase determination in this study. For this study, the DSC experiments were carried out by our collaborators in laboratory at the department of Chemistry of Hull University. The results are in the Appendix 1. Small angle X-ray diffraction experiments were performed by us at SRS Daresbury Laboratory, Synchrotron radiation source. All experimental results are presented by using a chart as shown in Figure 4-7 which a given studied material is represented by a column consisting of various colour bars. Each colour bar represents a particular phase observed in such material and the bars are shifted to the right and the left in alternate way in order to show whether there is the coexistence of two phases or not. The diffractograms of each material are also shown to confirm the results in the chart. The measured interplanar d-spacings of diffraction peaks of various phases at different temperatures, calculated unit cell parameters, and the calculated number of molecules in the unit cells are tabulated in Appendix 2.

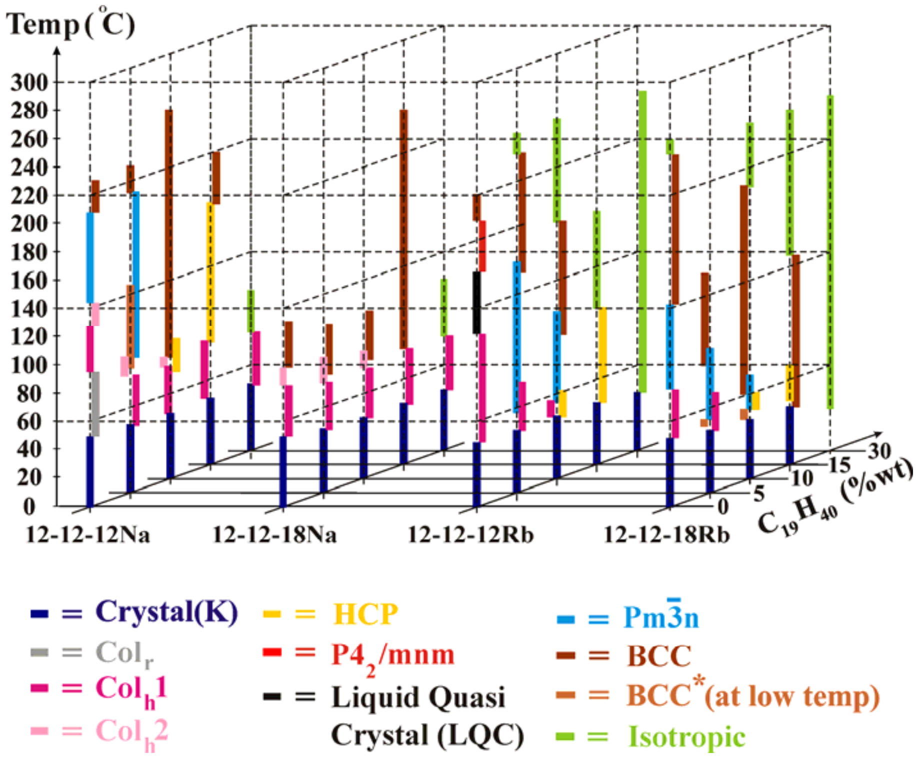

Figure 4-7 Graphical presentation of all phases observed in alkali metal salts of 3,4,5-trialkoxygallates, 12-12-12M and 12-12-18M where M=Na and Rb, and their mixtures with added various concentrations of $C_{19}H_{40}$.

Let us start with the results of 12-12-18Na and its mixtures with added 5%, 10%, 15%, and 30% by weight of n-nonadecane $C_{19}H_{40}$. According to the phase column of

12-12-18Na in the chart in Figure 4-7, the crystalline phase at low temperatures is followed by two hexagonal columnar phases, i.e. $\mathrm{Col_h1}$ and $\mathrm{Col_h2}$, with *p6mm* symmetry. Then, the body centred-cubic (BCC) phase (space group $Im\overline{3}m$) is obtained at higher temperatures. The SAXS diffractograms of 12-12-18Na are also shown in Figure 4-8 which the superscripts, e.g. * and #, in the diffractograms are used to identify which peaks and corresponding (*hkl*) indices belong to a particular phase. For example, the superscript '*' placing over the letter '$\mathrm{Col_h1}$' lets the readers know that the diffraction peaks specified by '$(hkl)^*$' indices belong to the $\mathrm{Col_h1}$ phase. Note that using superscripts to identify which peaks and corresponding (*hkl*) indices belong to a particular phase is also applied to other diffractograms of other materials.

For the $\mathrm{Col_h}$ phases of 12-12-18Na, the structure of supramolecular columns of 12-12-18Na is also investigated by using the wide angle X-ray diffraction (WAXD) technique. According to the WAXD patterns obtained from an oriented fiber of 12-12-18Na collected in the range of temperatures 55-80 °C (see Figure 4-9), it is shown that the molecules of 12-12-18Na are self-assembled into a helix. This is evidenced by the splitting of the diffuse at about 4.57 Å and the slightly splitting of the reflection at 7.37 Å, whereas the sharp reflection at 3.73 Å is not split. The splitting of the diffuse and the reflections is confirmed by their integrated intensities obtained from performing the azimuthal scan (see Figure 4-11). The observation of the sharp reflections at 3.73 Å and 7.37 Å in WAXD patterns of 12-12-18Na at low temperatures indicates that the low-temperature phase of the fiber of 12-12-18Na seems to be weakly crystalline phase, rather than a true liquid crystal phase. By contrast, according to the WAXD patterns of 12-12-18Na collected in the range of temperatures 85-95 °C (see Figure 4-10), the diffuse at about 3.96 Å and 7.97 Å is observed instead. This indicates that the high-temperature phase of 12-12-18Na fiber is a true columnar liquid crystal phase. According to the WAXD patterns of 12-12-18Na collected at low temperatures, the sharp reflection at 3.73 Å and the diffuse at 4.57 Å correspond to the aromatic and aliphatic part of 12-12-18Na molecules. The splitting of the diffuse at about 4.57 Å implies that the alkyl chains in 12-12-18Na are tilted while the non-splitting sharp reflection at 3.73 Å, situated on the meridian, implies that the aromatic ring is perpendicular to the column axis (see the molecular sketch in Figure 4-12).

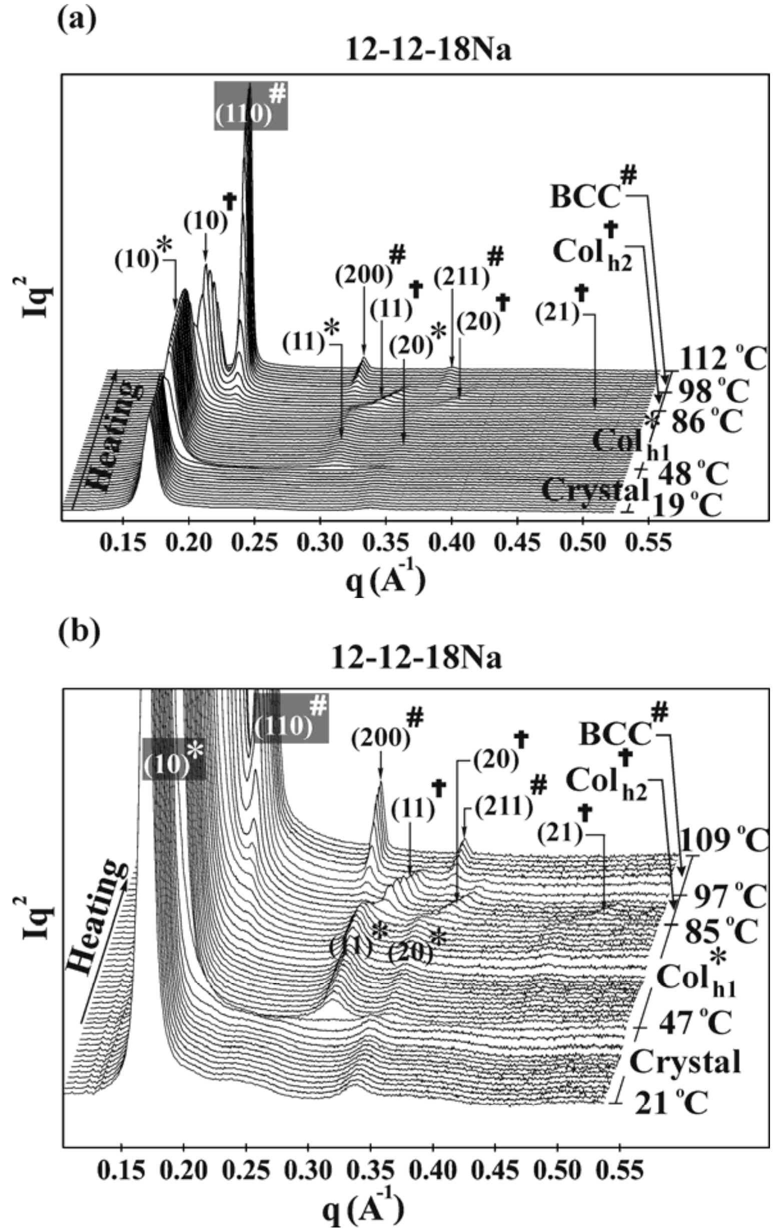

Figure 4-8 (a) Small angle X-ray diffraction result of 12-12-18Na. (b) A close view of weak diffraction peaks of 12-12-18Na in (a).

If the aromatic rings are tilted, the reflection 7.37Å would be split more. Hence, d-spacings of the sharp reflection on the meridian obtained at different temperatures, i.e. 3.73-3.97 Å, are used as the assumed values of the column layer thickness for the calculation of the number of 12-12-18Na molecules per column layer (see the calculation results in section 4.5.2). Using 3.73 Å as a column layer thickness yields 4.4 molecules per column layer, which could be approximated to 4 molecules per column layer. From indexing WAXD pattern of 12-12-18Na, the missing of (001) reflection implies that 4 molecules of 12-12-18Na are self-assembled into a 4_2 helix (see Figure 4-12), this is the extinction rule of 4_2 screw axis symmetry. The unit cell in the column direction is consisted of two molecular layers (i.e. one blue and one pink layers), which the *c* parameter is about 7.55Å. Above 85 °C, there is no tilting of alkyl chains in 12-12-18Na molecules as one can see the non-splitting of the diffuse at 4.55 Å. This is because at high temperatures the carbon atoms of the alkyl chains of 12-12-18Na have more gauche bonding than those at low temperatures, thereby requiring more space to occupy. However, the splitting of the diffuse at 8.02 Å for the WAXD pattern collected at 85 °C (see Figure 4-10a) or the splitting of the diffuse at 7.97 Å for the WAXD pattern collected at 95 °C (see Figure 4-10b) suggest that the supramolecular columns in the Col_h LC phase of 12-12-18Na also have a helical structure.

When 5% and 10% of $C_{19}H_{40}$ are added to 12-12-18Na, both of 12-12-18Na+5%C_{19} and 12-12-18Na+10%C_{19} give the same phase sequence as the pure compound of 12-12-18Na does, i.e. Crystal→Col_h1→Col_h2→BCC (see the phase columns of 12-12-18Na+5%C_{19} and 12-12-18Na+10%C_{19} in the chart in Figure 4-7). When 15% of $C_{19}H_{40}$ is added to 12-12-18Na, the mixture 12-12-18Na+15%C_{19} yields the simpler phase sequence, i.e. Crystal→Col_h→BCC. The structure of supramolecular columns of 12-12-18Na+15%C_{19} is also investigated by using wide angle X-ray diffraction (WAXD) technique. The WAXD patterns of an oriented fiber of 12-12-18Na+15%C_{19} collected at 52 °C, 60 °C, and 70 °C (see Figure 4-13) are similar to those of 12-12-18Na collected at 55-80 °C. So, the columns of 12-12-18Na+15%C_{19} also have a helical structure and the self-arrangement of 12-12-18Na molecules in the columns of 12-12-18Na+15%C_{19} are similar to that of pure 12-12-18Na (see Figure 4-12). When 30% of $C_{19}H_{40}$ is added to 12-12-18Na, the obtained phase sequence of 12-12-18Na+30%C_{19} is even simpler, i.e. Crystal→Col_h→Isotropic liquid. Although we do not have the WAXD data of 12-12-18Na+5%C_{19}, 12-12-18Na+10%C_{19} and 12-12-18Na+30%C_{19}, we believe that the supramolecular columns of these mixtures also have a helical structure like those of 12-12-18Na and 12-12-18Na+15%C_{19}. The diffractograms of 12-12-18Na+m%C_{19} where m= 5, 10, 15, 30 are shown in Figure 4-14 to Figure 4-17.

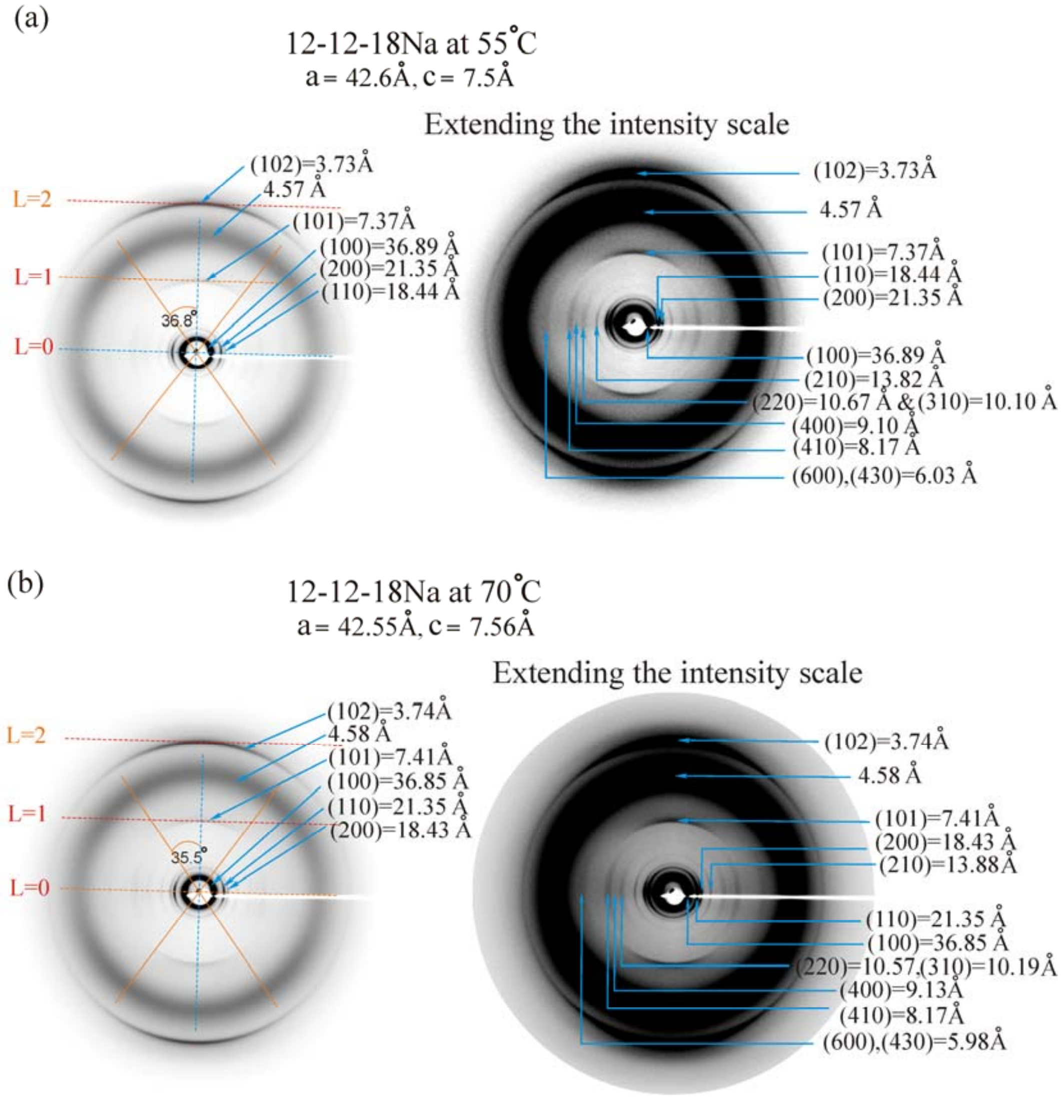

Figure 4-9 WAXD patterns of the fiber of 12-12-18Na at (a) 55°C and (b) 70 °C.

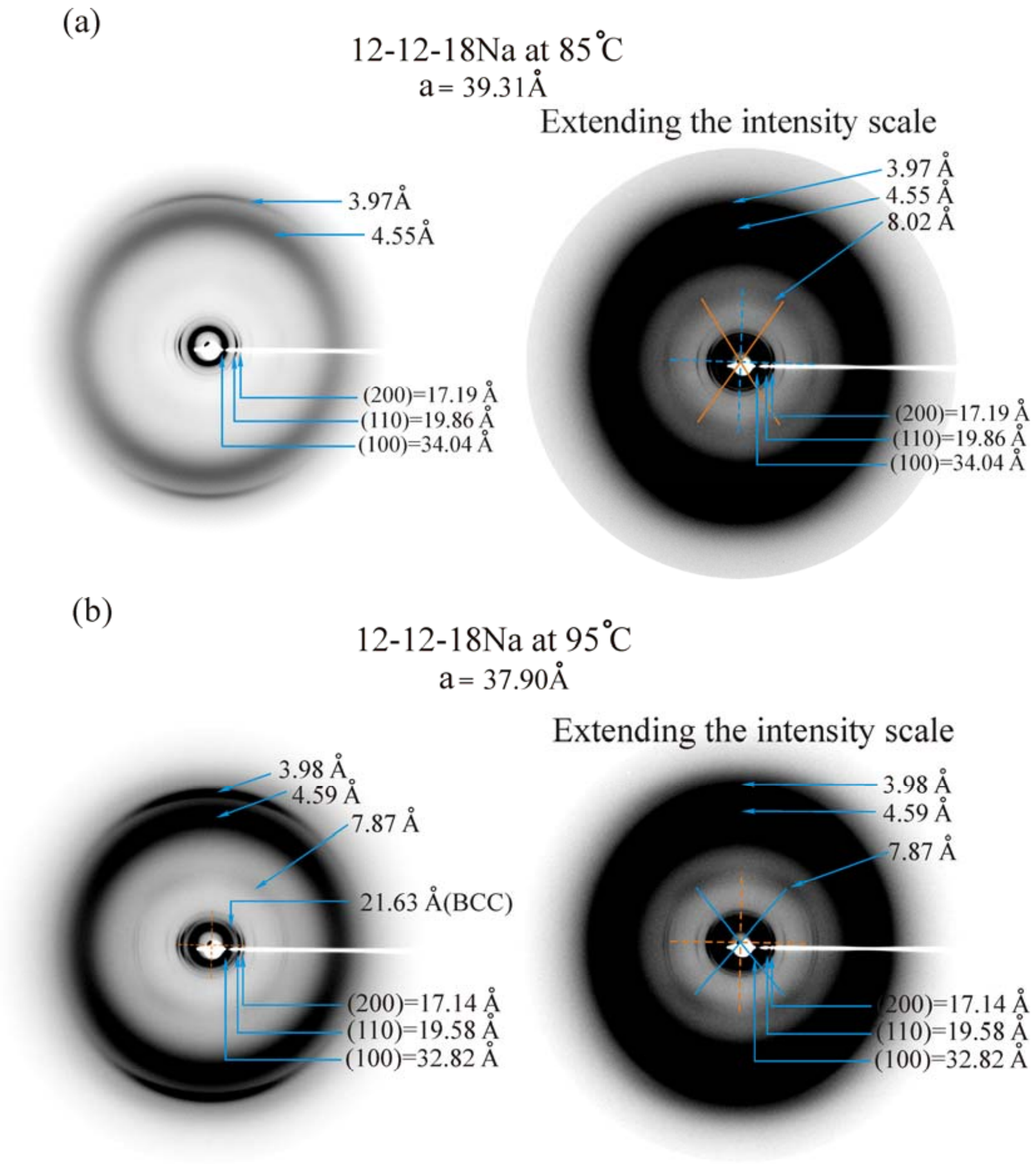

Figure 4-10 WAXD patterns of the fiber of 12-12-18Na at (a) 85°C and (b) 95 °C.

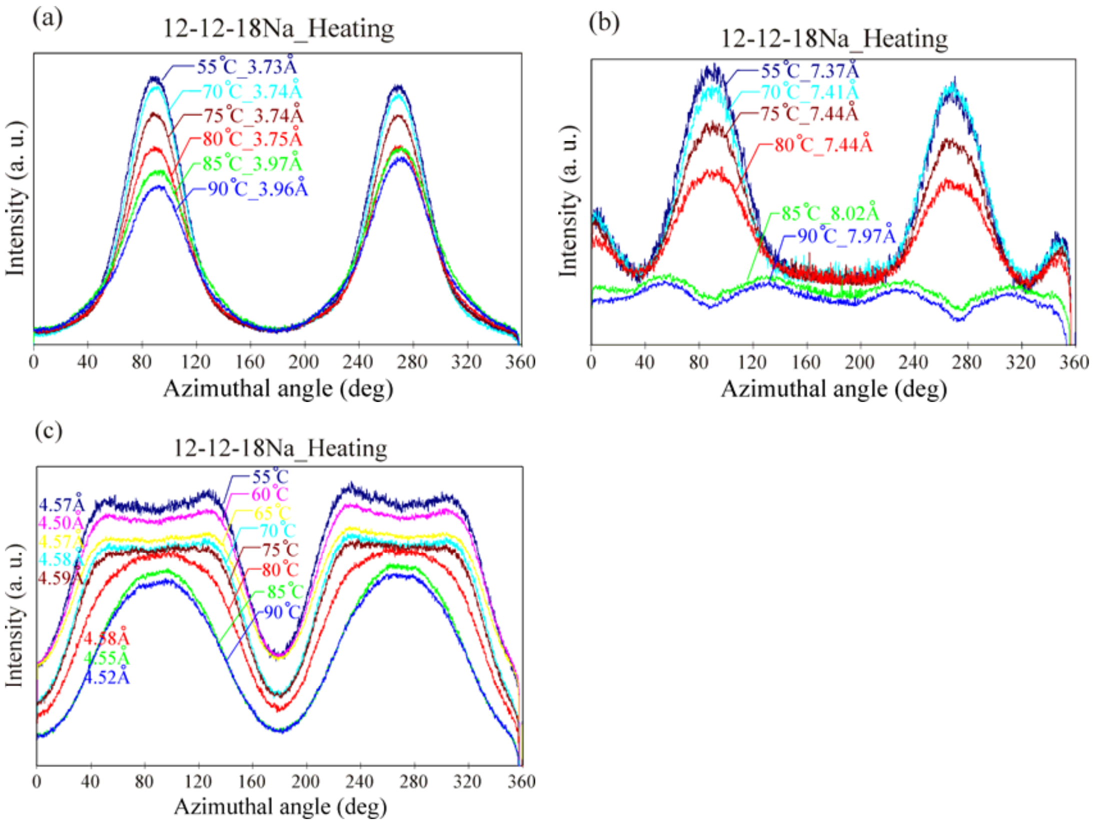

Figure 4-11 Integrated intensities, obtained from performing the azimuthal scan, of the reflections, (a) and (b), and the diffuse, (c), observed in WAXD patterns of the fiber of 12-12-18Na at different temperatures.

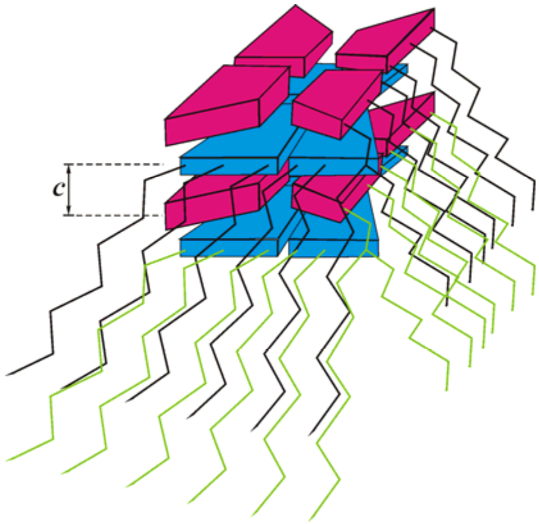

Figure 4-12 Helical packing of 12-12-18Na molecules into a 4_2 helix.

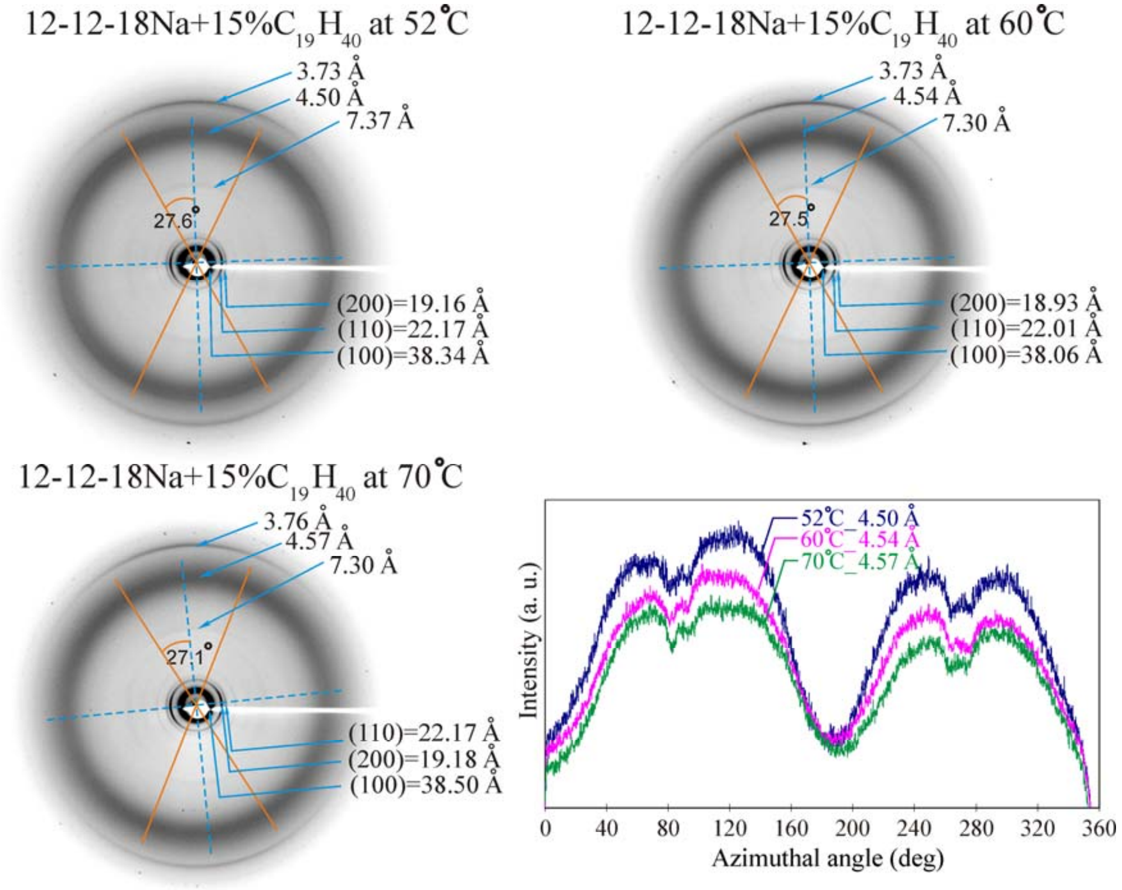

Figure 4-13 WAXD patterns of the fiber of 12-12-18Na+15%C_{19} at 52 °C, 60 °C, and 70 °C and integrated intensities of the diffuse obtained from performing the azimuthal scan.

For the pure compound of 12-12-18Rb, the SAXS results of 12-12-18Rb as presented by the phase column in Figure 4-7 shows that 12-12-18Rb yields a different phase sequence from that of 12-12-18Na. The crystalline phase at low temperatures is followed by the hexagonal columnar (Col_h) phase. Then, the cubic phase with symmetry $Pm\bar{3}n$ is obtained at higher temperatures, followed then by the BCC phase and the isotropic liquid phase. The diffractograms of 12-12-18Rb are shown in Figure 4-18. When 5% of $C_{19}H_{40}$ is added to 12-12-18Rb, the mixture 12-12-18Rb+5%C_{19} gives the phase sequence similar to that of 12-12-18Rb, i.e. Crystal → Col_h → BCC^*→ $Pm\bar{3}n$→ BCC. Note that the overlapping of the colour bars in the phase column of 12-12-18Rb+5%C_{19} in the chart in Figure 4-7 indicates that there are phase combinations, i.e. BCC*+Col$_h$ and $Pm\bar{3}n$+BCC, in a particular range of temperatures. The denotation 'BCC*' represents the BCC phase observed in the short range of low temperatures. The phase sequence of 12-12-18Rb+5%C$_{19}$ is an extraordinary phase sequence since the BCC phase is normally observed at high temperatures. The diffractograms of 12-12-18Rb+5%C$_{19}$ are shown in Figure 4-19.

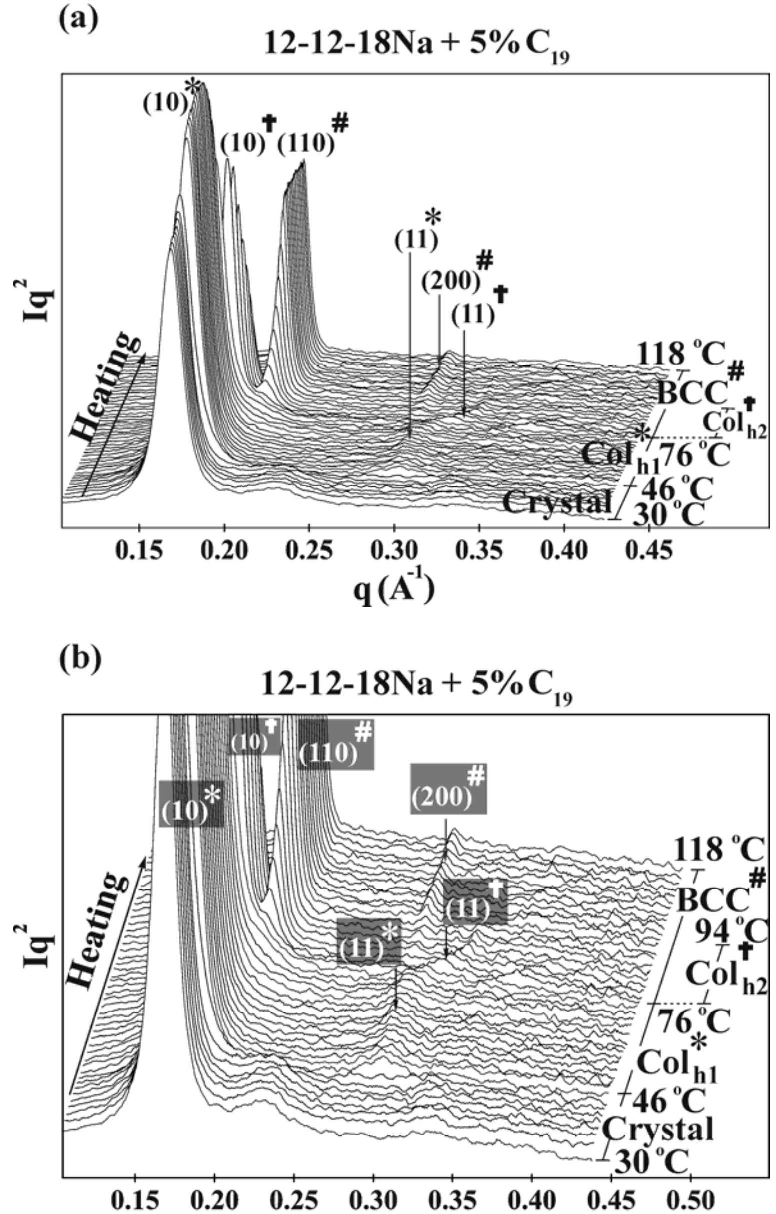

Figure 4-14 (a) Small angle X-ray diffraction result of 12-12-18Na+5%C$_{19}$. (b) A close view of weak diffraction peaks of 12-12-18Na+5%C$_{19}$ in (a).

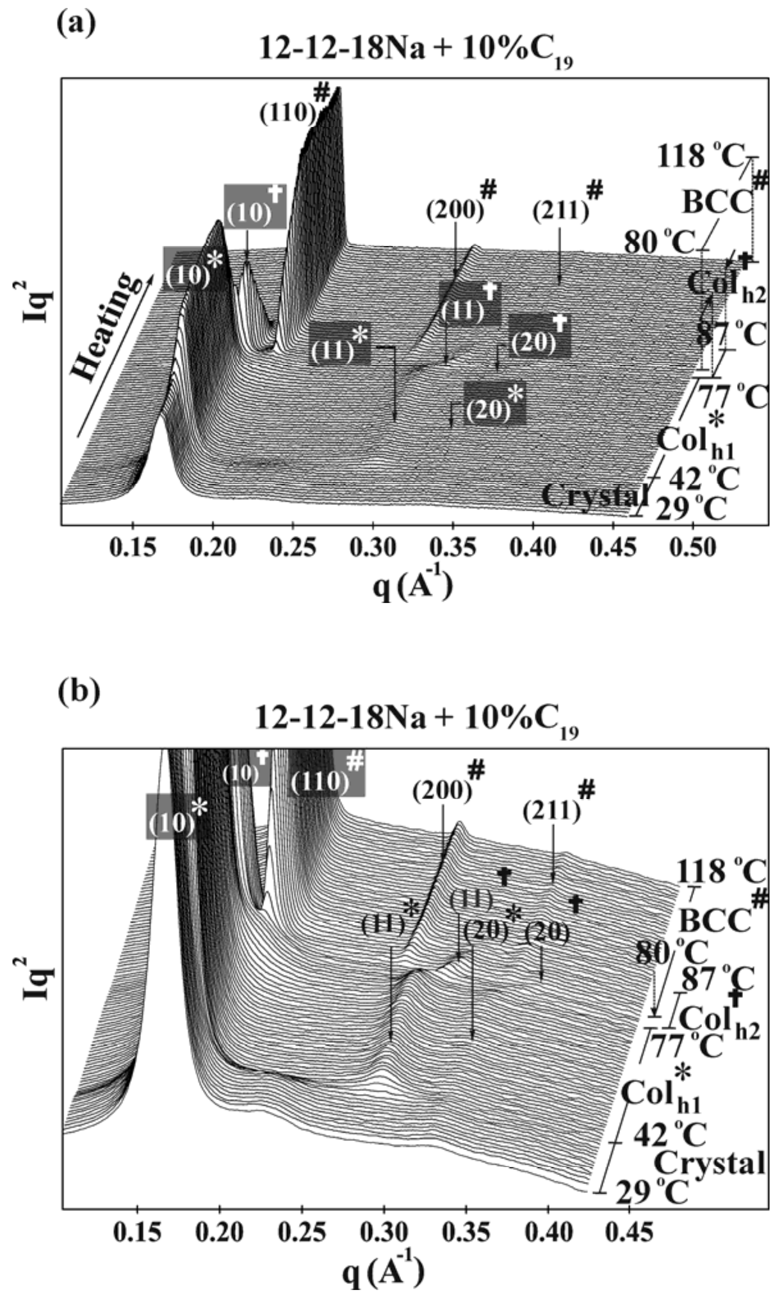

Figure 4-15 (a) Small angle X-ray diffraction result of 12-12-18Na+10%C_{19}. (b) A close view of weak diffraction peaks of 12-12-18Na+10%C_{19} in (a).

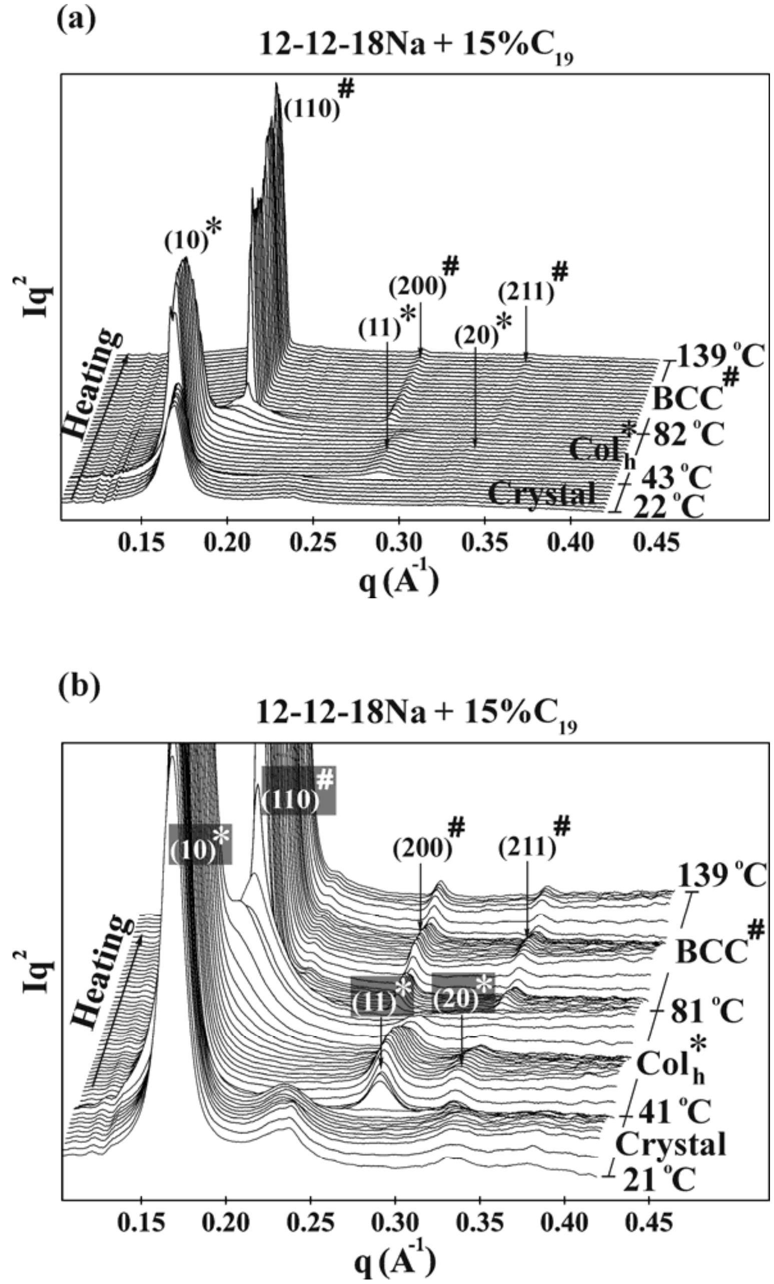

Figure 4-16 (a) Small angle X-ray diffraction result of 12-12-18Na+15%C_{19}. (b) A close view of weak diffraction peaks of 12-12-18Na+15%C_{19} in (a).

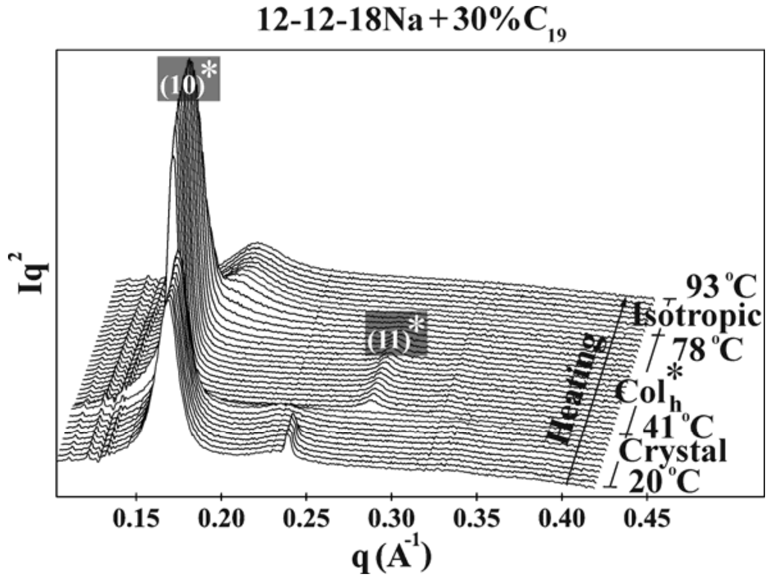

Figure 4-17 Small angle X-ray diffraction result of 12-12-18Na+30%C_{19}.

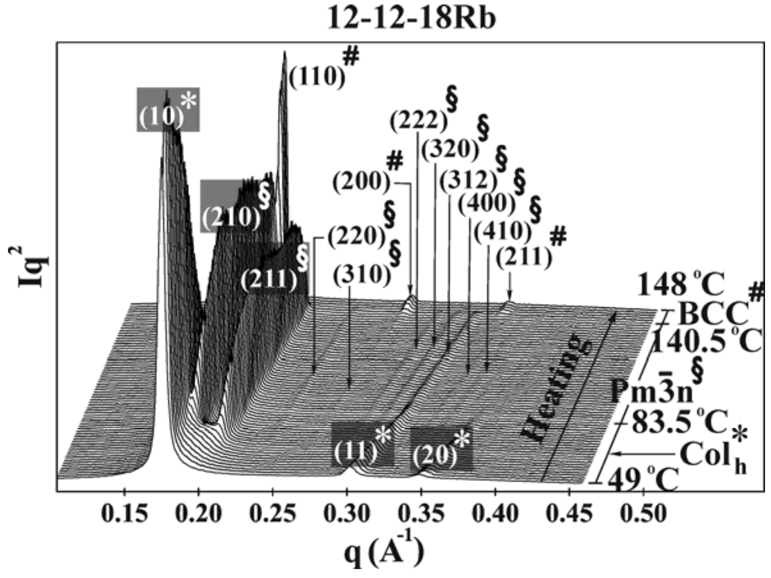

Figure 4-18 Small angle X-ray diffraction result of 12-12-18Rb.

The mixture 12-12-18Rb+10%C_{19} yields a different phase sequence from that of 12-12-18Rb+5%C_{19} (see Figure 4-7). The crystalline phase at low temperatures is followed by the BCC phase. Again, this BCC phase is observed during a short range of low temperatures. While the cubic $Pm\bar{3}n$ phase is developing at higher temperatures, the hexagonal close packed (HCP, space group $P6_3/mmc$) phase is also formed in a short range of temperatures. Then, the BCC phase reoccurs later at higher temperatures, followed then by the isotropic liquid phase. For the HCP unit cells, the calculated c/a ratios are about 1.631 which are close to a theoretical value 1.633. The diffractograms of 12-12-18Rb+10%C_{19} are shown in Figure 4-20.

When 15% of $C_{19}H_{40}$ is added to 12-12-18Rb, the mixture 12-12-18Rb+15%C_{19} yields a simpler phase sequence; the crystalline phase at low temperatures is followed by the BCC phase. While the BCC is developing, the HCP phase is also formed and coexists with the BCC phase in low temperature region of the BCC phase. Then, the phase sequence of 12-12-18Rb+15%C_{19} is ended with the isotropic liquid phase. Interestingly, the BCC phase regarded as the high temperature phase starts forming at low temperatures and still continues through the high temperature region. For the HCP unit cells, the calculated c/a ratios are about 1.622-1.631 which are close to a theoretical value 1.633. The diffractograms of 12-12-18Rb+15%C_{19} are shown in Figure 4-21. However, when 30% of $C_{19}H_{40}$ is added to 12-12-18Rb, it is found that only isotropic liquid phase is observed in this binary mixture. Hence, the small angle X-ray diffraction results of 12-12-18Rb+30%C_{19} are not shown here.

So far, all experimental results of alkali metal salts of 3,4,5-trialkoxygallate with two short and one long alkoxy chains, i.e. 12-12-18Na and 12-12-18Rb, and their mixtures with added various concentrations of $C_{19}H_{40}$ are reported. Only 12-12-18Rb+10%C_{19} and 12-12-18Rb+15%C_{19} give us the HCP phase. Next, the experimental results of 3,4,5-tridodecyloxygallate alkali metal salts, i.e. 12-12-12Na and 12-12-12Rb, and their mixtures with added various proportions of $C_{19}H_{40}$ are going to be reported. First of all, let us review the results of the previous study of 12-12-12Na[15b]. In such work, it was reported that on increase of temperature 12-12-12Na gives a phase sequence as follows: Crystal → rectangular columnar ($\mathrm{Col_r}$) phase → $\mathrm{Col_h}1$ → $\mathrm{Col_h}2$ → $Pm\bar{3}n$ →BCC and neither of the close packed structures HCP or FCC was observed in this compound. In this work, 5% by weight of $C_{19}H_{40}$ is added to 12-12-12Na. The SAXS results of 12-12-12Na+5%C_{19} as presented by the phase column in Figure 4-7 shows that 12-12-12Na+5%C_{19} yields a different phase sequence from that of 12-12-12Na. The crystalline phase at low temperatures is directly followed by two hexagonal columnar phases, i.e. Col_h1 and Col_h2, whereas the Col_r phase is not observed in this mixture. The BCC phase is formed later at higher temperatures and coexists with the cubic $Pm\bar{3}n$ phase which the latter is developed later at even higher temperatures. The BCC phase reoccurs at the end of the $Pm\bar{3}n$ phase and is followed by the isotropic liquid phase.

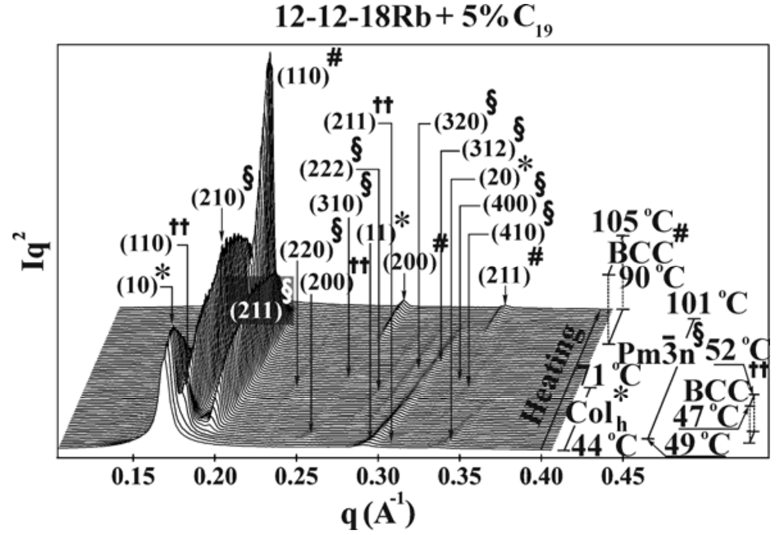

Figure 4-19 Small angle X-ray diffraction result of 12-12-18Rb +5%C_{19}.

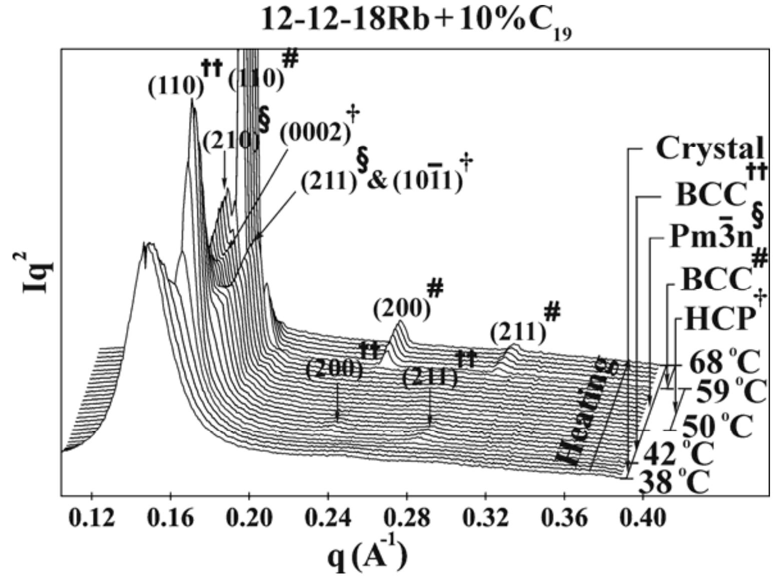

Figure 4-20 Small angle X-ray diffraction result of 12-12-18Rb+10%C_{19}.

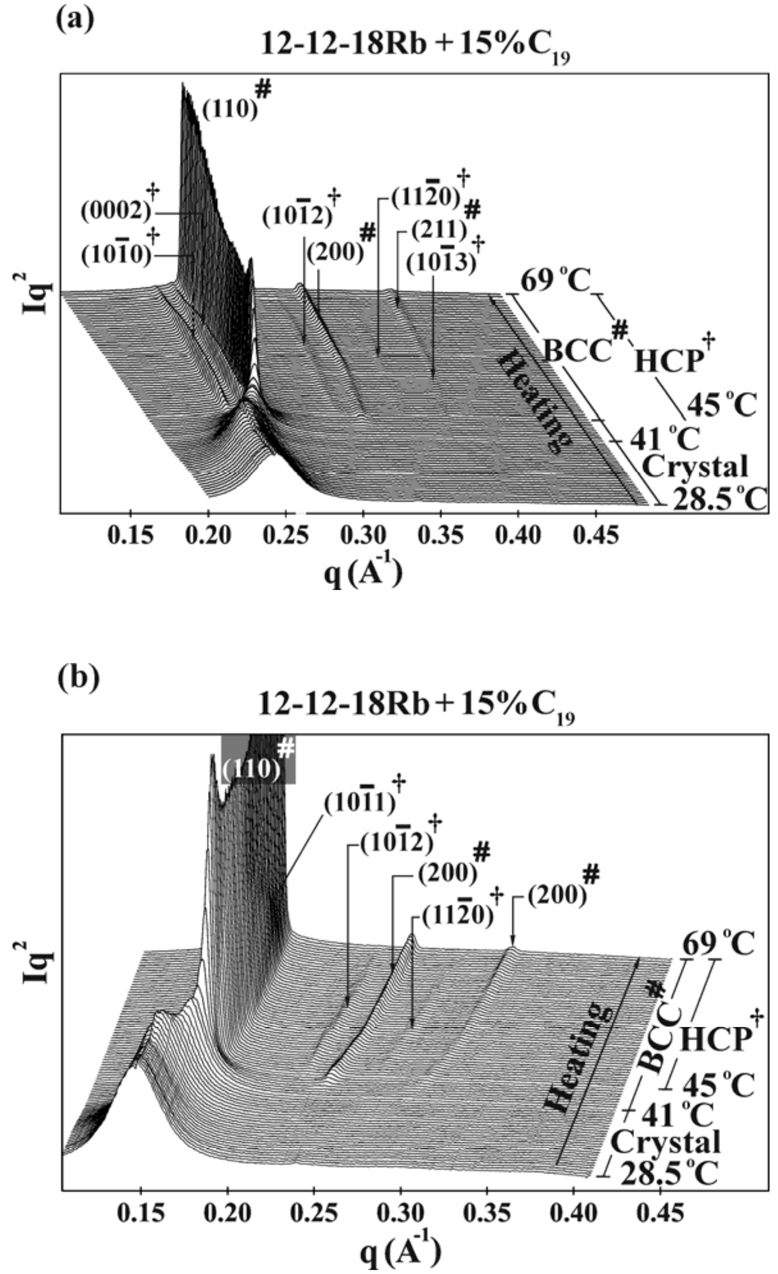

Figure 4-21 Small angle X-ray diffraction result of 12-12-18Rb+15%C_{19} (a) the left hand view (b) the right hand view.

The diffractograms of 12-12-12Na+5%C_{19} are shown in Figure 4-22. When 10% of $C_{19}H_{40}$ is added to 12-12-12Na, the phase sequence of the mixture 12-12-12Na+10%C_{19} is different from that of 12-12-12Na+5%C_{19}. The crystalline phase at low temperatures is still followed by Col_h1 and Col_h2 phases. While the Col_h2 is developing, the HCP phase is also formed. Then, the BCC is formed later at higher temperatures and coexists with the HCP phase. For the HCP unit cells, the calculated *c/a* ratios are about 1.628-1.631 which are close to a theoretical value 1.633. The diffractograms of 12-12-12Na+10%C_{19} is shown in Figure 4-23.

When 15% of $C_{19}H_{40}$ is added to 12-12-12Na, the mixture 12-12-12Na+15%C_{19} gives the extraordinary results – that is, the pure HCP phase is obtained. According to SAXS results of 12-12-12Na+15%C_{19} as presented by the phase column in Figure 4-7, the crystalline phase at low temperatures is followed by the Col_h phase. The pure HCP phase is then formed and followed by the BCC phase. For the HCP unit cells, the calculated *c/a* ratios are about 1.630-1.638 which are close to a theoretical value 1.633. The diffractograms of 12-12-12Na+15%C_{19} are shown in Figure 4-24. However, when 30% of $C_{19}H_{40}$ is added to 12-12-12Na, the HCP and BCC phases are not observed in 12-12-12Na+30%C_{19} and the phase sequence of 12-12-12Na+30%C_{19} is as follows: Crystal →Col_h→ Isotropic liquid. The diffractograms of 12-12-12Na+30%C_{19} are shown in Figure 4-25.

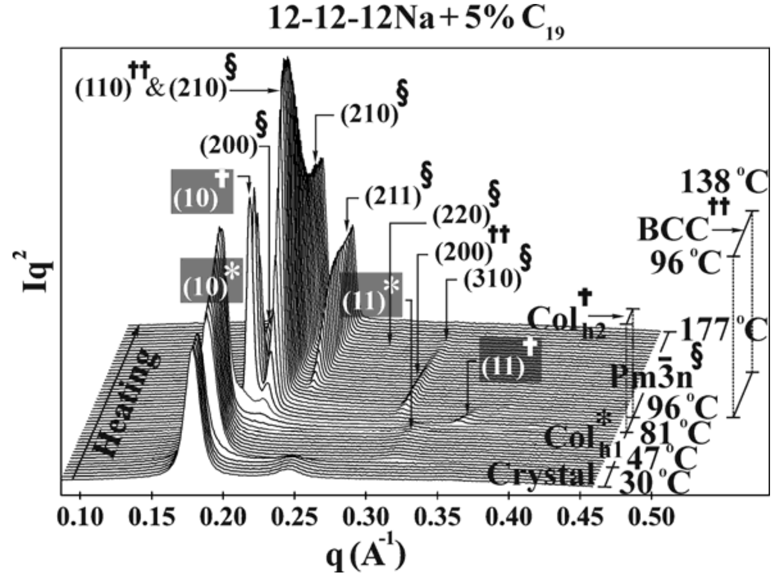

Figure 4-22 Small angle X-ray diffraction result of 12-12-12Na+5%C_{19}.

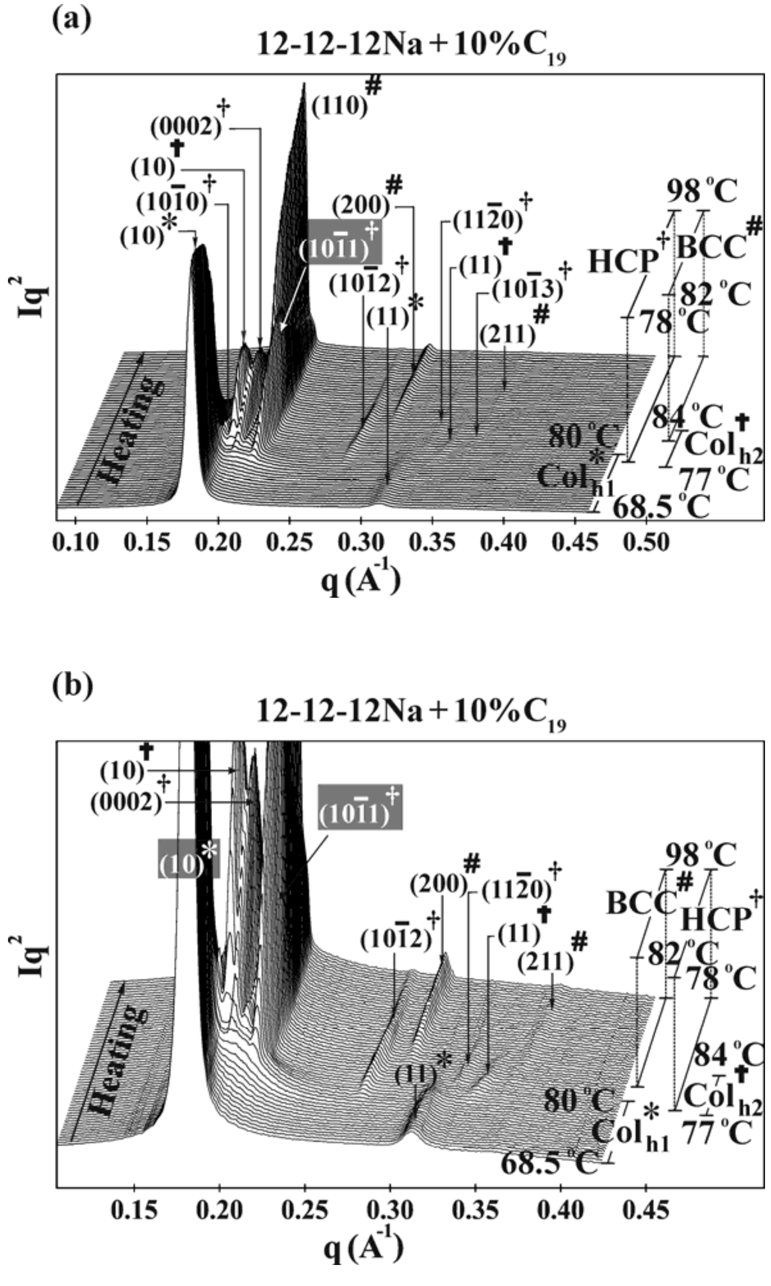

Figure 4-23 (a) Small angle X-ray diffraction result of 12-12-12Na+10%C_{19}. (b) A close view of weak diffraction peaks of 12-12-12Na+10%C_{19} in (a).

The last part of the experimental results is the results of the binary mixtures of 12-12-12Rb and various concentrations of $C_{19}H_{40}$. 12-12-12Rb was studied by our group[15b] and the novel structures, i.e. tetragonal $P4_2/mnm$ [12] phase and dodecagonal liquid quasicrystal (LQC)[13], were discovered in this compound. The phase sequence of

12-12-12Rb on increase of temperature, which is also presented in Figure 4-7, can be summarised as follows: Crystal→Col$_h$→LQC→ $P4_2/mnm$ →BCC. Again, neither of the close packed structures HCP or FCC was observed in this compound. In this work, 5% of $C_{19}H4_0$ is added to 12-12-12Rb. The SAXS results of 12-12-12Rb+5%C_{19} as represented by the phase column in Figure 4-7 show that the crystalline phase at low temperatures is followed by the Col$_h$ phase. The cubic $Pm\overline{3}n$ phase is then formed at higher temperatures and coexists with the preceding Col$_h$ phase. It can be seen that LQC and tetragonal phase existing in the phase sequence of 12-12-12Rb are not observed in this mixture. Instead, the cubic $Pm\overline{3}n$ phase is formed. When the temperature is increased further, the BCC phase is then developed and then followed by the isotropic liquid phase. The diffractograms of 12-12-12Rb+5%C_{19} are shown in Figure 4-26.Note that the cubic $Pm\overline{3}n$ and tetragonal $P4_2/mnm$ lattices are closely related since both of them are in the family of tetrahedrally close packed structures or Frank-Kasper phases[18-19]. In addition, cubic $Pm\overline{3}n$, tetragonal $P4_2/mnm$, and LQC lattices are also related in terms of that all these lattices can be generated by using the same kinds of 2D tiles of triangles and squares[13].

When 10% of $C_{19}H_{40}$ is added to 12-12-12Rb, the HCP is obtained. 12-12-12Rb+10%C_{19} yields the phase sequence quite similar to that of 12-12-12Rb+5%C_{19}. The difference between the phase sequence of 12-12-12Rb+10%C_{19} and that of 12-12-12Rb+5%C_{19} is that the former also includes the HCP phase, but the latter does not. The SAXS results of 12-12-12Rb+10%C_{19} (see Figure 4-7) show that the crystalline phase at low temperatures is followed by the Col$_h$ phase. While the Col$_h$ phase is developing, the HCP phase is also formed. The cubic $Pm\overline{3}n$ phase is formed later at higher temperatures, followed then by the BCC and then the isotropic liquid phases. For the HCP unit cells, the calculated *c/a* ratios are about 1.629-1.635 which are close to a theoretical value 1.633. The diffractograms of 12-12-12Rb+10%C_{19} are shown in Figure 4-27. When 15% of $C_{19}H_{40}$ is added to 12-12-12Rb, the mixture 12-12-12Rb+15%C_{19} gives us a pure HCP phase and this is the only liquidcrystalline phase obtained from this mixture. According to the SAXS scans of 12-12-12Rb+15%C_{19} in Figure 4-28, the crystalline phase at low temperatures is followed by the pure HCP phase first and then followed by the isotropic liquid phase. The calculated *c/a* ratios of the HCP unit cells are about 1.628-1.630 which are close to a theoretical value 1.633.

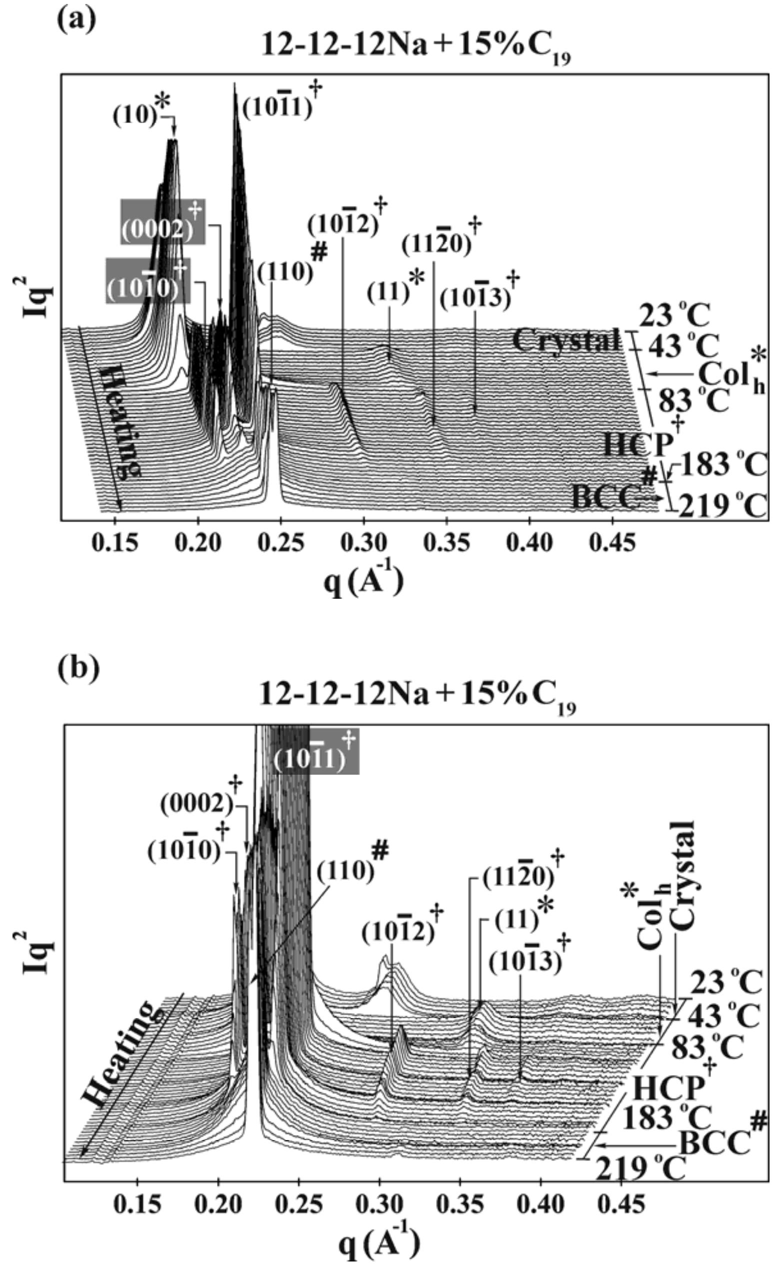

Figure 4-24 (a) Small angle X-ray diffraction result of 12-12-12Na+15%C_{19}. (b) A close view of weak diffraction peaks of 12-12-12Na+15%C_{19} in (a).

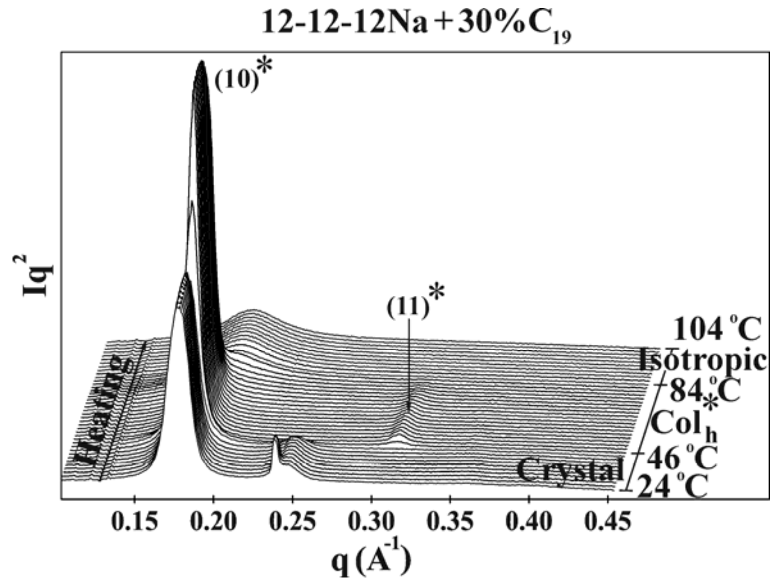

Figure 4-25 Small angle X-ray diffraction result of 12-12-12Na+30%C_{19}.

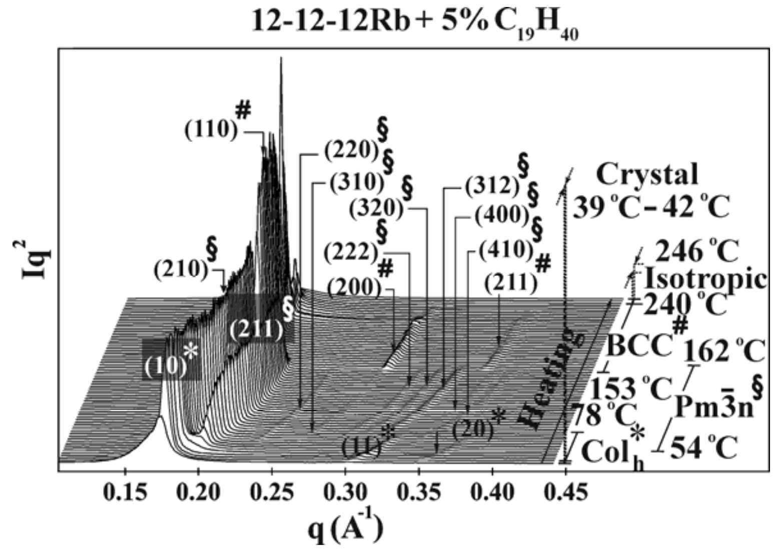

Figure 4-26 Small angle X-ray diffraction result of 12-12-12Rb+5%C_{19}.

When 30% of $C_{19}H_{40}$ is added to 12-12-12Rb, no liquidcrystalline phases are obtained from this mixture. So, the phase sequence of 12-12-12Rb+30%C_{19} is as follows: Crystal→Isotropic liquid. Hence, the diffractograms of 12-12-12Rb+30%C_{19} are not shown here.

Now, it can be seen that the extra proportion of the aliphatic part obtained from one long alkyl chain of n-octadecyl chain ($C_{18}H_{37}$) in 12-12-18Rb is not enough to fill the interstices occurring from packing of micelles to achieve the close packed structures. Therefore, 12-12-18Rb cannot afford the close packed structures. After 10% and especially 15% by weight of $C_{19}H_{40}$ are added to 12-12-18Rb, such interstices are filled and the HCP phase is then formed. Similarly, the close packed structures had never been obtained from the previously studied dendrons[15b] of 12-12-12Na and 12-12-12Rb. After 10% and 15% by weight of $C_{19}H_{40}$ are added to either 12-12-12Na or 12-12-12Rb, the HCP phase is then attained. Now, it can be concluded from currently studied results and previously studied results of 12-12-12M[15b], where M=Na and Rb, that the packing frustration in the close packed structures of micelles in 12-12-18Rb, 12-12-12Na, 12-12-12Rb is relieved after adding $C_{19}H_{40}$ to those compounds. A higher value of the packing fraction of the HCP and FCC, i.e. 0.74, than other structures, e.g. 0.68 for BCC and 0.52 for $Pm\bar{3}n$, also indicates that there is a higher degree of the packing frustration in the close packed structures than other structures. This is why the BCC and $Pm\bar{3}n$ micellar phases are more prevalent than the HCP phase in the dendrimeric systems. However, it is still not able to explain why the close packed structure found in this work is the HCP structure rather than the FCC structure, which the latter is regarded as the most stable structure for hard sphere model[20]. Nonetheless, it should be noted that the FCC structure was also found in the binary mixture of 12-12-18Rb+30%$C_{17}H_{36}$ whose the diffractogram recorded at 40 °C is shown in Figure 4-29.

The study of packing of dendrimers into any given lattice is quite relevant to the study of Kelvin[21] of packing of soap bubbles as froth of the minimum interfacial area since dendrimers and soap bubbles are regarded as soft and ultimately soft balls respectively. In 1887, Kelvin initially proposed that the BCC structure is the solution of the problem of finding the partition of 3D space into equal-volume cells with the minimum interfacial area, whereas Hales[22] proved that the regular hexagon is the solution of Kelvin problem in 2D space. However, in 1994 Weaire and Phelan discovered that the froth with the symmetry of A15 lattice (or $Pm\bar{3}n$ space group) gives a better solution of Kelvin problem; $Pm\bar{3}n$ lattice has an area smaller than BCC lattice by 0.3%[23]. Until recently, the liquid quasicrystal (LQC) with dodecagonal symmetry found in several dendrimeric compounds[13] still yield an even better solution of Kelvin problem. Apparently, most of structures obtained from the packing of dendrimers are all about the solutions in Kelvin problem. The reason is that the minimum area principle is associated with the soft tail and entropy of soft coronas of dendrimers or soft fuzzy balls[24-25]. This is clear when one thinks about the Voronoi cell occupied by inverse micelles of dendrimers. Some alkyl

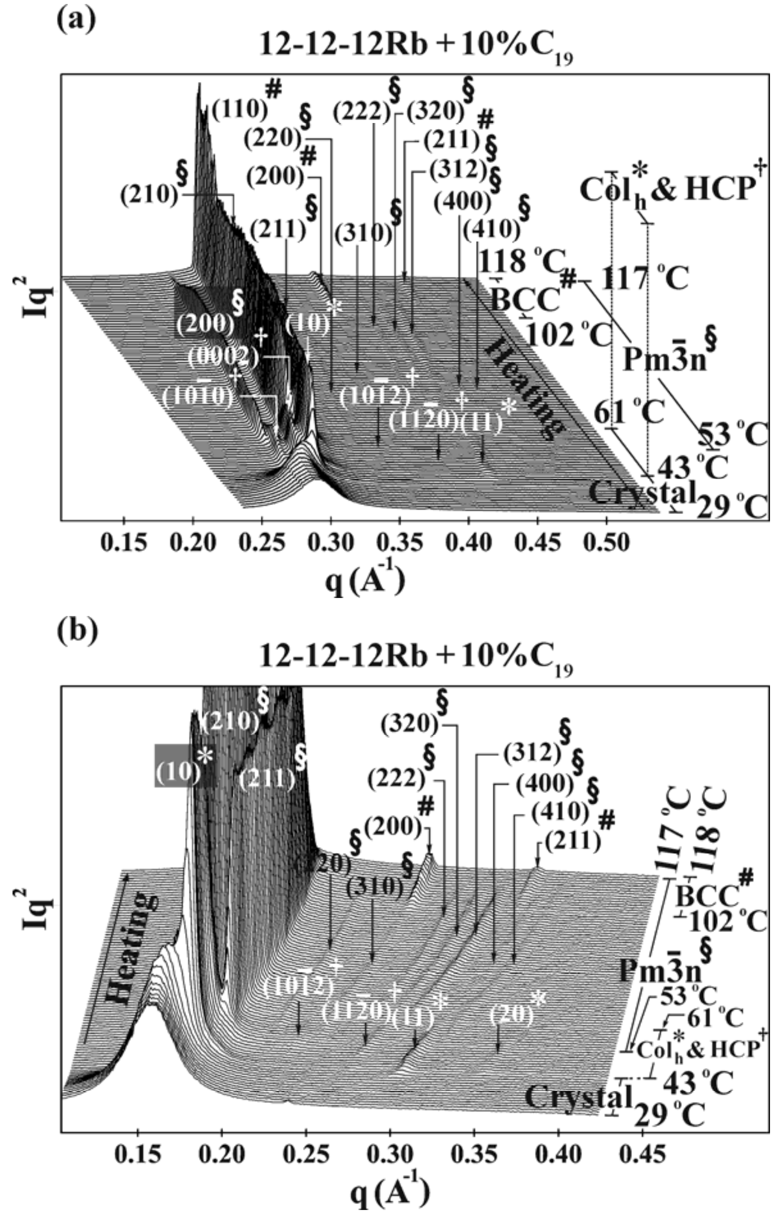

Figure 4-27 (a) Small angle X-ray diffraction result of 12-12-12Rb+10%C_{19}. (b) A close view of weak diffraction peaks of 12-12-12Rb+10%C_{19} in (a).

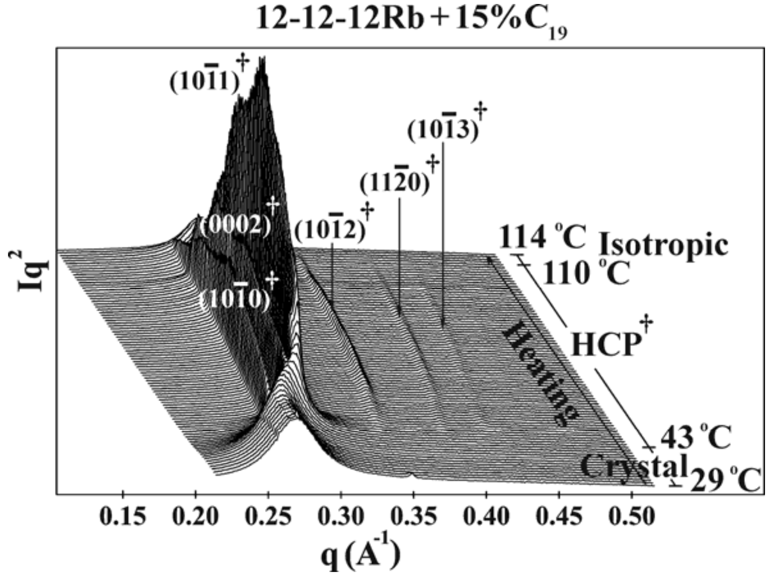

Figure 4-28 Small angle X-ray diffraction result of 12-12-12Rb+15%C_{19}.

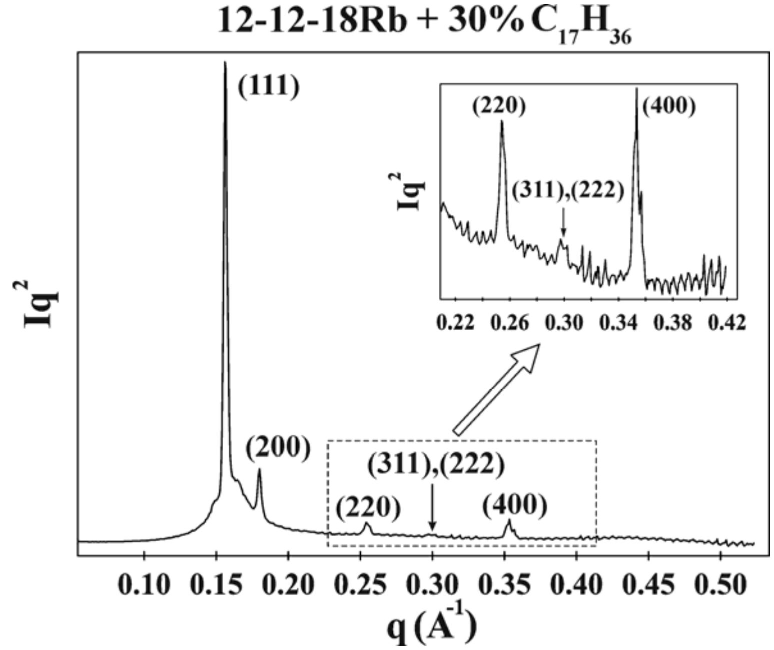

Figure 4-29 Small angle X-ray diffraction result of 12-12-18Rb+30%$C_{17}H_{36}$ recorded 40 °C for 10 minutes: the FCC phase.

chains of dendrimers are located around cell walls. Since one cell shares cell walls with the others, therefore, there are the repulsive interactions between alkyl chains of dendrimers. One way that micelles try to reduce interfacial energy caused by the repulsive interactions between coronal parts of micelles is to decrease the interfacial area of cells.

By contrast, the closely packing rule is associated with interactions and positional entropy of hard spheres. Therefore, this rule is suitably applied to the case of inverse micelles comprising of big hard core and thin peripheral coronal region. However, the micelles possessing too short alkyl chains cannot afford the liquid crystalline phases since the liquid crystalline properties are caused by the aliphatic part of micelles. Therefore, there must be a compromise between the lengths of alkyl chains which can cause the liquid crystalline properties and also possibly suit to achieving the close packed structures. Hence, in this work, alkali metal salts with the shortest alkoxy chains (12-12-12M) are then selected to modify the molecular shape to search for the close packed structures. According to our dendron candidates 12-12-18M (where M=Na, Rb) and previously studied dendrons of n-n-nM where M=Na, Rb and n=12, 14, 16, 18[15b], the volume ratio of aliphatic part to aromatic part of micelles is about 80:20. Therefore, the minimum area principle is more suitable for our studied micellar thermotropic systems than the closely packing rule is. Hence, most of structures obtained from packing of micelles without adding n-paraffin $C_{19}H_{40}$ to those compounds are non-close packed structures, e.g. BCC and $Pm\overline{3}n$, rather than the close packed structures.

Nonetheless, it has been recently reported that the HCP phase was found in the inverse micellar lyotropic system of the ternary lipid mixtures comprising of dioleoylphosphatidylcholine (DOP), dioleoylglycerol (DOG) and cholesterol, of molar ratios 1:2:1 and 1:2:2, in water[9]. In such system, the cores of micelles are consisted of water plus lipid headgroups and the peripheral fuzzy region of micelles is consisted of the hydrophobic parts of the lipid molecules. This exceptional formation of the HCP phase implies that the attempt to relieve the packing frustration in close packed structures of soft fuzzy balls in such lyotropic system is succeeded. Therefore, it might be conjectured that for inverse micellar systems there would be a competition between minimizing the interfacial energy and relieving the packing frustration in the close packed structures of micelles. If the micellar systems can minimise the interfacial energy better than they can reduce the packing frustration in the close packed structures, the $Pm\overline{3}n$ or the BCC phases will be obtained. Conversely, if the micellar systems can minimise the packing frustration in the close packed structures better than they can minimize the interfacial energy, the close packed structures, HCP and FCC, will be obtained instead. In case of that neither reducing the interfacial energy nor relieving the packing frustration in the close packed structures are dominant in the micellar systems, there would be the coexistence of non-close packed structures and close packed structures. The observation of non-close packed structures in our dendron candidates 12-12-18M (where M=Na, Rb) and previously studied dendrons n-n-nM[15b] where M=Na, Rb and n=12, 14, 16, 18 suggests that minimizing the interfacial energy could be done more easily than relieving the packing frustration in the close packed structures of micelles. Conversely, adding 15% by weight of n-nonadecane $C_{19}H_{40}$ to either 12-12-12M (where M=Na, Rb) or 12-12-18Rb helps relieve the packing frustration in the close packed structures a lot, then the HCP phase is obtained instead. The coexistence of the HCP phase and non-close packed phase, for example HCP+BCC in 12-12-12Na+10%C_{19}, or HCP+$Pm\overline{3}n$ in 12-12-12Rb+10%C_{19} and 12-12-18Rb+10%C_{19}, in a short range of temperatures would indicate that neither reducing the interfacial energy nor relieving the packing frustration in the close packed structures are dominant. Although 10% by weight of $C_{19}H_{40}$ added to 12-12-12M and 12-12-18Rb can actually reduce the packing frustration in the close packed structures of micelles, but it is not enough to make the packing frustration in the close packed structures reduce dramatically and dominate over the reducing of interfacial energy.

It should be noted that the HCP phase was also obtained from the direct micellar lyotropic system of nonionic surfactant $C_{12}EO_8$ in water[6], which water still plays the same role as n-nonodecane $C_{19}H_{40}$ does in our binary mixtures. Similarly, the FCC phase was also obtained from the direct micellar lyotropic system of nonionic surfactant $C_{12}EO_{12}$ in water[4], which water still play the same role as n-heptadecane $C_{17}H_{36}$ does in 12-12-18Rb+30%$C_{17}H_{36}$ giving the FCC phase. In addition, the FCC phase has been also found in a similar soft sphere system of the blend of a poly(ethylene oxide)-blockpoly(1,4-butadiene) (PEO-b-PB) and a PB homopolymer[26]. In this system, homopolymers do fill the interstices occurring from packing of block copolymer micelles. Relieving the packing frustration in the close packed structures by adding a compatible homopolymer to block copolymer micelles has been also mentioned[26-27]. However, it was reported later that the FCC phase exists in the diblock copolymers melt of PEO-b-PB[28], which the FCC phase is observed before it is changed to the disordered micellar phase on increasing of temperature.

4.5.2 The first order $\mathrm{Col_h}$-$\mathrm{Col_h}$ transition

As it is described in the previous section that the phase transition from the hexagonal columnar 1 ($\mathrm{Col_h1}$) to the hexagonal columnar 2 ($\mathrm{Col_h2}$) was observed only in 12-12-18Na, 12-12-18Na+m%C_{19}, and 12-12-12Na+m%C_{19} where m=5 and 10, this phase transition is regarded as the first order phase transition, whereas other phase transitions, for example from $\mathrm{Col_h}$ to $Pm\overline{3}n$ or from HCP to BCC, are considered as the second-order phase transition. The $\mathrm{Col_h}$-$\mathrm{Col_h}$ phase transition was also observed in previously studied dendrons in the family of 3,4,5-trialkoxygallate Na salts[15b], i.e. 3,4,5-tridodecyloxygallate and 3,4,5-tritetradecyloxygallate Na salts denoted as 12-12-12Na and 14-14-14Na respectively (see the molecular structure of 12-12-12Na and 14-14-14Na in Figure 4-5). Meanwhile, only one hexagonal columnar phase was observed in 12-12-18Na+m%C_{19} and 12-12-12Na+m%C_{19} where m= 15 and 30 and previously studied dendrons of 16-16-16Na and 18-18-18Na.

12-12-12Na, 14-14-14Na, 16-16-16Na and 18-18-18Na were studied by Yongsong Liu[29]. Figure 4-30, from his thesis, shows the calculation results of the diameters of supramolecular cylinders (i.e. the centre-to-centre distance between two nearest neighbour cylinders in the hexagonal columnar lattice) and the number of corresponding Na salt molecules per supramolecular disc in the rectangular (Rect) and two hexagonal columnar (HexI, and HexII) phases. Note that denotations Rect, HexI, and HexII in Figure 4-30 correspond to denotations $\mathrm{Col_r}$, $\mathrm{Col_h1}$, and $\mathrm{Col_h2}$ in this thesis. The calculation results of the number of molecules per supramolecular disc show that the $\mathrm{Col_h}$-$\mathrm{Col_h}$ phase transition observed in n-n-nNa where n=12, 14, 16, 18 is resulted from the loss of n-n-nNa molecules in the corresponding supramolecular columns during the phase transition. This can be understood from looking at the case of 12-12-12Na. In the Col_h1 lattice of 12-12-12Na, a supramolecular disc, with layer thickness of 4.5 Å, contains five molecules of 12-12-12Na. Then, the number of 12-12-12Na molecules is suddenly dropped to 4.2 molecules during the Col_h1- Col_h2 phase transition. During the Col_h2 phase of 12-12-12Na, the number of molecules of 12-12-12Na is gradually reduced and then approaches to 4 molecules in the end. Therefore, the unit cell of the Col_h1 lattice of 12-12-12Na loses one molecule of 12-12-12Na to form the Col_h2 lattice. The non-integer number of 12-12-12Na molecules, i.e. 4.2, in a supramolecular disc in the Col_h2 lattice is the average number of molecules; it means that most discs in the Col_h2 lattice have 4 molecules whereas some discs have 5 molecules. The discs having 5 molecules are bigger than those having 4 molecules. Therefore, the Col_h2 lattice of 12-12-12Na is formed by the packing of bigger and smaller supramolecular columns. The packing of supramolecular columns with different sizes leads to the distortion of the lattice and also causes the strain to the system, which is unfavorable to the system. To reduce the strain, one extra molecule in each column containing five molecules of 12-12-12Na must be expelled so that every column has four molecules. Then, the undistorted Col_h2 lattice of 12-12-12Na is finally attained by the packing of supramolecular columns with uniform size.

In case of 14-14-14Na, although the number of molecules per disc is non-integer number, the difference in size of supramolecular columns and the corresponding distortion of lattices are less than those of 12-12-12Na since the extra portion of a bit longer alkyl chains of tetradecyl chains ($C_{14}H_{29}$) helps reduce the gaps occurring from packing of small and big columns. The increase in the aliphatic content in 14-14-14Na leads to a smaller jump in decreasing of the number of 14-14-14Na molecules during the Col_h1-Col_h2 phase transition. This becomes clearer in case of 16-16-16Na and 18-18-18Na in particular. The extra portions of even longer alkyl chains of hexadecyl chains ($C_{16}H_{33}$) and octadecyl chains ($C_{18}H_{37}$) can fill the gaps between small and big columns even better so that the sizes of columns in the lattice are hardly different and the jump in decreasing of the number of molecules during the Col_h1-Col_h2 phase transition are disappeared. Therefore, in case of 16-16-16Na and 18-18-18Na the Col_h1 and Col_h2

phases are indistinguishable, and this is why only one Col_h phase was observed in SAXS scans of 16-16-16Na and 18-18-18Na[15b, 29].

According to Figure 4-31, with the column layer thickness of 3.73-3.97 Å obtained from WAXD patterns of 12-12-18Na and 12-12-18Na+15%C_{19} as shown in Figure 4-10 and Figure 4-13, the calculation results of the number of 12-12-18Na molecules per column layer, (see the details of calculation in Appendix 2), of 12-12-18Na and its mixtures 12-12-18Na+m%C_{19} where m=5, 10, 15, 30, shows that there is no jump of the decreasing in the number of 12-12-18Na molecules during the Col_h1-Col_h2 phase transition. The profiles of the decreasing of the number of 12-12-18Na molecules in 12-12-18Na, 12-12-18Na+5%C_{19}, and 12-12-18Na+10%C_{19} are similar to those of 16-16-16Na and 18-18-18Na. Again, this shows that the additional aliphatic content obtained from one extra long alkyl chain of octadecyl ($C_{18}H_{37}$) chain in 12-12-18Na and added n-paraffin $C_{19}H_{40}$ fill the gaps occurring from packing of small and big columns well so that the sizes of columns in the lattice are hardly different and a jump in decreasing of the number of molecules during the Col_h1-Col_h2 phase transition is not seen.

In case of mixtures 12-12-12Na+m%C_{19} where m=5, 10, 15, 30, the calculation results of the number of 12-12-12Na molecules per column layer, with layer thickness of 4.45 Å obtained from Material Studio program, in Figure 4-31b shows that adding 5% and 10% of $C_{19}H_{40}$ to 12-12-12Na reduces a jump of 12-12-12Na a bit. However, when 15% and 30% of $C_{19}H_{40}$ are added to 12-12-12Na, a jump is disappeared. All results of 12-12-12Na+m%C_{19} and 12-12-18Na+m%C_{19} still shows that the increasing in the *a* parameters of the Col_h unit cells of 12-12-12Na+m%C_{19} and 12-12-18Na+m%C_{19} is resulted from adding $C_{19}H_{90}$ to pure compounds of 12-12-12Na and 12-12-18Na. Added $C_{19}H_{40}$ can fill space better than the alkyl part of 12-12-12Na and 12-12-18Na does. Thus, although the *a* parameters of the Col_h unit cells is increased, the number of 12-12-12Na or that of 12-12-18Na required to fill space is reduced. This is different from the case of pure n-n-nNa (n=12, 14, 16, 18) since the *a* parameters of the Col_h unit cells of n-n-nNa is increased as a result of longer alkyl chains in n-n-nNa and more number of n-n-nNa molecules is required to fill the space.

According to the Col_h1-Col_h2 phase transition in 3,4,5-trialkoxygallate Na salts and their mixtures with added n-nonadecane $C_{19}H_{40}$, as shown in Figure 4-30 to Figure 4-31, the characteristic of the Col_h1-Col_h2 phase transition might remind someone about the critical phase transition in substances, e.g. water. The hexagonal columnar phase in 16-16-16Na can be considered as the critical phase since the indistinguishability between the Col_h1 and the Col_h2 starts being observed in this compound. The hexagonal columnar phase in 18-18-18Na can be considered as the supercritical phase since it exists above the critical point in 16-16-16Na. The Col_h1 and the Col_h2 phases in 12-12-12Na, 14-14-14Na, and 12-12-12Na+m%C_{19} where m=5 and 10 can be considered as subcritical phases.

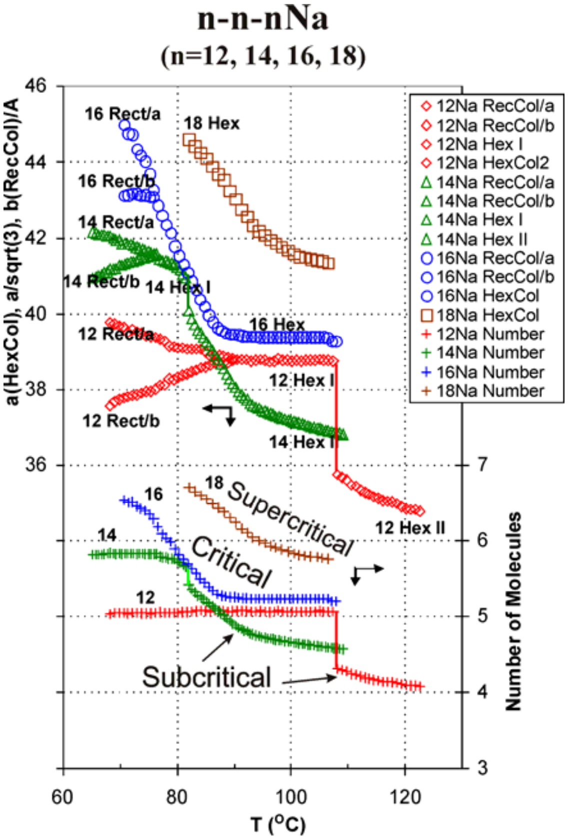

Figure 4-30 The diameters of supramolecular columns and the number of n-n-nNa molecules per supramolecular disc (with thickness 4.5 Å**)** in the Col_h phases of n-n-nNa where n=12, 14, 16, 18[29].

4.5.3 Characterisation of Unit Cells and Corresponding Supramolecular Building Objects

In this section, the size of unit cells of various lattices and corresponding supramolecular objects obtained from 12-12-18M+m%C_{19} and 12-12-12M+m%C_{19} where M= Na, Rb and m=0, 5, 10, 15, 30 are compared. With known lattice parameters of unit cells, the center-to-center distance (D_{cc}) between two attached nearest-neighbour supramolecular objects in unit cells of each structure, considered as the size of supramolecular objects, can be determined and expressed in unit cell parameters. For example, micelles in the BCC unit cell are in contact with each other along the body diagonal of the unit cell ($D_{cc}^{BCC} = \sqrt{3}a_c / 2$), whereas micelles in the cubic $Pm\overline{3}n$ unit cell

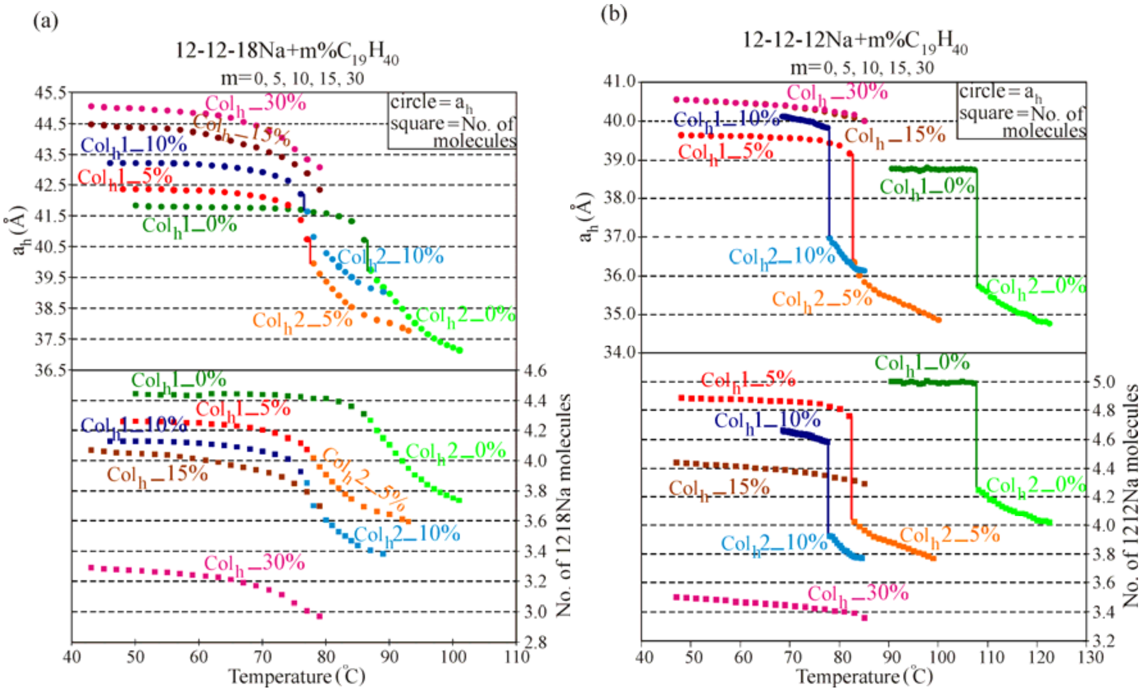

Figure 4-31 (a) The number of 12-12-18Na molecules per column layer (with layer thickness of 3.73-3.97Å) and diameters of supramolecular columns in the Col_h phases of 12-12-18Na+m%$C_{19}H_{40}$ where m=0, 5, 10, 15, 30. (b) The number of 12-12-12Na molecules per supramolecular disc (with thickness of 4.4Å) and diameters of supramolecular columns in the Col_h phases of 12-12-12Na+m%$C_{19}H_{40}$ where m=0, 5, 10, 15, 30.

are in contact with each other along the bisector of each face of the unit cell ($D_{cc}^{Pm\bar{3}n} = a_c/2$).

Figure 4-32 to Figure 4-35 are graphical presentations of the size of micelles and that of columns expressed in lattice parameters a and c, i.e. $D_{cc}^{Col_h} = a_h$, $D_{cc}^{HCP} = a_{hcp}$ or $0.5\sqrt{3/2}c$, $D_{cc}^{Pm\bar{3}n} = a_c/2$, and $D_{cc}^{BCC} = \sqrt{3}a_c/2$, where a_h, a_{hcp}, and a_c, are a lattice parameter of $\mathrm{Col_h}$, hcp, and cubic lattices. Note that calculated unit cell parameters of various lattices of some studied materials and all details of calculations of the size of corresponding supramolecular objects (D_{cc}), with the results, are given in the Appendix 2.

Let us start with the calculation results of unit cell parameters of $\mathrm{Col_h}$ and BCC lattices and the size of supramolecular columns and micelles obtained from 12-12-18Na+m%C_{19} where m= 0, 5, 10, 15, 30, as shown in Figure 4-32. Figure 4-32 shows that the size of unit cells of $\mathrm{Col_h}$1 and $\mathrm{Col_h}$2 lattices and that of corresponding supramolecular columns of 12-12-18Na is smaller than those of 12-12-18Na+m%C_{19}. Also, the size of BCC unit cell and that of corresponding micelles of 12-12-18Na is smaller than those of 12-12-18Na+m%C_{19} where m=5, 10, 15. Similarly, the increasing in the size of unit cells of $\mathrm{Col_h}$, HCP, $\mathrm{Pm\bar{3}n}$, and BCC lattices and that of corresponding supramolecular objects, as a result of adding $C_{19}H_{40}$ to pure compounds of 12-12-18Rb, 12-12-12Na, and 12-12-12Rb, is also seen in the case of 12-12-18Rb+m%C_{19}, 12-12-12Na+m%C_{19}, and 12-12-12Rb+m%C_{19} where m= 5, 10, 15, 30 (see Figure 4-33 to Figure 4-35 respectively). However, there are some exceptional cases that although the concentrations of $C_{19}H_{40}$ added to pure compounds of alkali salts is increased, the size of unit cells and that of corresponding supramolecular objects are not increased. For example, the size of unit cell of $\mathrm{Col_h}$ lattice of 12-12-12Na+15%C_{19} and 12-12-12Na+30%C_{19} are hardly different, or the size of unit cell of cubic $Pm\bar{3}n$ lattice of 12-12-12Na and 12-12-12Na+5%C_{19} are comparable (see Figure 4-34).

According to all results in Figure 4-32 to Figure 4-35, it is obvious that the increasing in size of unit cells and that of corresponding supramolecular objects in various lattices is resulted from adding n-nonadecane $C_{19}H_{40}$ to 12-12-18M and 12-12-12M, where M=Na and Rb. The added n-paraffin C_nH_{2n+2} becomes a part of supramolecular objects mainly formed by the self-assembling of molecules of 12-12-18M and 12-12-12M. Meanwhile, some of added n-paraffin C_nH_{2n+2} also helps fill the voids occurring from packing of supramolecular columns in the Col_h phase or the voids occurring from packing of micelles in cubic and HCP micellar phases. The increasing in size of unit cells and corresponding supramolecular objects in the columnar and micellar phases also occurred in previously studied 3,4,5-trialkoxygallate alkali metal salts with all same alkyl chain lengths (see Figure 4-5)[15].

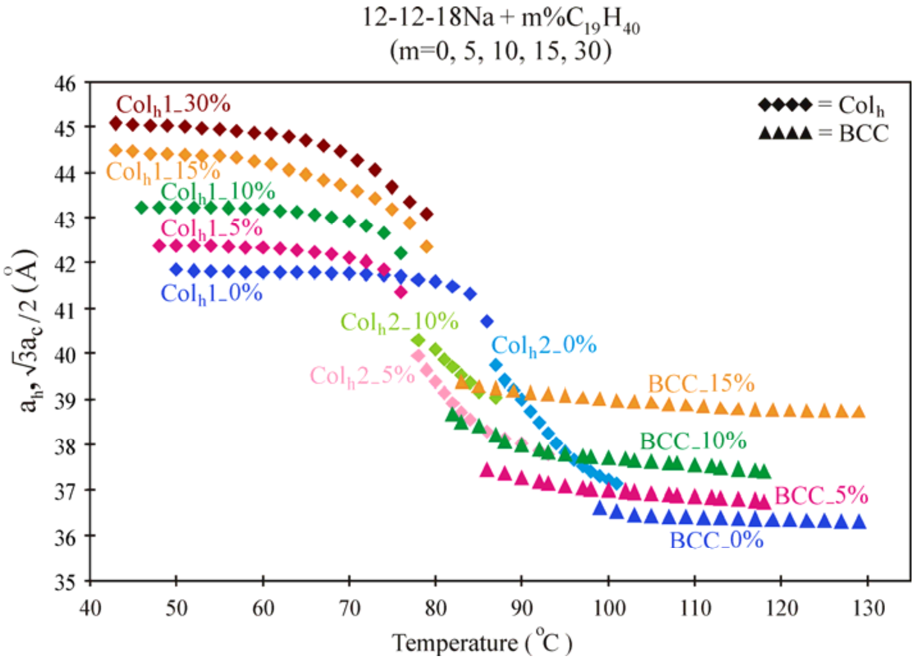

Figure 4-32 The size of unit cells of Col_h and BCC lattices and that of corresponding supramolecular columns and micelles of 12-12-18Na+m%$C_{19}H_{40}$ where m= 0, 5, 10, 15, and 30.

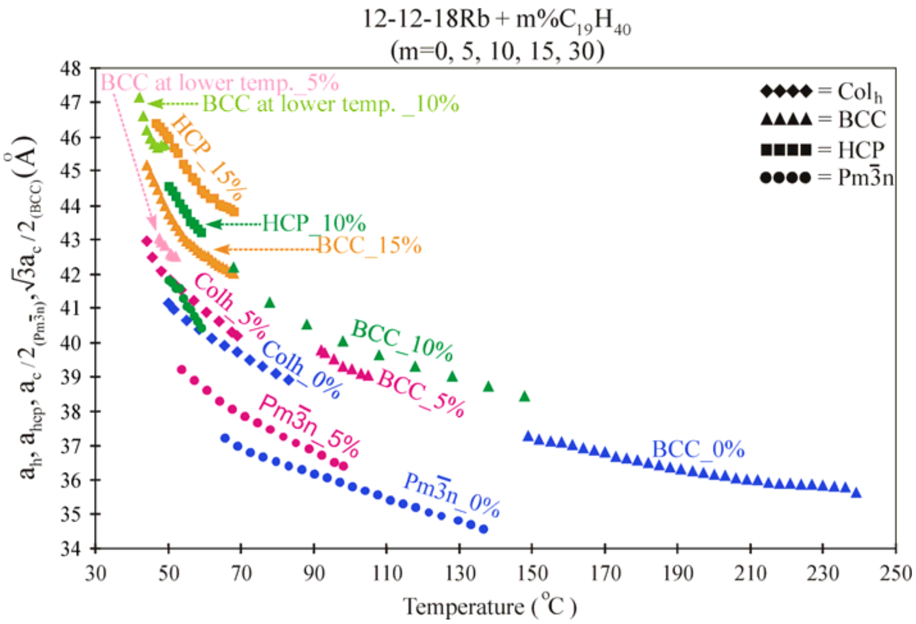

Figure 4-33 The size of unit cells of Col$_h$, HCP, Pm$\overline{3}$n, and BCC lattices and that of corresponding supramolecular columns and micelles of 12-12-18Rb+m%C$_{19}$ where m=0, 5, 10, 15, and 30.

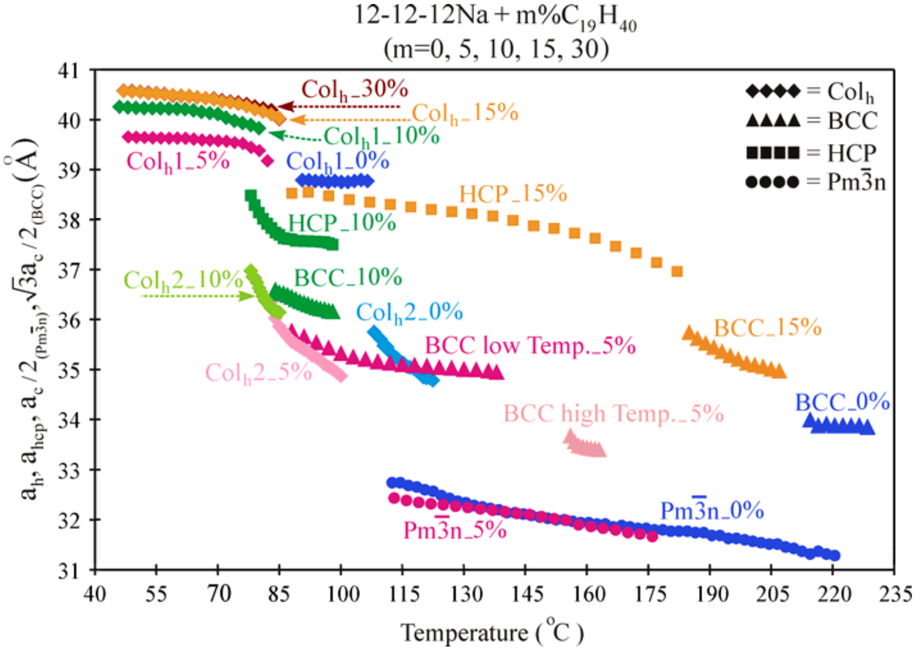

Figure 4-34 The size of unit cells of Col$_h$, HCP, Pm$\overline{3}$n, and BCC lattices and that of corresponding supramolecular columns and micelles of 12-12-12Na+m%C$_{19}$H$_{40}$ where m=0, 5, 10, 15, 30.

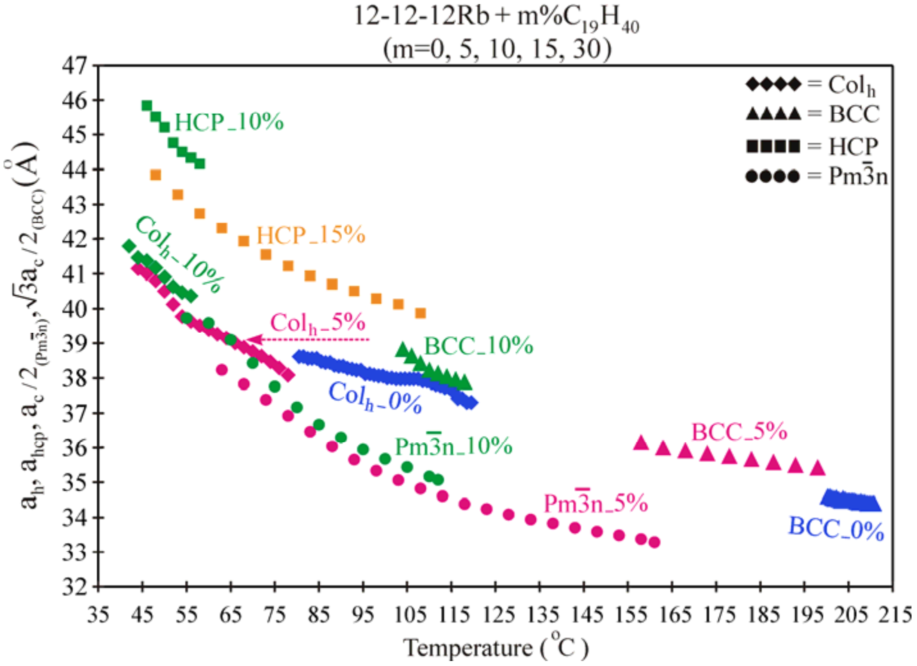

Figure 4-35 The size of unit cells of Col_h, HCP, $Pm\bar{3}n$, and BCC lattices and that of supramolecular columns and micelles obtained from in unit cells of 12-12-12Rb+m%$C_{19}H_{40}$ where m=0, 5, 10, 15, 30.

4.5.4 Binary Phase Diagrams

With all SAXS results of 12-12-12M and 12-12-18M, where M=Na and Rb, and their mixtures with added various concentrations of $C_{19}H_{40}$ as described in the section 4.5.1, the binary phase diagrams of 12-12-12M+m%C_{19} and 12-12-18M+m%C_{19}, where M=Na,Rb and m=0,5,10,15,30, are constructed. Let us start with the phase diagram of 12-12-18Na+m%C_{19} where m=0,5,10,15,30 in Figure 4-36. The phase diagram of 12-12-18Na+m%C_{19} is simple. Only few phases, i.e. the crystalline (K), Col_h1, Col_h2, BCC, and isotropic liquid phases, are seen in this two component system. One thing which one can notice in this binary system is that the transition temperature from the Col_h2 phase to the BCC phase of 12-12-18Na+C_{19} is lower than that of pure 12-12-18Na and it is even lower when more concentration of $C_{19}H_{40}$ is added to12-12-18Na. This also occurs in other binary systems of 12-12-18Rb+m%C_{19}, 12-12-12Na+m%C_{19}, and 12-12-12Rb+m%C_{19}, which the cubic or HCP micellar phases are developed at low temperatures. Note that the dash curves separating the isotropic liquid phase from the BCC+isotropic liquid phase and also separating the BCC phase from the BCC+isotropic liquid phase are proposed due to the lack of the information of the isotropic phase of each mixture.

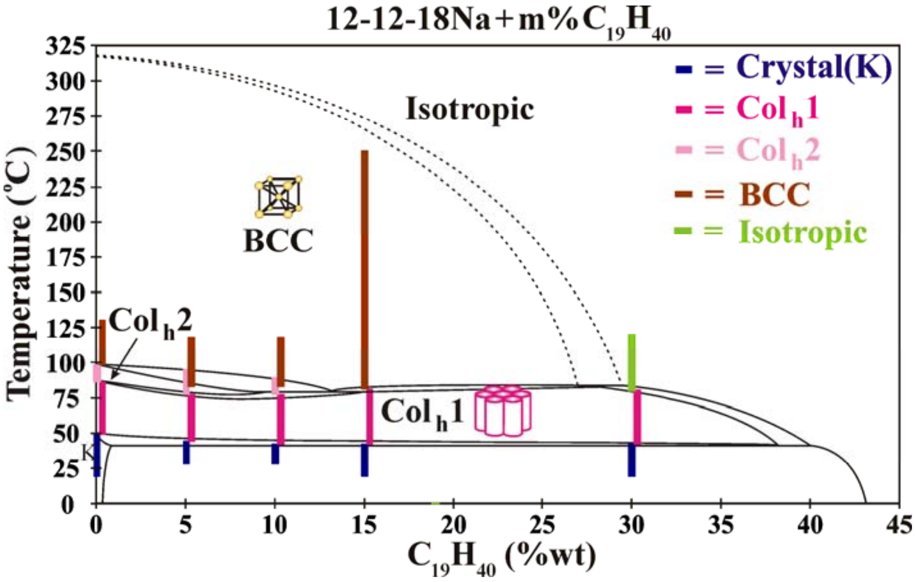

Figure 4-36 The binary phase diagram of 12-12-18Na+m%C_{19} where m= 0, 5, 10, 15, 30.

The phase diagram of 12-12-18Rb+m%C_{19} as shown in Figure 4-37 is more complicate than that of 12-12-18Na+m%C_{19}. The cubic $Pm\overline{3}n$ and the HCP phases, which are not observed in 12-12-18Na+C_{19}, are seen in these binary mixtures. The biphasic regions of the K+HCP and the K+BCC are in a very narrow range of temperatures. Therefore, one would see these phase combinations only if the mixtures are heated or cooled very slowly. In addition, when 8% of $C_{19}H_{40}$ or more are added to 12-12-18Rb, the Col_h phase which is usually observed at low temperatures is disappeared from the phase sequence of heating or cooling of the mixtures. So, the cubic or the hexagonal close packed (HCP) micellar phases are directly developed from the crystalline phase, and vice versa. Generally, the micellar phases are usually developed from the Col_h phase as a result of changing of the molecular shape of dendrons from tapered wedge shape to conical shape due to the increasing of the temperature or the increasing of the generation number of dendron[30-31].

By contrast, at low temperatures the changing of molecular shape of dendrons from tapered wedge shape to conical shape leading to the formation of the cubic or the HCP micellar phases of 12-12-18Rb+C_{19} is resulted from the adding of $C_{19}H_{40}$ to 12-12-18Rb. $C_{19}H_{40}$ begins to melt at 32 °C, i.e. the melting point, and mix with the aliphatic part of molecules of 12-12-18Rb. Mixing melted $C_{19}H_{40}$ into the aliphatic part of molecules of 12-12-18Rb makes the aliphatic part of 12-12-18Rb swollen and changes the molecular shape of 12-12-18Rb from a tapered wedge shape to a conical shape. Thus, the molecules of 12-12-18Rb tend to arrange themselves into spherical micelles rather than cylindrical micelles. Then, the self-organisation of spherical micelles of 12-12-18Rb+C_{19} yields to the cubic or the HCP structures. The change in the molecular shape of dendrons from tapered wedge shape to conical shape due to the addition of $C_{19}H_{40}$ can be also seen by drawing the isothermal line, for example at 70 °C, across the phase diagram. One will see that the Col_h phase is developed to the cubic $Pm\overline{3}n$ phase and then the BCC phase as the concentration of $C_{19}H_{40}$ added to 12-12-18Rb is increased. According to the diagram, the pure HCP phase would be obtained if 13-14% by weight of $C_{19}H_{40}$ is added to 12-12-18Rb.

The phase diagram of 12-12-12Na+m%C_{19} is shown in Figure 4-38. In this binary system, the pure HCP phase could be seen in a wider range of temperatures and concentrations of $C_{19}H_{40}$ than that in the binary system of 12-12-18Rb+m%C_{19}. Unlike the phase diagram of 12-12-18Rb+m%C_{19}, there is no phase transition from the crystalline phase to the micellar phase, but the phase transitions from the Col_h phase to the cubic micellar phases or to the HCP micellar phase still exist in this binary system. The change in the molecular shape of dendron from tapered wedge shape to conical shape due to the addition of $C_{19}H_{40}$ still can be seen in this binary system. For example, if the isothermal line at 110 °C is drawn across the phase diagram of 12-12-12Na+m%C_{19}, one will see that the Col_h phase is developed to the cubic $Pm\overline{3}n$ phase and then the BCC phase as the concentration of $C_{19}H_{40}$ added to 12-12-12Na is increased. The existence of the second order phase transition between the rectangular columnar (Col_r) phase and the

Col$_h$1 phase in 12-12-12Na and possibly in some binary mixtures of 12-12-12Na and very low concentrations of $C_{19}H_{40}$ is indicated by small area under the straight dash line. Note that the phase transition between the Col$_h$1 phase and the Col$_h$2 phase which is regarded as the first order phase transition is explained in detail in section 4.5.6. Again, the dash curves separating the isotropic liquid phase from the BCC+isotropic liquid phase and also separating the BCC phase from the BCC+isotropic liquid phase are proposed due to the lack of the information of the isotropic phase of each mixture.

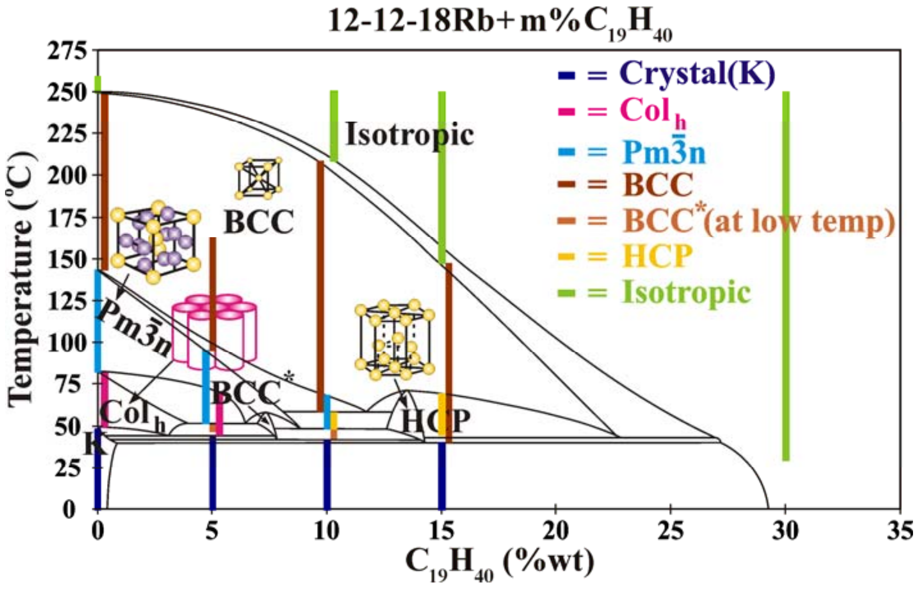

Figure 4-37 The binary phase diagram of 12-12-18Rb+m%C_{19} where m= 0, 5, 10, 15, 30.

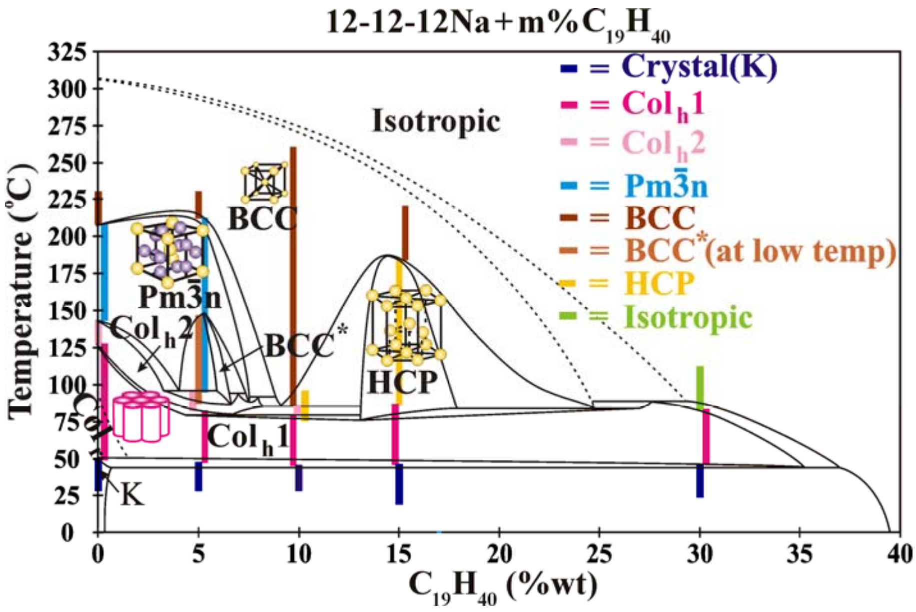

Figure 4-38 The binary phase diagram of 12-12-12Na+m%C_{19} where m= 0, 5, 10, 15, 30.

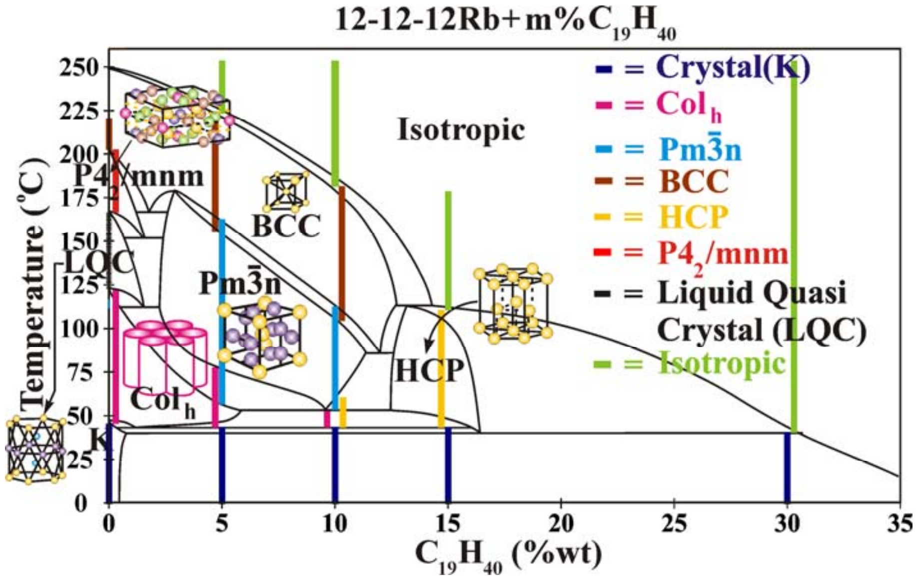

Figure 4-39 The binary phase diagram of 12-12-12Rb+m%C_{19} where m= 0, 5, 10, 15, 30.

The phase diagram of 12-12-12Rb+m%C_{19} is shown in Figure 4-39. According to the diagram, the liquid quasicrystal (LQC) and the tetragonal $P4_2/mnm$ phases, which do not exist in binary systems of 12-12-12Na+m%C_{19}, 12-12-18Na+m%C_{19}, and

12-12-18Rb+m%C_{19}, are seen in this binary system. The biphasic region of K+HCP is in a very narrow range of temperatures. So, one would see this phase combination only if the mixtures are heated or cooled very slowly. The phase transition from the crystalline phase to the HCP micellar phase still exists when around 15% of $C_{19}H_{40}$ is added to 12-12-12Rb. The change in the molecular shape of dendrons from tapered wedge shape to conical shape due to the addition of $C_{19}H_{40}$ still can be seen in this binary system. For example, if the isothermal line at $100\,^{\circ}\mathrm{C}$ is drawn across the diagram, the $\mathrm{Col_h}$ phase is developed to the cubic $Pm\overline{3}n$ phase first, followed then by the BCC phase and the HCP phase as the concentration of $C_{19}H_{40}$ added to 12-12-12Rb is increased.

4.5.5 Electron density reconstruction

From small angle X-ray diffraction results of 12-12-12M+15%C_{19} where M=Na and Rb, the 3D electron density maps of the HCP phase of 12-12-12M+15%C_{19} can be reconstructed by performing Fourier transform. Since the HCP structure has an inversion centre, the phase angle $\phi_{h,k,l}$ for each diffraction peak can be only either 0 or π and the simplified expression of the electron density equation according to eq. (2-12) is then used to reconstruct the electron density map. With the knowledge about the system, a choice of the phase combinations is made on the basis of the physical merits of the electron density maps and the corresponding histograms. The right choice should well define low- and high electron density regions[19]. In this case, choosing the right choice was done in two steps. Firstly, the electron density maps were reconstructed by using only the first five diffraction orders with all possible phase combinations and the best phase combination is chosen on the merits of the electron density maps and the corresponding histograms. Then, the phase combinations of two remaining diffraction orders were added to the best phase combination of the first five diffraction orders and the best phase combination of the remaining two diffraction orders is again chosen on the merits of the electron density maps and the corresponding histograms.

Figure 4-40a shows the 3D reconstructed electron density map of the HCP phase of 12-12-12Rb+15%C_{19}, with the sketch of different parts of micelles corresponding to different electron density levels. All relevant parameters used to recreate this electron density map are tabulated in Table 4-1, whereas electron density maps of the HCP phase of 12-12-12Na+15%C_{19} and those of 12-12-12Rb+15%C_{19} with different phase angle combinations are shown in the Appendix 3. The 3D map, with density gradient from the highest electron density (purple) to the lowest electron density (red), shows that micelles of 12-12-12Rb+15%C_{19} have high electron density cores (purple and navy) and lower electron density peripheral region (green, yellow, and red). The high electron density cores of micelles, comprised of aromatic rings and Rb atoms of 12-12-12Rb molecules, are quite small whereas the low electron density peripheral region, occupied by alkyl chains of 12-12-12Rb molecules and added n-nonadecane $C_{19}H_{40}$, is larger. This is in qualitative agreement with the calculated aliphatic volume fraction (v_{ali}) and the volume fraction of aromatic part plus alkali atom (v_{aro}+M), i.e. 83% and 17% respectively, in 12-12-12Rb+15%C_{19} (see details of calculation in Appendix 4). The histogram of electron density distribution in the HCP unit cell of 12-12-12Rb+15%C_{19} is shown in Figure 4-40b. The dashed line is drawn, based on the calculation of the aliphatic volume fraction and the volume fraction of aromatic part plus alkali atoms in 12-12-12Rb+15%C_{19}, to divide the whole region of histograms into two parts, i.e. the low density part corresponding to the aliphatic content in the mixture (i.e. the left region of the dashed line) and the high density part corresponding to the aromatic part plus alkali atom in the mixture (i.e. the right region of the dash line). According to the histogram, most of volume in the HCP unit cell of 12-12-12Rb+15%C19 is of low electron density, i.e. 83% of total volume, whereas 17% of total volume in the HCP unit cell of 12-12-12Rb+15%C19 is of high electron density. Figure 4-40c shows the packing of micelles into the HCP lattice. The unit cell, drawn with blue solid lines, contains two micelles. Figure 4-40d shows the ABAB… stacking sequence of layers of micelles; the micelles in the first layer (the layer A) pack into a 2D hexagonal lattice, i.e. the densest packing in 2D space. The micelles in the next layer (the layer B) are located in the hollows occurring from the packing of micelles in the layer A. The micelles in the third layer are situated directly above the micelles in the first layer, thereby obtaining the identical layer of micelles as A layer.

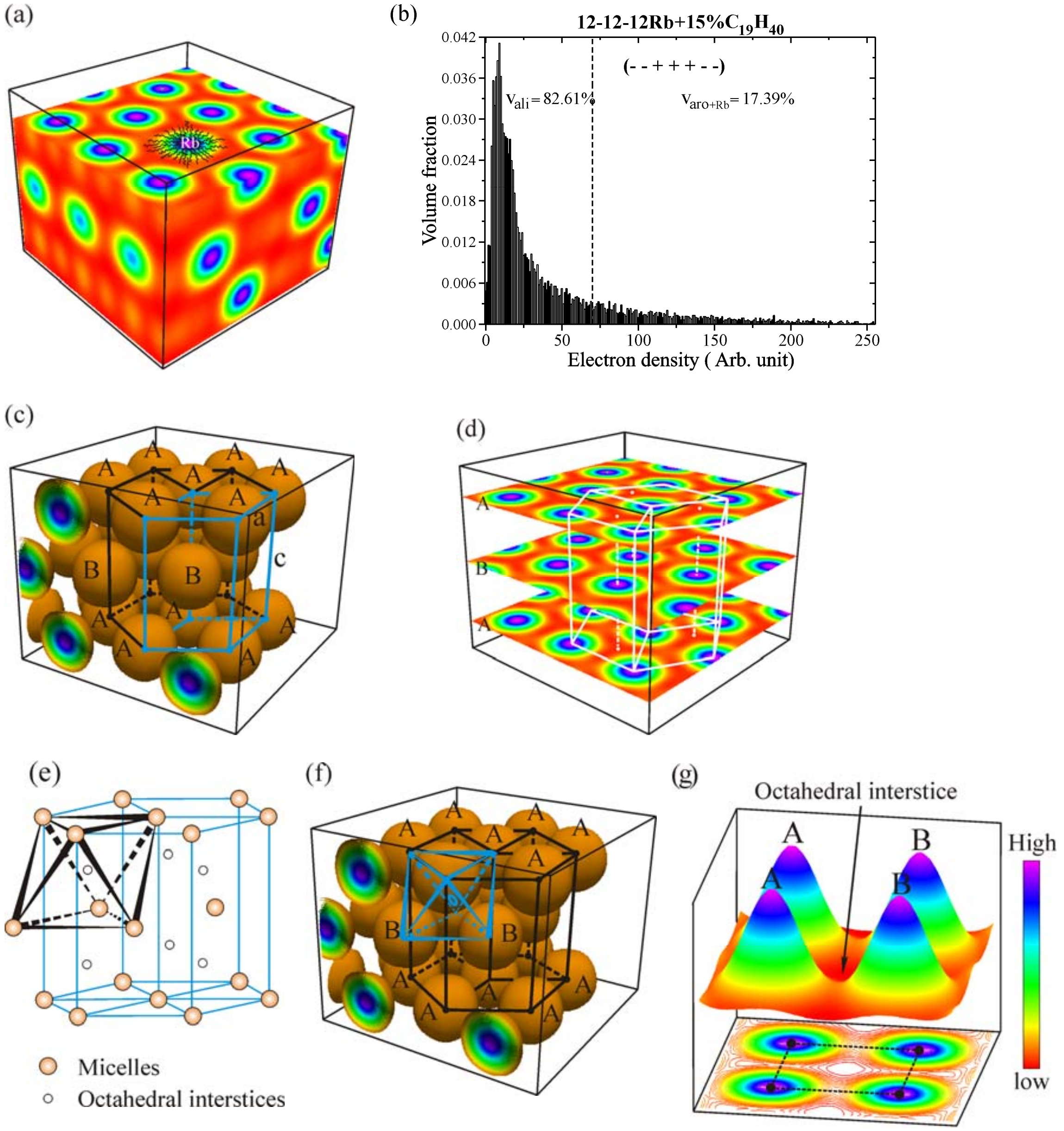

Figure 4-40 (a) The reconstructed electron density map and (b) the corresponding histogram of electron density distribution of the HCP phase of 12-12-12Rb+15%C_{19}. (c) The HCP unit cell. (d) ABA stacking sequence of layers of micelles in the HCP structure. (e) Octahedral interstices in the HCP lattice. (f) A sketch of the octahedron on the electron density map of the HCP phase of 12-12-12Rb+15%C_{19}. (g) The electron density on the clipping plane on which the centre of the octahedral interstice is located. The symbols + and – in (a) denote phase angles of diffraction peaks 0 and π respectively.

Figure 4-40e shows octahedral interstices in the HCP lattice. An octahedral interstice is surrounded by six motifs (i.e. micelles). To investigate the electron density at the centre of an octahedral interstice in the HCP lattice, the clipping plane which is co-planar with the square base of the octahedron is created (see the sketch in Figure 4-40f). According to Figure 4-40g, the centre of square base of octahedral interstitial site, i.e. the octahedral interstice, in the HCP lattice of 12-12-12Rb+15%C_{19} has the lowest electron density whereas all four corners of the square base have the highest electron density. This is as expected. The fact that the density at the centre of the octahedron is not significantly lower than elsewhere outside the aromatic cores is attributed the preferential presence of the alkane at this location, unaccessible to the alkoxy chains of the gallate. In addition, this result also confirms that the selected phase angle combination of diffraction peaks is the right choice.

4.5.6 Location of Rb^+ ions

To locate the Rb^+ ions in the electron density map of the HCP phase of 12-12-12Rb+15%C_{19}, subtraction of the electron density of the HCP phase of 12-12-12Na+15%C_{19} from that of 12-12-12-AG- Rb+15%C_{19} is performed. To make the low electron density region in those two maps cancel each other out as completely as possible, the electron density in the map of 12-12-12Na+15%C_{19} has to be rescaled so that the electron density in the low density region of 12-12-12Na+15%C_{19} is comparable to that of 12-12-12Rb+15%C_{19}. This can be done by multiplying the electron density map of 12-12-12Na+15%C_{19} with a scaling factor. The determination of the scaling factor is based on the fact that the two mixtures have the same aliphatic content, i.e. 3 dodecyl chains ($C_{12}H_{25}$) plus n-nonadecane $C_{19}H_{40}$ added. The curve within the aliphatic region of the scaled histogram of 12-12-12Na+15%C_{19} should be equal to that of the histogram of 12-12-12Rb+15%C_{19}.

Figure 4-41a shows the original histograms of the electron density distribution within the HCP unit cells of 12-12-12Na+15%C_{19} (blue) and 12-12-12Rb+15%C_{19} (red). The scaled histogram of 12-12-12Na+15%C_{19}, i.e. the blue curve multiplied by 0.74, is shown with the black line. Dashed lines delineate the volume fractions of the aliphatic (left) and non-aliphatic (right) contents. One can see that after rescaling the electron densities in the aliphatic (low-density) regions of the two mixtures overlap. Nonetheless, one still sees that some parts of low density regions in the HCP unit cell of 12-12-12Rb+15%C_{19} are not completely removed after subtraction. Figure 4-41b shows electron density map of 12-12-12Rb+15%C_{19} and the rescaled map of 12-12-12Na+15%C_{19}. One can see that the electron density at cores of micelles of 12-12-12Na+15%C_{19} is lower than that for 12-12-12Rb+15%C_{19}, whereas the electron densities in the peripheral region (i.e. the red region) of those two maps are comparable. Figure 4-41c shows the scan of electron density through centres of micelles of 12-12-12Na+15%C_{19} (black line) and 12-12-12Rb+15%C_{19} (red line). The electron density scans looks similar to a profile of a simple cosine function as one can see the periodicity of the maxima and the minima of the density at the centres of micelles and the points where any two adjacent micelles are touched each other respectively. The cosine-shaped curve of the scans would wonder someone why we do not see an artefact occurring from using a limited number of diffraction peaks to reconstruct the electron density map. This can be explained that the limitation of the electron density subtraction method is in the liquid crystal nature of the system whereby the size of fluctuations in micellar positions exceeds the spread of the cations within a micelle. The electron density difference function is a convolution of the two spreads, with the former function probably making a larger contribution to the spread.

The electron density difference map of Rb-Na, with plot of the electron density scan through centres of globular areas containing Rb^+ ions (i.e. green line) is also shown in Figure 4-41c. Figure 4-41d is the 3D electron density difference map of Rb-Na, in which some isoelectron surfaces at low electron density are not shown. According to the electron density scan of Rb-Na through centres of globular areas containing Rb^+ ions in the electron difference map in Figure 4-41c, the full width at half maximum (FWHM) of the Rb-Na profile is equal to 17.5 Å. This figure seems to be larger than our original belief that Rb^+ ions are located at the focal point of micelles of 12-12-12Rb+15%C_{19} since the ionic diameters of Rb^+ and Na^+ ions are 3.32 Å and 2.32 Å respectively[32]. Therefore, the difference in ionic diameters of Rb^+ and Na^+ is equal to 1 Å. Also, a micelle of 12-12-12Rb+15%C_{19} contains 32 molecules of 12-12-12Rb and a micelle of

12-12-12Na+15%C_{19} contains 28 molecules of 12-12-12Na. So, if Rb^+ and Na^+ ions are congregated at centres of micelles, the globular area containing Rb^+-Na^+ ions cannot have the diameter up to 17.5 Å. 17.5 Å of FWHM of Rb-Na profile in Figure 4-41c, which is twice the distance measurement from O atom in the alkoxy chains to Rb atom at the apex of 12-12-12Rb molecule (i.e. 8.0-8.5 Å), suggests that the apexes of molecules of 12-12-12Rb, in which the Rb^+ ions are located, point toward different points rather than the same point. The narrower electron density scan of Rb-Na (brown line), i.e. the green curve multiplied by 3.86, than the scan of 12-12-12Rb+15%C_{19} (red line) suggests that the Rb^+ ions of 12-12-12Rb molecules are scattered over aromatic rings of 12-12-12Rb molecules. Therefore, the core of micelle of 12-12-12Rb+15%C_{19} are formed by the aromatic rings and the scattered Rb^+ ions. The spread of Rb^+ ions could be the results of repulsive interactions between them. In addition, the micelle in 12-12-12Rb+15%C_{19} contains 32 salt molecules and it is difficult for all of them to reach the centre of the micelle. This is likely to add to the spread of the cations.

Table 4-1 Experimental and calculated *d*-spacings, multiplicity factor *p*, relative integrated intensities (I_{hkl}), and phase angles ($\phi_{h,k,l}$) used in reconstructing electron density map of the HCP phase obtained from 12-12-12Rb+15%C_{19} at 80 ºC.

(hkil)	d_{exp} (Å)	d_{cal} (Å)	I_{hkl}	*p*	$\phi_{h,k,l}$
$(10\bar{1}0)$	35.6	35.7	23.72	6	π
(0002)	33.4	33.5	31.44	2	π
$(10\bar{1}1)$	31.5	31.5	100.00	12	0
$(10\bar{1}2)$	24.4	24.4	5.99	12	0
$(11\bar{2}0)$	20.6	20.6	1.98	6	0
$(10\bar{1}3)$	18.9	18.9	1.19	12	π
$(11\bar{2}2)$	17.6	17.6	0.81	12	π
The size of unit cell *a* = 41.2Å and *c* = 67.0Å. *c*/*a*=1.626					

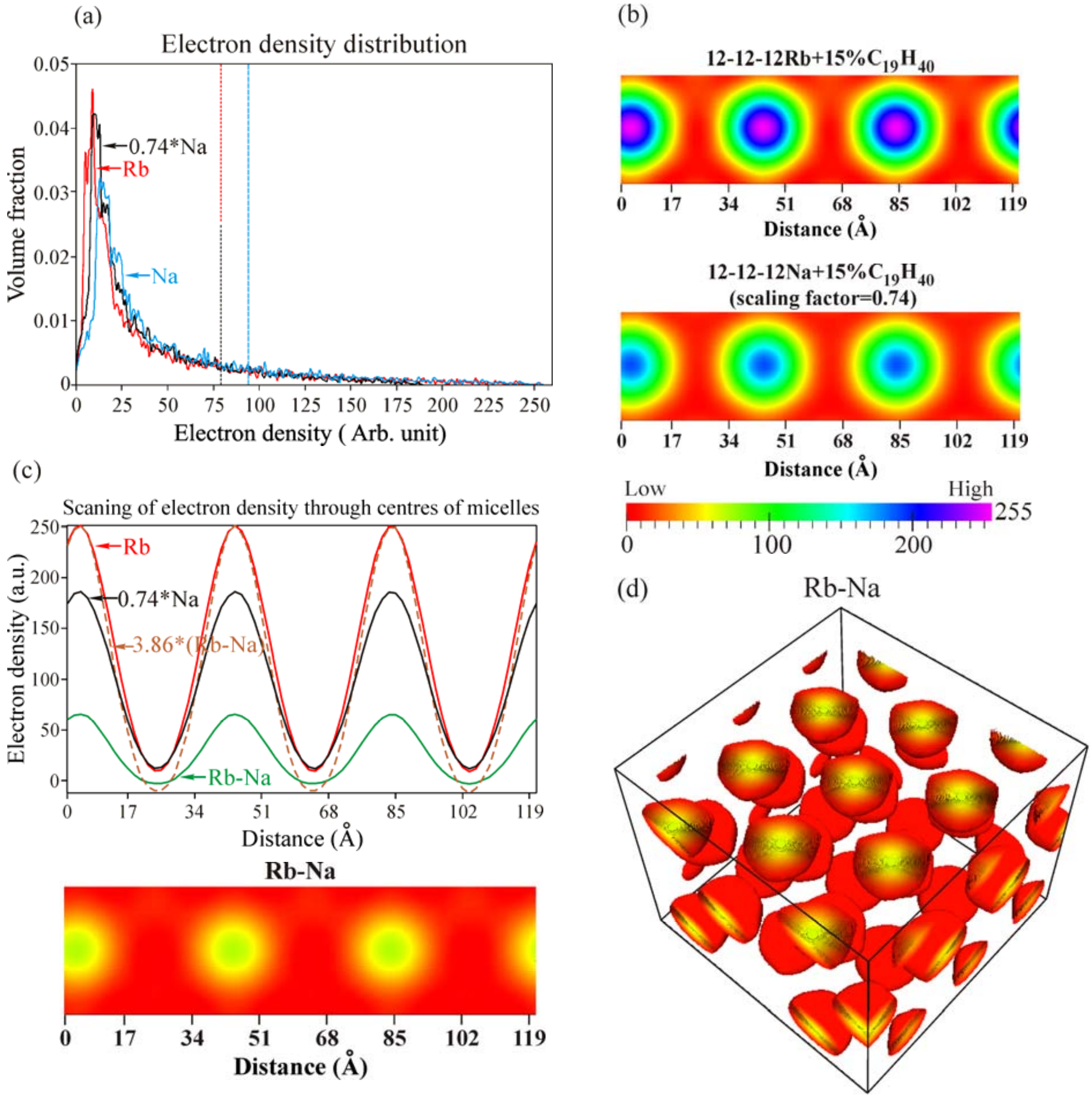

Figure 4-41 (a) Histograms of the electron density distribution for the hcp phase of 12-12-12Rb+15%C$_{19}$ (red) and 12-12-12Na+15%C$_{19}$ (blue). The scaled histogram of 12-12-12Na+15%C$_{19}$ is shown with the black line. (b) Electron density maps of the HCP phase of 12-12-12Rb+15%C$_{19}$ and 12-12-12Na+15%C$_{19}$, which the latter is obtained from rescaling the density. (c) Horizontal scans of electron density through centres of micelles of 12-12-12Rb+15%C$_{19}$ (red) and 12-12-12Na+15%C$_{19}$ (black) and the scan of electron density difference of Rb-Na, i.e. green (unscaling) and brown (scaling) lines. (d) 3D electron density difference map of Rb-Na. Note that, for convenience, Rb-0.74*Na is shortly written as Rb-Na in (c).

4.5 Conclusion

The dendrons of 3,4,5-trialkoxygallate alkali metal salts, with two short and one long alkoxy chains, denoted as 12-12-18M where M=Na and Rb, and their mixtures with added n-nonadecane $C_{19}H_{40}$ are studied to search for close packed micellar phases, HCP and FCC, which have never been observed in thermotropic liquid crystals. According to the study results, it is found that neither of pure compounds of 12-12-18M yields close packed structures. However, the HCP phase is obtained from 12-12-18Rb+m%C_{19} where m=10 and 15. For the previously studied dendrons of 3,4,5-tridodecyloxygallate alkali metal salts, 12-12-12M, which never yielded the close packed structures, the mixtures 12-12-12M+m%C_{19} where m=10 and 15 also yields the HCP structure. Nonetheless, the FCC phase is not observed in any mixtures of 12-12-18M+m%C_{19} and 12-12-12M+m%C_{19}, whereas it should be noted here that the FCC phase is obtained from the binary mixture of 12-12-18Rb+30%$C_{17}H_{36}$. With all results of current study, it can be concluded that it is possible to achieve the close packed structures in thermotropic liquid crystals from pure compounds if the dendrons have the right molecular shape, especially with the part of the alkyl tails which plays the most important role to fill the interstices occurring in the packing of micelles.

References

[1] E. Buhleier, W. Wehner and F. Vögtle, "Cascade and nonskid-chain-like Synthesis of molecular cavity topologies", Synthesis, 1978, 155-158.

[2] D. A. Tomalia, J. R. Dewald, M. R. Hall, S. J. Martin and P. B. Smith, Preprints of the 1st SPSJ International Polymer Conference, Society of Polymer Science Japan, Kyoto, 1984, p 65.

[3] A. M. Figueiredo Neto and S. R. A. Salinas, "The physics of lyotropic liquid crystals: Phase Transitions and Structural Properties (Monographs on the Physics and Chemistry of Materials)", illustrated edition, Oxford University Press, USA, 2005.

[4] P. Sakya, J. M. Seddon, R. H. Templer, R. J. Mirkin and G. J. T. Tiddy, “Micellar Cubic Phases and Their Structural Relationships: The Nonionic Surfactant System $C_{12}EO_{12}$/Water”, Langmuir, 1997, 13, 3706-3714.

[5] (a) R. Vargas, P. Mariani, A. Gulik and V. Luzzati, “Cubic phases of lipid-containing systems. The structure of phase Q223 (space group Pm3n). An X-ray scattering study.”, J. Mol. Biol., 1992, 225, 137-145; (b) V. Luzzati, R. Vargas, P. Mariani, A. Gulik and H. Delacroix, “Cubic phases of lipid-containing systems. Elements of a theory and biological connotations”, J. Mol. Biol., 1993, 229, 540-551.

[6] M. Clerc, “A new symmetry for the packing of amphiplilics direct micelles”, J. Phys. II France, 1996, 6 , 961-968.

[7] (a) J. M. Seddon, “An inverse face-centered cubic phase formed by diacylglycerol-phosphatidylcholine mixtures”, Biochemistry, 1990, 29, 7997–8002. (b) J. M. Seddon, J. Robins, T. Gulik-Krzywicki, H. Delacroix, “Inverse micellar phases of phospholipids and glycolipids Invited Lecture”, Phys. Chem. Chem. Phys. 2000, 2, 4485–4493.

[8] J. L Nieva, A. Alonso, G. Basanez, F. M. Goni, A. Gulik, R. Vargas, V. Luzati, “Topological properties of two cubic phases of a phospholipids:cholesterol: diacylglycerol aqueous system and their possible implications in the phospholipase C-induced liposome fusion”, FEBS Lett. 1995, 368, 143-147.

[9] G. C. Shearman, A. I. Tyler., N. J. Brooks, R. H. Templer, O. Ces, R. V. Law, and J. M. Seddon, “A 3-D Hexagonal Inverse Micellar Lyotropic Phase”, J. Am. Chem. Soc. 2009, 131, 1678-1679.

[10] D. J. P. Yeardley, G. Ungar, V. Percec, M.N. Holerca and G. Johansson, “Spherical supramolecular minidendrimers self organized in an inverse micellar-like thermotropic body-centered cubic liquid crystalline phase”, J. Am. Chem. Soc. 2000**,** 122*,* 1684-1689.

[11] V. S. K. Balagurusamy, G. Ungar, V. Percec and J. Johansson, “Rational design of the first spherical supramolecular dendrimers self-organised in a novel thermotropic cubic liquid-crystalline phase and the determination of their shape by X-ray analysis”, J. Am. Chem. Soc. 1997, 119, 1539-1555.

[12] G. Ungar, Y. S. Liu, X. B. Zeng, V. Percec and W. D. Cho, “Giant supramolecular liquid crystal lattice”, Science, 2003, 299, 1208-1211.

[13] X. B. Zeng, G. Ungar, Y. S. Liu, V. Percec, S. E. Dulcey, J. K. Hobbs, “Supramolecular dendritic liquid quasicrystals”, Nature, 2004, 428, 157-160.

[14] A. K. Sinha, Topologically Close Packed Structures in Transition Metal Alloys, Pergamon Press, Oxford, 1972.

[15] (a) V. Percec, W. D. Cho, G. Ungar and D. J. P. Yeadly, “Synthesis and structural analysis of two constitutional isomeric libraries of AB_2-based monodendrons and supramolecular dendrimers”, J. Am. Chem. Soc. 2001, 123, 1302-1315; (b) V. Percec, M. N. Holerca, S. Uchida, W. D. Cho, G. Ungar, Y. S. Lee and D. J. P. Yeardley, “Exploring and expanding the three-dimensional structural diversity of supramolecular dendrimers with the aid of libraries of alkali metals of their AB_3 minidendritic carboxylates”, Chem. Eur. J. 2002, 8, 1106-1117. (c) V. Percec, C. M. Mitchell, W. D. Cho, S. Uchida, M. Glodde, G. Ungar, X. B. Xeng et al., “Designing libraries of first generation AB_3 and AB_2 self-assembling dendrons via the primary structure generated from combinations of $(AB)_y$–AB_3 and $(AB)_y$–AB_2 building blocks”, J. Am. Chem. Soc. 2004, 126, 6078-6094.

[16] J. D. Bernal, “A geometrical approach to the structure of liquids”, Nature 1959, 183, 141-147.

[17] P. Ziherl and R. D. Kamien, “Maximizing Entropy by Minimizing Area: Towards a New Principle of Self-Organization”, J. Phys. Chem. B 2001, 105, 10147-10158.

[18] F. C. Frank and J. S. Kasper, “Complex alloy structures regarded as sphere packing. I. Definitions and basic principles”, Acta Crystallogr., 1958, 11, 184–190.

[19] G. Ungar and X. B. Zeng, “Frank-Kasper, quasicrystalline and related phase in liquid crystals”, Soft Matter, 2005, 1, 95-106.

[20] H. Koch, C. Radin, and L. Sadun, “Most stable structure for hard spheres”, Phys. Rev. E 2005, 72, 016708.

[21] W. Thomson, Philos. “On the Division of Space with Minimum Partitional Area”, Phil. Mag. 1887, 24, 503-514.

[22] T. C. Hales, “The honeycomb conjecture”, Discrete Comput. Geom. 2001, 25, 1-22.

[23] D. Weaire and R. Phelan, “A counterexample to Kelvin's conjecture on minimal surfaces” Philos. Mag. Lett. 1994, 69, 107-110.

[24] P. Ziherl and R. D. Kaminen, “Soap Froaths and Crystal Structures”, Phy. Rev. Lett. 2000, 85, 3528-3531.

[25] P. Ziherl and R. D. Kamien, “Towards a new principle of self-organization”, J. Phys. Chem. B. 2001, 105, 10148-10158.

[26] Y. Y. Huang, H. L. Chen and T. Hashimoto, “Face-Centered Cubic Lattice of Spherical Micelles in Block Copolymer/Homopolymer Blends”, Macromolecules 2003**,** 36, 764-770.

[27] M. W. Matsen, “Phase behavior of block copolymer/homopolymer blends”, Macromolecules 1995, 28, 5765-5773.

[28] Y. Y. Huang, J. Y. Hsu, H.-L. Chen and T. Hashimoto, “Existence of fcc-Packed Spherical Micelles in Diblock Copolymer Melt”, Macromolecules 2007, 40, 406-409.

[29] Y. Liu, “Two- and three-dimensional liquid crystalline structures in self-assembled supramolecular dendrimers.”, Thesis (Ph.D.), University of Sheffield, Department of Engineering Materials, 2004.

[30] V. S. K. Balagurusamy, G. Ungar, V. Percec and J. Johansson, “Rational design of the first spherical supramolecular dendrimers self-organised in a novel thermotropic cubic liquid-crystalline phase and the determination of their shape by X-ray analysis”, J. Am. Chem. Soc. 1997, 119, 1539-1555.

[31] V. Percec, W. D. Cho, P.E. Mosier, G. Ungar and D. J. P. Yeardley, “Structural analysis of cylindrical and spherical supramolecular dendrimers quantifies the concept of monodendron shape control by generation number”, J. Am. Chem. Soc., 1998, 120, 11061-11070.

[32] The Mineral Information Institut (MII):http://www.eoearth.org/profile/MII/.

Chapter 5

Hexagonal Columnar Superlattice in the Binary Mixtures of Li salt of 3,4,5-Trialkoxygallate and n-Paraffins C_nH_{2n+2} (n=15, 17)

5.1 Introduction

A superlattice is a periodic structure in which the two lattices coexist having the same symmetry. For example, superlattices in semiconductors[1-3] are formed by two semiconductor materials with different energy band gap. The structure is formed by growing two different semiconductor materials which are deposited alternately on each other to form periodic layers in the growth direction. Superlattices have also been found in supramolecular dendrimers of twin-tapered dendritic molecules acting as side groups of polymers[4,5]. The twin-tapered dendritic molecules are self-assembled to a bundle of 3 or 4 supramolecular cylinders where the voids occurring in grouping of these cylinders are occupied by polymer backbones. The coexistence of two lattices obtained from packing of bundles, i.e. one of cylinders and another one of polymers backbones, leads to the formation of superlattices. The 3D hexagonal columnar superlattices[6,7], which were formed by the closely packing of undulated supramolecular columns, were also found. Even in biological lipid membranes, superlattice model is also proposed to explain how the head groups of two different lipid molecules arrange themselves in the bilayers of cell membranes[8-10].

In this chapter, hexagonal columnar superlattices (Col_s) are presented, found in binary mixtures of Li salt of 3,4,5-trialkoxygallte with two shorter and one longer alkoxy chains (12-12-18Li) and added n-paraffins C_nH_{2n+2}, where n= 15 and 17. The structural analysis by small angle X-ray diffraction is described in the first part of experimental results and discussion. Then, the electron density maps of the hexagonal columnar lattice (Col_h) and the hexagonal columnar superlattice (Col_s) are reconstructed. The size of unit cell and the number of molecules contained in the unit cell after adding n-paraffins are discussed subsequently. The conclusion of this study is in the final part of this chapter.

5.2 The materials studied: Li salt of 3,4,5-trialkoxygallate and its binary mixtures with added n-paraffins (12-12-18Li+m%C_nH_{2n+2} where m=0, 5, 10, 15, 30 and n=15, 17)

Li salt of 3,4,5-trialkoxygallate with two dodecyloxy and one octadecyloxy chains (12-12-18Li, Figure 5-1a) were synthesised by our collaborators from Hull University. The idea of synthesising 12-12-18Li as a modification of the previously studied 3,4,5-tridodecyloxygallate Li salt (the case of n=12 in Figure 5-1b) actually came from our intention to obtain the close packed (HCP or FCC) structures of dendrimers, as explained in detail in Chapter 4. Similarly, the binary mixtures of 12-12-18Li and m% by weight of n-paraffins C_nH_{2n+2} where m=15, 30 and n= 15, 17, denoted as 12-12-18Li+m%C_n, were prepared in order for the n-paraffin to help fill the interstices between the spherical dendrimers. For the preparation of the mixtures, 12-12-18Li+m%C_n (where m=15, 30, n= 15, 17) were directly mixed in glass capillaries. Next, the capillaries with 12-12-18Li+m%C_n were heated in order to melt and homogenize the 12-12-18Li and C_nH_{2n+2} mixture. Then, the melted mixtures were taken out the beaker and left at room temperature in order to get the mixture in the solid form.

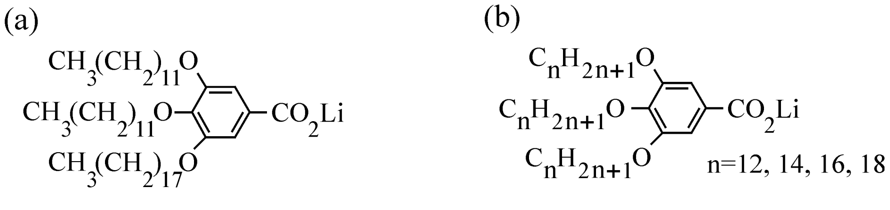

12-12-18Li **n-n-nLi**

Figure 5-1 (a) 12-12-18Li (b) n-n-nLi where n= 12, 14, 16, 18.

5.3 Experimental Results and Discussion

5.3.1 SAXS results and phase identification

The SAXS experiments were performed at SRS Daresbury Laboratory, Synchrotron radiation source. The interplanar d-spacings of diffraction peaks of various phase structures at different temperatures are measured and indexed to identify the phase (see Appendix 5). Let us start with the result of small angle X-ray diffraction of 12-12-18Li. According to the diffractograms of the heating of 12-12-18Li in Figure 5-2, the crystalline phase at low temperatures is followed by the hexagonal columnar (Col_h) phase, followed then by the body-centred cubic (BCC) phase at higher temperatures. The phase sequence of 12-12-18Li is summarized in Diagram 5-1.

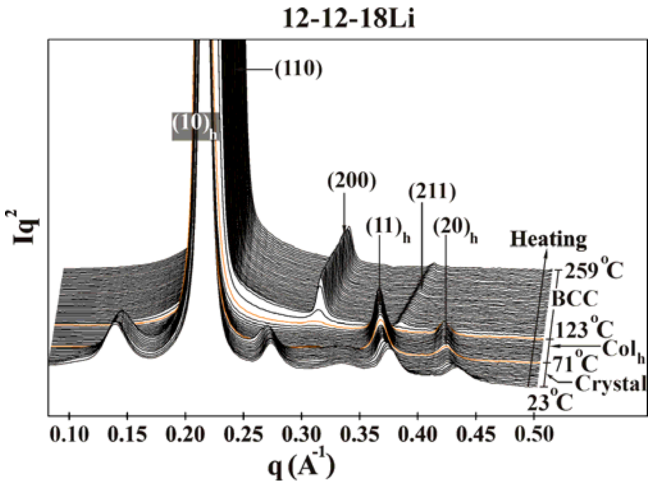

Figure 5-2 Small angle X-ray diffraction results of the heating of 12-12-18Li. The subscript h letter stands for the hexagonal columnar (Col_h) phase.

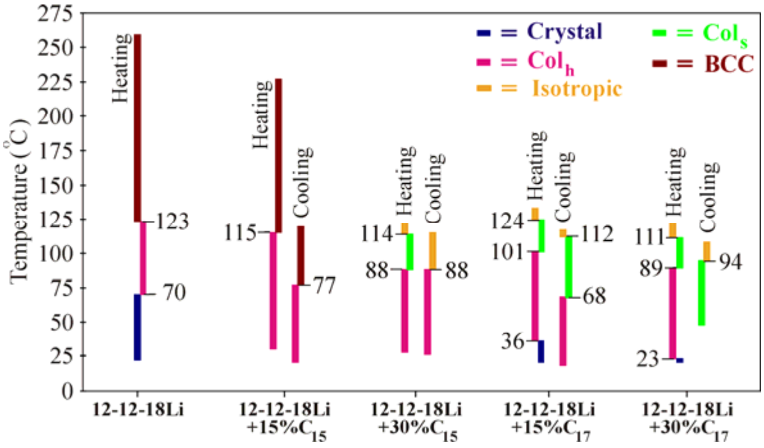

Diagram 5-1 Phase sequences of 12-12-18Li+m%C_n, where m=0, 15, 30 and n= 15, 17, observed in heating and cooling materials.

For the $\mathrm{Col_h}$ phases of 12-12-18Li, the structure of supramolecular columns of 12-12-18Li is also investigated by using the wide angle X-ray diffraction (WAXD) technique. According to the WAXD patterns obtained from an oriented fiber of 12-12-18Li collected at 75 °C, 100 °C, and 120 °C (see Figure 5-3 and Figure 5-4a), it is shown that the molecules of 12-12-18Li are self-assembled into a helix. This is evidenced by the splitting of the reflection at about 8.78 Å and the slightly splitting of the reflection at about 7.37 Å, whereas the sharp reflection at 4.21 Å and the diffuse at about 4.58 Å are not split. The splitting of the reflections is proved by plotting their integrated intensities obtained from performing the azimuthal scans versus azimuthal angles (see Figure 5-5). The sharp reflections at 4.21 Å and 7.37 Å observed in WAXD patterns of 12-12-18Li at 75 °C, 100 °C, and 120 °C indicates that the hexagonal columnar phase of the fiber of 12-12-18Li observed at 75-120 °C seems to be weakly crystalline phase, rather than a true liquid crystal phase. By contrast, according to the WAXD patterns of 12-12-18Na collected at 127 °C, the sharp reflection at 4.21 Å, usually observed at 75 °C-120 °C, has disappeared and the diffuse at about 10.0 Å is observed instead. This indicates that at 127 °C this hexagonal columnar phase of 12-12-18Li fiber is a true liquid crystal phase. At 127 °C, the supramolecular columns of 12-12-18Li do not have a helical structure, but they are formed by the packing of tilted molecules of 12-12-18Li. According to the WAXD patterns of 12-12-18Li collected at 75-120 °C, the sharp reflection at 4.21 Å and the diffuse at 4.58 Å correspond to the aromatic and aliphatic part of 12-12-18Li molecules. The non-splitting of the diffuse at about 4.58 Å implies that the alkyl chains in 12-12-18Li are not tilted and they are perpendicular to the column axis. Hence, d-spacing of the diffuse at about 4.58 Å is used as the assumed values of the column layer thickness for the calculation of the number of 12-12-18Li molecules per column layer (see more details in the next section).

When 15% of n-pentadecane $C_{15}H_{32}$ is added to 12-12-18Li, diffractograms recorded during the heating and the cooling scan of 12-12-18Li+15%C_{15} show the same phase sequence as for the pure 12-12-18Li (see Figure 5-6a and Figure 5-6b), with the columnar-cubic transition temperature on heating reduced from that of 12-12-18Li from 123 °C to 115°C (see Diagram 5-1). When 30% of n-pentadecane $C_{15}H_{32}$ is added to 12-12-18Li, a different phase sequence is obtained from heating material, i.e. $\mathrm{Col_h}$ → hexagonal columnar superlattice ($\mathrm{Col_s}$) → isotropic liquid. Figure 5-7a is the diffractograms of the heating of 12-12-18Li+30%C_{15} showing that

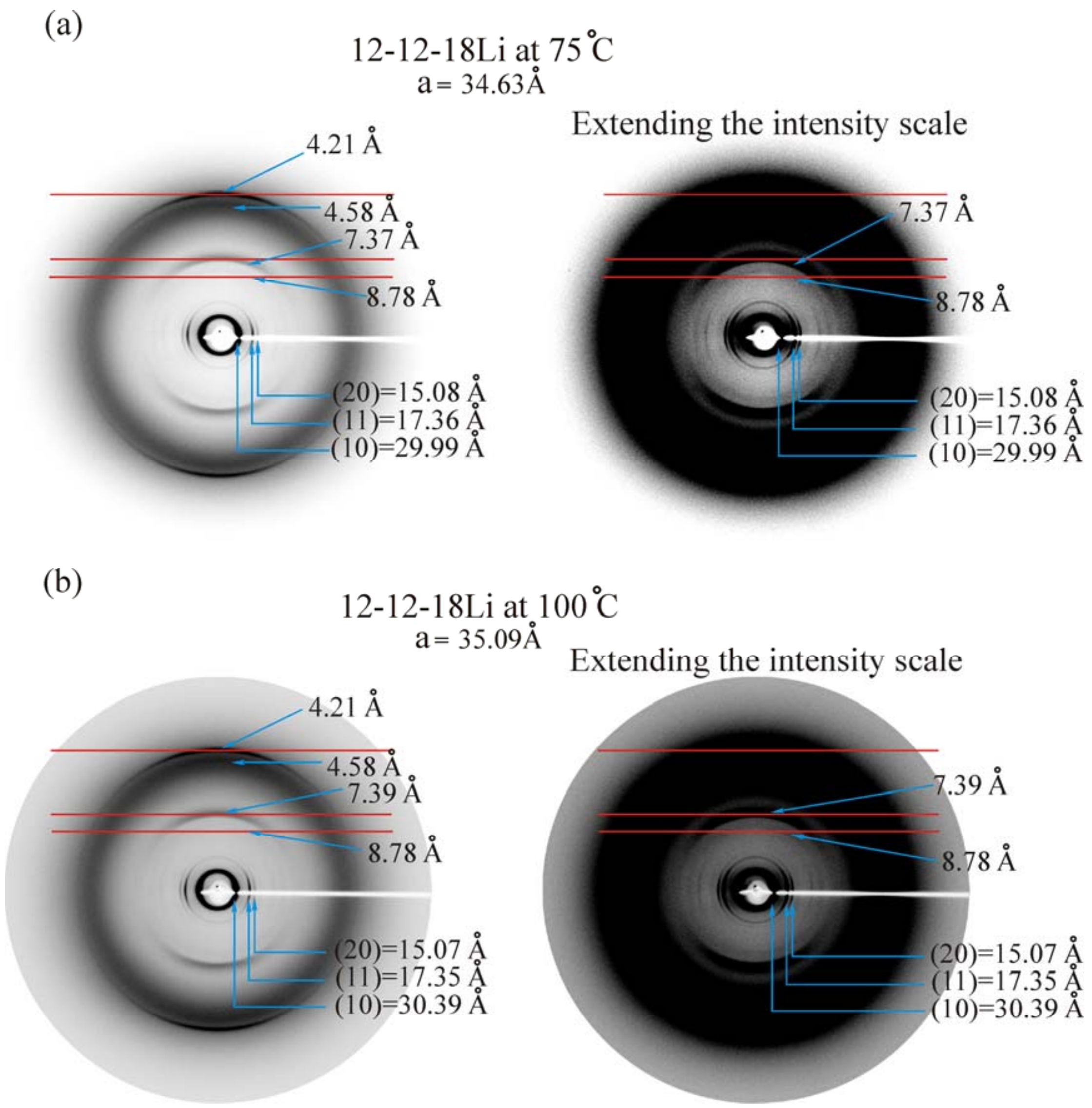

Figure 5-3 WAXD patterns of the fiber of 12-12-18Li at (a) 75°C and (b) 100 °C.

the BCC phase does not occur in this mixture, but the $\mathrm{Col_s}$ phase is formed instead. The phase transition from the $\mathrm{Col_h}$ phase to the $\mathrm{Col_s}$ phase is evidenced by the development of two additional diffraction peaks of the $\mathrm{Col_s}$ phase, i.e. $(10)_s$ and $(21)_s$ (see Figure 5-7a andFigure 5-7b), and the shifting of diffraction peaks in the direction of larger *q*-value at the transition temperature. The $(20)_s$ reflection was not observed in the diffraction patterns of 12-12-18Li+30%C_{15}. This is just because of very low intensity of $(20)_s$ reflection. The absence of $(20)_s$ cannot be a systematic absence as the symmetry of the hexagonal columnar superlattice of 12-12-18Li+30%C_{15} is *p6mm*, which has no systematic extinctions. Note that the subscript h and s letters in diffractograms of 12-12-18Li+30%C_{15} in Figure 5-7 correspond to the hexagonal columnar (Col_h) phase and the hexagonal columnar superlattice (Col_s) respectively. The shifting of diffraction peaks in the Col_s phase of 12-12-18Li+30%C_{15} in the direction of larger *q*-value implies that unit cells suddenly start shrinking with the increasing of temperature as the superlattice forms. The abruptly shrinking of unit cells is resulted from the loss of molecules in columns in the Col_h lattice, which will be discussed in more detail later. However, the Col_s phase does not occur in the cooling of 12-12-18Li+30%C_{15}. Diffractograms of the cooling of 12-12-18Li+30%C_{15} in Figure 5-7c show that the isotropic liquid phase is followed by the Col_h phase.

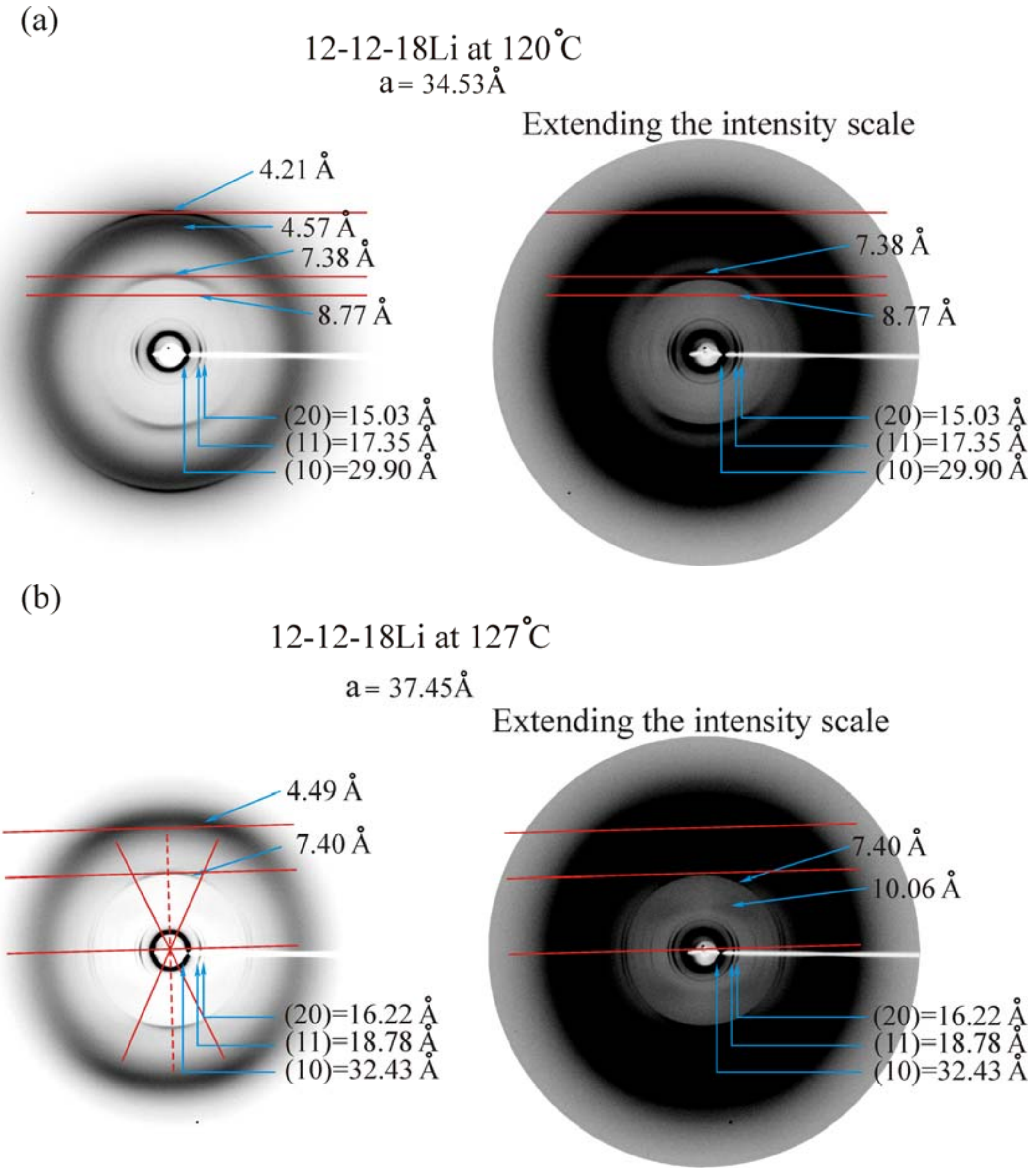

Figure 5-4 WAXD patterns of the fiber of 12-12-18Li at (a) 120°C and (b) 127 °C.

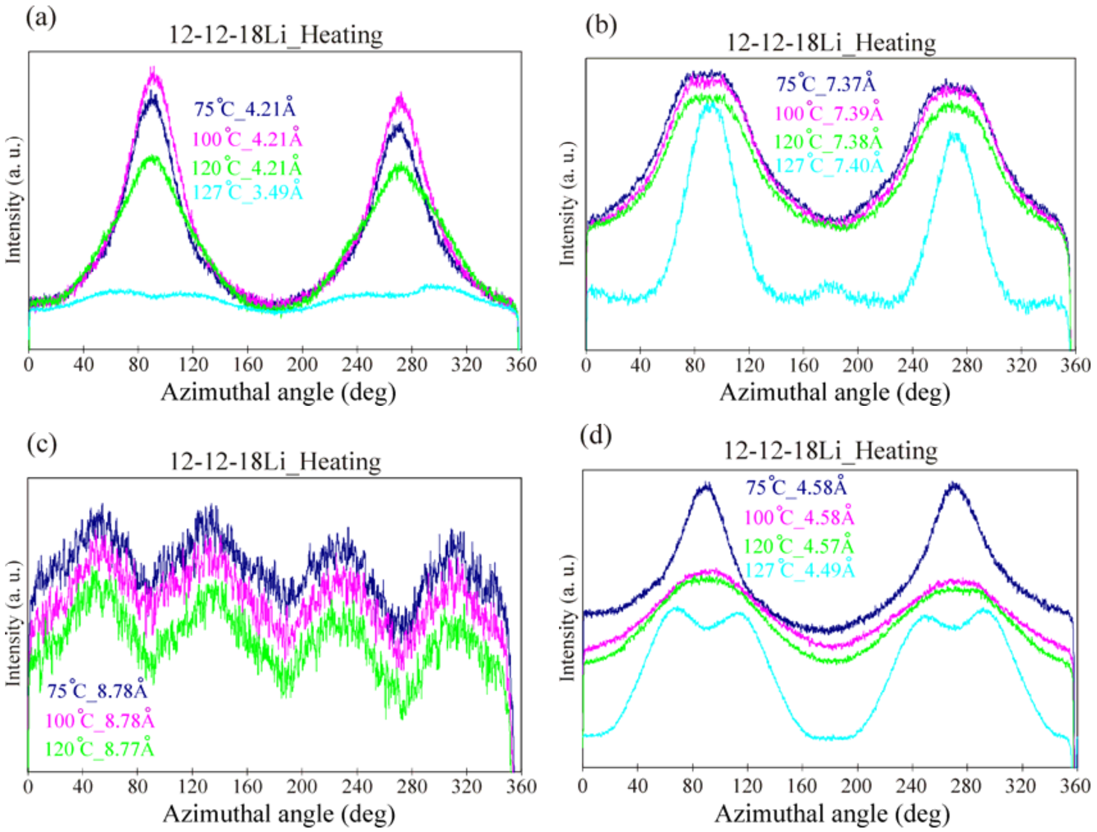

Figure 5-5 Integrated intensities of the reflections (a-c) and the diffuse (d), obtained from performing the azimuthal scans, observed in WAXD patterns of the fiber of 12-12-18Li at different temperatures.

Unlike 12-12-18Li+15%C_{15}, when 15% of the longer paraffin n-heptadecane $C_{17}H_{36}$ is added to 12-12-18Li, the Col$_s$ phase is also obtained. According to the diffractograms recorded during the heating of 12-12-18Li+15%C_{17} in Figure 5-8a, the crystalline phase at low temperatures is followed by the Col$_h$ phase, followed then by the Col$_s$ phase at higher temperatures, and ends with the isotropic liquid phase. The phase sequence of the heating of 12-12-18Li+15%C_{17}, as summarized in Diagram 5-1, is similar to the phase sequence of the heating of 12-12-18Li+30%C_{15}, but the phase sequence of the cooling of 12-12-18Li+15%C_{17} is different from the phase sequence of the cooling of 12-12-18Li+30%C_{15}. Diffractograms recorded during the cooling of 12-12-18Li+15%C_{17} in Figure 5-8c show that the Col$_s$ phase also occurs in the cooling of materials and the obtained phase sequence is in reverse order when compared to the phase sequence in the heating scan of 12-12-18Li+15%C_{17}, i.e. isotropic liquid → Col$_s$ → Col$_h$. Again, the phase transition from the Col$_h$ phase to the

Col_s phase in 12-12-18Li+15%C_{17} is evidenced by the developing of two additional diffraction peaks of the Col_s phase, i.e. $(10)_s$ and $(21)_s$ (see Figure 5-8a and Figure 5-8b), and the shifting of diffraction peaks in the direction of larger *q*-value at the transition temperature. The $(20)_s$ reflection was also not observed in the diffraction patterns of 12-12-18Li+15%C_{17} because of very low intensity of $(20)_s$ reflection.

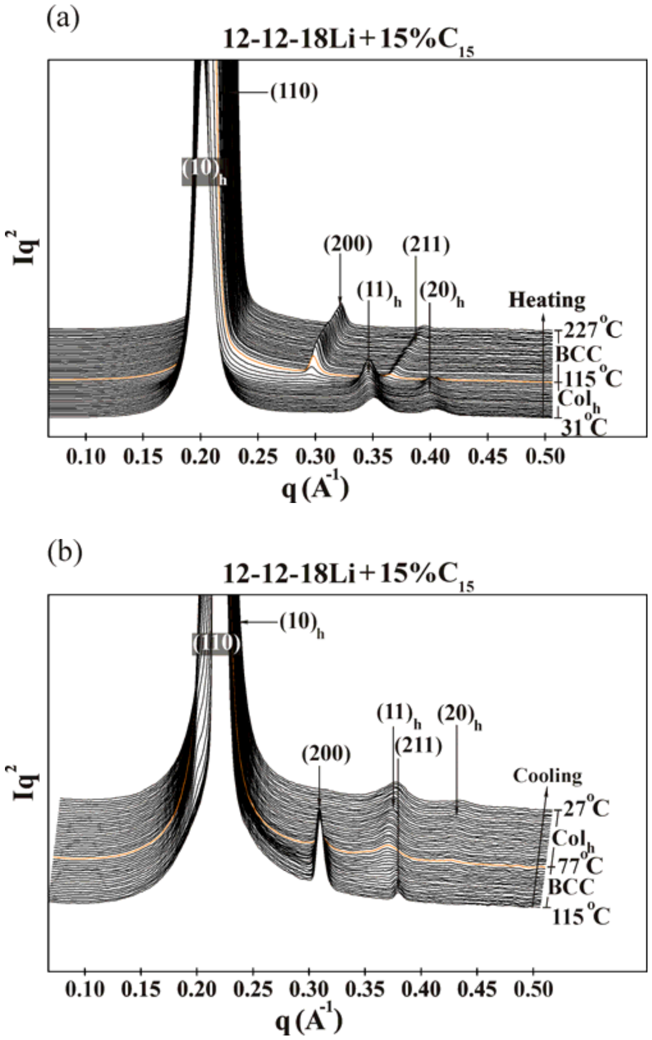

Figure 5-6 Small angle X-ray diffraction results of (a) the heating and (b) the cooling of 12-12-18Li+15%C_{15}. The subscript h letter corresponds to the hexagonal columnar (Col_h) phase.

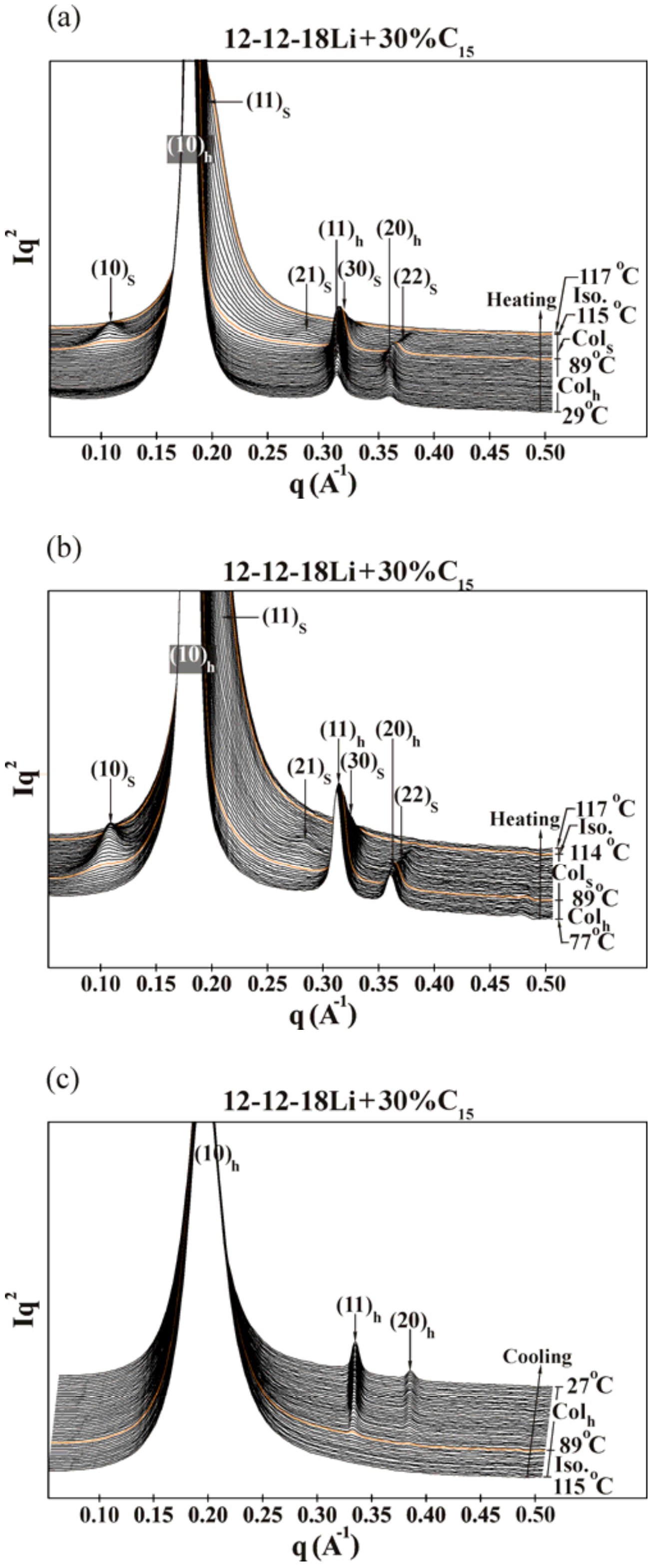

Figure 5-7 Small angle X-ray diffraction results of (a) the heating of 12-12-18Li+30%C_{15} (b) the hexagonal columnar superlattice (Col_s) observed in the heating scan (c) the cooling of 12-12-18Li+30%C_{15}. The subscript h and s letters correspond to the hexagonal columnar (Col_h) phase and the superlattice (Col_s) respectively.

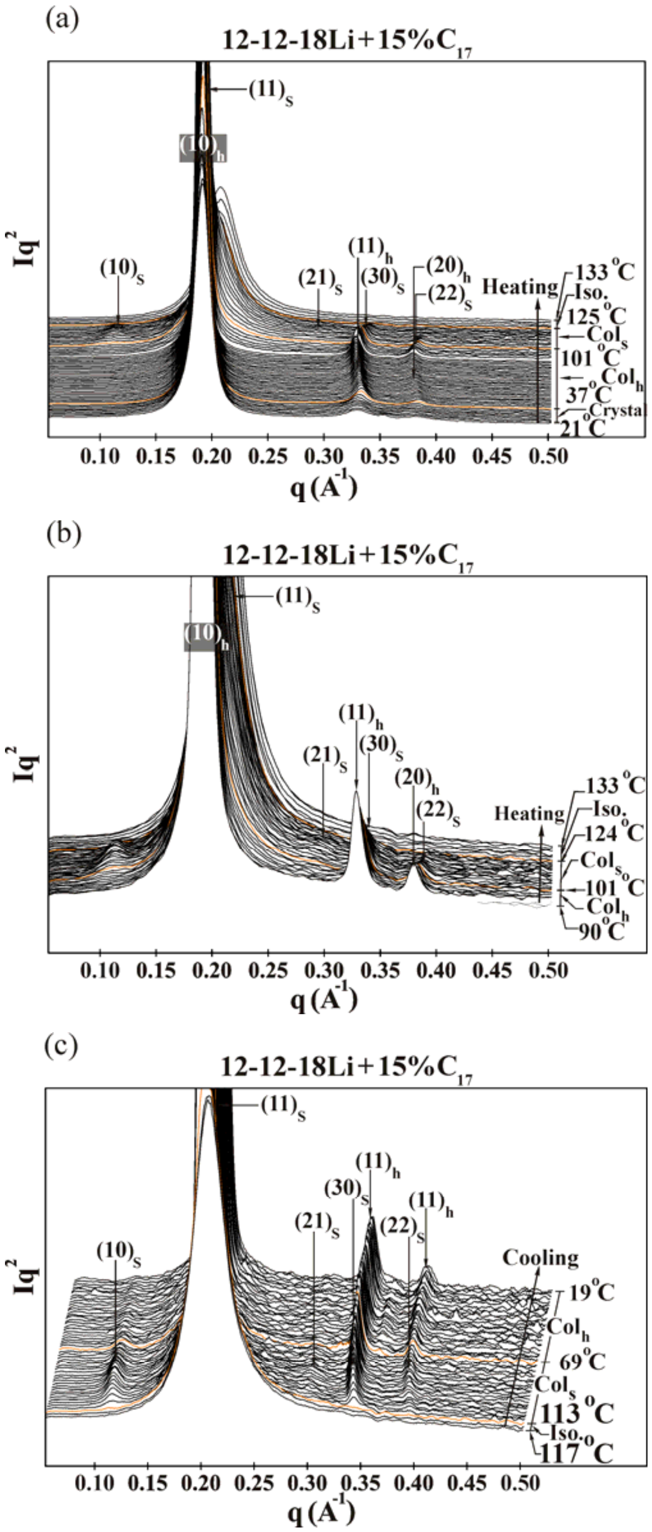

Figure 5-8 Small angle X-ray diffraction results of (a) the heating of 12-12-18Li+15%C$_{17}$ (b) the hexagonal columnar superlattice (Col$_s$) observed in the heating scan (c) the cooling of 12-12-18Li+15%C$_{17}$. The subscript h and s letters correspond to the hexagonal columnar (Col$_h$) phase and the superlattice (Col$_s$) respectively.

Like 12-12-18Li+30%C_{15} and 12-12-18Li+15%C_{17}, when 30% of n-heptadecane $C_{17}H_{36}$ is added to 12-12-18Li, the Col_s phase is also obtained. Diffractograms recorded during the heating of 12-12-18Li+30%C_{17} in Figure 5-9a shows that this mixture yields the same phase sequence as obtained from the heating of 12-12-18Li+30%C_{15} and 12-12-18Li+15%C_{17}, i.e. Crystal → Col_h → Col_s → isotropic liquid (see Diagram 5-1). The Col_s phase is also observed in the cooling of 12-12-18Li+30%C_{17} which the obtained phase sequence is in reverse order when compared to the phase sequence obtained from the heating of 12-12-18Li+30%C_{17}, i.e. isotropic liquid → Col_s (see Figure 5-9c).

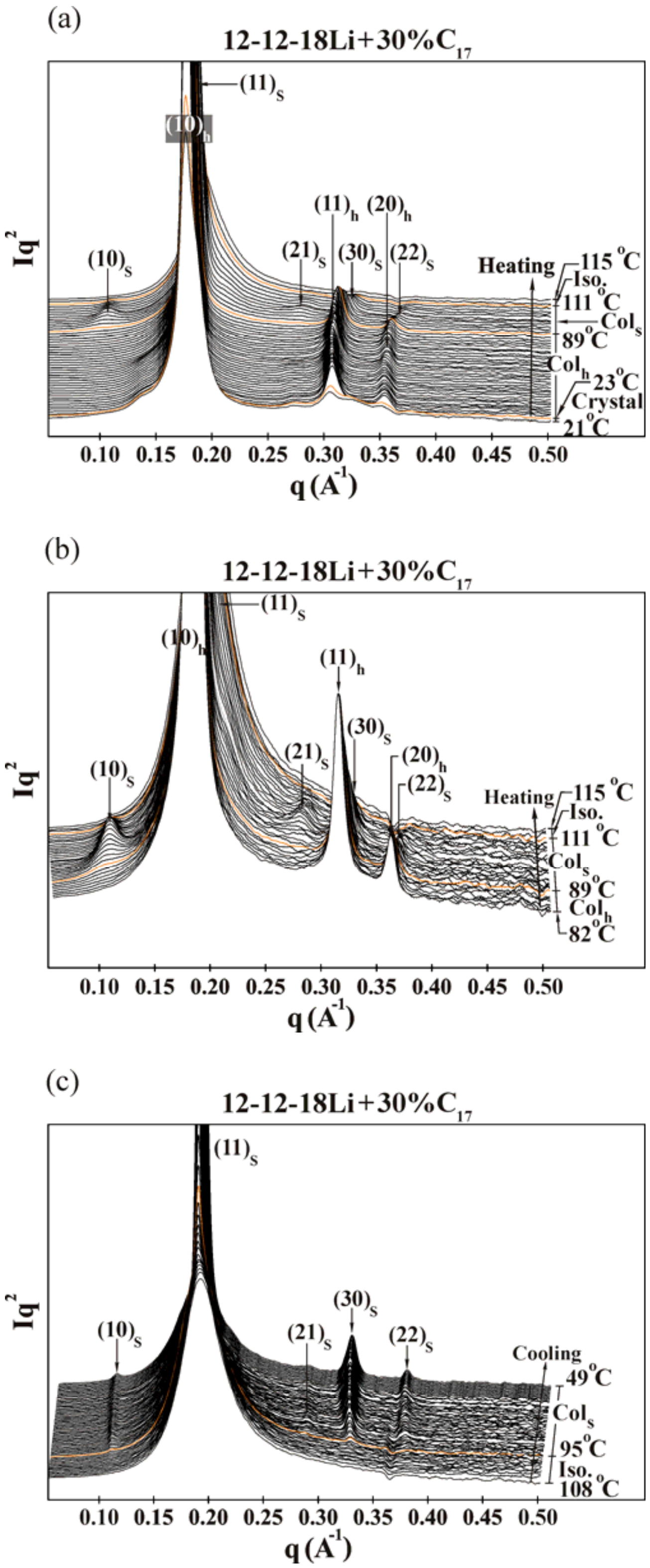

Figure 5-9 Small angle X-ray diffraction results of (a) the heating of 12-12-18Li+30%C_{17} (b) the hexagonal columnar superlattice (Col_s) observed in the heating scan (c) the cooling of 12-12-18Li+30%C_{17}. The subscript h and s letters correspond to the hexagonal columnar (Col_h) phase and the superlattice (Col_s) respectively.

5.3.2 Characterisation of the unit cell and the corresponding supramolecular building object

With the measured d-spacings of diffraction peaks of the Col_h and Col_s phases of 12-12-18Li+m%C_n where m=0, 15, 30 and n=15, 17, the lattice parameters of unit cells, the center-to-center distance between two nearest-neighbour columns in unit cells and the number of molecules 12-12-18Li and C_nH_{2n+2} per column are calculated and compared. All details of calculations and results are given in the Appendix 5 while Figure 5-10 and Figure 5-11 are graphical presentations of the calculation results. According to Figure 5-10, the a lattice parameter of the Col_h unit cell (a_h) of 12-12-18Li, on average, is equal to 34.1 Å. The center-to-center distance between two nearest-neighbour columns in the Col_h unit cell is equal to the a lattice parameter of the unit cell, i.e. 34.1 Å. With the height of column layer l=4.58 Å obtained from wide angle X-ray diffraction (WAXD) patterns collected from the oriented fiber of 12-12-18Li (see Figure 5-3), the Col_h unit cell, containing one disc, contains 3.8 molecules of 12-12-18Li.

When 15% of $C_{15}H_{32}$ is added to 12-12-18Li, 12-12-18Li+15%C_{15} yields the Col_h lattice with a_h lattice parameter being equal to 36.2 Å, which is increased from that of 12-12-18Li by 6.2%. With the assumed height of column layer l=4.58 Å of 12-12-18Li+15%C_{15}, the unit cell of the Col_h lattice of 12-12-18Li+15%C_{15} contains 3.4 molecules of 12-12-18Li and 2 molecules of $C_{15}H_{32}$, or 3.4(12-12-18Li)+2($C_{15}H_{32}$) for short in writing. When 30% of $C_{15}H_{32}$ is added to 12-12-18Li, 12-12-18Li+30%C_{15} yields the Col_h lattice with a_h being equal to 40.1 Å and the superlattice with a lattice parameter of the unit cell (a_s) being equal to 67.3 Å, which is $1.7 \approx \sqrt{3}$ times bigger than the a_h parameter of the Col_h unit cell of the same mixture. The unit cell of the Col_h lattice of 12-12-18Li+30%C_{15} contains 3.3 molecules of 12-12-18Li and 5 molecules of $C_{15}H_{32}$, or 3.3(12-12-18Li)+5($C_{15}H_{32}$) for short. With the assumed height of column layer l=4.58 Å of 12-12-18Li+30%C_{15}, the unit cell of the superlattice of 12-12-18Li+30%C_{15} contains 9.0-9.4 molecules of 12-12-18Li and 13.9-14.5 molecules of $C_{15}H_{32}$.

When 15% of the longer paraffin n-heptadecane $C_{17}H_{36}$ is added to 12-12-18Li, 12-12-18Li+15%C_{17} yields the Col_h lattice and the superlattice (Col_s)

with a_h and a_s lattice parameters being equal to 38.0 Å and 64.5 Å respectively. The a_h lattice parameter of the Col_h unit cell of 12-12-18Li+15%C_{17} is increased from that of 12-12-18Li+15%C_{15} by 5.1%. The a_s lattice parameter of the Col_s unit cell of 12-12-18Li+15%C_{17} is $1.7 \approx \sqrt{3}$ times bigger than the a_h parameter of the Col_h unit cell of the same mixture and it is smaller than that of 12-12-18Li+30%C_{15} by 4.2%. With the assumed height of column layer l=4.58 Å, the unit cell of the Col_h lattice of 12-12-18Li+15%C_{17} contains 3.7 molecules of 12-12-18Li and 2 molecules of $C_{17}H_{36}$, or 3.7(12-12-18Li)+2($C_{17}H_{36}$) for short. The unit cell of the superlattice of 12-12-18Li+15%C_{17} contains 10.8 molecules of 12-12-18Li and 6 molecules of $C_{17}H_{36}$, or 10.8(12-12-18Li)+6($C_{17}H_{36}$).

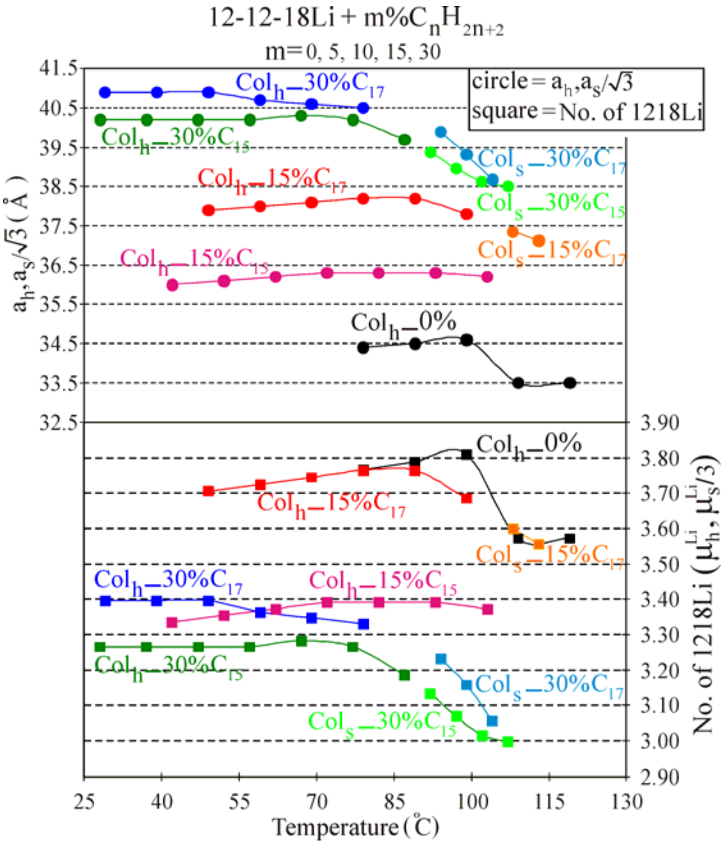

Figure 5-10 The centre-to-centre distance between two nearest-neighbour columns in unit cells of the hexagonal columnar lattice (Col_h), i.e. a_h, of 12-12-18Li+m%C_n where m=0, 15, 30 and n=15, 17. $a_s/\sqrt{3}$ is the scaled a lattice parameters of the unit cell of the superlattice.

When 30% of $C_{17}H_{36}$ is added to 12-12-18Li, 12-12-18Li+30%C_{17} yields the Col$_h$ lattice and the superlattice (Col$_s$) with a_h and a_s lattice parameters being equal to 40.8 Å and 68.1 Å respectively. The a_h lattice parameter of the Col$_h$ unit cell of 12-12-18Li+30%C_{17} is increased from that of 12-12-18Li+15%C_{17} and 12-12-18Li+30%C_{15} by 7.3% and 1.6% respectively. The a_s lattice parameter of the Col$_s$ unit cell of 12-12-18Li+30%C_{17} is $1.7 \approx \sqrt{3}$ times bigger than the a_h parameter of the Col$_h$ unit cell of the same mixture and it is increased from that of 12-12-18Li+15%C_{17} and 12-12-18Li+30%C_{15} by 5.6% and 1.2% respectively. With the assumed height of column layer l=4.58 Å, the unit cell of the Col$_h$ lattice of 12-12-18Li+30%C_{17} contains 3.4 molecules of 12-12-18Li and 4.6 molecules of $C_{17}H_{36}$, or 3.4(12-12-18Li)+4.6($C_{17}H_{36}$) for short. The unit cell of the superlattice of 12-12-18Li+30%C_{17} contains 9.5 molecules of 12-12-18Li and 13 molecules of $C_{17}H_{36}$, or 9.5(12-12-18Li)+13($C_{17}H_{36}$) for short.

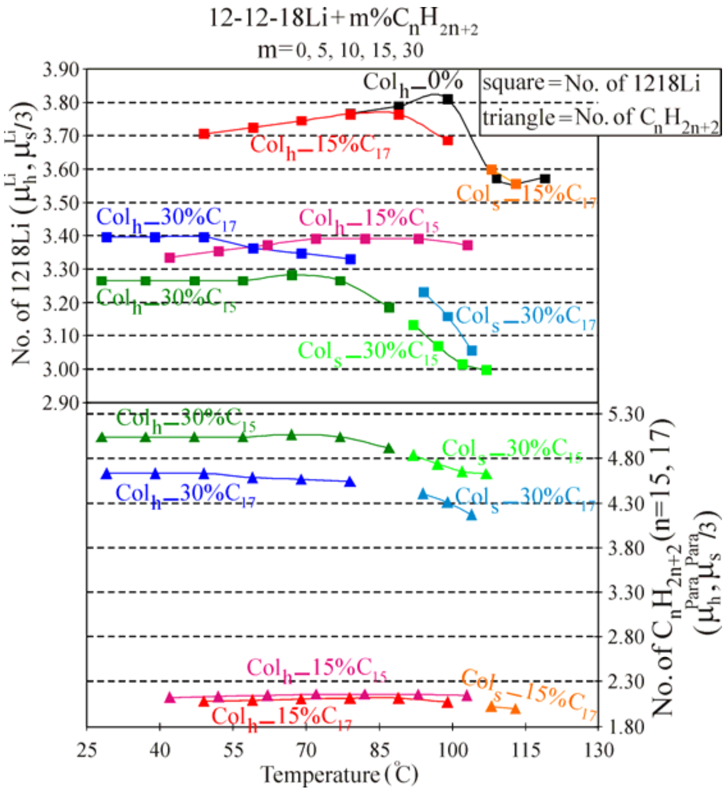

Figure 5-11 The number of 12-12-18Li and C_nH_{2n+2} molecules (n=15, 17) in unit cells of the hexagonal columnar (Col$_h$) lattice and the superlattice (Col$_S$) of 12-12-18Li+m%C_n where m=0, 15, 30 and n=15, 17.

The increasing in size of supramolecular columns in the Col_h and Col_s phases and the increasing of corresponding a_h and a_s unit cell parameters, as a result of adding n-paraffin C_nH_{2n+2} (n=15, 17) to 12-12-18Li, can be explained that some of added paraffin becomes a part of columns mainly formed by the self-assembling of 12-12-18Li molecules. The combination of n-alkane and alkyl chains of 12-12-18Li increases the peripheral aliphatic region of supramolecular columms of 12-12-18Li, thereby obtaining bigger supramolecular columms and bigger a_h and a_s lattice parameters of Col_h and Col_s lattices. In addition, adding paraffin to 12-12-18Li also makes the wedge-shaped of 12-12-18Li dendrons wider, and this results in the decreasing of the number of 12-12-18Li molecules per column layer as the smaller number of 12-12-18Li molecules are required to form a supramolecular disc.

The increasing in size of supramolecular objects and corresponding unit cells of the columnar and the cubic lattices and the decreasing of the number of salts molecules per supramolecular objects also occur in the mixtures of either Na and Rb salts with added n-nonadecane $C_{19}H_{40}$, as previously described in section 4.5.3 in chapter 4.

5.3.3 Electron density reconstruction

Contours and surface plots of electron density distributions in the plane normal to the columns of Col_h and Col_s phases of 12-12-18Li and its mixtures with added 15% and 30% of C_nH_{2n+2} (n=15, 17) are shown in Figure 5-12 to Figure 5-16. The relevant parameters used to reconstruct the electron density maps are tabulated in Table 5-1. Figure 5-12a and Figure 5-12b are the contour and the surface plot of electron density distributions in columns of Col_h phase of 12-12-18Li, obtained from the preferred phase combination (10) +, (11) +, (20) + where the symbol + represents the phase angle of 0. The contour map shows the close packing of cylinders in the hexagonal columnar lattice. The surface plot, with density gradient from the highest (purple) to the lowest electron density (red), shows that columns have high electron density cores (purple and navy) and lower electron density peripheral region (green, yellow, and red). The high electron density cores of columns are quite small whereas the low electron density peripheral region is larger. This is in qualitative agreement with the known aromatic and aliphatic fractions, i.e. 17% and 83% respectively, of

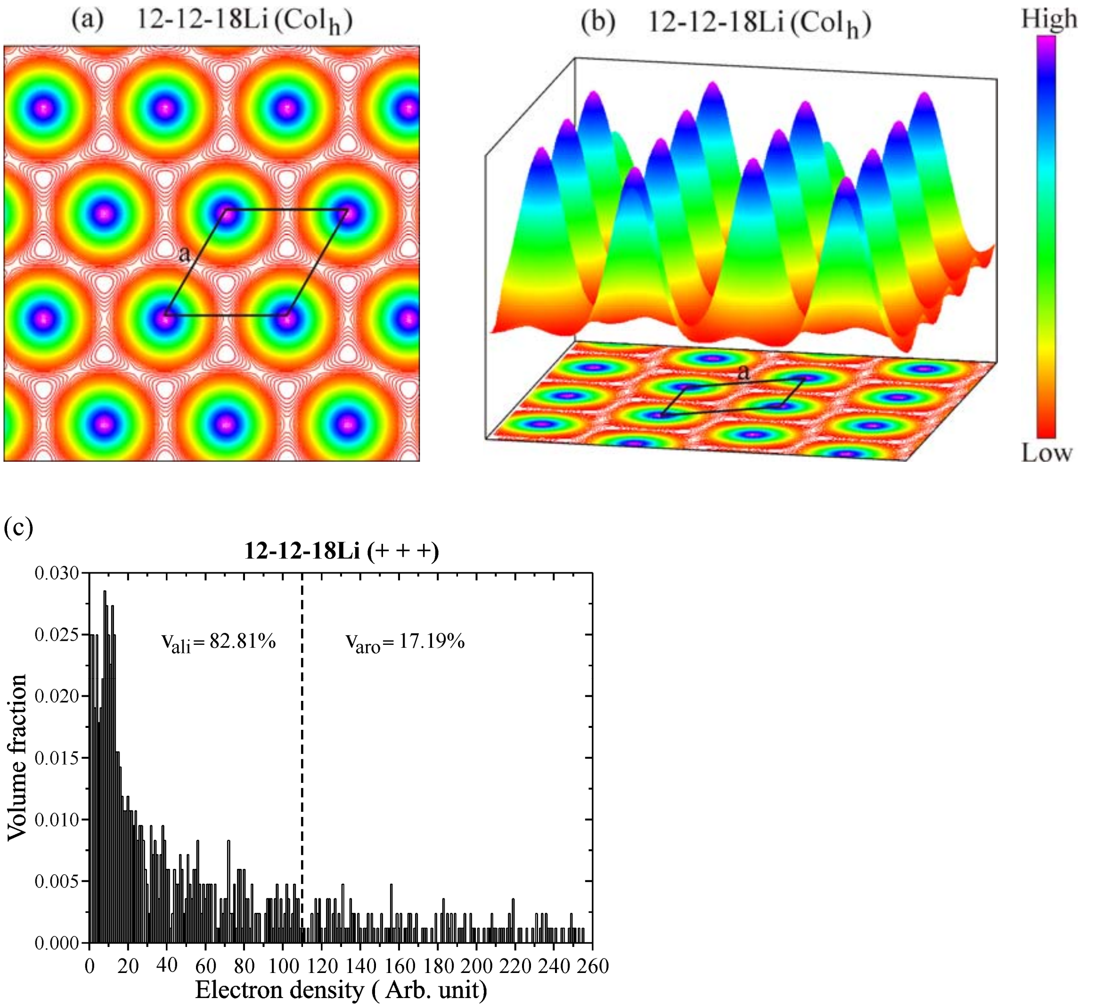

Figure 5-12 (a) Contour and (b) surface plot of electron density distributions in the columns of the hexagonal columnar (Col_h) phase of 12-12-18Li at 99 °C. (c) is the histogram of electron density distributions for electron density map in (b).

12-12-18Li. The unit cell of the Col_h lattice, drawn with solid line, contains only one column.

The maps of 12-12-18Li+15%C_n and 12-12-18Li+30%C_n where n= 15, 17 are shown in Figure 5-13a,b to Figure 5-16a,b. All of them are similar to those of 12-12-18Li, whereas the histograms of the electron density distribution for the Col_h phase of 12-12-18Li+15%C_{17} and 12-12-18Li+30%C_n where n=15, 17 (see Figure 5-13e to Figure 5-16e) clearly show the increasing of the height of the lowest electron density peak, i.e. 0^{th} level, as a result of the increasing of the alkane content in the mixtures. This is as expected since the low density peak originated from the alkyl regions of nearly constant density. Electron density maps of the Col_s phase of

12-12-18Li+30%C_{15} and 12-12-18Li+30%C_{17} obtained from the phase combination (10) +, (11) +, (21) -, (30) +, (22) +, where the symbol + and – represent the phase angles of 0 and π respectively, are shown in Figure 5-14c,d and Figure 5-16c,d respectively. According to the electron density contours of such two materials in Figure 5-14c and Figure 5-16c, the Col_s lattice is formed by the coexistence of two lattices formed by the bigger and the smaller hexagons. The cores of bigger hexagons have higher electron density than those of smaller hexagons. This can be seen from the maps that the cores of bigger hexagons are purple (i.e. the highest electron density) and the cores of the smaller hexagons are blue (i.e. lower electron density). Two different types of hexagons in the Col_s lattice of 12-12-18Li+30%C_{15} and 12-12-18Li+30%C_{17} represent two different types of columns containing different number of molecules of 12-12-18Li and C_nH_{2n+2} (n=15, 17), (see more details in the next section). The unit cell of the Col_s lattice, drawn with solid line, contains one column with higher electron density aromatic core and two columns with lower electron density aromatic cores. Note that different phase combinations, e.g. (10) -, (11) +, (21) +, (30) +, (22) + or (10) -, (11) +, (21) -, (30) +, (22) +, yield electron density maps which are contrary to those in Figure 5-14c,d and Figure 5-16c,d (see Appendix 6). According to those maps, the Col_s lattice is still formed by the coexistence of two lattices formed by the bigger and the smaller hexagons, but the unit cell of the Col_s lattice contains two bigger and one smaller hexagons instead. Like electron density maps obtained from phase combination (10) +, (11) +, (21) -, (30) +, (22) + as shown in Figure 5-14c,d and Figure 5-16c,d, the electron density at the cores of bigger hexagons is higher than that of the cores of smaller hexagons. At this point, the unit cell of Col_s lattice can be either the one having one bigger and two smaller hexagons or the one having two bigger and one smaller hexagons. To make a decision which the phase combination is the most preferred, the number of 12-12-18Li molecules in the supercell is determined, and different combinations of 12-12-18Li molecules in two different types of columns are varied to get a good fitting between the calculated electron density and the integrated electron density of columns, which the latter is obtained from the electron density maps. In case of 12-12-18Li+30%C_{15} and 12-12-18Li+30%C_{17}, our preferred choice is (10) +, (11) +, (21) -, (30) +, (22) +, and the unit cell of Col_s lattice of such two materials contains one column (one bigger hexagon) having 4 molecules of 12-12-18Li and two columns (two smaller hexagons) having 3 molecules of 12-12-18Li. More details of the determination of the number of 12-12-18Li molecules in the $\mathrm{Col_s}$ unit cell and two different types of columns are given in the next section.

Unlike the maps of the $\mathrm{Col_s}$ phase of 12-12-18Li+30%$\mathrm{C_{15}}$ and 12-12-18Li+30%$\mathrm{C_{17}}$, those of the $\mathrm{Col_s}$ phase of 12-12-18Li+15%$\mathrm{C_{17}}$ in Figure 5-15c and Figure 5-15d, obtained from the preferred phase combination (10) -, (11) +, (21) +, (30) +, (22) +, show that the unit cell of $\mathrm{Col_s}$ lattice contains two bigger and one smaller hexagons, and the aromatic cores of two different types of hexagons have nearly the same electron density. According to the determination of the number of 12-12-18Li molecules in the $\mathrm{Col_s}$ unit cell and two different types of columns (see more details in the next section), each of two columns in unit cell represented by a

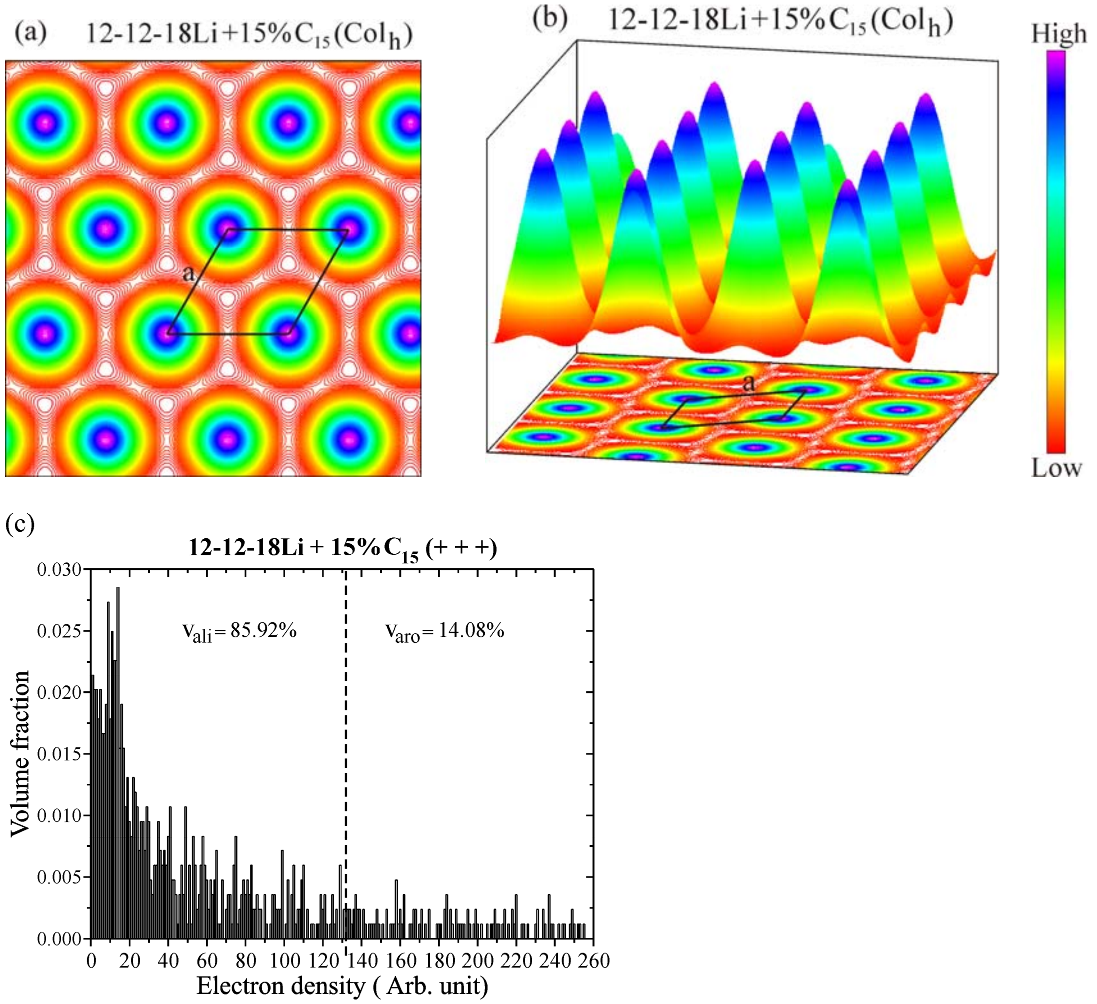

Figure 5-13 (a) Contour and (b) surface plot of electron density distributions in the columns of the hexagonal columnar ($\mathrm{Col_h}$) phase of 12-12-18Li+15%$\mathrm{C_{15}}$ at 72 °C. (c) is the histogram of electron density distribution for electron density map in (b).

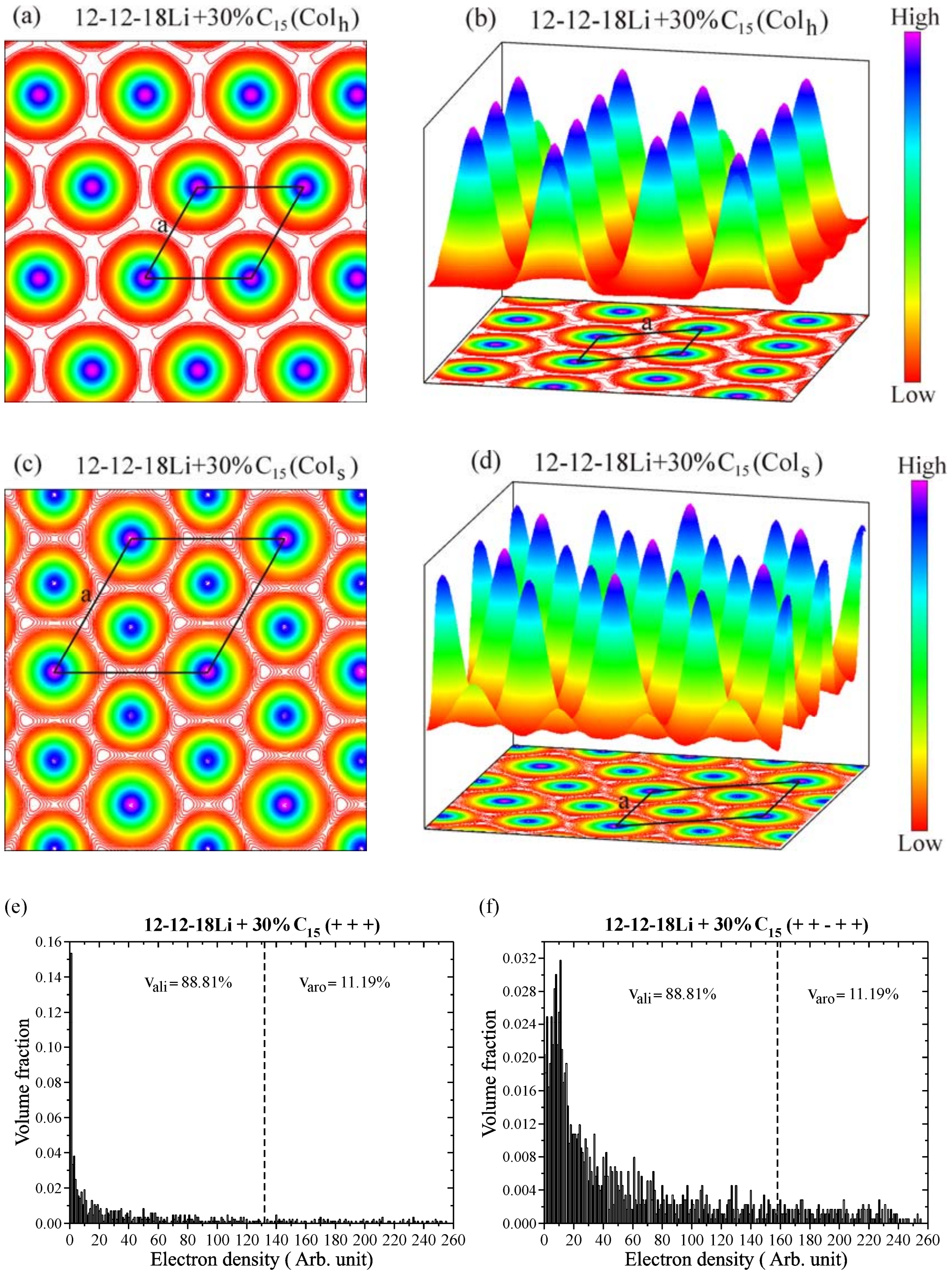

Figure 5-14 Contours and surface plots of electron density ditributions in the columns of (a,b) the hexagonal columnar (Col_h) phase at 67 °C and (c,d) the hexagonal columnar superlattice (Col_s) at 102 °C of 12-12-18Li+30%C_{15}. (e) and (f) are histograms of electron density distributions for electron density maps in (b) and (d) respectively.

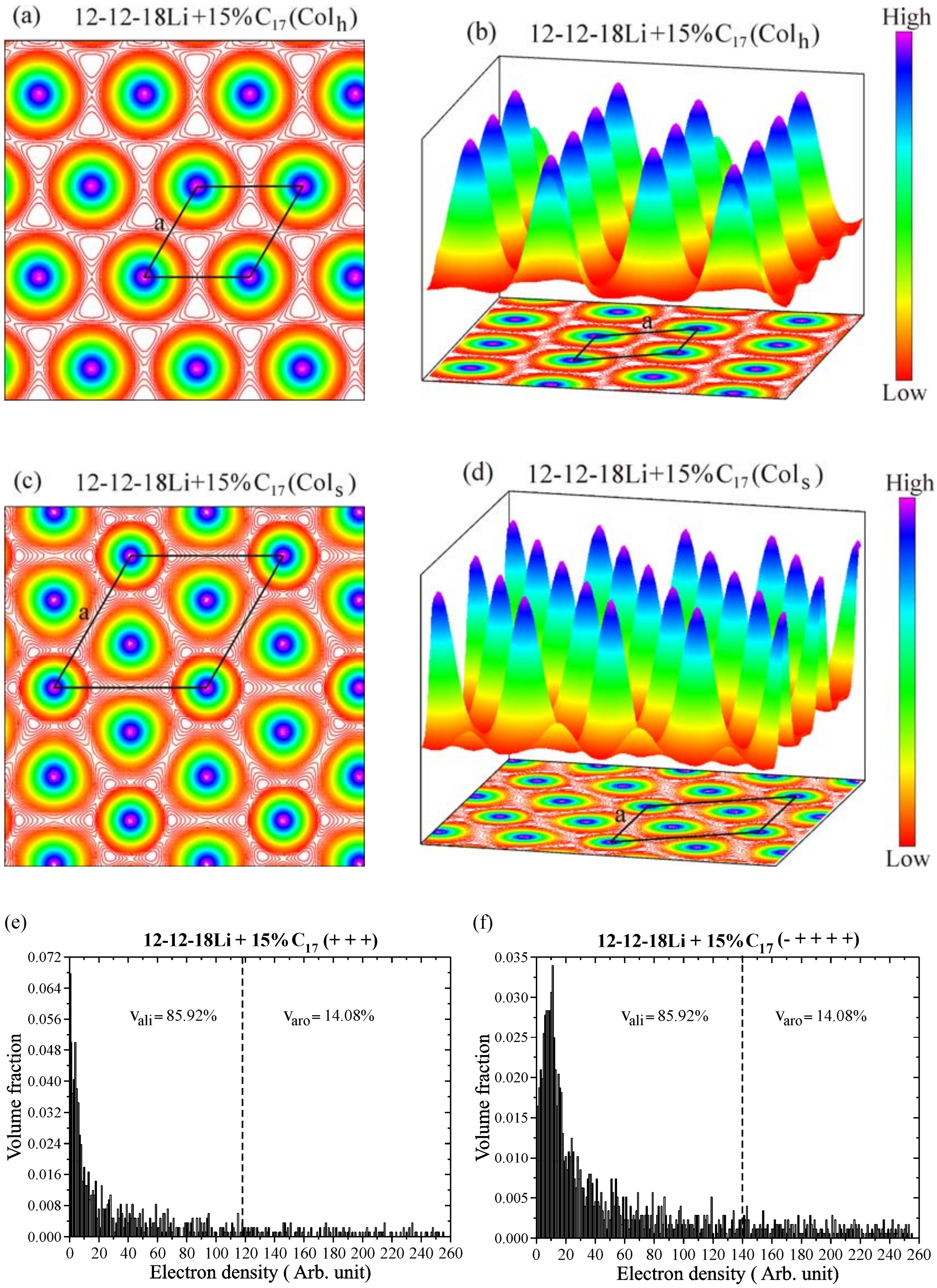

Figure 5-15 Contours and surface plots of electron density distributions in the columns of (a,b) the hexagonal columnar (Col_h) phase at 74 °C and (c,d) the hexagonal columnar superlattice (Col_s) at 108 °C of 12-12-18Li+15%C_{17}. (e) and (f) are histograms of electron density distributions for electron density maps in (b) and (d) respectively.

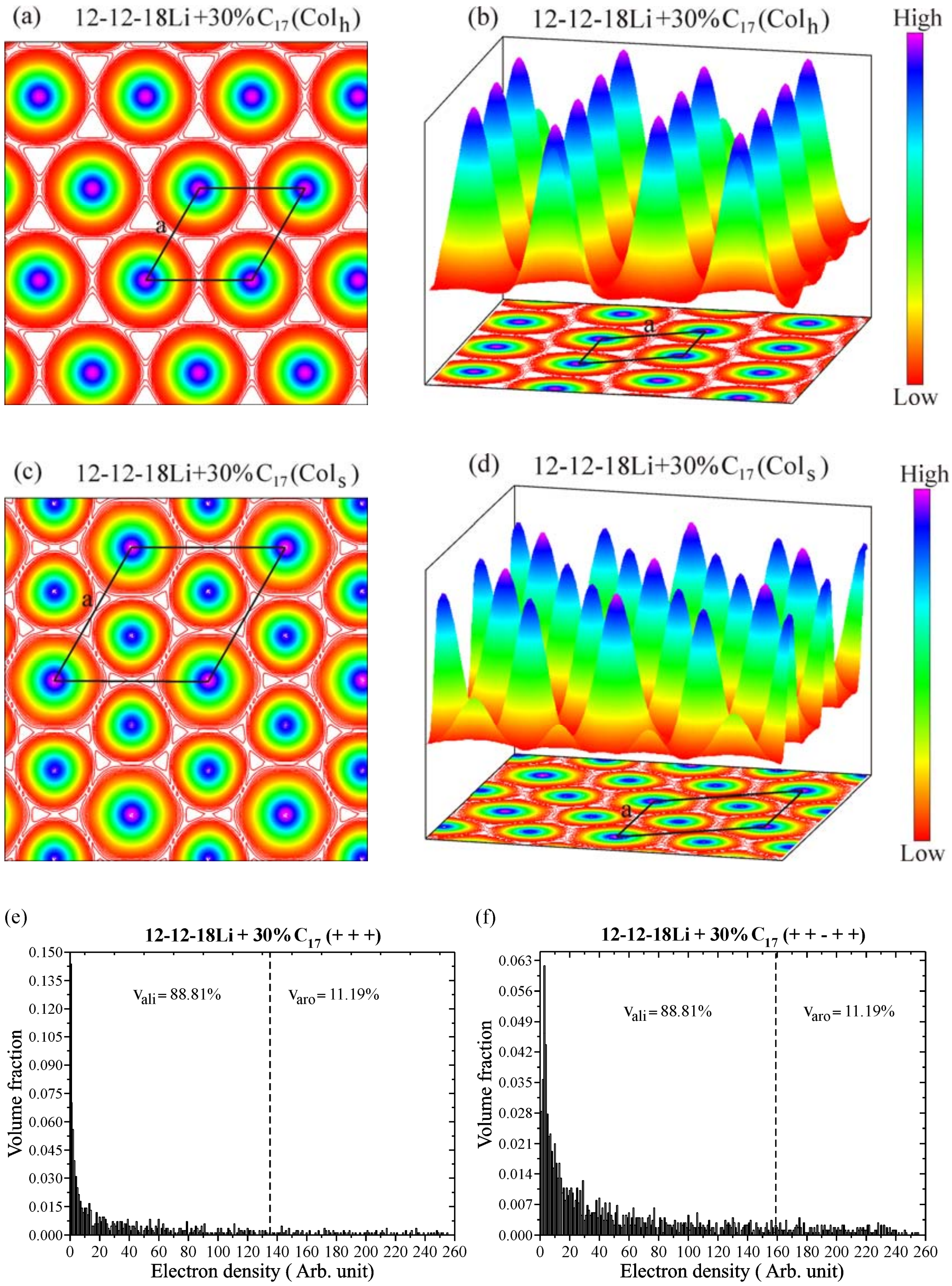

Figure 5-16 Contours and surface plots of electron density distributions in the columns of (a,b) the hexagonal columnar (Col_h) phase at 59 °C and (c,d) the hexagonal columnar superlattice (Col_s) at 99 °C of 12-12-18Li+30%C_{17}. (e) and (f) are histograms of electron density distributions for electron density maps in (b) and (d) respectively.

Table 5-1 Measured interplanar *d*-spacings, relative integrated intensities I_{hk}, multiplicity factors *p*, and phases ϕ_{hk} of difraction peaks used in reconstructing electron density maps.

Materials	**T (°C)**	**Lattice**	**(hk)**	***d*(Å)**	**a_h, $a_s/\sqrt{3}$ (Å)**	**I_{hk} (a.u.)**	***p***	**ϕ_{hk}**
12-12-18Li	99	Col$_h$	(10)	29.9	34.6	100.00	6	0
			(11)	17.3		2.83	6	0
			(20)	15.0		0.72	6	0
			$\mu_{cell}^{cal} = 3.8$(12-12-18Li)					
12-12-18Li+15%C$_{15}$	72	Col$_h$	(10)	31.4	36.3	100.00	6	0
			(11)	18.1		2.46	6	0
			(20)	15.7		0.68	6	0
			$\mu_{cell}^{cal} = 3.4$(12-12-18Li)+2.2($C_{15}H_{32}$)					
12-12-18Li+30%C$_{15}$	67	Col$_h$	(10)	34.8	40.3	100.00	6	0
			(11)	20.1		7.27	6	0
			(20)	17.5		1.49	6	0
			$\mu_{cell}^{cal} = 3.3$(12-12-18Li)+5.1($C_{15}H_{32}$)					
	102	Col$_s$	(10)	57.9	38.6	2.97	6	0
			(11)	33.4		100.00	6	0
			(21)	22.0		0.21	12	π
			(30)	19.3		2.74	6	0
			(22)	16.7		0.67	6	0
			$\mu_{cell}^{cal} = 9.1$(12-12-18Li)+14.0($C_{15}H_{32}$)					
12-12-18Li+15%C$_{17}$	74	Col$_h$	(10)	33.0	38.1	100.00	6	0
			(11)	19.1		4.99	6	0
			(20)	16.5		1.20	6	0
			$\mu_{cell}^{cal} = 3.8$(12-12-18Li)+2.1($C_{17}H_{36}$)					
	108	Col$_s$	(10)	55.9	37.4	0.93	6	0
			(11)	32.3		100.00	6	0
			(21)	21.2		0.30	12	π
			(30)	18.7		4.41	6	0
			(22)	16.2		1.29	6	0
			$\mu_{cell}^{cal} = 10.8$(12-12-18Li)+6.1($C_{17}H_{36}$)					
12-12-18Li+30%C$_{17}$	59	Col$_h$	(10)	35.2	40.7	100.00	6	0
			(11)	20.4		5.96	6	0
			(20)	17.6		1.30	6	0
			$\mu_{cell}^{cal} = 3.4$(12-12-18Li)+4.6($C_{17}H_{36}$)					
	99	Col$_s$	(10)	58.9	39.3	3.69	6	0
			(11)	34.0		100.00	6	0
			(21)	22.4		0.34	12	π
			(30)	19.7		3.21	6	0
			(22)	17.0		0.33	6	0
			$\mu_{cell}^{cal} = 9.5$(12-12-18Li)+12.9($C_{17}H_{36}$)					

bigger hexagon contains 4 molecules of 12-12-18Li whereas one column represented by a smaller hexagon contains 3 molecules of 12-12-18Li.

5.3.4 Determination of the number of 12-12-18Li and C_nH_{2n+2} (n=15, 30) molecules in supramolecular columns in the superlattice

The number of 12-12-18Li and paraffin molecules in the column in the Col_h phase can be determined from calculating the number of molecules 12-12-18Li and n-paraffin C_nH_{2n+2} in the Col_h unit cell since the Col_h unit cell contains only one column. For the Col_s lattice made up of two different types of columns, the number of 12-12-18Li molecules in columns in the Col_s phase can be determined from calculating the number of 12-12-18Li molecules in the Col_s unit cell and also considering the integrated electron density of two different types of hexagons in the electron density map of the Col_s unit cell. These integrals will give us the ratios only of 12-12-18Li molecules, not the combination of 12-12-18Li and paraffin molecules, in columns in the Col_s unit cell. Meanwhile, the number of paraffin molecules in columns can be determined from calculating the number of n-paraffin C_nH_{2n+2} (n=15, 30) in the Col_s unit cell (see more details in Appendix 5) and also considering the best combinations of 12-12-18Li and C_nH_{2n+2} (n=15, 17) molecules which gives the smallest difference in size of two different types of columns. The packing of columns of comparable sizes will reduce the distortion of the lattice and the corresponding strain of the system. Figure 5-17a-c shows the partitioning of space in the superlattice of 12-12-18Li+30%C_{15}, 12-12-18Li+15%C_{17}, and 12-12-18Li+30%C_{17} in order to determine the integrated electron density (e_{integ}) of any given hexagon in the superlattice. To determine how many molecules of 12-12-18Li two different type of columns in the Col_s unit cell should contain, different combinations of 12-12-18Li molecules are varied and the ratios of the number of electrons of such combination of molecules to the total number of electrons of total molecules in the unit cell is calculated and compared to the integrated electron density. Table 5-2 gives the suggested number of 12-12-18Li and C_nH_{2n+2} (n=15, 17) molecules in two different types of columns (i.e. Col1 for type 1 and Col2 for type 2) in the Col_s unit cell (Ucell), from considering the calculated number of 12-12-18Li and C_nH_{2n+2} molecules in the

Col$_s$ unit cell, the integrated electron density (e_{integ}) of hexagons, and the combination of molecules giving the smallest difference in size among those columns.

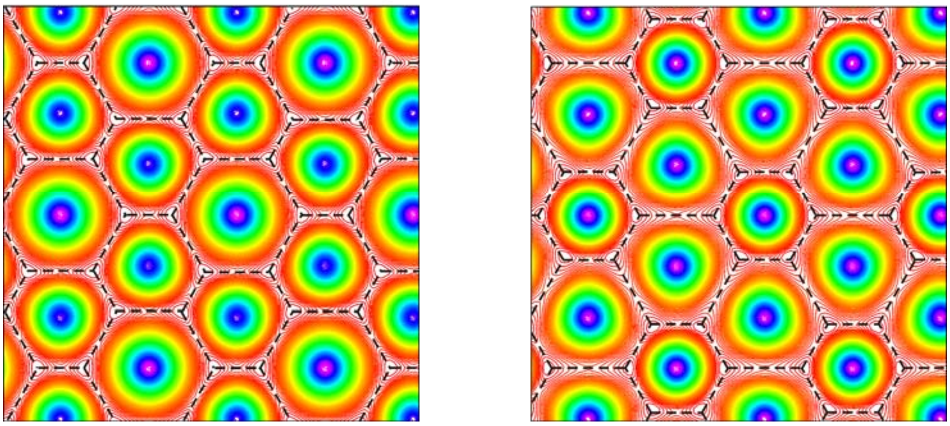

(a) 12-12-18Li+30%C_{15} (Col$_S$)

(b) 12-12-18Li+15%C_{17} (Col$_S$)

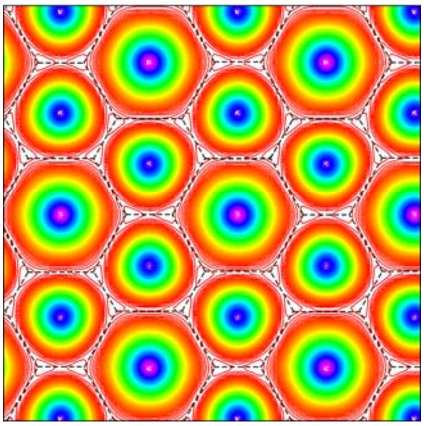

(c) 12-12-18Li+30%C_{17} (Col$_S$)

Figure 5-17 The partitioning of space in the superlattice for the determination of the integrated electron density and the number of 12-12-18Li and C_nH_{2n+2}(n=15, 17) in two different types of columns.

According to the 5th column of Table 5-2, the integrated electron density of bigger and smaller hexagons in the electron density map of 12-12-18Li+30%C_{15} are 0.394 and 0.303 respectively, whereas the integrated electron density of the Col$_s$ unit cell is equal to 1. From the best combination of 12-12-18Li molecules in three columns (the 3rd column of Table 5-2), based on the best fitting between the calculated electron ratios (the 4th column of Table 5-2) and the integrated electron density ratios (the 5th column of Table 5-2), the unit cell of the Col$_s$ lattice of 12-12-18Li+30%C_{15} should contain 10 molecules of 12-12-18Li. The column with higher electron density aromatic core, represented by a bigger hexagon in the contour map of the Col$_s$ unit cell of 12-12-18Li+30%C_{15}, should contain 4 molecules of 12-12-18Li, whereas each of other two columns with lower electron density aromatic cores, represented by a smaller hexagon, should contain 3 molecules of 12-12-18Li. The calculated electron ratio of the bigger hexagon in the Col$_s$ unit cell of 12-12-18Li+30%C_{15} is 0.400, which is close to the integrated electron density of bigger hexagons, i.e. 0.394. The calculated electron ratio of the smaller hexagon is 0.300, which is also close to the integrated electron density of the smaller hexagon, i.e. 0.303. The best combination of 12-12-18Li and $C_{15}H_{32}$ molecules in two different types of columns in the Col$_s$ unit cell of 12-12-18Li+30%C_{15} is also given in the 3rd column of Table 5-2; one column should have 4.0(12-12-18Li)+4.0($C_{15}H_{32}$) whereas each of other two columns should have 3.0(12-12-18Li)+5.0($C_{15}H_{32}$).

For the superlattice of 12-12-18Li+15%C_{17}, the integrated electron density of bigger and smaller hexagons in the Col$_s$ unit cell of 12-12-18Li+15%C_{17} are 0.365 and 0.270 respectively. From the best combination of 12-12-18Li molecules in three columns (the 3rd column of Table 5-2), based on the best fitting between the calculated electron ratios (the 4th column of Table 5-2) and the integrated electron density ratios (the 5th column of Table 5-2), the unit cell of the Col$_s$ lattice of 12-12-18Li+15%C_{17} should contain 11 molecules of 12-12-18Li. Each of two columns represented by a bigger hexagon in the Col$_s$ unit cell of 12-12-18Li+15%C_{17} should contain 4 molecules of 12-12-18Li whereas a column represented by a smaller hexagon contains 3 molecules of 12-12-18Li. The calculated electron ratios of bigger and smaller hexagons in the Col$_s$ unit cell of 12-12-18Li+15%C_{17} are 0.364 and 0.273 respectively, which are close to the integrated electron density of bigger and smaller hexagons of 12-12-18Li+15%C_{17}, i.e. 0.365 for a bigger hexagon and 0.270 for a smaller hexagon. The best combination of 12-12-18Li and $C_{17}H_{36}$ molecules in two different types of columns in the Col$_s$ unit cell of 12-12-18Li+15%C_{17} is also given in the 3rd column of Table 5-2; one column should have 4.0(12-12-18Li)+2.0($C_{17}H_{36}$) whereas each of other two columns in unit cell should have 3.0(12-12-18Li)+2.0($C_{17}H_{36}$).

Table 5-2 The calculated number and the suggested number of 12-12-18Li and C_nH_{2n+2}(n=15, 17) molecules in the unit cell and two different types of columns of the superlattice of 12-12-18Li+15%C_{17}, 12-12-18Li+30%C_{15}, and 12-12-18Li+30%C_{17}.

Materials	**Calculation**		**Suggestion**		e_{cal}	e_{integ}
	No. of 12-12-18Li+C_nH_{2n+2}		**No. of 12-12-18Li+C_nH_{2n+2}**			
12-12-18Li +30%C_{15} at 102 °C	Ucell	9.1(12-12-18Li) +14.0($C_{15}H_{32}$)	Ucell	10.0(12-12-18Li) +14.0($C_{15}H_{32}$)	1.000	1.000
			Col1	4(12-12-18Li) +4.0($C_{15}H_{32}$)	0.400	0.394
			Col2	3(12-12-18Li) +5.0($C_{15}H_{32}$)	0.300	0.303
			Ucell=1*Col1+2*Col2			
12-12-18Li +15%C_{17} at 108 °C	Ucell	10.8(12-12-18Li) +6.1($C_{17}H_{36}$)	Ucell	11.0(12-12-18Li) +6.0($C_{17}H_{36}$)	1.000	1.000
			Col1	4.0(12-12-18Li) +2.0($C_{17}H_{36}$)	0.364	0.365
			Col2	3.0(12-12-18Li) +2.0($C_{17}H_{36}$)	0.273	0.270
			Ucell=2*Col1+1*Col2			
12-12-18Li +30%C_{17} at 99 °C	Ucell	9.5(12-12-18Li) +12.9($C_{17}H_{36}$)	Ucell	10.0(12-12-18Li) +13.0($C_{17}H_{36}$)	1.000	1.000
			Col1	4.0(12-12-18Li) +3.0($C_{17}H_{36}$)	0.400	0.399
			Col2	3.0(12-12-18Li) +5.0($C_{17}H_{36}$)	0.300	0.300
			Ucell=1*Col1+2*Col2			

For the superlattice of 12-12-18Li+30%C_{17}, the integrated electron density of bigger and smaller hexagons in the electron density map of 12-12-18Li+30%C_{17} are 0.399 and 0.300 respectively. From the best combination of 12-12-18Li molecules in three columns (the 3rd column of Table 5-2), based on the best fitting between the calculated electron ratios (the 4th column of Table 5-2) and the integrated electron density ratios (the 5th column of Table 5-2), the unit cell of the Col_s lattice of 12-12-18Li+30%C_{17} should contain 10 molecules of 12-12-18Li. A column with higher electron density aromatic core, represented by a bigger hexagon in the Col_s unit cell of 12-12-18Li+30%C_{17}, should contain 4 molecules of 12-12-18Li whereas each of two columns with lower electron density aromatic core, represented by a smaller hexagon in the Col_s unit cell, should contain 3 molecules of 12-12-18Li. The calculated electron ratios of bigger and smaller hexagons in the Col_s unit cell of 12-12-18Li+30%C_{17} are 0.400 and 0.300 respectively, which are close to the integrated electron density of bigger and smaller hexagons of 12-12-18Li+30%C_{17}, i.e. 0.399 for a bigger hexagon and 0.300 for a smaller hexagon. The best combination of 12-12-18Li and $C_{17}H_{36}$ molecules in two different types of columns in the Col_s unit cell of 12-12-18Li+30%C_{17} is also given in the 3rd column of Table 5-2; one column should have 4.0(12-12-18Li)+3.0($C_{17}H_{36}$) whereas each of other two columns in unit cell should have 3.0(12-12-18Li)+5.0($C_{17}H_{36}$).

5.3.5 The Col_h-Col_s phase transition

According to SAXS experimental results of 12-12-18Li and its mixtures with added n-paraffin C_nH_{2n+2} (n=15, 17), we found that the formation of the superlattice is associated with the adding of n-paraffin C_nH_{2n+2} to a pure compound of 12-12-18Li. According to Figure 5-10, the number of 12-12-18Li molecules per column layer (or per disc) in the Col_h and Col_s phases (i.e. μ_h^{Li} for Col_h and $\mu_s^{Li}/3$ for Col_s) of 12-12-18Li and its mixtures are non-integer numbers; it is between 3 and 4. Also, according to Table 5-2, the integrated electron densities of two different types of hexagons in the Col_s unit cell suggest that the columns in the superlattice can have either 3 or 4 molecules of 12-12-18Li. 3 and 4 are the ideal numbers (i.e. the integer number) of 12-12-18Li dendrons per disc since there must be an integer number of dendrons in a disc. Since some columns would have 3 and some would have 4 dendrons, the Col_h and Col_s lattices are formed by the packing of columns with two different sizes, and this leads to the distortion of the lattice and the corresponding lattice strain. However, we believe that the phase transition from the Col_h phase to Col_s phase is attributed to the redistribution of supramolecular columns into a new hexagonal lattice with lower the lattice strain. The added alkane allows evening out of the differences in column size by locating preferentially around the periphery of the smaller columns. The superlattice lowers the lattice strain by creating a regular array of larger dendron-rich (4 dendrons) and smaller alkane-rich (3 dendron) columns, all of them having a similar overall cross-section area.

5.3.6 Molecular dynamics simulation

The molecular dynamics simulation of molecules of 12-12-18Li and $C_{17}H_{36}$ self-assembled and self-organised into the hexagonal columnar superlattice (Col_s), for example the Col_s of 12-12-18Li+30%C_{17}, was run by using Materials studio v. 4.0. In the simulation, we assume that the columns in the Col_s phase of 12-12-18Li+30%C_{17} have a non-helical structure and are formed by non-tilted 12-12-18Li molecules, plus alkane molecules of $C_{17}H_{36}$. The Col_s unit cell of 12-12-18Li+30%C_{17} contains 10(12-12-18Li)+13($C_{17}H_{36}$). One column in the unit cell contains 4(12-12-18Li)+3($C_{17}H_{36}$), whereas each of the other two columns contains 3(12-12-18Li)+5($C_{17}H_{36}$). After performing geometry optimization and then running the annealing process, the result of simulation shows that the structure of the hexagonal columnar superlattice of 12-12-18Li+30%C_{17} is stable, and the space is fully filled with the alkyl chains of 12-12-18Li and alkane added.

Figure 5-18b is the snapshot of the molecular dynamics simulation of the Col_s of 12-12-18Li+30%C_{17} viewed down the column axis. Color coding is as follows: yellow and red = alkyl chains, blue = aromatic rings. According to the electron density contour of the Col_s of 12-12-18Li+30%C_{17} in Figure 5-18a and the snapshot of the molecular dynamics simulation in Figure 5-18c, the hexagonal columnar superlattice of 12-12-18Li+30%C_{17} can be sketched to Figure 5-18c and Figure 5-18d; the yellow and red columns represent two different types of columns forming their own lattices. The coexistence of two lattices leads to the formation of the superlattice.

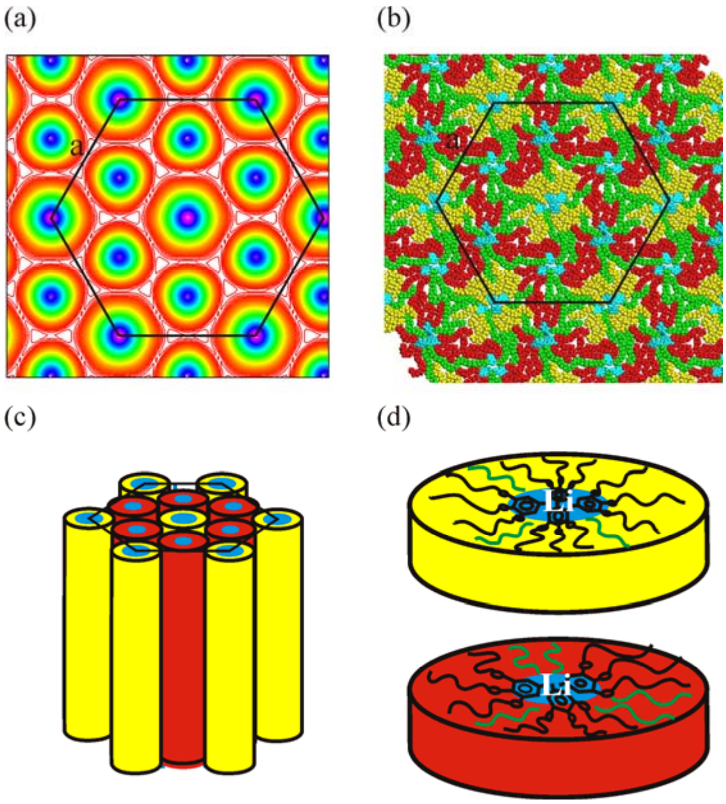

Figure 5-18 12-12-18Li+30%C_{17}: (a) electron density contour (b) snapshot of molecular dynamics simulation of the structure viewed down the column axis. Color coding is as follows: yellow and red = alkyl chains, green= alkane added, blue = aromatic rings. According to (b), the hexagonal superlattice can be sketched to (c) and (d). The yellow and red columns represent two different types of columns in the superlattice. The blue cores of yellow and red columns are the area in which Li atoms and aromatic rings occupy.

5.4 Conclusion

Although 12-12-18Li and its mixtures with added n-paraffin C_nH_{2n+2} (n=15, 17) cannot afford the close packed structures, the mixtures still yield the hexagonal columnar superlattice, which was never obtained from liquid crystal molecules in the same family of 3,4,5-trialoxygallate Li salt, with all same chain lengths of alkyl chains. It is believed that the formation of the superlattice is resulted from the redistribution of supramoleucular columns into a new hexagonal lattice with the lower lattice strain. The lower lattice strain in the superlattice is attributed to the help of added alkane reducing the difference in size of columns and the corresponding lattice strain.

References

[1] Y. Matsui, H. Hayashi, M. Takahashi, K. Kikuchi and K. Yoshida, "(InAs)m(GaAs)n Superlattices grown by molecular beam epitaxy", Journal of Crystal Growth 1985, 71, 280-282.

[2] R. Mazurczyk, "Semiconductor superlattices", Chaos, Solitons and Fractals 1999, 10, 1971-1982.

[3] X. S. Fang, Y. Bando, U. K. Gautam, T. Y. Zhai, S. Gradecak and D. Golberg, "Heterostructures and superlattices in one-dimensional nanoscale semiconductors", J. Mater. Chem. 2009, 19, 5683-5689.

[4] V. Percec, C. H. Ahn, T. K. Bera, G. Ungar, D. J. P. Yeardley, "Coassembly of a Hexagonal Columnar Liquid Crystalline Superlattice from Polymer(s) coated with a three-cylindrical bundle supramolecular dendrimer", Chem. Eur. J. 1999, 5, 1070-1083.

[5] V. Percec, T. K. Bera, M. Glodde, Q. Y. Fu, V.S.K. Balagurusamy, and P. A. Heiney, "Hierarchical self-assembly, coassembly, and self-organization of novel liquid crystalline lattices and superlattices from a twin-tapered dendritic benzamide and its four-cylinder-bundle supramolecular polymer", Chem. Eur. J. 2003, 9, 921-935.

[6] M. Peterca, M. R. Imam, C. H. Ahn, V. S. K. Balagurusamy, D. A. Wilson, B. M. Rosen, and V. Percec, "Transfer, amplification, and inversion of helical chirality mediated by concerted interactions of C_3-supramolecular dendrimers", J. Am. Chem. Soc., 2011, 133, 2311–2328.

[7] B. M. Rosen, M. Peterca, C. Huang, X. B. Zeng, G. Ungar, and V. Percec, "Deconstruction as a strategy for the design of libraries of self-assembling dendrons", Angew. Chem. Int. Ed., 2010, 49, 7002 –7005.

[8] K. H. Cheng, M. Ruonala, J. Virtanen and P. Somerharju, "Evidence for superlattice arrangemens in fluid phosphatidylcholine", Biophysical Journal 1997, 73, 1967-1976.

[9] P. Somerharju, J. A. Virtanen, K. H. Cheng, "Lateral organisation of membrane lipids: The superlattice view", Biochimica et Biophysica Acta 1999, 1440, 32-48.

[10] J. A. Virtanen, K. H. Cheng, and P. Somerharju, "Phospholipid composition of the mammalian red cell membrane can be rationalized by a superlattice model", Proc. Natl. Acad. Sci. USA 1998, 95, 4964-4969.

[11] V. Percec, M.N. Holerca, S. Uchida, W.D. Cho, G. Ungar, Y.S. Lee and D.J.P. Yeardley, "Exploring and expanding the three-dimensional structural diversity of supramolecular dendrimers with the aid of libraries of alkali metals of their AB_3 minidendritic carboxylates", Chem. Eur. J. 2002, 8, 1106-1117.

Chapter 6

Bilayer Supramolecular Cylindrical Columns and Wiggly Layer Structure of Methyl 3,4-(4′-Alkoxy Biphenylmethyl-4-Yloxy) Benzoate

6.1 Introduction

The hexagonal columnar ($\mathrm{Col_h}$) phase is one of most common phases in thermotropic liquid crystals (LCs). This phase can be obtained from self-organisation of supramolecular columns, formed by the stacking up of disc-like mesogens[1-3] or by the stacking up of supramolecular discs formed by wedge-shaped dendrons[4-7]. More interestingly, it has been reported that hexagonal columnar phases can be obtained from pyramidal[8-10] and helical[11,12] supramolecular columns. Recently, hexagonal columnar lattices formed by hollow monolayer[10,13-15] and hollow and non-hollow bilayer columns[16] of self-assembling dendrons have been reported. Similarly, lamellar smectic A phases with different structural features have also been reported in self-assembling dendrons. The most common one is the non-modulated bilayer structure of interdigitated smectic A ($\mathrm{Sm_{Ad}}$)[17-19], whereas the modulated bilayer structure[19] and the non-modulated tetralayer structure[20] of interdigitated smectic A have also been reported.

In this chapter, results on non-hollow bilayer supramolecular columns and wiggly layer structure of hybrid dendrons, methyl 3,4-(4′-alkoxy biphenylmethyl-4-yloxy) benzoate, are presented. In the following sections, after describing the dendrons studied, the SAXS results on these compounds are presented, followed by discussions on the wiggly layer structure of the lamellar phase and the bilayer structure of columns in the hexagonal columnar phase. Next, simulation of the SAXS data of the $\mathrm{Col_h}$ phase by using a two-level core-shell model is described, and electron density maps reconstructed from experimental and simulated results are compared. Molecular dynamics simulation, carried out to confirm the stability of the non-hollow bilayer columns, is also described. Conclusion of the study of these hybrid dendrons is in the final part of the chapter.

6.2 The material studied: methyl 3,4-(4′-alkoxy biphenylmethyl-4-yloxy) benzoate

The hybrid dendrons of methyl 3,4-(4′-alkoxy biphenylmethyl-4-yloxy) benzoate with four different lengths of peripheral alkoxy chains, denoted as Bn where n= 12, 14, 16, 18 (see Figure 6-1a), were studied. This series of compounds was synthesised by our collaborators, Prof. Percec's group at the University of Pennsylvania. The molecular architecture of Bn is derived from the replacement of 3,4-benzyl ether internal units in [4-3,4]12G1-CO_2CH_3[21], as shown in Figure 6-1b, with corresponding biphenyl-4-methy ether units. In addition, the length of the peripheral alkoxy chains attached to 3′,4′-biphenyl-4-methy ether internal units of Bn is also varied to facilitate the possible formation of new supramolecular structures of these hybrid dendrons. It should be noted here that B12 was previously studied and reported by Percec et al.[16]. In that report, B12 is denoted as [4Bp-3,4]12G1-CO_2CH_3. The hexagonal columnar lattice of B12 is thought to form from hollow-core polyhedral columns, and an unidentified phase observed at high temperatures was assumed to be a columnar phase. Here, more reasonable explanation of the self-assembly of B12 into columns is provided. In addition, the high temperature phase is identified. The results of structural analysis on other dendrons in this series of compounds, i.e. B14, B16, and B18, are also reported.

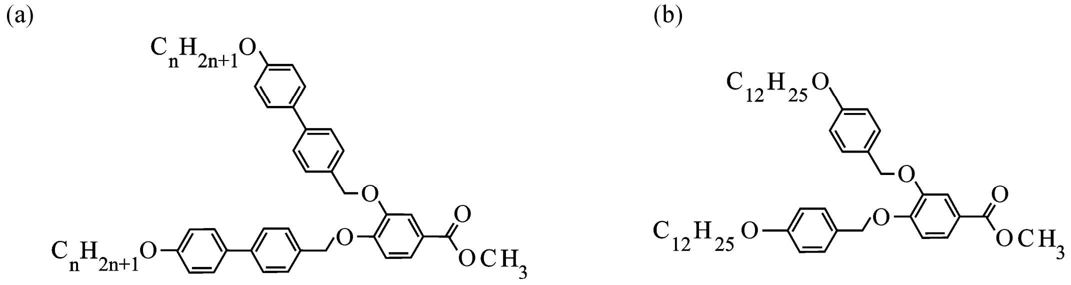

Bn
n=12,14,16,18

[4-3,4]12G1-CO_2CH_3

Figure 6-1 (a) Compounds Bn studied in this thesis, here n=12, 14, 16, 18. (b) Previously studied benzyl ether dendrons [4-3,4]12G1-CO_2CH_3[21].

6.3 Experimental Results and Discussion

6.3.1 SAXS results and phase identification

The supramolecular structures of Bn where n= 12, 14, 16, 18 were determined by a combination of differential scanning calorimetry (DSC) and small angle X-ray diffraction experiments. The DSC is used for determining how many phases there are in the material and what the transition temperatures are from one phase to another. However, DSC cannot identify the structures of phases, and X-ray diffraction is the method used for structure determination in this study. DSC experiments were carried out by our collaborators from University of Pennsylvania, and the results are in Appendix 7. Small angle X-ray diffraction experiments were performed at station I22, Diamond Light Source. The SAXS diffractograms for Bn compounds are shown in Figure 6-2 to Figure 6-5 respectively. All compounds show the same phase sequence on heating; a crystalline phase (K) at low temperatures is followed by a hexagonal columnar (Col_h) phase, followed then by a lamellar phase and then the isotropic liquid phase (according to the DSC data there is a transient unknown phase in B14 but it is not observed by SAXS). In Figure 6-6, the phase sequence of each compound is represented by a column consisting of several colour bars, each representing a particular phase observed. For the Col_h and lamellar phases, the measured d-spacings of diffraction peaks, the corresponding unit cell parameters, and the calculated number of Bn molecules in the unit cells are tabulated in Appendix 8.

As stated before, hexagonal columnar and lamellar phases are very common in thermotropic liquid crystals. However, there are remarkable differences in the diffractograms of the hexagonal columnar and lamellar phases observed in Bn compounds, to those obtained from other dendrons previously studied. Take the diffractogram of B12 (Figure 6-2) as an example. For the hexagonal columnar (Col_h) phase in B12, its diffractograms show that the intensity of higher order diffraction peaks are markedly increased. The intensities of the (11) and (20) peaks are only slightly less than that of the (10) peak, while for other dendrons previously studied the (10) peak is the single strongest peak of the hexagonal columnar phase[7-22]. Moreover, many higher order reflections such as (30), (22), (31) etc., which were not seen before in such dendrons, are observed. What is also peculiar is that the *a* lattice parameter of the hexagonal columnar (Col_h) unit cell of B12, a = 72.5 Å, is much larger than the normal values observed for dendron of similar size. The fact that the Col_h phase is found in temperatures below those of the lamellar phase is also peculiar, as in previously studied dendrons the Col_h phase is normally found at higher temperatures. The remarkable structure of columns and corresponding Col_h lattice of Bn molecules, which are the origin of such unusual diffractograms of the Col_h phase and the unusual phase sequence of Bn compounds, will be discussed below. Before that, the new lamellar phase obtained in Bn compounds is introduced first. The knowledge of how Bn molecules are self-arranged into a layer structure provides important clues about how the Bn molecules are self-assembled into columns and the corresponding Col_h lattice.

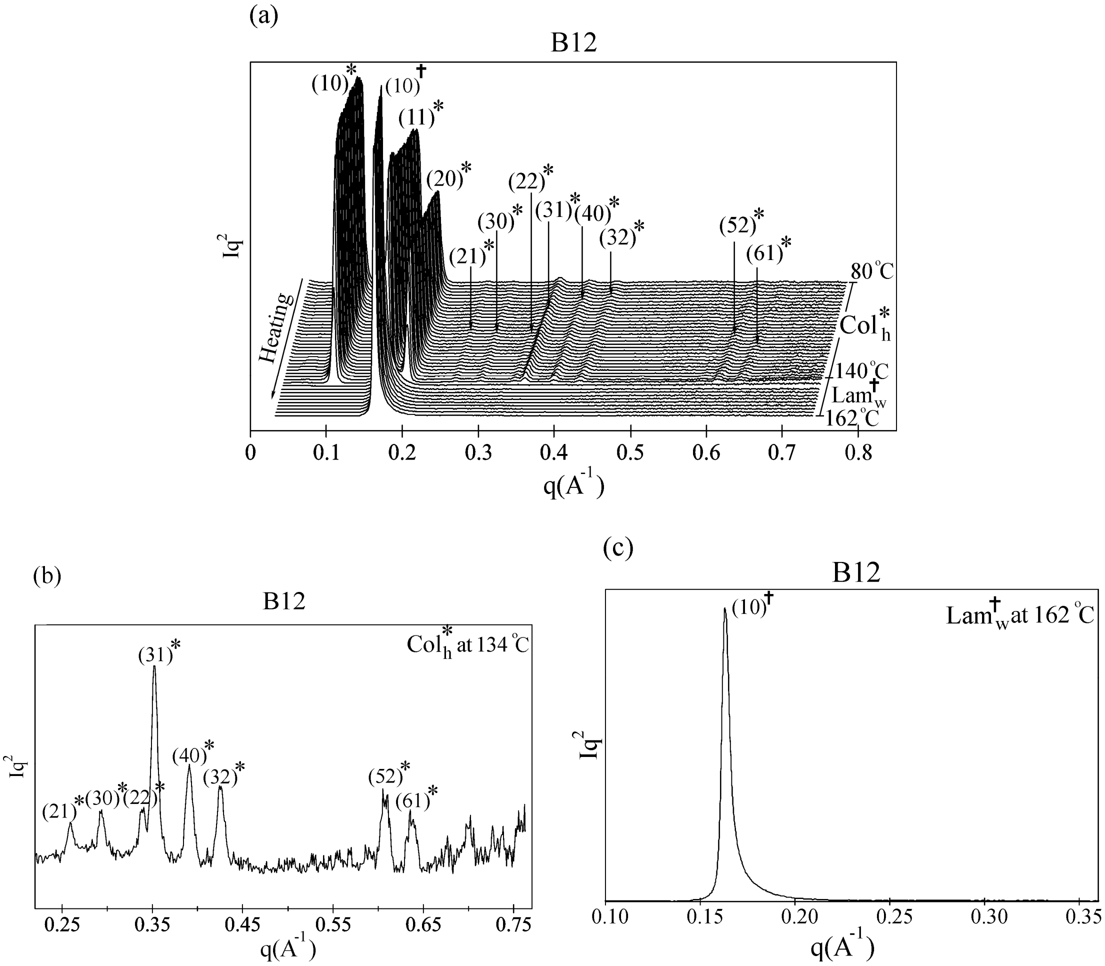

Figure 6-2 (a) Small angle X-ray diffraction result of B12 on the heating run with heating rate 4 °C/min. Diffraction peaks are marked with their indices for the hexagonal columnar (Col_h, *) and wiggly layer (Lam_w, †) phases. (b) A close view of weak diffraction peaks in the hexagonal columnar phase at 134 °C. (c) (10) diffraction peak in the wiggly lamellar phase of B12 at 162 °C.

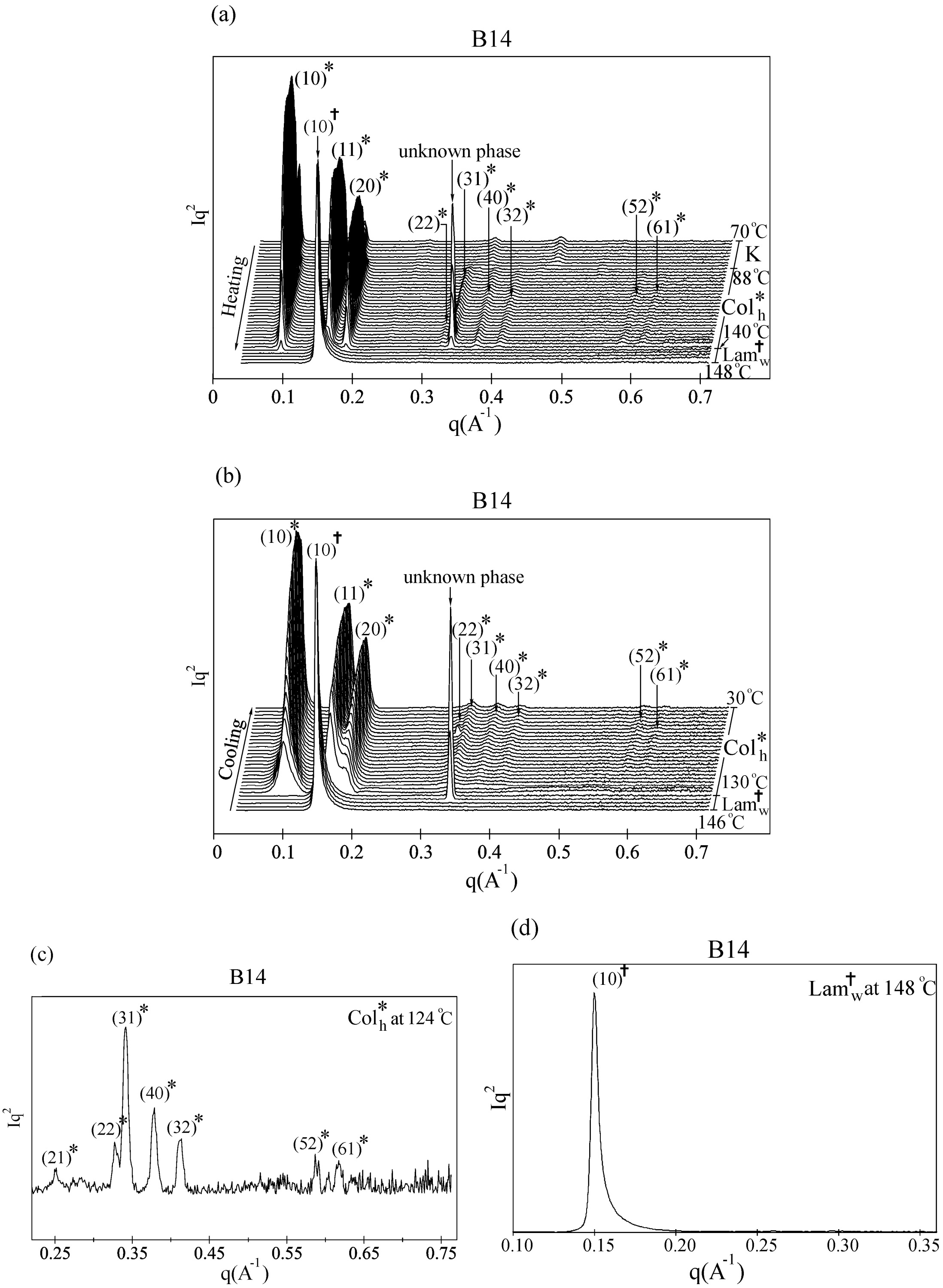

Figure 6-3 Small angle X-ray diffraction results of B14 on (a) the heating run with heating rate 2 ºC/min. (b) The cooling run with cooling rate 3 ºC/min. Diffraction peaks are marked with their indices for the hexagonal columnar ($\mathrm{Col_h}$, *) and wiggly layer ($\mathrm{Lam_w}$, †) phases. (c) A close view of weak diffraction peaks in the hexagonal columnar phase at 124 ºC. (d) (10) diffraction peak in the wiggly lamellar phase at 148 ºC.

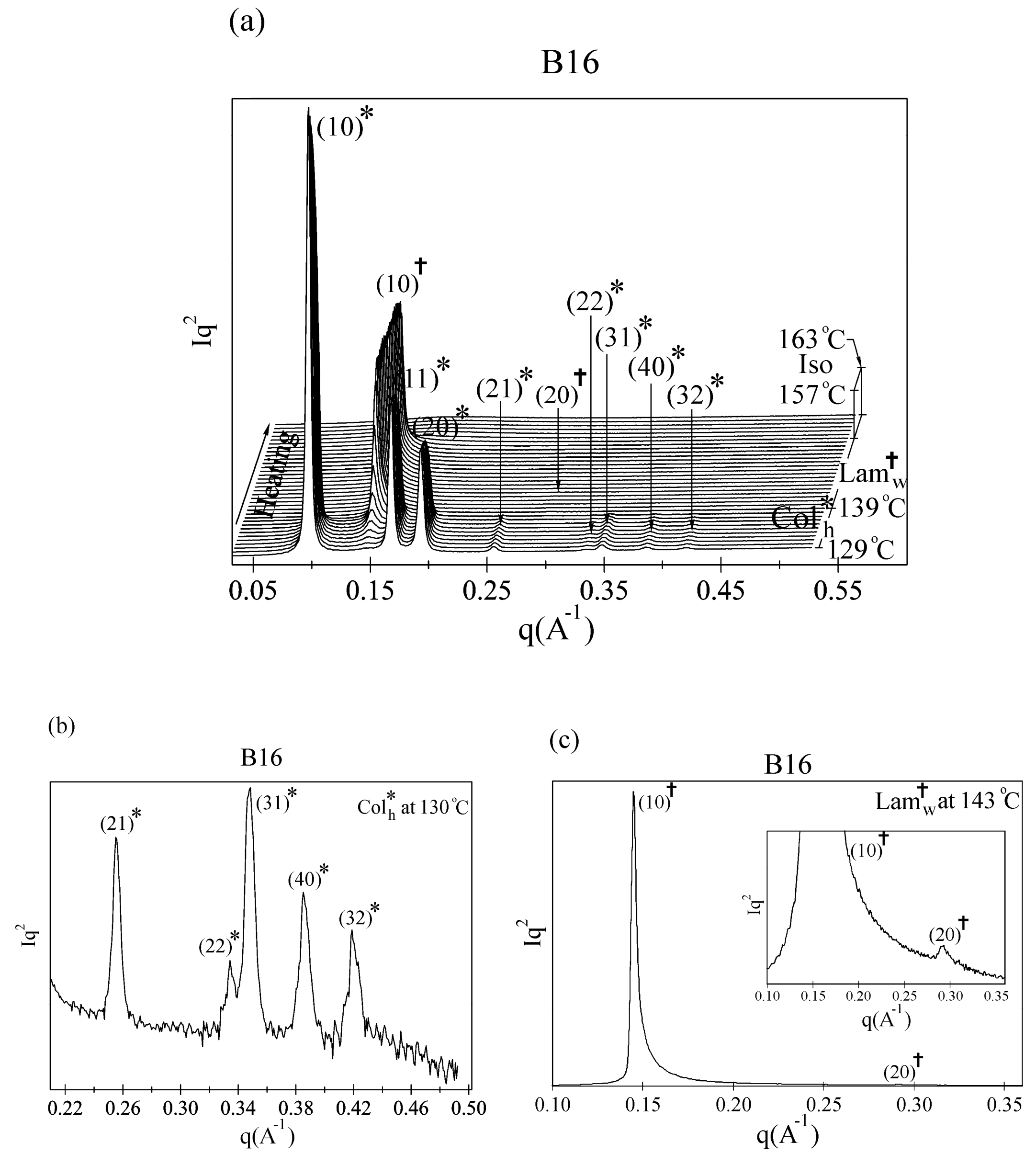

Figure 6-4 (a) Small angle X-ray diffraction result of B16 on the heating run with heating rate 2 ºC/min. Diffraction peaks are marked with their indices for the hexagonal columnar (Col$_h$, *) and wiggly layer (Lam$_w$, †) phases. (b) A close view of weak diffraction peaks in the hexagonal columnar phase at 130 ºC. (c) (10) and (20) diffraction peaks in the wiggly lamellar phase of B16 at 143 ºC.

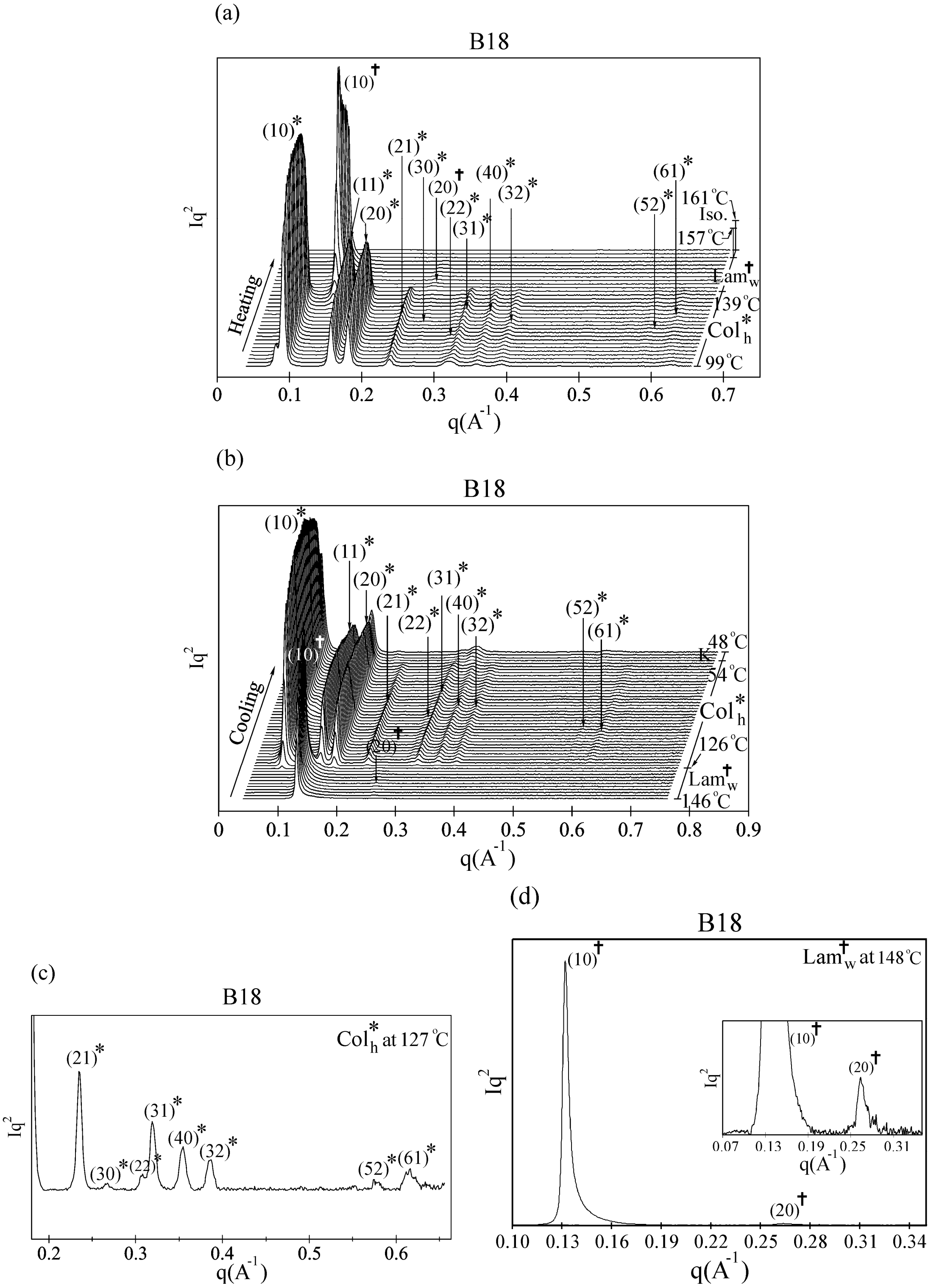

Figure 6-5 Small angle X-ray diffraction result of B18 on (a) the heating run with heating rate 2 °C/min. (b) The cooling run with cooling rate 2 °C/min. Diffraction peaks are marked with their indices for the hexagonal columnar (Col$_h$, *) and wiggly layer (Lam$_w$, †) phases. (c) A close view of weak diffraction peaks in the hexagonal columnar phase at 127 °C. (d) (10) and (20) diffraction peaks in the wiggly lamellar phase of B18 at 148 °C.

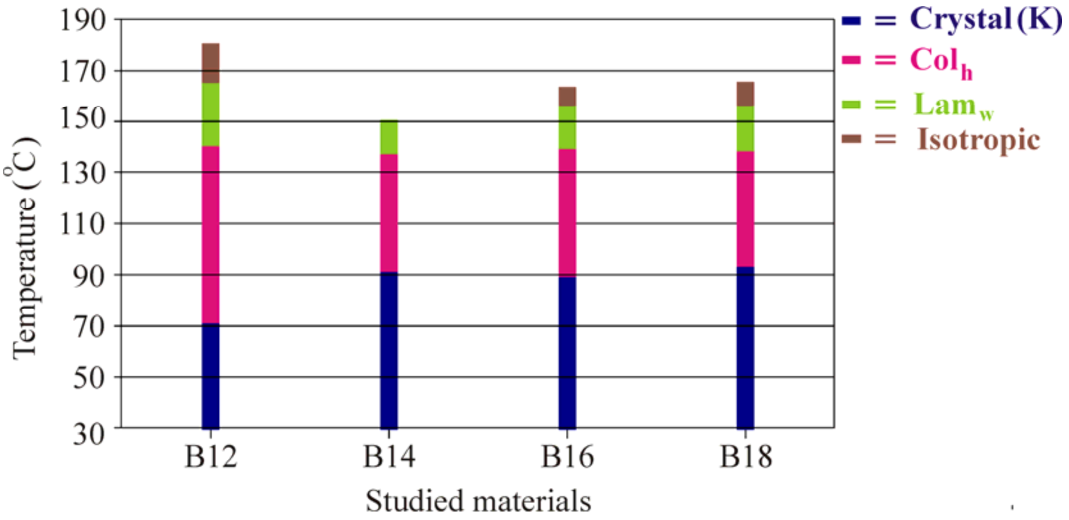

Figure 6-6 Graphical presentation of all phases observed for AB_2 hybrid dendrons B12, B14, B16, and B18.

6.3.2 Wiggly lamellar phase

The high temperature phase in B12 was first reported in the paper by Percec et al.[16], but as only one diffraction peak was observed the phase cannot be determined and it was assumed to be another columnar phase in the paper. Here, according to the diffractograms of the other compounds in the series, (see Figure 6-4d and Figure 6-5d for B16 and B18 respectively), another diffraction peak, albeit weak, can be observed and its *q* value is exactly twice that of the first peak. This suggests to us that the high temperature phase in B12, including that in B14, B16, and B18, is the lamellar phase. The unusual asymmetry in the peak shape of (10) and (20) in this lamellar phase also indicates that this lamellar phase is somehow different from the many lamellar phases obtained from other dendrons previously studied. According to Figure 6-2d to Figure 6-5d, the intensity of (10) and (20) peaks drops down very sharply at the lower *q* side of the peaks, while it decreases much slowly at the higher *q* side and a long tail is observed. The unusual asymmetry in the peak shape of this lamellar phase can be understood better by grazing incidence small angle X-ray scattering (GISAXS) on oriented thin film samples prepared on a silicon substrate. Orientation of the thin films is found to form spontaneously on the substrate surface, with the layer normal of the lamellar phase always perpendicular to it. According to the GISAXS patterns for B12 and B18 as shown in Figure 6-7, it is evident that (10) and (20) peaks are much more spread in the horizontal than in the vertical direction (almost streak like). Such a diffraction peak would then produce the asymmetrical peak shape which is observed in the powder diffraction pattern.

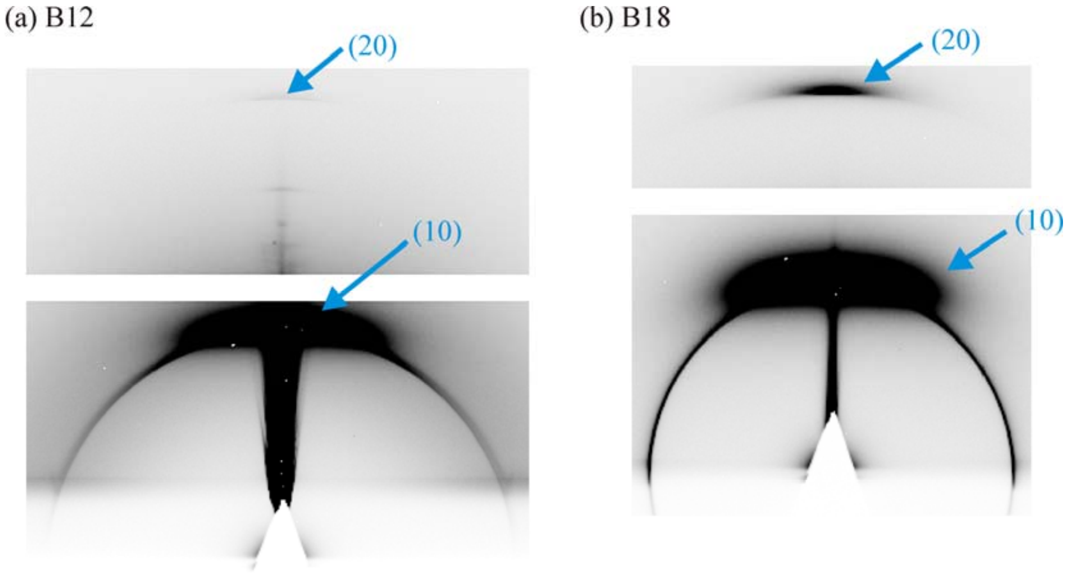

Figure 6-7 The grazing incidence small angle X-ray scattering (GISAXS) results of (a) B12 at 140 ºC (b) B18 at 150 ºC.

The unusual shape of the diffraction peaks suggests to us that the lamellar phase of Bn compounds has a “wiggly” layer structure, where the layer surfaces fluctuate instead of staying flat. However, such fluctuations are only local since the spread of diffraction peak in the horizontal direction does not show any indication of long range periodicity. From the measurements of the lamellar spacings and the lengths of stretched Bn molecules (see Table 6-1), the lamellar spacings of a series of Bn are always a bit longer than the lengths of the corresponding molecules, and at the same time it is much shorter than a double of those values. Considering the shape of Bn molecules, the natural molecular model for the wiggly lamellar phase is a bilayer structure consisting of alternate aromatic and aliphatic layers, where the molecules are arranged themselves into the interdigitated way as shown in Figure 6-8a. The bilayer structure of interdigitated molecules has also been used to explain the formation of the lamellar phases observed in other dendrons previously studied[17-19,23] (see Figure 6-8b). It is believed by us that the fluctuation of the layer surfaces is resulted from the local variation of the orientation of Bn molecules within the layers, possibly in an attempt to keep local H-bonding between aromatic cores of molecules (which would otherwise be lost by interdigitation of molecules).

Table 6-1 Comparison of experimental lamellar spacings and the stretched molecule length (estimated using Materials Studio^{TM}) for compounds Bn where n=12, 14, 16, 18.

Sample	Lamellar Spacing (Å)	Stretched molecule length (Å)
B12	38.6 (150 °C)	35.8
B14	42.0 (142 °C)	39.1
B16	42.6 (150 °C)	42.1
B18	47.3 (151 °C)	46.1

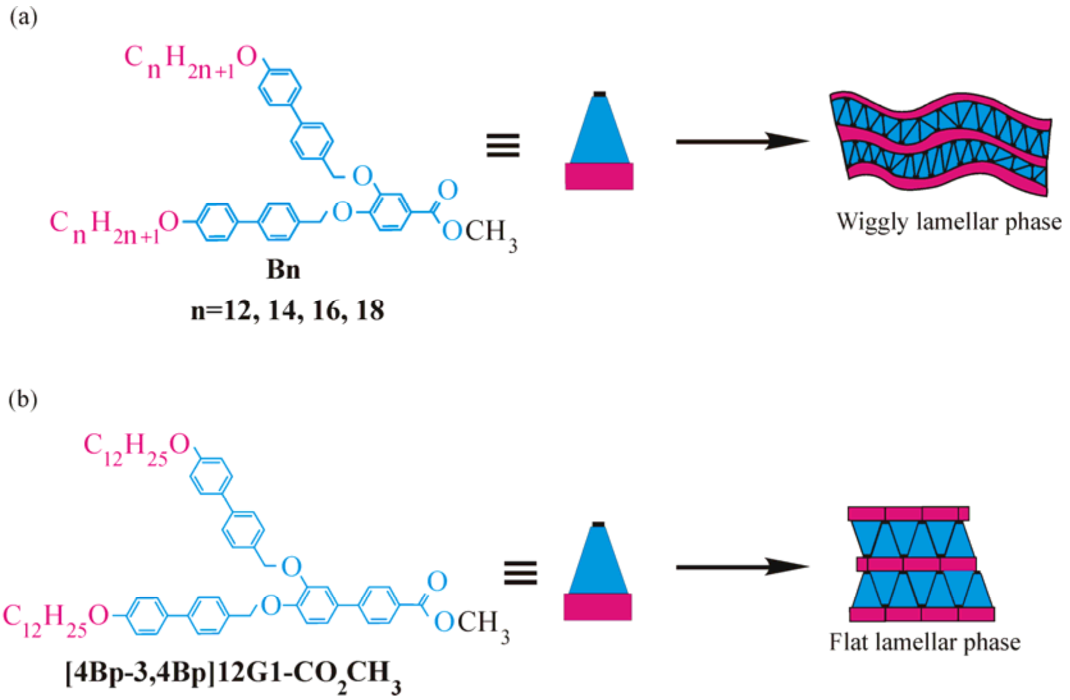

Figure 6-8 The formation of (a) the wiggly lamellar (Lam$_w$) phase of Bn where n=12, 14, 16, 18 and (b) the flat lamellar phase of previously studied dendron[23].

6.3.3 Bilayer hexagonal columnar phase

The considerable increase in the lattice parameter and the intensity of the higher order diffraction peaks in the Col$_h$ phase of B12 were claimed to originate from the presence of a hollow core in each supramolecular column by Percec'group[16]. According to ref. 16, three different hollow-core models of columns as shown in Figure 6-9 were used to calculate structure factors of diffraction peaks in the Col$_h$

phase of B12. Instead of fitting intensities of diffraction peaks, structure factors calculated from experimental intensities of first 7 diffraction peaks in the Col$_h$ phase of B12 were fit with ones calculated from using those three models. Percec reported that the *hhc* model gives the best structure factor fitting. The hollow core of supramolecular columns of B12 is about 14.8 Å. The size of this empty core is by no means small. Hence, it is difficult to justify in terms of the free energy of the system.

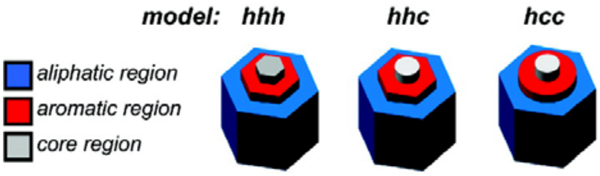

Figure 6-9 hhc, hhh, hcc models[16].

Here we proposed a more realistic model of the hexagonal columnar phase, in which the cores of supramolecular columns are not empty, but occupied by alkyl chains of some molecules turning themselves in the inverse direction to most molecules in such columns. Simulation of the diffraction intensities, on the basis of this model, has been carried out and fits very well the experimental observations. All details are provided in the next section. In addition, molecular dynamics simulation has been carried out to confirm the stability of such a model.

Support for the new model also comes from the molecular shape of Bn molecules. Since the aromatic part of Bn molecules has a wide-angle shape, not all Bn molecules can reach the centre of columns. Therefore, some Bn molecules have to turn around itself in the inverse direction to most of molecules in columns, with their alkyl chains pointing toward the centre of column, to avoid the formation of a hole at the centre of the column, which will cause a huge energy penalty to the system. The end-to-end arrangement of Bn molecules also helps stabilise the structure of columns because of the H-bonds between aromatic parts of molecules. However, the hydrogen bondings become weak at high temperatures and the increasing of gauche bonds of aliphatic chains at higher temperatures requires more lateral space, therefore requires normally a higher surface curvature. This is achieved by interdigitation of the aromatic cores with sacrifice in the H-bondings between them, and the lamellar phase is therefore unexpectedly obtained at high temperatures in this series of hybrid dendrons. Weak H-bonding still present between neighbouring Bn molecules also results in the local variation of the orientation of Bn molecules within the layers, leading to the fluctuation of the layer surfaces and the wiggly lamellar phase. The arrangement of Bn molecules in the bilayer columns and its transformation to the wiggly lamellar (Lam_w) phases is schematically presented in Figure 6-10.

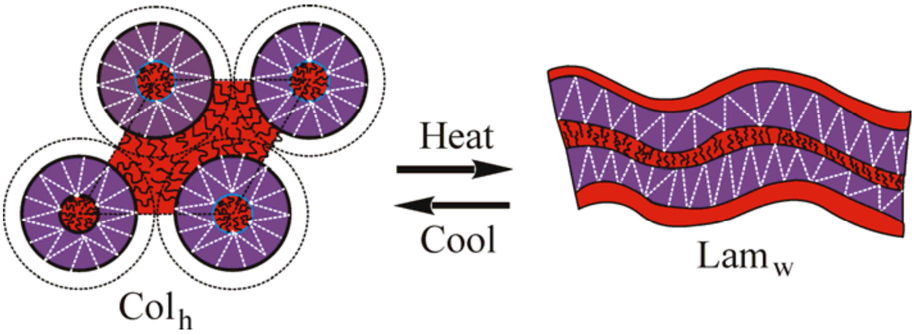

Figure 6-10 Schematic arrangements of molecules in the hexagonal columnar (Col_h) phase and in the wiggly lamellar phase (Lam_w) for compounds Bn.

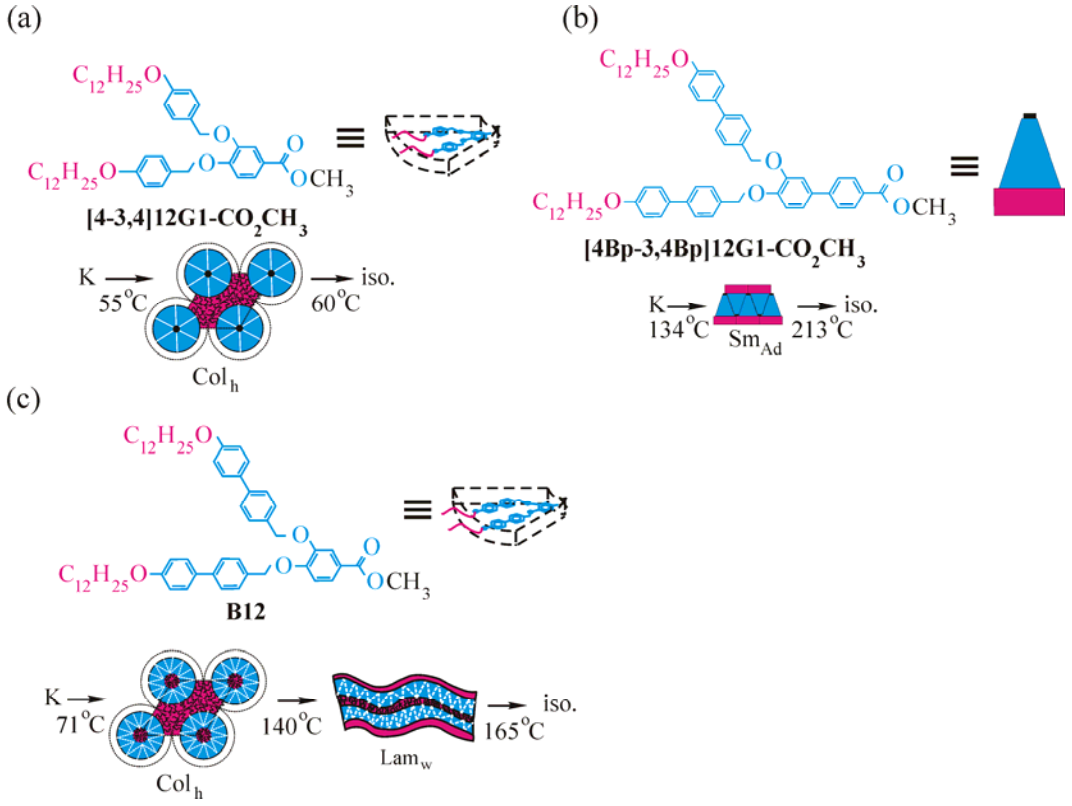

Figure 6-11 Comparison of molecular architecture and corresponding phase sequence of some previously studied dendrons (a)-(b)[21-23] with those of currently studied dendron (c).

Figure 6-11a and Figure 6-11b shows previously studied dendrons having molecular structures similar to B12 (Figure 6-11c). One can see that the molecular structure of B12 is the combination of the molecular structure of the benzyl ether based dendron [4-3,4]12G1-CO_2CH_3[21] (Figure 6-11a) and that of the biphenyl methyl ether based dendron [4Bp-3,4Bp]12G1-CO_2CH_3[23] (Figure 6-11b). The phase sequence obtained from B12 can be viewed as a combination of phase sequences obtained from [4-3,4]12G1-CO_2CH_3 and [4Bp-3,4Bp]12G1-CO_2CH_3.

6.3.4 Simulation of the powder X-ray diffraction data

To support our bilayer model for the hexagonal columnar (Col_h) lattice of Bn, the powder X-ray diffraction data of the Col_h phase of Bn are simulated and compared to the experimental data. The geometrical model of columns used for simulating the powder X-ray diffraction data is shown in Figure 6-12. The column is comprised of three regions, i.e. the aliphatic core (red), the aromatic middle region (purple), and the outer aliphatic region (red). The aliphatic core has a diameter of $2r_1$ and the electron density within the core is assumed to be equal to that of aliphatic shell, represented by the same level of red horizontal lines. The aromatic region of the column, having a higher electron density than the aliphatic core and shell, has an outer diameter of $2r_2$. The electron density in this region is represented by the purple blocks, its difference to the aliphatic background is η, as shown in Figure 6-12.

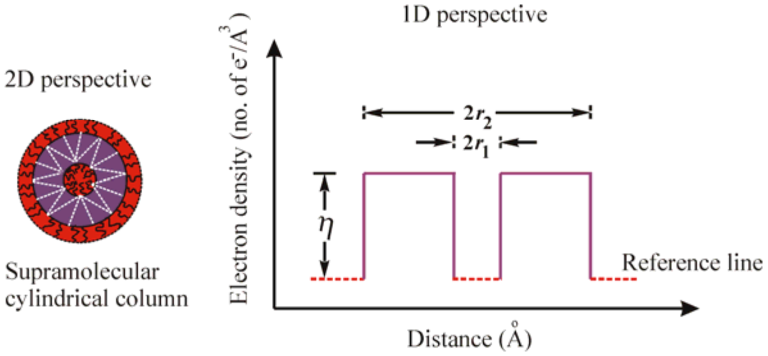

Figure 6-12 1D and 2D perspectives of the geometrical model of bilayer supramolecular columns in the Col_h phase of compounds Bn where n=12, 14, 16, 18.

The general equation that is used to calculate the intensity $I_{hkl}(q)$ of each diffraction peak (*hkl*) is expressed in Eq. (6-1), where $F_{hkl}(q)$ and p_{hkl} are the structure factor and the multiplicity factor of (*hkl*) reflection respectively. q is the magnitude of a reciprocal lattice vector $\vec{q}$.

$$I_{hkl}(q) = \left|F_{hkl}(q)\right|^2 p_{hkl} \quad \ldots\ldots\ldots\ldots\ldots\ldots\ldots\ldots\ldots\ldots(6\text{-}1)$$

The structure factor $F_{hkl}(q)$ can be calculated by using Eq. (6-2), where $f_n(q)$ is the form factor of the n^th^ motif situated at position (u_n, v_n, w_n) in the unit cell.

$$F_{hkl}(q) = \sum_n f_n(q)\exp[\ 2\pi i(hu_n + kv_n + lw_n)] \quad \ldots\ldots\ldots\ldots\ldots\ldots\ldots(6\text{-}2)$$

The form factor for a disk with the radius r and electron density η is given in Eq. (6-3).

$$f(q) = 2\pi r\eta \frac{J_1(rq)}{q} \quad \ldots\ldots\ldots\ldots\ldots\ldots\ldots\ldots\ldots\ldots\ (6\text{-}3)$$

Here, $J_1(x)$ is the Bessel function of the first kind.

The unit cell of the bilayer hexagonal columnar lattice can be considered as containing two columns, both at (0,0,0) position of the unit cell. One has diameter $2r_2$ and constant electron density η, plus the other which has diameter $2r_1$ and negative constant electron density $-\eta$. The intensity of $I_{hkl}(q)$ can then be expressed as

$$I_{hkl}(q) = F(q)^2\, p_{hkl} = \left[2\pi\eta r_2\ \frac{J_1(r_2 q)}{q} - 2\pi\eta r_1\ \frac{J_1(r_1 q)}{q}\right]^2 p_{hkl} \qquad \ldots\ldots\ldots\ldots\ldots\ldots(6\text{-}4).$$

The values of r_1, r_2, and η giving the best intensity fitting between experimental intensities I^{exp} and simulated intensities I^{sim} are determined by minimising the square of the differences between the two sets of data as expressed in Eq. (6-5)

$$Min\ (\sum_{i=1}^{n}(I_i^{\exp} - k\ I_i^{sim})^2) \qquad \ldots\ldots\ldots\ldots\ldots\ldots\ldots\ldots(6\text{-}5)$$

where k is the scaling factor. The minimization is done numerically using Mathematica v. 7.0. As the diffraction intensities were measured in arbitrary unit instead of absolute unit, the value of η is included in the unknown scaling factor and cannot be determined.

Table 6-2 shows values of r_1 and r_2 which yield the best fitting between experimental intensities I^{exp} and simulated intensities I^{sim} of diffraction peaks of the $\mathrm{Col_h}$ phase of Bn compounds. A comparison between experimental intensities I^{exp} and simulated intensities I^{sim} is provided in Table 6-3, which shows very satisfactory fitting between those two sets of intensities. According to the simulation results, the radii of aliphatic cores of supramolecular columns are about 7 Å, and the outer radii of the aromatic region are about 30 Å. From the calculation of the total number of Bn molecules in the unit cell and the number of molecules turning themselves in the inverse direction, it can be estimated that about 7-10% of dendrons are turned around with their aliphatic chains pointing towards the centre of the column. The results also fit well with the lengths and volume of the aromatic part of Bn molecules. According to the simulation, the thickness of the aromatic shell, l_{aro}^{sim}, are about 22-23 Å. This is very close to the length of the aromatic part of Bn molecules, $l_{aro}^{meas} \approx 20$ Å, measured from molecular models using Material Studio. Volume fractions of the aromatic shell from simulation, v_{aro}^{sim}, are also quite close to those obtained from using Materials Studio (v_{aro}^{meas}). The thickness of the aliphatic layers, $\boldsymbol{l_{aliph}^{sim}}$, are shorter than the stretched lengths of the corresponding aliphatic tails, l_{aliph}^{meas}, but this is only expected as the aliphatic chains are known to be fairly flexible in the temperature range studied.

Table 6-2 Values of r_1 and r_2 giving the best intensity fitting between experimental intensities I^{exp} and simulated intensities I^{sim} of the diffraction peaks of the $\mathrm{Col_h}$ phase of Bn where n= 12, 14, 16, 18.

n	$\boldsymbol{r_1}$ **(Å)**	$\boldsymbol{r_2}$ **(Å)**	***a*** **(Å)**	$\boldsymbol{\mu_{obj}^{cal}}$	$\boldsymbol{\mu_{in}}$	$\boldsymbol{v_{aro}^{meas}}$	$\boldsymbol{v_{aro}^{sim}}$	$\boldsymbol{l_{aro}^{meas}}$ **(Å)**	$\boldsymbol{l_{aro}^{sim}}$ **(Å)**	$\boldsymbol{l_{aliph}^{meas}}$ **(Å)**	$\boldsymbol{l_{aliph}^{sim}}$ **(Å)**
12	7.2	29.5	72.5	15.3	1.6	0.54	0.55	20.1	22.4	15.6	7.31
14	7.0	30.3	76.4	16.0	1.3	0.50	0.54	20.1	23.3	19.0	7.91
16	6.7	29.8	75.4	14.7	1.0	0.47	0.54	20.1	23.1	21.9	7.93
18	7.8	29.4	81.6	16.3	1.2	0.44	0.44	20.1	21.7	25.7	11.38

μ_{in} = the number of molecules turning around, with their aliphatic chains pointing toward the centre of the column: $\mu_{in} = \pi r_1^2 l/V_{aliph}^{Bn}$.

μ_{obj}^{cal} = the number of molecules in the Col$_h$ unit cell: $\mu_{obj}^{cal} = (\sqrt{3}/2)N_A a^2 l\rho/M_{aliph}^{Bn}$

(r_1 = radius of the aliphatic core of column, l= column layer thickness, V_{aliph}^{Bn} = occupied volume of alkyl chains of Bn, Avogadro's number $N_A = 6.022\times10^{23}$ mol^{-1}, ρ = the density of Bn compounds, M_{aliph}^{Bn} = molecular weight of Bn molecules. The density of B12 is 1.08g/cm^3 [16], whereas the density of B14, B16, and B18 is assumed being equal to that of B12. The column layer thickness is assumed 4.5 Å, based on the thickness measurements of Bn molecules by using Materials Studio program. Occupied volume of alkyl chains of Bn is measured by using Materials Studio v. 4.0: $V_{aliph}^{B12} = 464.8$ Å^3, $V_{aliph}^{B14} = 543.6$ Å^3, $V_{aliph}^{B16} = 619.0$ Å^3, and $V_{aliph}^{B18} = 692.1$ Å^3.)

6.3.5 Electron density reconstruction

Figure 6-13 to Figure 6-16 show electron density maps of the hexagonal columnar (Col$_h$) phase of B12, B14, B16, and B18. For each compound two electron maps are shown; one is reconstructed from using the experimental diffraction peak intensities and the other is from best-fit simulated intensities. This is done in order to visualize more easily the differences between our geometrical model and that from experiment in the real space. Symbols + and – below the maps represent the phase angles 0 and π of diffraction peaks respectively, which are obtained from simulated structure factors from best-fit models and are also tabulated in Table 6-3. In the electron density maps, different electron density levels are represented by different colours. The highest electron density is represented by purple and the lowest electron density is represented by red. The experimental and simulated electron density maps are indeed very similar, and clearly show that the supramolecular columns are consisted of a low electron density cores and a high electron density shell, surrounded by low electron density regions outside, as predicted by our bilayer molecular model. The low electron density cores of columns are quite small whereas the high electron density shells of columns are somewhat bigger. These are consistent with simulation results that the radii of aliphatic cores and the thickness of aromatic shells of columns are about 7-8 Å and 22-23 Å respectively (see Table 6.2). When the electron density maps of the Col_h phase of Bn molecules (n=12, 14, 16, 18) are compared to those of 12-12-18Li and 12-12-18Li+m%C_n (m=15, 30 and n= 15, 17), shown in Figure 5-12 to Figure 5-16, section 5.3.3, one can see that the columns of Bn molecules have a bigger area of high electron density region than those of 12-12-18Li+m%C_n. This is because Bn molecules have a bigger volume fraction of the aromatic part (0.44-0.54) than 12-12-18Li and 12-12-18Li+m%C_n have (0.17 for 12-12-18Li and 0.11-0.14 for 12-12-18Li+m%C_n).

In addition, the electron density maps of Bn also have a relatively steeper electron density gradient at the boundary between the aromatic core (purple and blue) and the aliphatic region (green, yellow, and red) than those of 12-12-18Li and its mixtures have. For Bn compounds nine diffraction peaks up to peak (32) were observed experimentally, whereas for 12-12-18Li and 12-12-18Li+m%C_n only three diffraction peaks up to (20) is observed. This is a result of the fact that the unit cell parameters of Bn compounds is more than twice of those in salts, and consequently more peaks were used in reconstructing the electron density maps of Bn compounds. Similar to the case of representing the square-wave function by Fourier series, when only one term of the Fourier series, i.e. the first term or sin *x*, is used to approximate the square-wave function, the discontinuities at the jumps of the square-wave function is not well represented. However, the discontinuities can be better represented when more terms of the Fourier series are used.

Artefact in the reconstructed electron density maps, arising from using a limited number of diffraction peaks, can also be observed. The electron density in the low and high density regions are not perfectly uniform; there are some small drops in the electron density (i.e. blue patches) in the high density region (purple), and there is a slight increase in the electron density (i.e. yellow patches) in the low density region (red). This is also similar to the case of reconstructing a square-wave function, whose flat parts are approximated by the ripples of the summation of several terms in the Fourier series.

Figure 6-13 to Figure 6-16 also show the comparison of electron density maps reconstructed from experimental intensities and simulated intensities. The biggest difference between the experimental and simulated maps is that in the simulated maps the electron density in the peripheral region of columns is somehow higher than that of cores of columns. Such difference is believed to be resulted from differences between experimental intensities I^{exp} and simulated intensities I^{sim} at higher diffraction orders, as one can see in Table 6-3. This is resulted from the fact that in the model all the boundaries between different electron densities are sharp, and no thermal disorder effect, i.e. Debye-Waller factor (for details see Chapter 3, section 3.5.3), is considered.

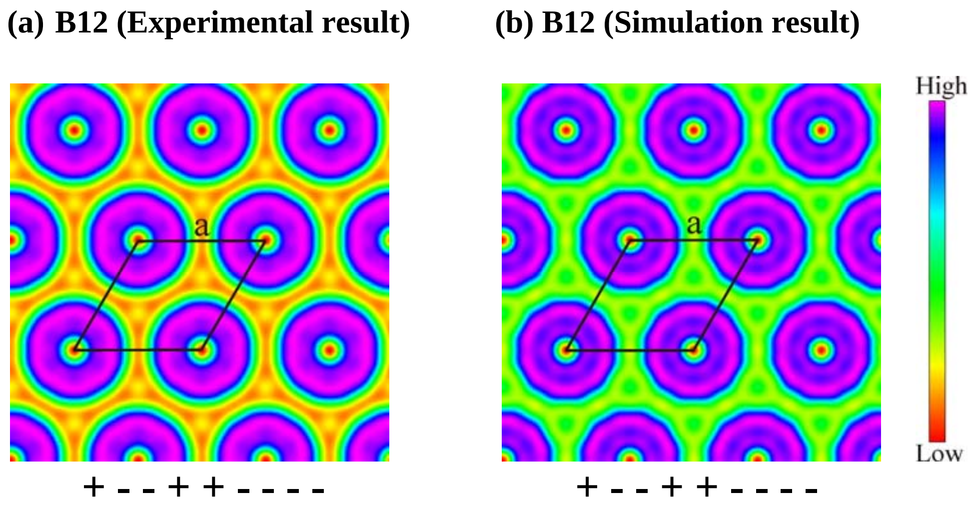
(a) B12 (Experimental result)

(b) B12 (Simulation result)

Figure 6-13 2D electron density maps of the Col$_h$ phase of B12, reconstructed on the basis of (a) experimental and (b) simulated diffraction peak intensities.

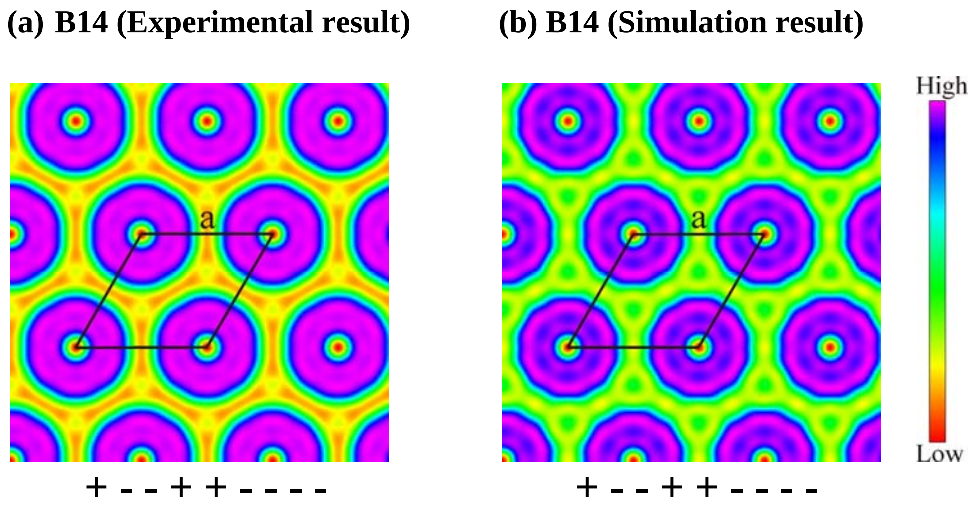
(a) B14 (Experimental result)

(b) B14 (Simulation result)

Figure 6-14 2D electron density maps of the Col$_h$ phase of B14, reconstructed on the basis of (a) experimental and (b) simulated diffraction peak intensities.

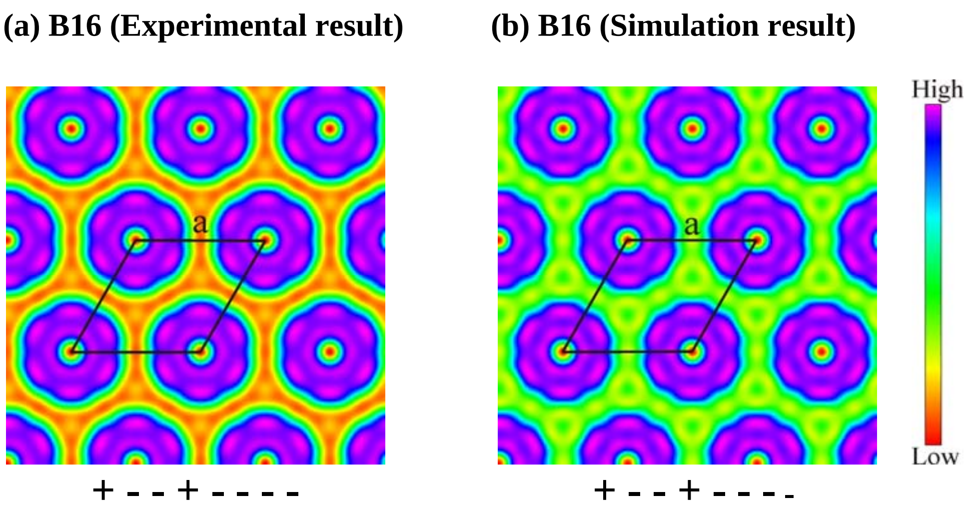
(a) B16 (Experimental result) (b) B16 (Simulation result)

Figure 6-15 2D electron density maps of the Col$_h$ phase of B16, reconstructed on the basis of (a) experimental and (b) simulated diffraction peak intensities.

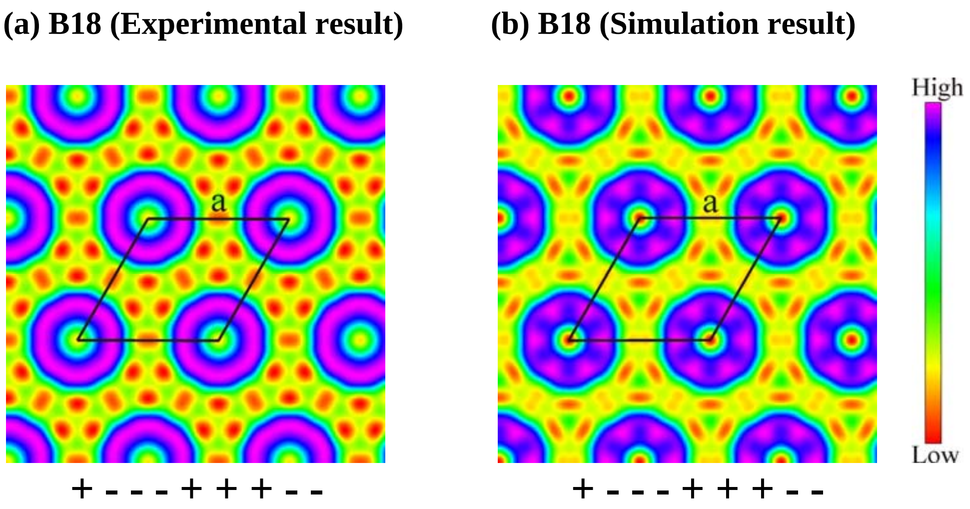
(a) B18 (Experimental result) (b) B18 (Simulation result)

Figure 6-16 2D electron density maps of the Col$_h$ phase of B18, reconstructed on the basis of (a) experimental and (b) simulated diffraction peak intensities.

Figure 6-17a shows 3D electron density maps of B12 reconstructed from experimental intensities of first 7 diffraction peaks and two different phase combinations, i.e. + - - - - - - and + - - + + - -. The phase combinations + - - - - - - and + - - + + - - are obtained from calculating structure factors of diffraction peaks by using the *hhc* model of Percec et al.[16] and our bilayer columns model respectively. According to Figure 6-17b, the electron density map of B12 with phase combination + - - - - - - shows that the electron density at cores of columns (red) is lower than that of the outer aliphatic region (yellow) whereas the electron density in the intermediate area of columns is high (purple). However, if cores of columns are truly empty, electron density at cores of columns should be much lower than that in the outer aliphatic region. The electron density map with phase combination + - - - - - - in fact does not provide a good support to Percec's model that B12 molecules are self-assembled into columns with a hollow core. Our model, in comparison, shows that the electron density at cores of columns is almost the same as that outside of columns.

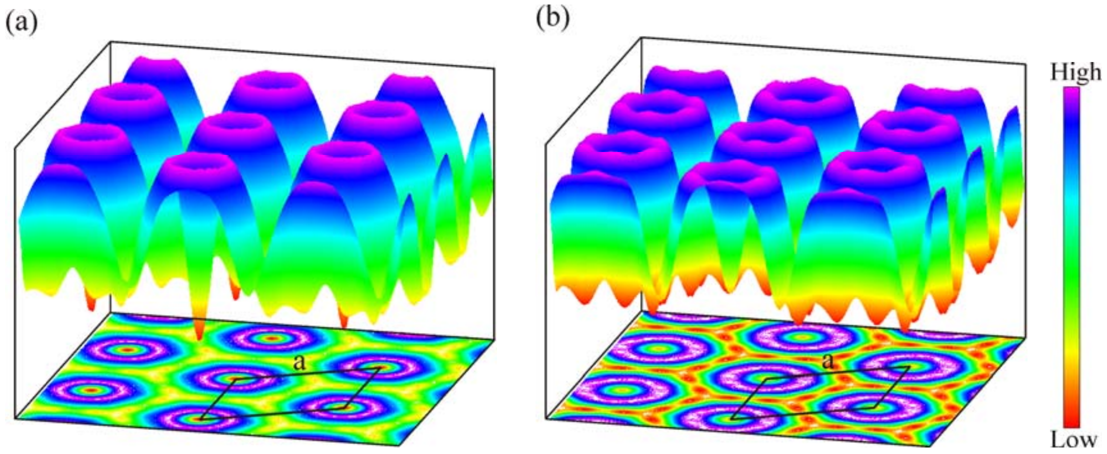

+ - - - - - -

+ - - + + - -

Figure 6-17 A comparison of reconstructed electron density maps obtained from experimental results with the phase combination obtained from (a) hhc model and (b) bilayer column model.

Table 6-3 Powder X-ray diffraction data of the Col_h lattice of Bn where n=12, 14, 16, 18 obtained from the experiments and the simulations.

B12						
nth peak	**q (Å^{-1})**	**Indices**	**Multiplicity**	$\mathbf{I^{exp}}$	$\mathbf{I^{sim}}$	ϕ_{hkl}
1	0.100058	(10)	6	100.00	98.80	0
2	0.17216	(11)	6	93.59	92.17	π
3	0.198131	(20)	6	61.14	63.11	π
4	0.261678	(21)	12	1.06	0.76	0
5	0.295258	(30)	6	1.30	2.60	0
6	0.341055	(22)	6	0.76	1.03	π
7	0.354947	(31)	12	4.23	7.51	π

B12						
nth peak	**q (Å^{-1})**	**Indices**	**Multiplicity**	**I^{exp}**	**I^{sim}**	ϕ_{hkl}
8	0.393679	(40)	6	2.17	9.18	π
9	0.428594	(32)	12	1.76	6.69	π

B14						
nth peak	**q (Å^{-1})**	**Indices**	**Multiplicity**	**I^{exp}**	**I^{sim}**	ϕ_{hkl}
1	0.096481	(10)	6	100.00	99.03	0
2	0.165939	(11)	6	75.62	75.98	π
3	0.191168	(20)	6	55.92	55.37	π
4	0.252289	(21)	12	0.71	0.36	0
5	0.284524	(30)	6	0.45	2.54	0
6	0.329077	(22)	6	1.11	0.50	π
7	0.342428	(31)	12	5.66	5.09	π
8	0.379583	(40)	6	2.44	8.19	π
9	0.4133	(32)	12	1.56	7.86	π

B16						
nth peak	**q (Å^{-1})**	**Indices**	**Multiplicity**	**I^{exp}**	**I^{sim}**	ϕ_{hkl}
1	0.096924	(10)	6	100.00	99.47	0
2	0.167214	(11)	6	62.25	63.51	π
3	0.19272	(20)	6	50.72	48.94	π
4	0.25496	(21)	12	3.02	0.21	0
5	0.333715	(22)	6	1.10	0.34	π
6	0.347154	(31)	12	5.86	4.00	π
7	0.385106	(40)	6	3.09	7.18	π
8	0.419328	(32)	12	2.20	7.44	π

B18						
nth peak	**q (Å^{-1})**	**Indices**	**Multiplicity**	**I^{exp}**	**I^{sim}**	ϕ_{hkl}
1	0.090305	(10)	6	100.00	99.29	0
2	0.155128	(11)	6	39.32	36.15	π
3	0.178721	(20)	6	41.47	44.81	π
4	0.235734	(21)	12	7.37	6.74	π

B18						
nth peak	**q (Å^{-1})**	**Indices**	**Multiplicity**	**I^{exp}**	**I^{sim}**	ϕ_{hkl}
5	0.267106	(30)	6	0.29	0.33	0
6	0.307948	(22)	6	0.74	0.63	0
7	0.3204	(31)	12	4.95	0.22	0
8	0.354972	(40)	6	3.10	1.53	π
9	0.386433	(32)	12	2.10	7.73	π

6.3.6 Molecular dynamics simulation

Molecular dynamics simulation is carried out to confirm the stability of the hexagonal bilayer columnar phase. In the simulation, a 3D structure of columns of B12 is constructed. For simplicity, rather than creating the infinite columns only a single column layer of B12 is constructed. The layer thickness of 4.5 Å, which is the normal average distance between layers of aromatic part of B12, has been chosen. With the density measurement of B12 (1.06 g.cm^{-3}) and calculated *a* lattice parameter of the Col$_h$ unit cell (a_h =72.5 Å), each unit cell contains 15 molecules, two of which turn around in the inverse direction to the other 13 molecules, with their alkyl chains pointing toward the centre of the column. The molecular dynamics simulation is carried out using Materials Studio and the results show that the bilayer structure of columns is indeed stable. Figure 6-18a is a snapshot of the molecular dynamics simulation of B12 viewed down the column axis. The snapshot is also consistent with the reconstructed electron density map of the Col$_h$ phase of B12 as shown in Figure 6-18b.

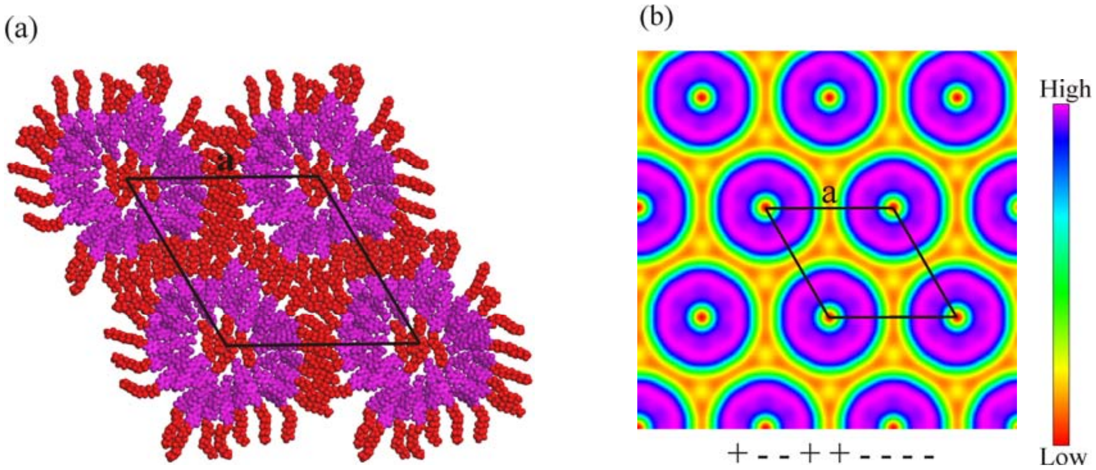

Figure 6-18 (a) Snapshot of molecular dynamics simulation of the columnar structure of B12 viewed down the column axis. Color coding is as follows: red = alkyl chains, purple = aromatic rings. (b) 2D electron density map of the Col$_h$ phase of B12.

6.4 Conclusion

Hybrid dendrons, B12, B14, B16, and B18, are found to self-assemble into columns with a bilayer structure. The bilayer columns model is able to satisfactorily explain the powder diffraction data and it is also supported by the reconstruction of electron density maps of their hexagonal columnar (Col$_h$) phase and the confirmation of stability of the structure from running molecular dynamics simulation. Also, a wiggly lamellar (Lam$_w$) phase is obtained at higher temperatures. A phase transition from the hexagonal columnar phase to the wiggly lamellar phase can be satisfactorily explained by more lateral space demanded by alkyl chains and also the weaker H-bonding between aromatic cores of molecules at higher temperatures.

References

[1] S. Chandrasekhar and G. S. Ranganath, “Discotic liquid crystals”, Rep. Prog. Phys. 1990, 53, 57-84.

[2] H. Meier and M. Lehmann, “Stilbenoid dendrimers”, Angew. Chem. Int. Ed. 1998, 37, 643-645.

[3] H. Meier, M. Lehmann and U. Kolb, “Stilbenoid dendrimers”, Chem. Eur. J. 2000, 6, 2462-2469.

[4] V. Percec, W.D. Cho, P.E. Mosier, G. Ungar and D.J.P. Yeardley, “Structural analysis of cylindrical and spherical supramolecular dendrimers quantifies the concept of monodendron shape control by generation number”, J. Am. Chem. Soc., 1998, 120, 11061-11070.

[5] V. Percec, W. D. Cho and G. Ungar, “Increasing the diameter of cylindrical and spherical supramolecular dendrimers by decreasing the solid angle of their monodendrons via periphery functionalization”, J. Am. Chem. Soc. 2000, 122, 10273-10281.

[6] V. Percec, W.D. Cho, G. Ungar and D.J.P. Yeardley, “From molecular flat tapers, discs and cones to supramolecular cylinders and spheres using Fréchet-type monodendrons modified on the periphery”, Angew. Chem. Int. Ed., 2000, 39, 1597-1602.

[7] V. Percec, W. D. Cho, G. Ungar, D. J. P. Yeardley, “Synthesis and structural analysis of two constitutional isomeric libraries of AB_2-based monodendrons and supramolecular dendrimers”, J. Am. Chem. Soc. 2001, 123, 1302-1315.

[8] V. Percec, M.R. Imam, T.K. Bera, V.S.K. Balagurusamy, M. Peterca and P.A. Heiney, “Self-Assembly of Semifluorinated Janus-Dendritic Benzamides into Bilayered Pyramidal Columns”, Angew. Chem. Int. Ed. 2005, 44, 4739-4745.

[9] V. Percec, M. Glodde, G. Johansson, V.S.K. Balagurusamy and P.A. Heiney, “Transformation of a spherical suprmaolecular dendrimer into a pyramidal columnar supramolecular dendrimer mediated by the fluorophobic effect.”, Angew. Chem. Int. Ed. 2003, 42, 4338-4342.

[10] V. Percec, B. C. Won, M. Peterca, and P. A. Heiney, “Expanding the Structural Diversity of Self-Assembling Dendrons and Supramolecular Dendrimers via Complex Building Blocks”, J. Am. Chem. Soc. 2007, 129, 11265-11278.

[11] M. Peterca, V. Percec, M. R. Imam, P. Leonawat, K. Morimitsu, and P. A. Heiney, “Molecular Structure of Helical Supramolecular Dendrimers”, J. Am. Chem. Soc. 2008, 130, 14840-14852.

[12] V. Percec, M. R. Imam, M. Peterca, D. A. Wilson, R. Graf, H. W. Spiess, V. S. K. Balagurusamy and P. A. Heiney, “Self-Assembly of Dendronized Triphenylenes into Helical Pyramidal Columns and Chiral Spheres”, J. Am. Chem. Soc., 2009, 131, 7662–7677.

[13] V. Percec, J. Smidrkal, M. Peterca, C. M. Mitchell, S. Nummellin, A. E. Dulcey, M. J. Sienkowska, and P. A. Heiney, “Self-Assembling Phenylpropyl Ether Dendronized Helical Polyphenylacetylenes”, Chem. Eur. J. 2007, 13, 3989-4007.

[14] V. Percec, A. E. Dulcey, M. Peterca, M. Ilies, S. Nummelin, M. J. Sienkowska, and P. A. Heiney, “Principles of self-assembly of helical pores from dendritic dipeptides”, Proc. Nat. Acad. Sci. U.S.A. 2006, 103, 2518-2523.

[15] V. Percec, A. E. Dulcey, V. S. K. Balagurusamy, Y. Miura, J. Smidrkal, M. Peterca, S. Nummelin, U. Edlund, S. D. Hudson, P. A. Heiney, H. Duan, S. N. Maganov, S. A. Vinogradov, “Self-assembly of amphiphilic dendritic dipeptides into helical pores”, Nature 2004, 430, 764-768.

[16] M. Peterca, M. R. Imam, P. Leowanawat, B. M. Rosen, D. A. Wilson, C. J. Wilson, X. B. Zeng, G. Ungar, P. A. Heiney, and V. Percec, “Self-assembly of hybrid dendrons into doubly segregated supramolecular polyhedral columns and vesicles”, J. Am. Chem. Soc. 2010, 132, 11288-1305.

[17] V. Percec, M. Peterca, M. J. Sienkowska, M. A. Ilies, E. Aqad, J. Smidrkal, P. A. Heiney, “Synthesis and Retrostructural Analysis of Libraries of AB3 and Constitutional Isomeric AB_2 Phenylpropyl Ether-Based Supramolecular Dendrimers”, J. Am. Chem. Soc. 2006, 128, 3324-3334.

[18]V. Percec, M. N. Holerca, S. Nummellin, J. J. Morrison, M. Glodde, J. Smidrkal, M. Peterca, B. M. Rosen, S. Uchida, V. S. K. Balagurusamy, M. J. Sienkowska, P. A. Heiney, “Exploring and expanding the structural diversity of self-assembling dendrons through combinations of AB, constitutional isomeric AB_2, and AB_3 biphenyl-4-methyl ether building blocks”, Chem. Eur. J. 2006, 12, 6216-6241.

[19] V. Percec, C. M. Mitchell, W. D. Cho, S. Uchida, M. Glodde, G. Ungar, X. B. Xeng et al., “Designing libraries of first generation AB_3 and AB_2 self-assembling dendrons via the primary structure generated from combinations of $(AB)_y$–AB_3 and $(AB)_y$–AB_2 building blocks”, J. Am. Chem. Soc. 2004, 126, 6078-6094.

[20] B. M. Rosen, D. A. Wilson, C. J. Wilson, M. PetercA, B. C. Won, C. H. Huang, L. R. Lipski, X. B. Zeng, G. Ungar, P. A. Heiney, and V. Percec, Predicting the Structure of Supramolecular Dendrimers via the Analysis of Libraries of AB_3 and Constitutional Isomeric AB_2 Biphenylpropyl Ether Self-Assembling Dendrons”, J. Am. Chem. Soc., 2009, 131, 17500–17521.

[21] V. Percec, W. D. Cho, G. Ungar and D. J. P. Yeadly, "Synthesis and structural analysis of two constitutional isomeric libraries of AB_2-based monodendrons and supramolecular dendrimers", J. Am. Chem. Soc. 2001, 123, 1302-1315.

[22] V. Percec, M.N. Holerca, S. Uchida, W.D. Cho, G. Ungar, Y.S. Lee and D.J.P. Yeardley "Exploring and expanding the three-dimensional structural diversity of supramolecular dendrimers with the aid of libraries of alkali metals of their AB_3 minidendritic carboxylates", Chem. Eur. J. 2002, 8, 1106-1117.

[23] V. Percec, M. N. Holerca, S. Nummelin, J. J. Morrison, M. Glodde, J. Smidrkal, M. Peterca, B. M. Rosen, S. Uchida, V. S. K. Balagurusamy, M. J Sienkowska, and P. A. Heiney, "Exploring and expanding the structural diversity of self-assembling dendrons through combinations of AB, cnstitutional isomeric AB_2, and AB_3 biphenyl-4-methyl ether building blocks", Chem. Eur. J. *2*006, 12, 6216-6241.

Summary

Wedge-shaped liquid crystal-forming molecules of 3,4,5-trialkoxygallate alkali metal salts, with two short and one long alkyl chains, are studied in search for close packed micellar phases, which have never been observed before in thermotropic liquid crystals. The longer alkyl chain in the molecules is designed to help fill the octahedral interstices in a structure of close packed spheres. To fill the octahedral interstices even better, various proportions of n-paraffin C_nH_{2n+2} where n= 15, 17, 19, are also added to these dendrons. For comparison, 3,4,5-tridodecyloxygallates, which did not afford the close packed structures, are also studied with varying proportions of added $C_{19}H_{40}$. According to the experimental results of small-angle X-ray diffraction (SAXD) experiments carried out to identify the phase structures at different temperatures, it is found that neither of the pure compounds yields the close packed structures, and it is only in the mixtures of Na or Rb salts with added $C_{19}H_{40}$ which the hexagonal close packed (HCP) phase is obtained, whereas face centred cubic (FCC), known as the cubic close packed structure, is also found in the mixture of Rb salt and n-heptadecane ($C_{17}H_{36}$). These results show that it is possible to achieve the close packed structures in tree-like liquid crystal molecules, if the molecules have a right molecular shape and a sufficient amount of the aliphatic part of molecule to fill octahedral interstices in the close packed structures. In addition, the first order phase transition from the hexagonal columnar phase to another hexagonal columnar phase is also observed in pure compounds of Na salts and their mixtures with added $C_{19}H_{40}$ whereas the hexagonal columnar superlattice is also obtained from the mixtures of Li salt and n-alkane C_nH_{2n+2} (n=15, 17).

For the second subject of this thesis, hybrid dendrons of methyl 3,4-(4′-alkoxy biphenylmethyl-4-yloxy) benzoate, with different lengths of alkyl chains, are studied to search for new structures in thermotropic liquid crystals. The molecular structure of these dendrons is a combination of molecular structures of previously studied benzyl ether based dendrons and biphenyl methyl ether based dendrons. According to the experimental results of SAXD experiments, it is found that these dendrons yield the wiggly lamellar phase, as well as the hexagonal columnar phase of core-shell supramolecular columns. The obtained phase sequence of these hybrid dendrons, i.e. crystal → hexagonal columnar phase → lamellar phase with the

increasing of temperature, is different from that of many previously studied dendrons which the lamellar phase is always observed at lower temperatures than the hexagonal columnar phase. The core-shell structure of supramolecular columns of these dendrons, obtained from the arrangement of molecules in the interdigitated way, is confirmed by the good results of the intensity fitting between experimental intensities and intensities calculated from core-shell models, as well as by reconstructing electron density maps and performing molecular dynamics simulations.

Future works

- Studying the structures of supramolecular columns in the Col_h phase of 12-12-12M+m%$C_{19}H_{40}$ and 12-12-18M+m%$C_{19}H_{40}$ (M= Na, Rb and m=0, 5, 10, 15, 30) by performing wide angle X-ray diffraction (WAXD) experiments of the oriented fibers of such materials.

- Indexing WAXD patterns of 12-12-12M+m%$C_{19}H_{40}$ and 12-12-18M+ m%$C_{19}H_{40}$ to determine the *c* parameters of the Col_h unit cells as well as studying the effect of adding $C_{19}H_{40}$ to 12-12-12M and 12-12-18M on the *c* parameters. With known *c* parameters, the number of 12-12-12M and 12-12-18M molecules per unit cell is recalculated, and these new results would help us understand causes of the Col_h-Col_h phase transition even better.

- Preparing other mixtures of 12-12-18Li and n-paraffin C_nH_{2n+2} (n=15, 17), i.e. at 5% and 10% of C_nH_{2n+2}, and performing small angle X-ray diffraction (SAXD) experiments.

- Studying the structures of supramolecular columns in the Col_h and Col_s phases of 12-12-18Li+m%C_nH_{2n+2} (m=0, 5, 10, 15, 30 and n=15, 17) by performing wide angle X-ray diffraction (WAXD) experiments of the oriented fibers of such materials.

- Indexing WAXD patterns of 12-12-18Li+m%C_nH_{2n+2} to determine the *c* parameters of the Col_h and Col_s unit cells as well as studying the effect of adding alkane to 12-12-18Li on the *c* parameters. With known *c* parameters, the number of 12-12-18Li molecules per unit cell is recalculated, and these new results would help us understand causes of the Col_h-Col_s phase transition even better.

- Constructing the binary phase diagram of 12-12-18Li+m%C_nH_{2n+2} (m=0, 5, 10, 15, 30 and n=15, 17) in order to understand the phase relationship between the Col_h and Col_s phases observed in these binary systems.

Appendix 1

Differential scanning calorimetry (DSC) data for 3,4,5-trialkoxygallate alkali metal salts, 12-12-18M, and binary mixtures 12-12-18M+m%$C_{19}H_{40}$ and 12-12-12M+m%$C_{19}H_{40}$ where M=Na, Rb and m=0, 5, 10, 15, 30. The heating and the cooling rates are 10 °C /minute.

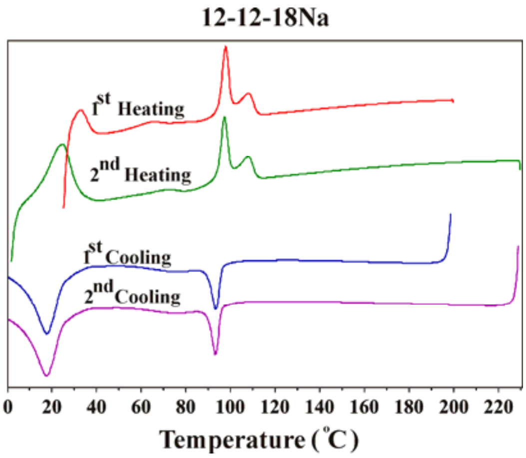

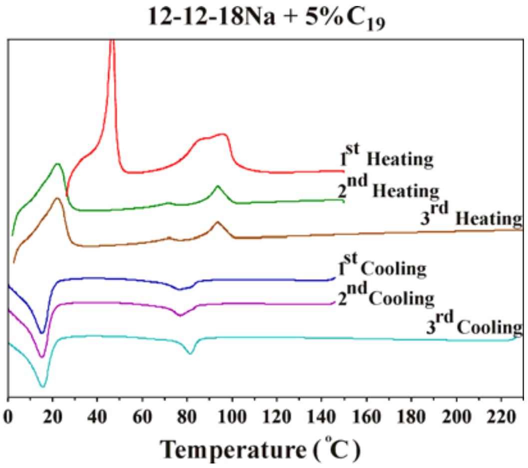

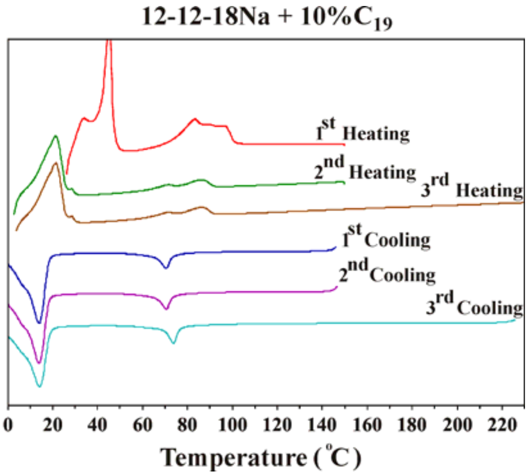

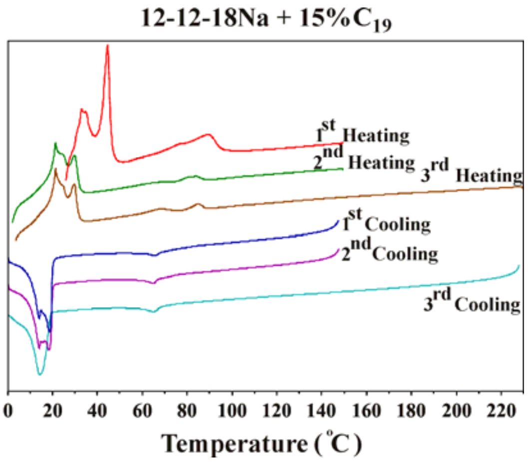

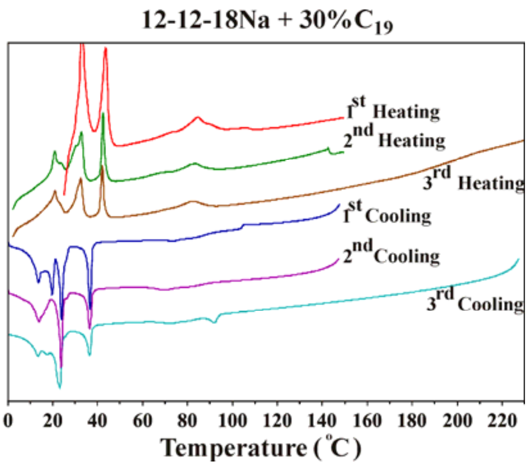

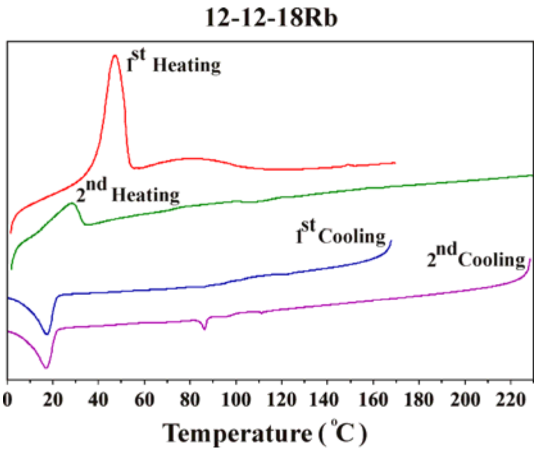

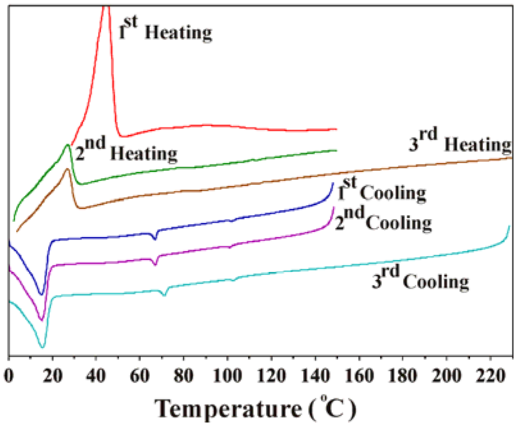
12-12-18Rb + 5%C_{19}

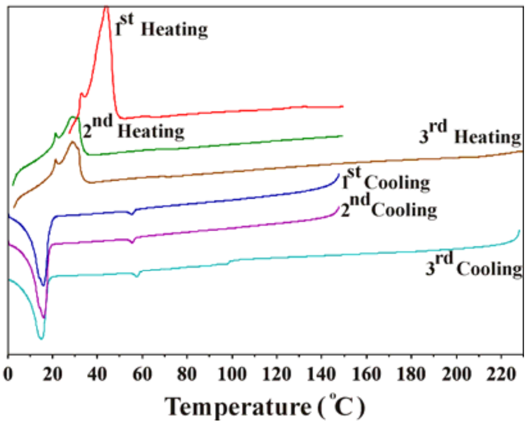
12-12-18Rb + 10%C_{19}

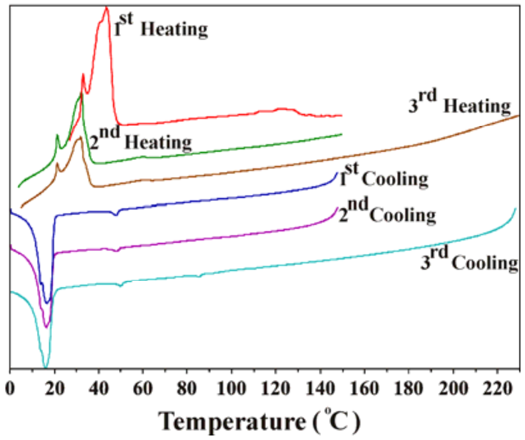
12-12-18Rb + 15%C_{19}

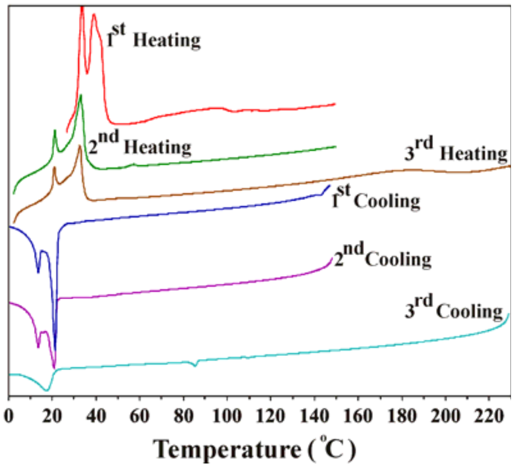
12-12-18Rb + 30%C_{19}

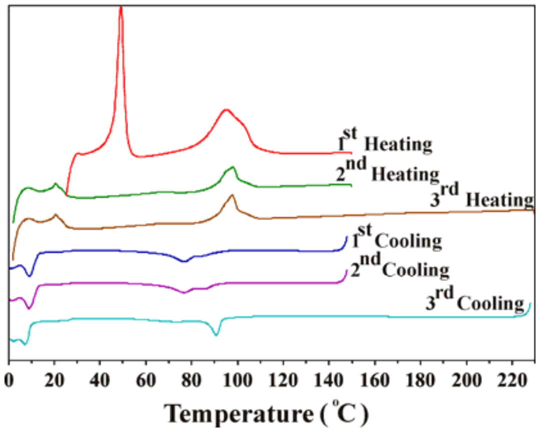
12-12-12Na + 5%C_{19}

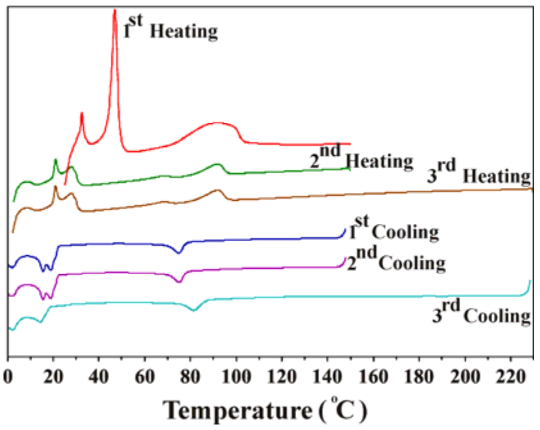
12-12-12Na + 10% C_{19}

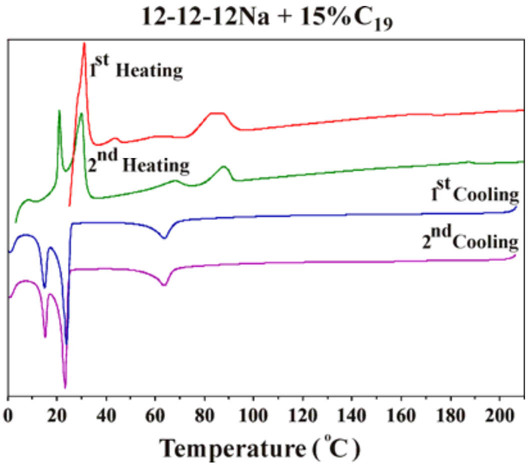
12-12-12Na + 15%C_{19}

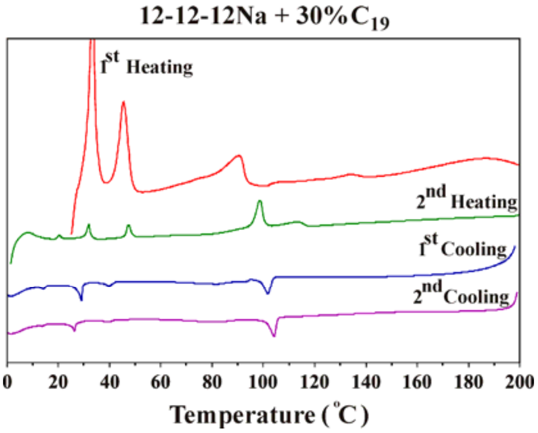
12-12-12Na + 30%C_{19}

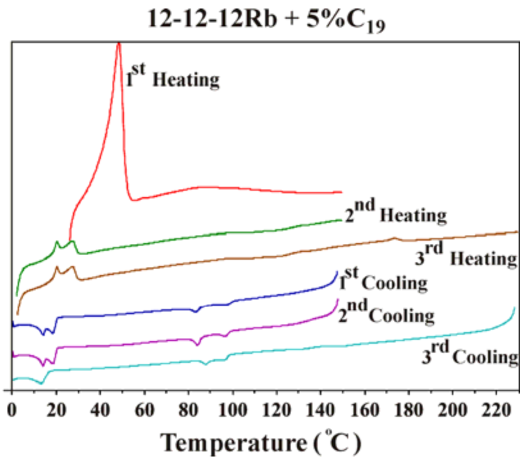
12-12-12Rb + 5%C_{19}

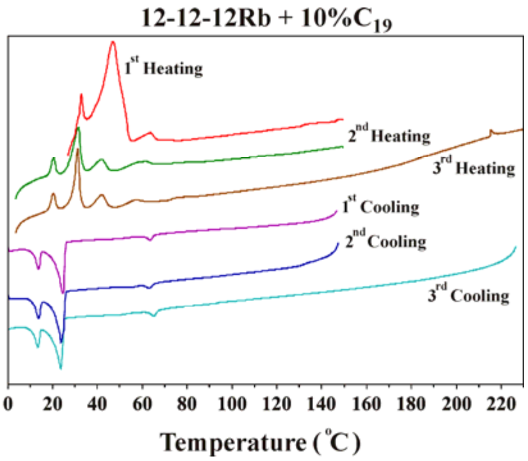
12-12-12Rb + 10%C_{19}

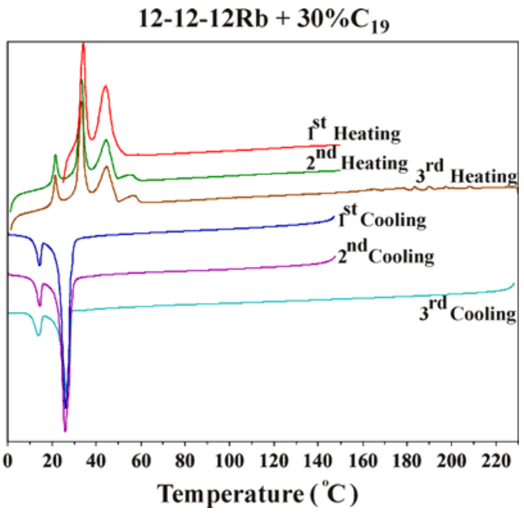
12-12-12Rb + 30%C_{19}

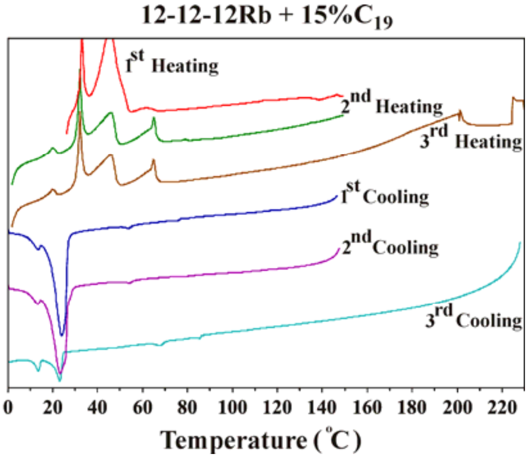
12-12-12Rb + 15%C_{19}

Appendix 2

Measured d-spacings of diffraction peaks at different temperatures for the hexagonal columnar (Col_h) lattice, hexagonal close packed (HCP) lattice, cubic $Pm\overline{3}n$ and body-centred cubic (BCC) lattices formed by 12-12-18M+m%$C_{19}H_{40}$ and 12-12-12M+15%$C_{19}H_{40}$ where M=Na, Rb and m=0, 15.

Materials	**T (°C)**	**Lattice**	**(*hkl*)**	**d_{hk} (Å)**	**a (Å)**	**c (Å)**	**D_{cc}[a] (Å)**	**$\mu^{cal}_{12-12-18Na}$ [b]**
12-12-18Na	56	Col_h1	(10) (11) (20) (21)	36.3 21.0 18.2 13.7	42.0	-	42.0	4.4
	72	Col_h1	(10) (11) (20) (21)	36.3 21.0 18.2 13.8	42.0	-	42.0	4.4
	86	Col_h1	(10) (11) (20) (21)	34.2 21.0 18.2 13.8	41.9	-	41.9	4.3
	90	Col_h2	(10) (11) (20)	34.5 20.0 17.3	39.9	-	39.9	4.1
	97	Col_h2	(10) (11) (20)	33.0 19.1 16.6	38.2	-	38.2	3.8
	105	BCC	(110) (200) (211)	29.7 21.1 17.2	42.1	-	36.5	29.3
	125	BCC	(110) (200) (211)	29.6 21.0 17.2	42.0	-	36.4	29.1
12-12-18Na+15%C_{19}	45	Col_h	(10) (11)	38.5 22.3	44.5	-	44.5	4.1
	65	Col_h	(10) (11)	38.1 22.1	44.0	-	44.0	4.0
	85	BCC	(110) (200) (211)	32.1 22.7 18.6	45.3	-	39.3	29.4
	105	BCC	(110) (200) (211)	31.8 22.5 18.4	44.9	-	38.9	28.5

Materials	**T (°C)**	**Lattice**	**(*hkl*)**	**d_{hk} (Å)**	***a* (Å)**	***c* (Å)**	**D_{cc}[a] (Å)**	**$\mu^{cal}_{12-12-18M}$ [b]**
12-12-18Na+15%C_{19}	125	BCC	(110) (200) (211)	31.6 22.3 18.3	44.7	-	38.7	28.1
12-12-18Rb	50	Col_h	(10) (11) (20)	35.7 20.7 17.9	41.3	-	41.3	4.7
	62	Col_h	(10) (11) (20)	34.8 20.2 17.4	40.3	-	40.3	4.5
	76	Col_h	(10) (11) (20)	34.0 19.7 17.1	39.4	-	39.4	4.3
	86.5	$Pm\bar{3}n$	(200) (210) (211) (220) (310) (222) (320) (312) (400)	36.2 32.5 29.6 25.7 - 21.0 20.2 19.5 18.3	72.8	-	36.4	35.1
	100.5	$Pm\bar{3}n$	(200) (210) (211) (220) (310) (222) (320) (312) (400)	35.8 32.0 29.3 25.4 22.7 20.7 19.9 19.2 18.0	71.9	-	36.0	33.8
	114.5	$Pm\bar{3}n$	(200) (210) (211) (220) (310) (222) (320) (312) (400)	35.3 31.6 28.8 25.0 - 20.5 19.7 18.9 17.7	70.8	-	35.4	32.3
	129.5	$Pm\bar{3}n$	(200) (210) (211) (220) (310) (222) (320) (312) (400)	34.8 31.2 28.4 24.7 - 20.2 19.3 18.6 17.5	69.8	-	34.9	30.9
	155	BCC	(110) (200) (211)	30.3 21.5 17.6	42.9	-	37.1	28.7

Materials	**T (°C)**	**Lattice**	**(*hkl*)**	**d_{hk} (Å)**	**a (Å)**	**c (Å)**	**D_{cc}[a] (Å)**	**$\mu^{cal}_{12-12-18Rb}$ [b]**
12-12-18Rb	176	BCC	(110) (200) (211)	29.9 21.2 17.3	42.3	-	36.6	27.5
	197	BCC	(110) (200) (211)	29.6 21.0 17.1	41.8	-	36.2	26.6
	215	BCC	(110) (200) (211)	29.3 20.9 17.0	41.5	-	35.9	26.0
12-12-18Rb+15%C_{19}	47.5	HCP	$(10\bar{1}0)$ (0002) $(10\bar{1}1)$ $(10\bar{1}2)$ $(11\bar{2}0)$ $(10\bar{1}3)$ $(11\bar{2}2)$	40.1 37.6 35.7 27.6 23.3 -	46.3	75.1	46.2	41.1
	57.5	HCP	$(10\bar{1}0)$ (0002) $(10\bar{1}1)$ $(10\bar{1}2)$ $(11\bar{2}0)$ $(10\bar{1}3)$ $(11\bar{2}2)$	38.7 36.4 34.3 26.7 22.5 - -	44.7	72.8	44.7	41.0
	62.5	HCP	$(10\bar{1}0)$ (0002) $(10\bar{1}1)$ $(10\bar{1}2)$ $(11\bar{2}0)$ $(10\bar{1}3)$ $(11\bar{2}2)$	38.3 36.1 34.2 26.4 22.2 - -	44.2	72.1	44.2	41.0
	44	BCC	(110) (200) (211)	36.9 26.2 21.7	52.8	45.7	45.7	43.4
	54	BCC	(110) (200) (211)	35.2 25.0 20.4	50.0	43.3	43.3	36.8
	64	BCC	(110) (200) (211)	34.5 24.5 20.0	49.0	42.4	42.4	34.6

Materials	**T (°C)**	**Lattice**	**(*hkl*)**	**d_{hk} (Å)**	**a (Å)**	**c (Å)**	**D_{cc}[a] (Å)**	**$\mu^{cal}_{12-12-12Na}$ [b]**
12-12-12Na+15%C_{19}	49	Col_h	(10) (11) (20)	35.1 20.3 -	40.6	-	40.6	4.4
	59	Col_h	(10) (11) (20)	35.1 20.3 -	40.5	-	40.5	4.4
	69	Col_h	(10) (11) (20)	35.0 20.2 -	40.4	-	40.4	4.4
	79	Col_h	(10) (11) (20)	34.8 20.1 -	40.2	-	40.2	4.3
	102	HCP	$(10\bar{1}0)$ (0002) $(10\bar{1}1)$ $(10\bar{1}2)$ $(11\bar{2}0)$ $(10\bar{1}3)$ $(11\bar{2}2)$	33.3 31.4 29.4 22.9 19.3 17.8 -	38.4	62.8	38.4	28.3
	122	HCP	$(10\bar{1}0)$ (0002) $(10\bar{1}1)$ $(10\bar{1}2)$ $(11\bar{2}0)$ $(10\bar{1}3)$ $(11\bar{2}2)$	33.1 31.3 29.3 22.7 19.1 17.7 -	38.2	62.5	38.2	28.2
	142	HCP	$(10\bar{1}0)$ (0002) $(10\bar{1}1)$ $(10\bar{1}2)$ $(11\bar{2}0)$ $(10\bar{1}3)$ $(11\bar{2}2)$	32.9 31.1 29.1 22.6 19.0 17.6 -	38.0	62.2	38.0	28.1

Materials	**T (°C)**	**Lattice**	**(*hkl*)**	**d_{hk} (Å)**	**a (Å)**	**c (Å)**	**D_{cc}[a] (Å)**	**$\mu^{cal\ [b]}_{12-12-12M}$**
12-12-12Na+15%C_{19}	162	HCP	$(10\bar{1}0)$ (0002) $(10\bar{1}1)$ $(10\bar{1}2)$ $(11\bar{2}0)$ $(10\bar{1}3)$ $(11\bar{2}2)$	32.6 30.7 28.7 22.4 18.8 - -	37.6	61.3	37.6	28.0
	182	HCP	$(10\bar{1}0)$ (0002) $(10\bar{1}1)$ $(10\bar{1}2)$ $(11\bar{2}0)$ $(10\bar{1}3)$ $(11\bar{2}2)$	32.0 30.2 29.2 - - - -	37.0	60.3	37.0	27.8
	185	BCC	(110) (200) (211)	29.2 - -	41.2	-	35.7	24.1
	195	BCC	(110) (200) (211)	28.8 - -	40.7	-	35.3	23.2
	205	BCC	(110) (200) (211)	28.6 - -	40.4	-	35.0	22.7
12-12-12Rb+15%C_{19}	63	HCP	$(10\bar{1}0)$ (0002) $(10\bar{1}1)$ $(10\bar{1}2)$ $(11\bar{2}0)$ $(10\bar{1}3)$ $(11\bar{2}2)$	36.6 34.5 32.4 25.2 21.3 19.6 -	42.3	68.9	42.3	37.1
	83	HCP	$(10\bar{1}0)$ (0002) $(10\bar{1}1)$ $(10\bar{1}2)$ $(11\bar{2}0)$ $(10\bar{1}3)$ $(11\bar{2}2)$	35.5 33.3 31.3 24.3 20.6 18.9 -	40.9	66.6	40.9	37.0

Materials	**T (°C)**	**Lattice**	**(*hkl*)**	**d_{hk} (Å)**	**a (Å)**	**c (Å)**	**D_{cc}[a] (Å)**	**$\mu^{cal}_{12-12-12Rb}$ [b]**
12-12-12Rb+15%C_{19}	103	HCP	$(10\bar{1}0)$ (0002) $(10\bar{1}1)$ $(10\bar{1}2)$ $(11\bar{2}0)$ $(10\bar{1}3)$ $(11\bar{2}2)$	34.8 32.7 30.7 23.8 20.1 18.6 -	40.1	65.3	40.1	36.9

[a] D_{cc} is the centre-to-centre distance between two nearest neighbour supramolecular objects in the unit cell of a given lattice.

Col_h: $D_{cc} = a$

HCP: $D_{cc} = a$ or $0.5\sqrt{3/2}c$

$Pm\bar{3}n$: $D_{cc} = a/2$

BCC: $D_{cc} = \sqrt{3}a/2$

[b] For hexagonal columnar lattice, the number of molecules of 12-12-18M (or 12-12-12M) and $C_{19}H_{40}$ per column layer =

$$\mu^{cal}_{obj} = \mu^{cal}_{12\text{-}12\text{-}18M} + \mu^{cal}_{C19H40}$$

$$\mu^{cal}_{12\text{-}12\text{-}18M} = \frac{\sqrt{3}N_A a^2 l}{2.\left(\frac{M_{12\text{-}12\text{-}18M}}{\rho_{12\text{-}12\text{-}18M}} + \left(\frac{m_{C19H40}.M_{12\text{-}12\text{-}18M}}{m_{12\text{-}12\text{-}18M}.M_{C19H40}}\right).\frac{M_{C19H40}}{\rho_{C19H40}}\right)}$$

$$\mu^{cal}_{C19H40} = \left(\frac{m_{C19H40}.M_{12\text{-}12\text{-}18M}}{m_{12\text{-}12\text{-}18M}.M_{C19H40}}\right).\mu^{cal}_{12\text{-}12\text{-}18M}$$

For cubic lattices, the number of molecules of 12-12-18M (or 12-12-12M) and $C_{19}H_{40}$ per micelle =

$$\mu^{cal}_{obj} = \mu^{cal}_{12\text{-}12\text{-}18M} + \mu^{cal}_{C19H40}$$

BCC:
$$\mu^{cal}_{12\text{-}12\text{-}18M} = \frac{N_A a^3}{2.\left(\frac{M_{12\text{-}12\text{-}18M}}{\rho_{12\text{-}12\text{-}18M}} + \left(\frac{m_{C19H40}.M_{12\text{-}12\text{-}18M}}{m_{12\text{-}12\text{-}18M}.M_{C19H40}}\right).\frac{M_{C19H40}}{\rho_{C19H40}}\right)}$$

$Pm\bar{3}n$:
$$\mu^{cal}_{12\text{-}12\text{-}18M} = \frac{N_A a^3}{8.\left(\frac{M_{12\text{-}12\text{-}18M}}{\rho_{12\text{-}12\text{-}18M}} + \left(\frac{m_{C19H40}.M_{12\text{-}12\text{-}18M}}{m_{12\text{-}12\text{-}18M}.M_{C19H40}}\right).\frac{M_{C19H40}}{\rho_{C19H40}}\right)}$$

$$\mu_{C19H40}^{cal} = \left(\frac{m_{C19H40} . M_{12\text{-}12\text{-}18M}}{m_{12\text{-}12\text{-}18M} . M_{C19H40}} \right) . \mu_{12\text{-}12\text{-}18M}^{cal}$$

For HCP lattice, the number of molecules of 12-12-18M (or 12-12-12M) and $C_{19}H_{40}$ per micelle =

$$\mu_{obj}^{cal} = \mu_{12\text{-}12\text{-}18M}^{cal} + \mu_{C19H\,40}^{cal}$$

$$\mu_{12\text{-}12\text{-}18M}^{cal} = \frac{\sqrt{3} N_A a^2 c}{4.\left(\frac{M_{12\text{-}12\text{-}18M}}{\rho_{12\text{-}12\text{-}18M}} + \left(\frac{m_{C19H40} . M_{12\text{-}12\text{-}18M}}{m_{12\text{-}12\text{-}18M} . M_{C19H40}} \right) . \frac{M_{C19H40}}{\rho_{C19H40}} \right)}$$

$$\mu_{C19H40}^{cal} = \left(\frac{m_{C19H40} . M_{12\text{-}12\text{-}18M}}{m_{12\text{-}12\text{-}18M} . M_{C19H40}} \right) . \mu_{12\text{-}12\text{-}18M}^{cal}$$

(Avogadro's number $N_A = 6.022 \times 10^{23}\ mol^{-1}$, l=column layer thickness, $\rho_{12\text{-}12\text{-}18M} =$ the density of 12-12-18M, $\rho_{C19H40} =$ the density of n-nonadecane $C_{19}H_{40}$, $M_{12\text{-}12\text{-}18M} =$ molecular weight of 12-12-18M, $M_{C19H40} =$ molecular weight of n-nonadecane $C_{19}H_{40}$). a and c are unit cell parameters. The density of n-nonadecane $C_{19}H_{40}$[1] is equal to 0.7752-0.000660*(T-35) g/cm^3 where T is temperature. The densities of 12-12-18M and 12-12-12M are assumed to be 1.02 g/cm^3 and 1.01 g/cm^3 respectively. The values of column layer thickness of 12-12-18M, 12-12-12M and their mixtures, used in the calculation of the number of salt molecules per column layer, are given in Table A1. According to Table A1, the values of column layer thickness of 12-12-18Na and 12-12-18Na+15%$C_{19}H_{40}$ are obtained from wide-angle X-ray diffraction (WAXD) data whereas those of 12-12-18Rb, 12-12-12Na, 12-12-12Rb and their mixtures are obtained from Material Studio program, based on the assumption that those salts molecules are not tilted.

Table A1 The values of column layer thickness of 12-12-12M+m%$C_{19}H_{40}$ and 12-12-18M+m%$C_{19}H_{40}$ (M=Na, Rb and m=0, 5, 10, 15, 30) used in the calcualtion of the number of salt molecules per column layer.

Materials	**Temperature** (°C)	**Phase**	**Column layer thickness (Å)**
12-12-18Na	50-60	$\mathrm{Col_h}1$	3.73
	62-78	$\mathrm{Col_h}1$	3.74

Materials	**Temperature** (°C)	**Phase**	**Column layer thickness (Å)**
12-12-18Na	80-84 86 87-94 95-101	Col_h1 Col_h1 Col_h2 Col_h2	3.75 3.82 3.97 3.98
12-12-18Na+5%C_{19}	48-74 76 77 78-93	Col_h1 Col_h1 Col_h1 Col_h2	3.73 3.79 3.87 3.97
12-12-18Na+10%C_{19}	46-76 77-89	Col_h1 Col_h2	3.73 3.76
12-12-18Na+15%C_{19}	43-61 63-65 67-69 71-79	Col_h Col_h Col_h Col_h	3.73 3.74 3.75 3.76
12-12-18Na+30%C_{19}	43-79	Col_h	3.73
12-12-18Rb+m%C_{19} m=0, 5	all temperatures	Col_h	4.40
12-12-12Na+m%C_{19} m=0, 5, 10, 15, 30	all temperatures	Col_h1 & Col_h2	4.40 4.40
12-12-12Rb+m%C_{19} m=0, 5, 10	all temperatures	Col_h	4.40

[1] L. T. Chu, C. Sindilariua, A. Freilicha, and V. Fried, “Some physical properties of long chain hydrocarbons”, Can. J. Chem., 64, 1986, 481-483.

Appendix 3

Electron density maps and corresponding histograms of electron density distribution, based on calculations of electron density using different phase angle combinations, for the HCP lattice of 12-12-12M+15%$C_{19}H_{40}$, where M=Na and Rb. For each phase angle combination, the electron density map and the electron density contour of the clipping plane on which the centre of the octahedral interstice in the HCP structure is located are also shown.

(a) 12-12-12Na+15%C_{19}

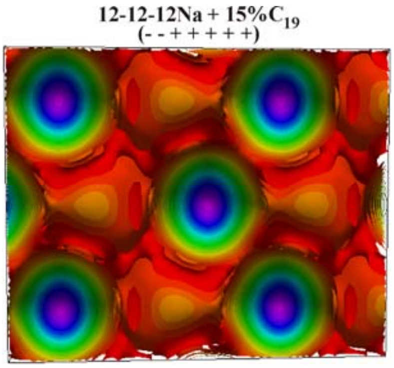

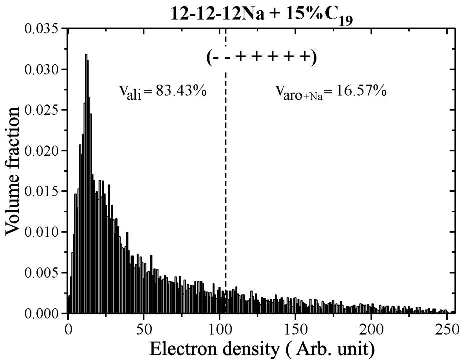

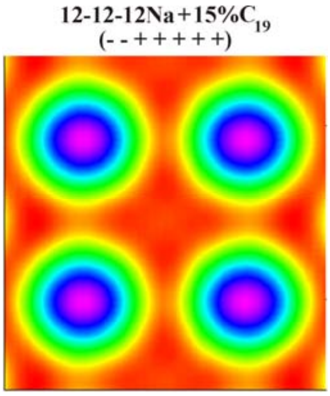

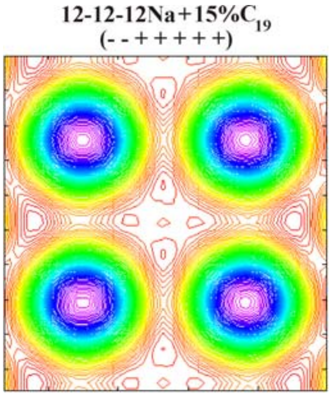

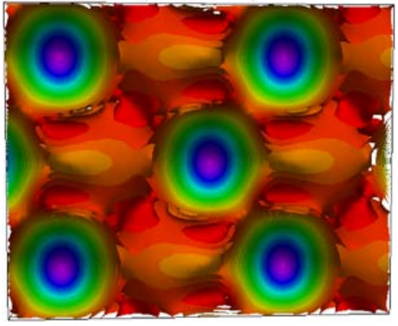
12-12-12Na + 15%C_{19}
(- - + + + + -)

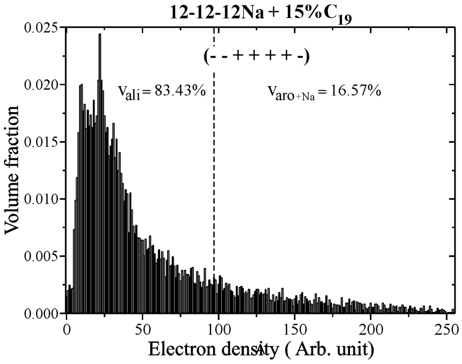
12-12-12Na + 15%C_{19}

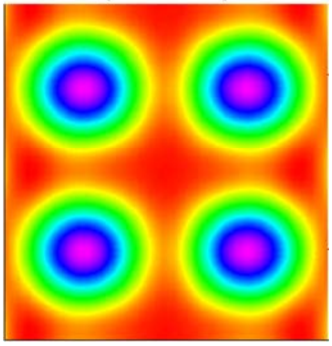
12-12-12Na+15%C_{19}
(- - + + + + -)

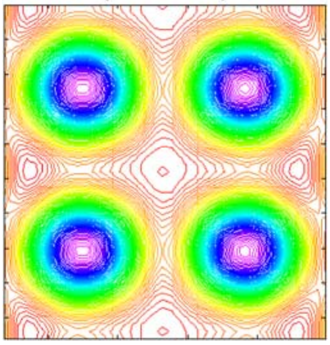
12-12-12Na+15%C_{19}
(- - + + + + -)

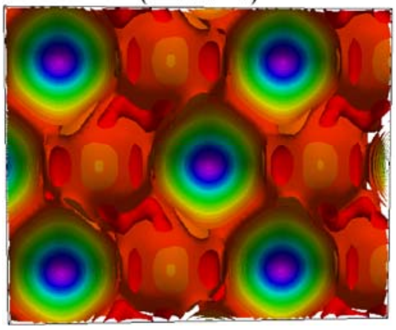
12-12-12Na + 15%C_{19}
(- - + + + - +)

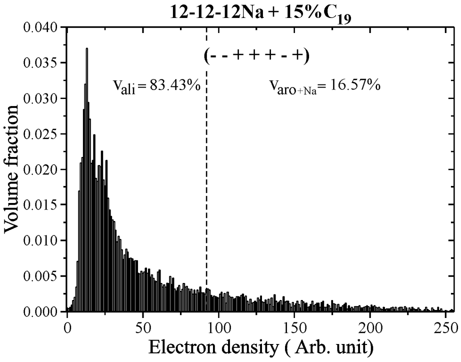
12-12-12Na + 15%C_{19}

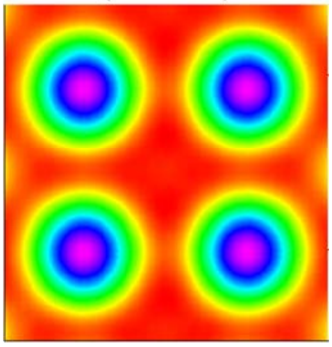
12-12-12Na+15%C_{19}
(- - + + + - +)

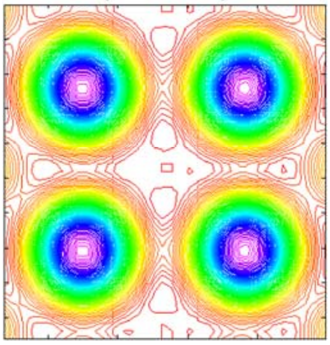
12-12-12Na+15%C_{19}
(- - + + + - +)

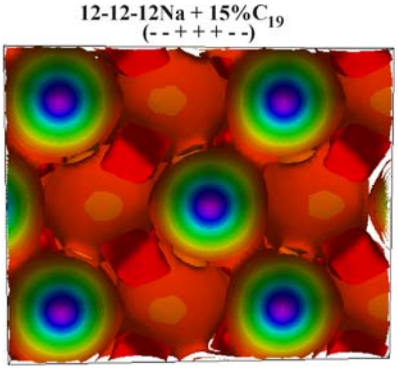
12-12-12Na + 15%C_{19}
(- - + + + - -)

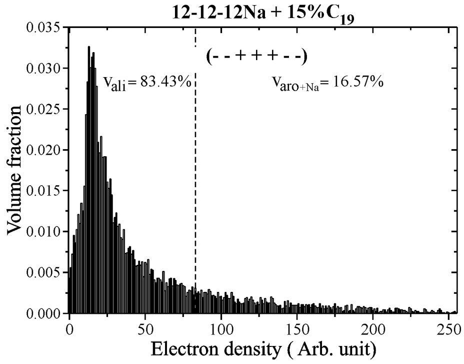
12-12-12Na + 15%C_{19}
(- - + + + - -)
V_{ali} = 83.43%
V_{aro+Na} = 16.57%
Volume fraction
0.000
0.005
0.010
0.015
0.020
0.025
0.030
0.035
0
50
100
150
200
250
Electron density (Arb. unit)

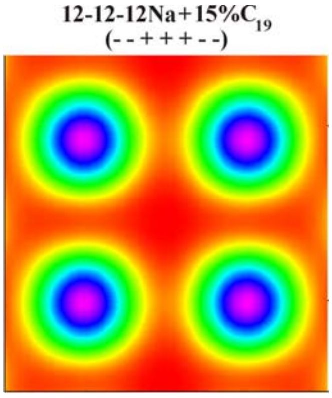
12-12-12Na+15%C_{19}
(- - + + + - -)

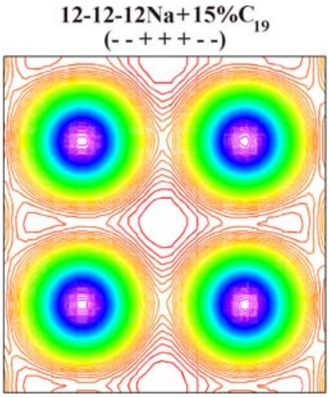
12-12-12Na+15%C_{19}
(- - + + + - -)

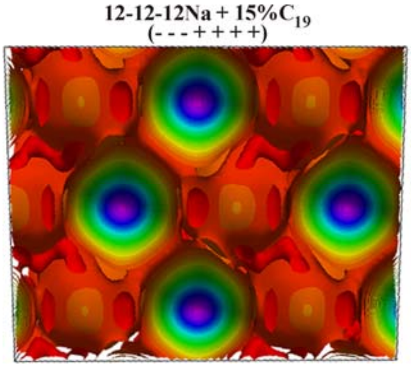
12-12-12Na + 15%C_{19}
(- - - + + + +)

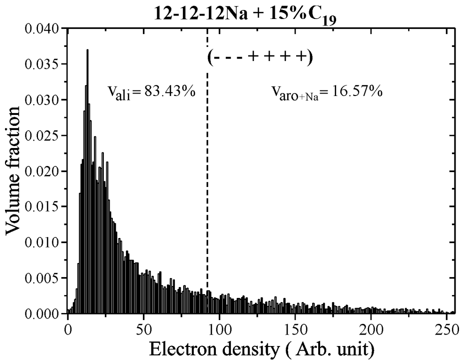
12-12-12Na + 15%C_{19}
(- - - + + + +)
V_{ali} = 83.43%
V_{aro+Na} = 16.57%
Volume fraction
0.000
0.005
0.010
0.015
0.020
0.025
0.030
0.035
0.040
0
50
100
150
200
250
Electron density (Arb. unit)

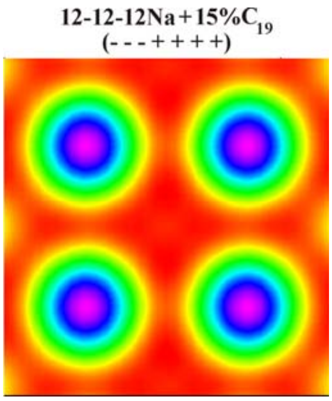
12-12-12Na+15%C_{19}
(- - - + + + +)

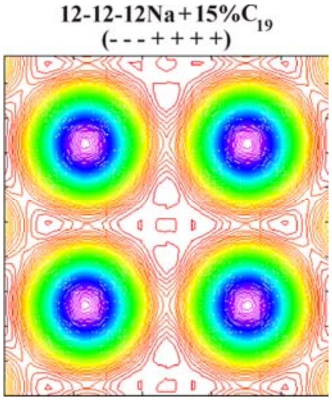
12-12-12Na+15%C_{19}
(- - - + + + +)

12-12-12Na + 15%C_{19}
(- - - + + + -)

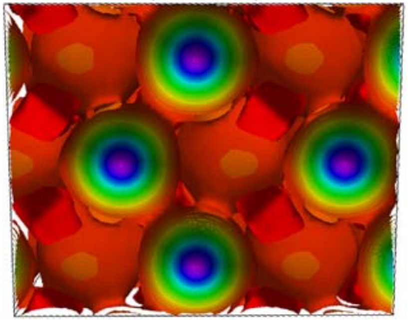

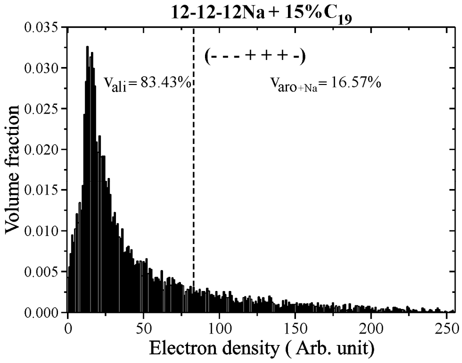

12-12-12Na+15%C_{19}
(- - - + + + -)

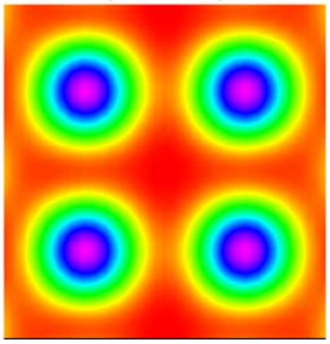

12-12-12Na+15%C_{19}
(- - - + + + -)

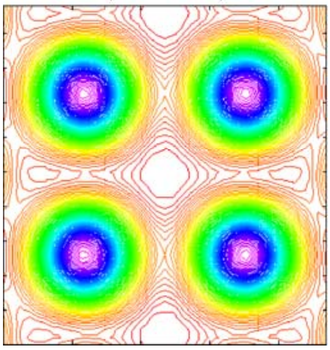

12-12-12Na + 15%C_{19}
(- - - + + - +)

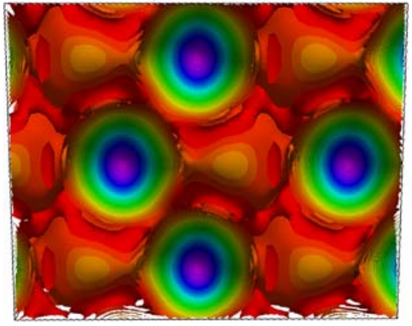

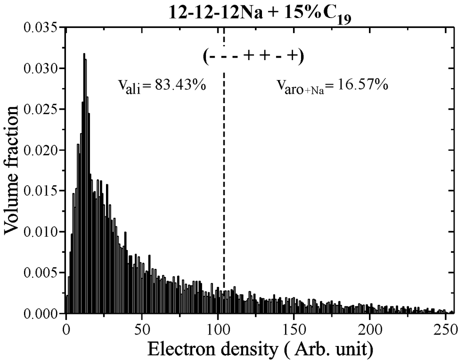

12-12-12Na+15%C_{19}
(- - - + + - +)

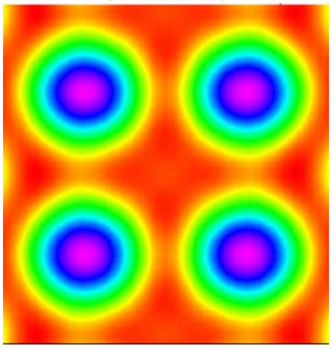

12-12-12Na+15%C_{19}
(- - - + + - +)

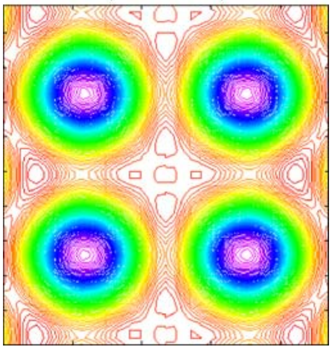

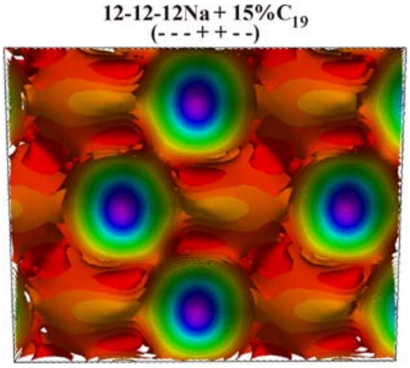
12-12-12Na + 15%C_{19} (- - - + + - -)

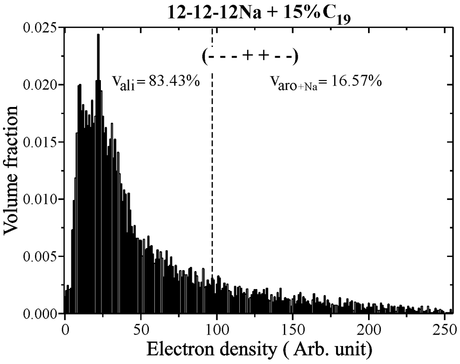
12-12-12Na + 15%C_{19}

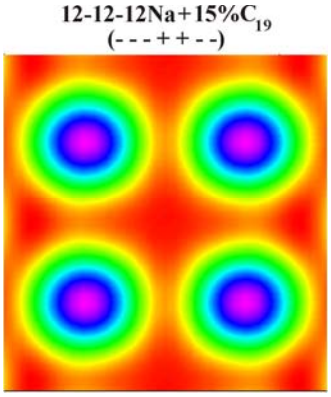
12-12-12Na+15%C_{19} (- - - + + - -)

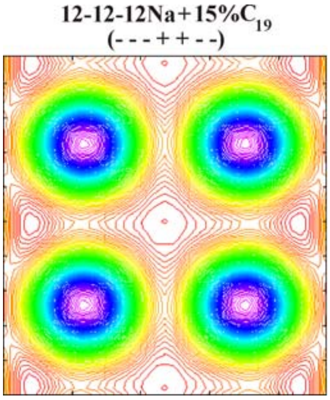
12-12-12Na+15%C_{19} (- - - + + - -)

(b) 12-12-12Rb+15%C_{19}

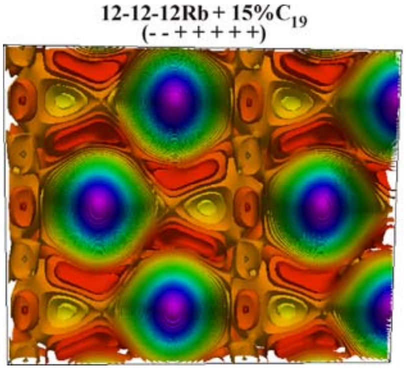
12-12-12Rb + 15%C_{19} (- - + + + + +)

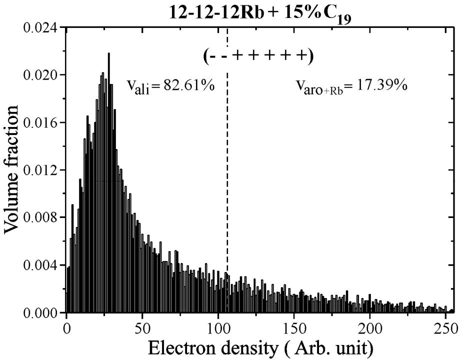
12-12-12Rb + 15%C_{19}

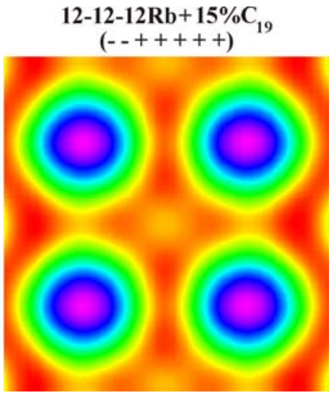
12-12-12Rb+15%C_{19} (- - + + + + +)

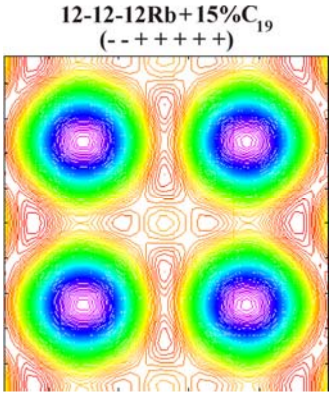
12-12-12Rb+15%C_{19} (- - + + + + +)

12-12-12Rb + 15%C_{19}
(- - + + + + -)

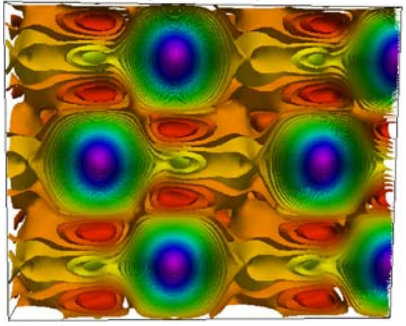

12-12-12Rb + 15%C_{19}

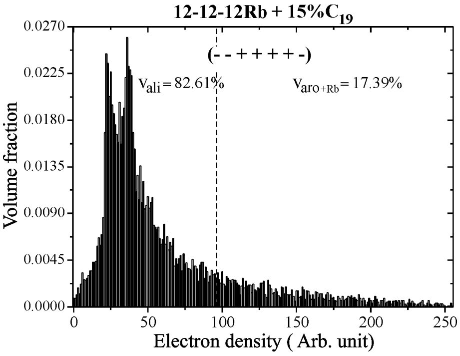

12-12-12Rb+15%C_{19}
(- - + + + + -)

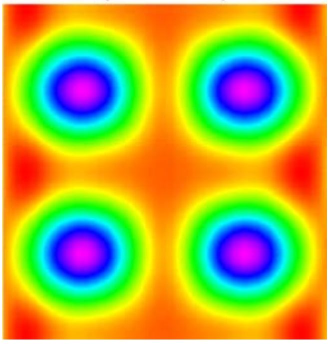

12-12-12Rb+15%C_{19}
(- - + + + + -)

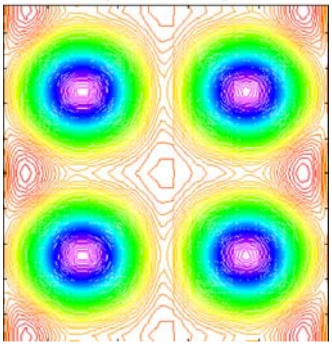

12-12-12Rb+ 15%C_{19}
(- - + + + - +)

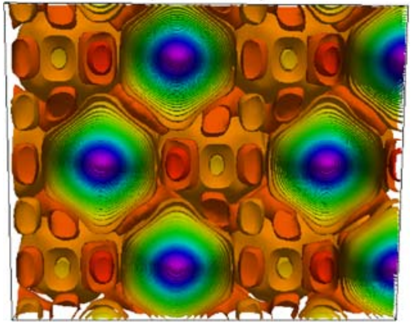

12-12-12Rb + 15%C_{19}

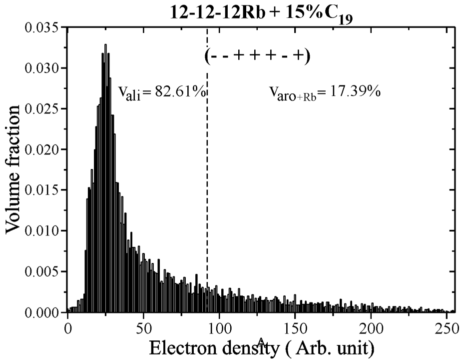

12-12-12Rb+15%C_{19}
(- - + + + - +)

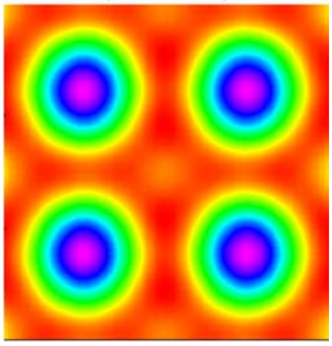

12-12-12Rb+15%C_{19}
(- - + + + - +)

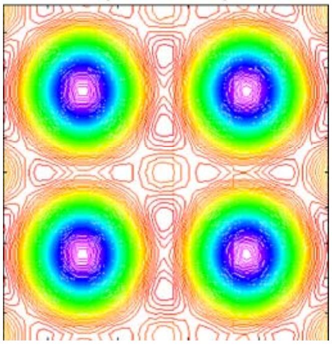

12-12-12Rb + 15%C_{19}
(- - + + + - -)

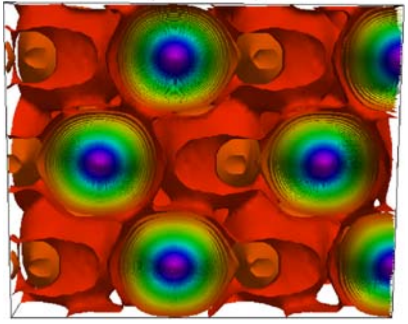

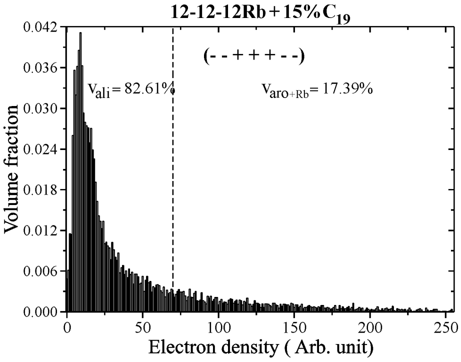

12-12-12Rb + 15%C_{19}
(- - + + + - -)

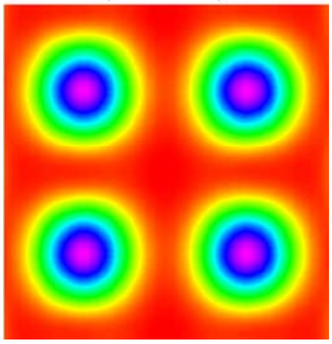

12-12-12Rb + 15%C_{19}
(- - + + + - -)

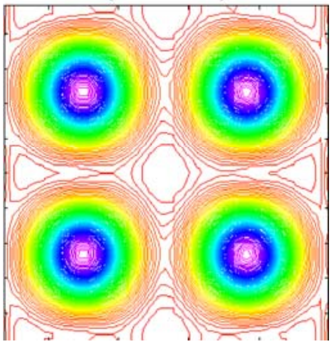

12-12-12Rb + 15%C_{19}
(- - - + + + +)

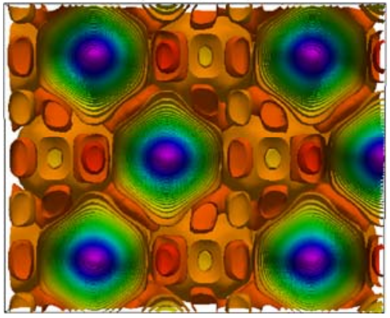

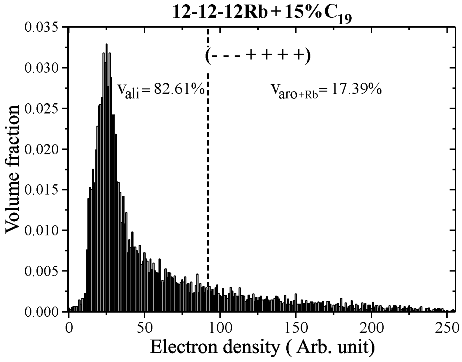

12-12-12Rb + 15%C_{19}
(- - - + + + +)

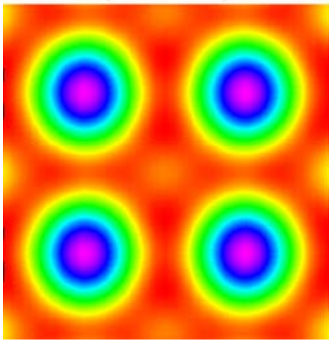

12-12-12Rb + 15%C_{19}
(- - - + + + +)

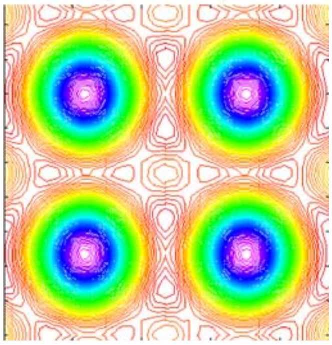

12-12-12Rb + 15%C$_{19}$
(- - - + + + -)

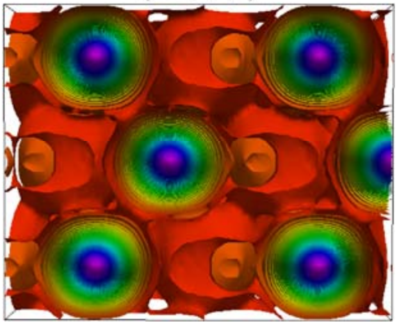

12-12-12Rb + 15%C$_{19}$

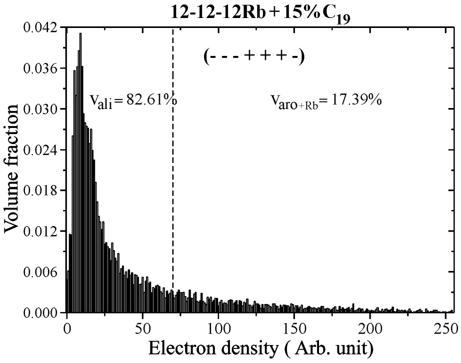

12-12-12Rb + 15%C$_{19}$
(- - - + + + -)

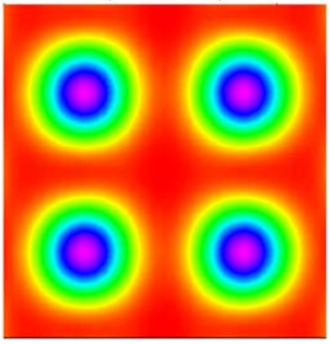

12-12-12Rb + 15%C$_{19}$
(- - - + + + -)

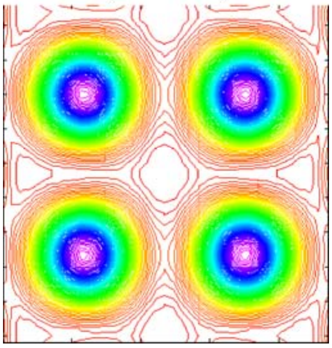

12-12-12Rb + 15%C$_{19}$
(- - - + + - +)

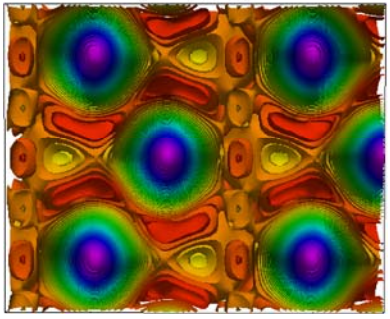

12-12-12Rb + 15%C$_{19}$

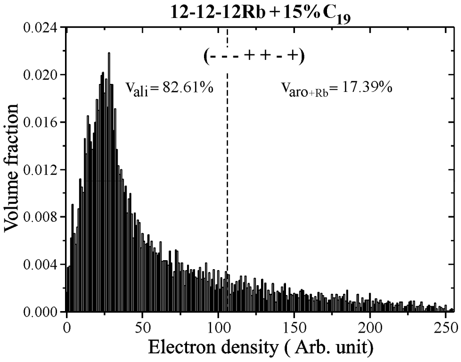

12-12-12Rb + 15%C$_{19}$
(- - - + + - +)

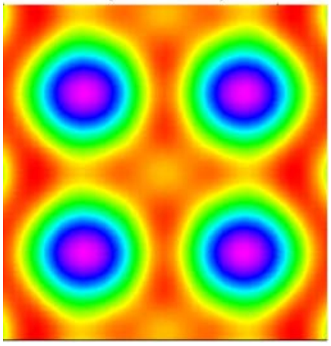

12-12-12Rb + 15%C$_{19}$
(- - - + + - +)

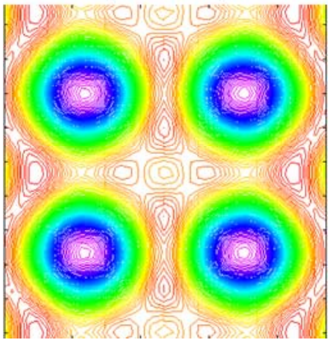

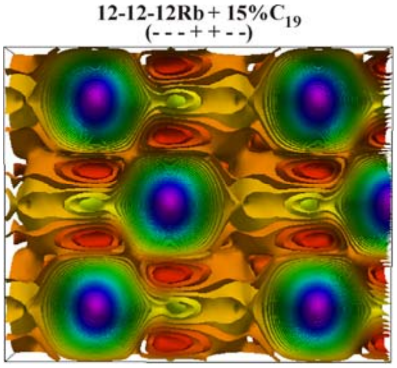

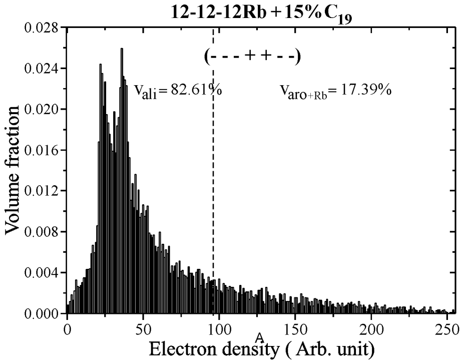

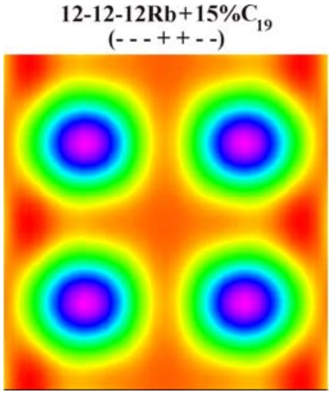

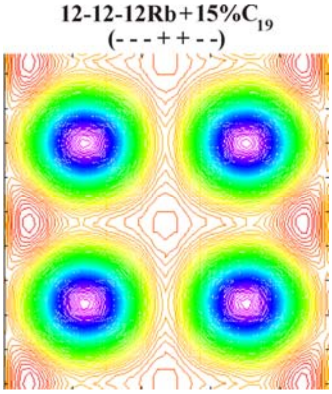

Table A1 Experimental and calculated *d*-spacings, multiplicity factor *p*, relative integrated intensities (I_{hkl}), and preferred phase angle ($\phi_{h,k,l}$) combinations used in reconstructing electron density map of the HCP phase obtained from 12-12-12Na+15%$C_{19}H_{40}$ at 122 °C.

(hkil)	d_{exp} (Å)	d_{cal} (Å)	I_{hkl}	*p*	$\phi_{h,k,l}$
$(10\bar{1}0)$	33.1	33.2	31.08	6	π
(0002)	31.3	31.3	27.47	2	π
$(10\bar{1}1)$	29.2	29.3	100.00	12	0
$(10\bar{1}2)$	22.7	22.7	4.22	12	0
$(11\bar{2}0)$	19.1	19.1	1.39	6	0
$(10\bar{1}3)$	17.7	17.7	0.64	12	π
$(11\bar{2}2)$	16.4	16.3	0.25	12	π
The size of unit cell *a*= 38.3 Å and *c*=62.6 Å. *c/a*=1.634					

Appendix 4

The derivation of equation used for calculating the volume fraction of the aliphatic content of 12-12-12M+m%$C_{19}H_{40}$ where M=Na and Rb.

From
$$\rho = \frac{m}{V} \text{ ....(A4.1)}$$

the ratio between the density of 12-12-12M and that of $C_{19}H_{40}$ can be, therefore, written

$$\frac{\rho_{12\text{-}12\text{-}12M}}{\rho_{C19H40}} = \frac{m_{12\text{-}12\text{-}12M}}{m_{C19H40}} \cdot \frac{V_{C19H40}}{V_{12\text{-}12\text{-}12M}} \text{ ....(A4.2).}$$

From eq. (A4.2), we will obtain

$$V_{C19H40} = \left(\frac{\rho_{12\text{-}12\text{-}12M}}{\rho_{C19H40}} \cdot \frac{m_{C19H40}}{m_{12\text{-}12\text{-}12M}} \right) . V_{12\text{-}12\text{-}12M} \text{ ....(A4.3).}$$

Since
$$V_{tot} = V_{12\text{-}12\text{-}12M} + V_{C19H40} \text{ ....(A4.4)}$$

Substitute (A4.3) in (A4.4), we will obtain

$$V_{tot} = V_{12\text{-}12\text{-}12M} + \left(\frac{\rho_{12\text{-}12\text{-}12M}}{\rho_{C19H40}} \cdot \frac{m_{C19H40}}{m_{12\text{-}12\text{-}12M}} \right) V_{12\text{-}12\text{-}12M} \text{ ....(A4.5)}$$

$$= \left(1 + \frac{\rho_{12\text{-}12\text{-}12M}}{\rho_{C19H40}} \cdot \frac{m_{C19H40}}{m_{12\text{-}12\text{-}12M}} \right) V_{12\text{-}12\text{-}12M} \text{ ....(A4.6)}$$

Equation (A4.6) can be rearranged to

$$v_{12-12-12M} = \frac{V_{12\text{-}12\text{-}12M}}{V_{tot}} = \frac{1}{\left(1 + \frac{\rho_{12\text{-}12\text{-}12M}}{\rho_{C19H40}} \cdot \frac{m_{C19H40}}{m_{12\text{-}12\text{-}12M}} \right)} \text{ ....(A4.7)}$$

Note that $v_{12-12-12M}$ is the volume fraction of 12-12-12M in 12-12-12M+m%C_{19}.

From Eq. (A4.1), the density of the mixture can be expressed as

$$\rho_{mixture} . V_{tot} = m_{mixture} \text{ ....(A4.8)}$$

$$\rho_{mixture}.V_{tot} = m_{C19H40} + m_{12\text{-}12\text{-}12M} \quad \text{..(A4.9)}$$

$$= \rho_{C19H40}.V_{C19H40} + \rho_{12\text{-}12\text{-}12M}.V_{12\text{-}12\text{-}12M} \quad \text{..........................(A4.10).}$$

From eq. (A4.4) and (A4.10) , therefore, we will obtain

$$\rho_{mixture}.V_{tot} = \rho_{C19H40}.(V_{tot} - V_{12\text{-}12\text{-}12M}) + \rho_{12\text{-}12\text{-}12M}.V_{12\text{-}12\text{-}12M} \quad \text{........................ ...(A4.11)}$$

$$= \rho_{C19H40}.V_{tot} + V_{12\text{-}12\text{-}12M}(\rho_{12\text{-}12\text{-}12M} - \rho_{C19H40}) \quad \text{..............................(A4.12)}$$

Therefore,

$$\rho_{mixture} = \rho_{C19H40} + v_{12\text{-}12\text{-}12M}(\rho_{12\text{-}12\text{-}12M} - \rho_{C19H40}) \quad \text{.....................................(A4.13)}$$

Substitute (A4.7) in (A4.13), we will obtain

$$\rho_{mixture} = \rho_{C19H40} + \frac{\left(\rho_{12\text{-}12\text{-}12M} - \rho_{C19H40}\right)}{\left(1 + \frac{\rho_{12\text{-}12\text{-}12M}}{\rho_{C19H40}}.\frac{m_{C19H40}}{m_{12\text{-}12\text{-}12M}}\right)} \quad \text{.......................................(A4.14).}$$

Since

$$v_{dodecyl} + v_{aromatic+M} = 1 \quad \text{..(A4.15)}$$

where $v_{dodecyl} = \frac{V_{dodecyl}}{V_{12\text{-}12\text{-}12M}}$ and $v_{aromatic+M} = \frac{V_{aromatic+M}}{V_{12\text{-}12\text{-}12M}}$, multiplying $v_{12\text{-}12\text{-}12M}$ to the equation (A4.15), we will obtain

$$v_{dodecyl}.v_{12\text{-}12\text{-}12M} + v_{aromatic+M}.v_{12\text{-}12\text{-}12M} = v_{12\text{-}12\text{-}12M} \quad \text{............................(A4.16)}$$

Since

$$v_{C19H40} + v_{12\text{-}12\text{-}12M} = 1 \quad \text{..(A4.17)}$$

Substitute (A4.16) in (A4.17), we will obtain

$$v_{C19H40} + (v_{dodecyl}.v_{12\text{-}12\text{-}12M} + v_{aromatic+M}.v_{12\text{-}12\text{-}12M}) = 1 \quad \text{..........................(A4.18)}$$

Let $v_{ali} \equiv v_{C19H40} + (v_{dodecyl}.v_{12\text{-}12\text{-}12M})$

$v_{aro+M} \equiv v_{aromatic+M}.v_{12\text{-}12\text{-}12M}$

from equation (A4.18), therefore, we will obtain

$$v_{ali} + v_{aro+M} = 1 \quad \text{..(A4.19)}$$

and $$v_{ali} = 1 - v_{12\text{-}12\text{-}12M} + v_{dodecyl} . v_{12\text{-}12\text{-}12M} \quad \text{.......................................(A4.20)}$$

Substitute (A4.7) in (A4.20), we will obtain

$$v_{ali} = 1 - \frac{1}{\left(1 + \frac{\rho_{12\text{-}12\text{-}12M}}{\rho_{C19H40}} . \frac{m_{C19H40}}{m_{12\text{-}12\text{-}12M}}\right)} + \frac{v_{dodecyl}}{\left(1 + \frac{\rho_{12\text{-}12\text{-}12M}}{\rho_{C19H40}} . \frac{m_{C19H40}}{m_{12\text{-}12\text{-}12M}}\right)} \quad \text{.....................(A4.21)}$$

$$v_{ali} = 1 + \frac{v_{dodecyl} - 1}{\left(1 + \frac{\rho_{12\text{-}12\text{-}12M}}{\rho_{C19H40}} . \frac{m_{C19H40}}{m_{12\text{-}12\text{-}12M}}\right)} \quad \text{..(A4.22).}$$

Note that v_{ali} is the fraction of volume in the mixture of 12-12-12M+m%$C_{19}H_{40}$ which is taken by $C_{19}H_{40}$ and dodecyl chains of 12-12-12M.

$m_{12\text{-}12\text{-}12M}$ = the mass of 12-12-12M

$m_{C_{19}H_{40}}$ = the mass of $C_{19}H_{40}$

$\rho_{mixture}$ = the density of mixture

$\rho_{12\text{-}12\text{-}12M}$ = the density of 12-12-12M, where M=Na and Rb (i.e. 1 g/cm^3)

$\rho_{C_{19}H_{40}}$ = the density of $C_{19}H_{40}$ (i.e. 0.8 g/cm^3)

$V_{12\text{-}12\text{-}12M}$ = the volume of 12-12-12M

$V_{dodecyl}$ = the volume of three dodedcyl chains in 12-12-12M

$V_{aromatic+M}$ = the volume of aromatic ring plus *M* alkali atom in 12-12-12M

$V_{C_{19}H_{40}}$ = the volume of $C_{19}H_{40}$ in the mixture of 12-12-12M+m%$C_{19}H_{40}$

$v_{12\text{-}12\text{-}12M}$ = the volume fraction of 12-12-12M in the mixture of 12-12-12M+m%C_{19}

$v_{C_{19}H_{40}}$ = the volume fraction of $C_{19}H_{40}$ in the mixture

$v_{dodecyl}$ = the volume fraction of three dodecyl chains in 12-12-12M

$v_{aromatic+M}$ = the volume fraction of aromatic ring plus *M* alkali atom in 12-12-12M

Note that $v_{dodecyl}$ and $v_{aromatic+M}$ are determined by using Materials Studio v.4.0 by measuring the volume occupied by each part of 12-12-12M.

Appendix 5

Measured d-spacings of diffraction peaks at different temperatures for the hexagonal columnar lattice (Col$_h$), hexagonal columnar superlattice (Col$_S$), and body-centred cubic (BCC) lattice formed by 12-12-18Li+m%C_nH_{2n+2} where m=0, 15, 30 and n=15, 17.

Materials	**T (°C)**	**Lattice**	**(*hkl*)**	d_{hk} **(Å)**	a_h, $a_s/\sqrt{3}$, a_c **(Å)**	D_{cc}[a] **(Å)**	μ_{obj}^{cal} [b]
12-12-18Li	79	Col$_h$	(10) (11) (20)	29.7 17.2 14.9	34.4	34.4	3.8(12-12-18Li)
	89	Col$_h$	(10) (11) (20)	29.8 17.2 14.9	34.5	34.5	3.8(12-12-18Li)
	99	Col$_h$	(10) (11) (20)	29.8 17.3 15.0	34.6	34.6	3.8(12-12-18Li)
	109	Col$_h$	(10) (11) (20)	29.9 17.3 15.0	33.5	33.5	3.6(12-12-18Li)
	119	Col$_h$	(10) (11) (20)	29.9 17.4 15.0	33.5	33.5	3.6(12-12-18Li)
	139	BCC	(110) (200) (211)	28.4 20.2 16.5	40.3	34.9	26.3(12-12-18Li)
	159	BCC	(110) (200) (211)	28.2 20.0 16.4	40.0	34.6	25.7(12-12-18Li)
	179	BCC	(110) (200) (211)	28.0 19.8 16.2	39.6	34.3	24.9(12-12-18Li)
	199	BCC	(110) (200) (211)	27.7 19.7 16.1	39.3	34.0	24.4(12-12-18Li)
	219	BCC	(110) (200) (211)	27.5 19.5 15.9	39.0	33.8	23.8(12-12-18Li)
	239	BCC	(110) (200) (211)	27.3 19.3 -	38.6	33.4	23.1(12-12-18Li)
	259	BCC	(110) (200) (211)	27.0 19.1 -	38.2	33.1	22.4(12-12-18Li)

Materials	**T (°C)**	**Lattice**	**(*hkl*)**	**d_{hk} (Å)**	**a_h, $a_s/\sqrt{3}$, a_c (Å)**	**D_{cc}[a] (Å)**	μ_{obj}^{cal} [b]
12-12-18Li	279	BCC	(110) (200) (211)	26.8 19.0 -	38.0	32.9	22.0(12-12-18Li)
	299	BCC	(110) (200) (211)	26.7 18.9 -	37.7	32.6	21.5(12-12-18Li)
12-12-18Li+15%C_{15}	42	Col_h	(10) (11) (20)	31.2 18.0 15.6	36.0	36.0	3.3(12-12-18Li) +2.1($C_{15}H_{32}$)
	52	Col_h	(10) (11) (20)	31.3 18.0 15.6	36.1	36.1	3.4(12-12-18Li) +2.1($C_{15}H_{32}$)
	62	Col_h	(10) (11) (20)	31.3 18.1 15.7	36.2	36.2	3.4(12-12-18Li) +2.1($C_{15}H_{32}$)
	72	Col_h	(10) (11) (20)	31.4 18.1 15.7	36.3	36.3	3.4(12-12-18Li) +2.2($C_{15}H_{32}$)
	82	Col_h	(10) (11) (20)	31.5 18.1 15.7	36.3	36.3	3.4(12-12-18Li) +2.2($C_{15}H_{32}$)
	93	Col_h	(10) (11) (20)	31.4 18.1 15.7	36.3	36.3	3.4(12-12-18Li) +2.2($C_{15}H_{32}$)
	103	Col_h	(10) (11) (20)	31.3 18.1 15.7	36.2	36.2	3.4(12-12-18Li) +2.1($C_{15}H_{32}$)
	137	BCC	(110) (200) (211)	29.1 20.6 16.8	41.2	35.7	22.7(12-12-18Li) +14.4($C_{15}H_{32}$)
	147	BCC	(110) (200) (211)	28.9 20.5 16.7	41.0	35.5	22.4(12-12-18Li) +14.2($C_{15}H_{32}$)
	157	BCC	(110) (200) (211)	28.7 20.4 16.6	40.7	35.2	21.9(12-12-18Li) +13.9($C_{15}H_{32}$)
	167	BCC	(110) (200) (211)	28.6 20.2 16.5	40.4	35.0	21.4(12-12-18Li) +13.6($C_{15}H_{32}$)
	177	BCC	(110) (200) (211)	28.4 20.1 16.4	40.2	34.8	21.1(12-12-18Li) +13.4($C_{15}H_{32}$)
	187	BCC	(110) (200) (211)	28.2 19.9 16.3	39.9	34.6	20.6(12-12-18Li) +13.1($C_{15}H_{32}$)

Materials	**T (°C)**	**Lattice**	**(*hkl*)**	d_{hk} **(Å)**	a_h, $a_s/\sqrt{3}$, a_c **(Å)**	D_{cc}[a] **(Å)**	μ_{obj}^{cal} [b]
12-12-18Li+15%C_{15}	197	BCC	(110) (200) (211)	28.0 19.8 16.2	39.6	34.3	20.2(12-12-18Li) +12.8($C_{15}H_{32}$)
	207	BCC	(110) (200) (211)	27.8 19.6 16.0	39.3	34.0	19.7(12-12-18Li) +12.5($C_{15}H_{32}$)
	217	BCC	(110) (200) (211)	27.6 19.5 15.9	39.1	33.9	19.4(12-12-18Li) +12.3($C_{15}H_{32}$)
	227	BCC	(110) (200) (211)	27.5 19.4 15.9	38.9	33.7	19.1(12-12-18Li) +12.1($C_{15}H_{32}$)
12-12-18Li+30%C_{15}	28	Col_h	(10) (11) (20)	34.8 20.1 17.4	40.2	40.2	3.3(12-12-18Li) +5.0($C_{15}H_{32}$)
	37	Col_h	(10) (11) (20)	34.7 20.1 17.4	40.2	40.2	3.3(12-12-18Li) +5.0($C_{15}H_{32}$)
	47	Col_h	(10) (11) (20)	34.8 20.1 17.4	40.2	40.2	3.3(12-12-18Li) +5.0($C_{15}H_{32}$)
	57	Col_h	(10) (11) (20)	34.8 20.1 17.4	40.2	40.2	3.3(12-12-18Li) +5.0($C_{15}H_{32}$)
	67	Col_h	(10) (11) (20)	34.8 20.1 17.5	40.3	40.3	3.3(12-12-18Li) +5.1($C_{15}H_{32}$)
	77	Col_h	(10) (11) (20)	34.7 20.1 17.4	40.2	40.2	3.3(12-12-18Li) +5.0($C_{15}H_{32}$)
	87	Col_h	(10) (11) (20)	34.4 19.9 17.2	39.7	39.7	3.2(12-12-18Li) +4.9($C_{15}H_{32}$)
	92	Col_S	(10) (11) (21) (30) (22)	60.5 34.1 - 19.7 17.0	39.4	-	9.4(12-12-18Li) +14.5($C_{15}H_{32}$)
	97	Col_S	(10) (11) (21) (30) (22)	58.9 33.7 22.2 19.5 16.9	39.0	-	9.2(12-12-18Li) +14.2($C_{15}H_{32}$)
	102	Col_S	(10) (11) (21) (30) (22)	57.9 33.4 22.0 19.3 16.7	38.6	-	9.1(12-12-18Li) +14.0($C_{15}H_{32}$)

Materials	**T (°C)**	**Lattice**	**(*hkl*)**	**d_{hk} (Å)**	**a_h, $a_s/\sqrt{3}$, a_c (Å)**	**D_{cc}[a] (Å)**	**μ_{obj}^{cal} [b]**
12-12-18Li+30%C$_{15}$	107	Col_S	(10) (11) (21) (30) (22)	57.9 33.4 22.0 19.1 16.7	38.5	-	9.0(12-12-18Li) +13.9($C_{15}H_{32}$)
12-12-18Li+15%C$_{17}$	49	Col_h	(10) (11) (20)	32.7 18.9 16.4	37.9	37.9	3.7(12-12-18Li) +2.1($C_{17}H_{36}$)
	59	Col_h	(10) (11) (20)	32.8 19.0 16.5	38.0	38.0	3.7(12-12-18Li) +2.1($C_{17}H_{36}$)
	69	Col_h	(10) (11) (20)	32.9 19.0 16.5	38.1	38.1	3.8(12-12-18Li) +2.1($C_{17}H_{36}$)
	79	Col_h	(10) (11) (20)	33.0 19.0 16.6	38.2	38.2	3.8(12-12-18Li) +2.1($C_{17}H_{36}$)
	89	Col_h	(10) (11) (20)	33.0 19.1 16.5	38.2	38.2	3.8(12-12-18Li) +2.1($C_{17}H_{36}$)
	99	Col_h	(10) (11) (20)	32.7 18.9 16.4	37.8	37.8	3.7(12-12-18Li) +2.1($C_{17}H_{36}$)
	108	Col_S	(10) (11) (21) (30) (22)	55.9 32.3 21.2 18.7 16.2	37.4	-	10.8(12-12-18Li) +6.1($C_{17}H_{36}$)
	113	Col_S	(10) (11) (21) (30) (22)	55.4 32.1 20.6 18.6 16.1	37.1	-	10.7(12-12-18Li) +6.0($C_{17}H_{36}$)
12-12-18Li+30%C$_{17}$	29	Col_h	(10) (11) (20)	35.3 20.4 17.7	40.9	40.9	3.4(12-12-18Li) +4.6($C_{17}H_{36}$)
	39	Col_h	(10) (11) (20)	35.3 20.4 17.7	40.9	40.9	3.4(12-12-18Li) +4.6($C_{17}H_{36}$)
	49	Col_h	(10) (11) (20)	35.4 20.4 17.7	40.9	40.9	3.4(12-12-18Li) +4.6($C_{17}H_{36}$)
	59	Col_h	(10) (11) (20)	35.2 20.4 17.6	40.7	40.7	3.4(12-12-18Li) +4.6($C_{17}H_{36}$)
	69	Col_h	(10) (11) (20)	35.1 20.3 17.6	40.6	40.6	3.4(12-12-18Li) +4.6($C_{17}H_{36}$)

Materials	**T (°C)**	**Lattice**	**(*hkl*)**	**d_{hk} (Å)**	**a_h, $a_s/\sqrt{3}$, a_c (Å)**	**D_{cc}[a] (Å)**	μ_{obj}^{cal} [b]
12-12-18Li+30%C_{17}	79	$\mathrm{Col_h}$	(10) (11) (20)	35.0 20.2 17.6	40.5	40.5	3.3(12-12-18Li) +4.5($C_{17}H_{36}$)
	94	$\mathrm{Col_S}$	(10) (11) (21) (30) (22)	60.6 34.4 - 19.9 17.3	39.9	-	9.7(12-12-18Li) +13.2($C_{17}H_{36}$)
	99	$\mathrm{Col_S}$	(10) (11) (21) (30) (22)	58.9 34.0 22.4 19.7 17.0	39.3	-	9.5(12-12-18Li) +12.9($C_{17}H_{36}$)
	104	$\mathrm{Col_S}$	(10) (11) (21) (30) (22)	57.9 33.3 22.0 19.4 16.7	38.7	-	9.2(12-12-18Li) +12.5($C_{17}H_{36}$)

[a] D_{cc} is the centre-to-centre distance between two nearest neighbour supramolecular objects in the unit cell of hexagonal columnar lattice, i.e. $D_{cc}= a_h$, and BCC lattice, i.e. $D_{cc}= \sqrt{3}a_c/2$.

[b] For hexagonal columnar lattice, the number of molecules of 12-12-18Li and C_nH_{2n+2} (n=15, 17) per column layer =

$$\mu_{obj}^{cal} = \mu_{12\text{-}12\text{-}18Li}^{cal} + \mu_{CnH\,2n+2}^{cal}$$

$$\mu_{12\text{-}12\text{-}18Li}^{cal} = \frac{\sqrt{3}N_A {a_h}^2 l}{2.\left(\frac{M_{12\text{-}12\text{-}18Li}}{\rho_{12\text{-}12\text{-}18Li}} + \left(\frac{m_{CnH\,2n+2}.M_{12\text{-}12\text{-}18Li}}{m_{12\text{-}12\text{-}18Li}.M_{CnH\,2n+2}}\right).\frac{M_{CnH\,2n+2}}{\rho_{CnH\,2n+2}}\right)}$$

$$\mu_{CnH\,2n+2}^{cal} = \left(\frac{m_{CnH\,2n+2}.M_{12\text{-}12\text{-}18Li}}{m_{12\text{-}12\text{-}18Li}.M_{CnH\,2n+2}}\right).\mu_{12\text{-}12\text{-}18Li}^{cal}$$

For BCC lattice, the number of molecules of 12-12-18Li and C_nH_{2n+2} (n=15, 17) per micelle =

$$\mu_{obj}^{cal} = \mu_{12\text{-}12\text{-}18Li}^{cal} + \mu_{CnH\,2n+2}^{cal}$$

$$\mu_{12\text{-}12\text{-}18Li}^{cal} = \frac{N_A a_c^{\ 3}}{2.\left(\frac{M_{12\text{-}12\text{-}18Li}}{\rho_{12\text{-}12\text{-}18Li}} + \left(\frac{m_{CnH\,2n+2}.M_{12\text{-}12\text{-}18Li}}{m_{12\text{-}12\text{-}18Li}.M_{CnH\,2n+2}}\right).\frac{M_{CnH\,2n+2}}{\rho_{CnH\,2n+2}}\right)}$$

$$\mu_{CnH\,2n+2}^{cal} = \left(\frac{m_{CnH\,2n+2}.M_{12\text{-}12\text{-}18Li}}{m_{12\text{-}12\text{-}18Li}.M_{CnH\,2n+2}}\right).\mu_{12\text{-}12\text{-}18Li}^{cal}$$

For hexagonal columnar superlattice, the unit cell contains three supramolecular cylinders with the same size. Two of them have the same number of 12-12-18Li molecules whereas the other one contains the smaller or the bigger number of 12-12-18Li molecules than those two do. Thus, the number of 12-12-18Li molecules per column layer cannot be calculated directly.

(Avogadro's number $N_\mathrm{A} = 6.022\times10^{23}$ mol^{-1}, *l*= the column layer thickness, $\rho_{12\text{-}12\text{-}18Li}$ = the density of 12-12-18Li, $\rho_{CnH\,2n+2}$ = the density of n-paraffin C_nH_{2n+2}, $M_{12\text{-}12\text{-}18Li}$ = molecular weight of 12-12-18Li, $M_{CnH\,2n+2}$ = molecular weight of n-paraffin C_nH_{2n+2}). The value of column layer thickness of 12-12-18Li, i.e. 4.58 Å, is obtained from wide-angle X-ray diffraction (WAXD) pattern of 12-12-18Li whereas that of 12-12-18Li+m%C_nH_{2n+2} (m=15, 30 and n=15, 17) is assumed to be 4.58 Å. The density of 12-12-18Li is assumed to be 1.02 g/cm^3. The densities of n-pentadecane $C_{15}H_{32}$ and n-heptadecane $C_{17}H_{36}$ are assumed to be 0.76 and 0.77 g/cm^3 respectively.

Appendix 6

2D electron density contours, 2D electron density maps, with different phase combinations, and corresponding histograms of electron density distribution for the hexagonal columnar superlattice of 12-12-18Li+30%$C_{15}H_{32}$, 12-12-18Li+15%$C_{17}H_{36}$, and 12-12-18Li+30%$C_{17}H_{36}$.

(a) 12-12-18Li+30%C_{15}

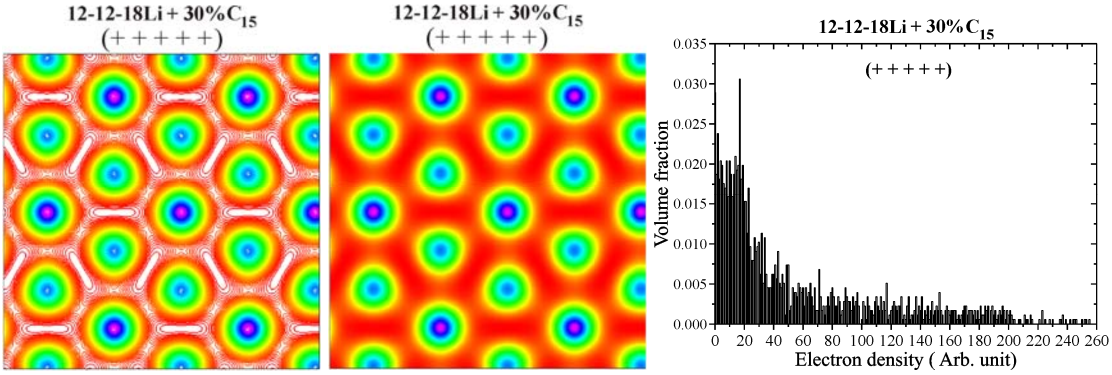

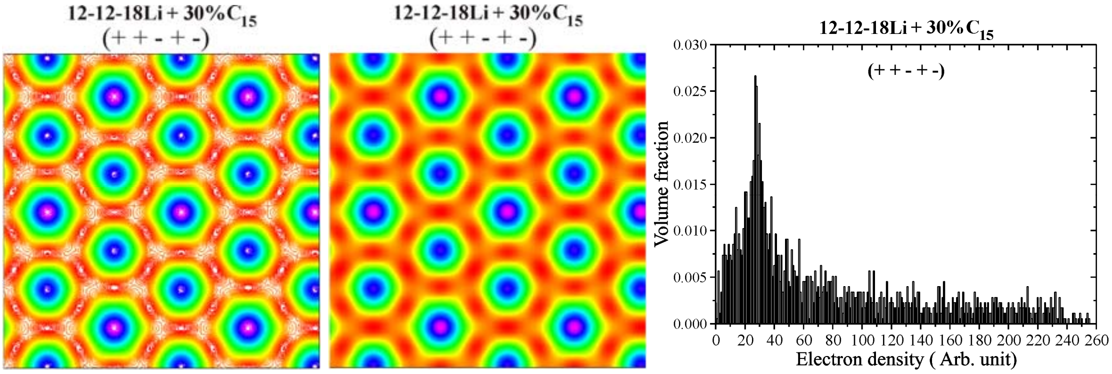

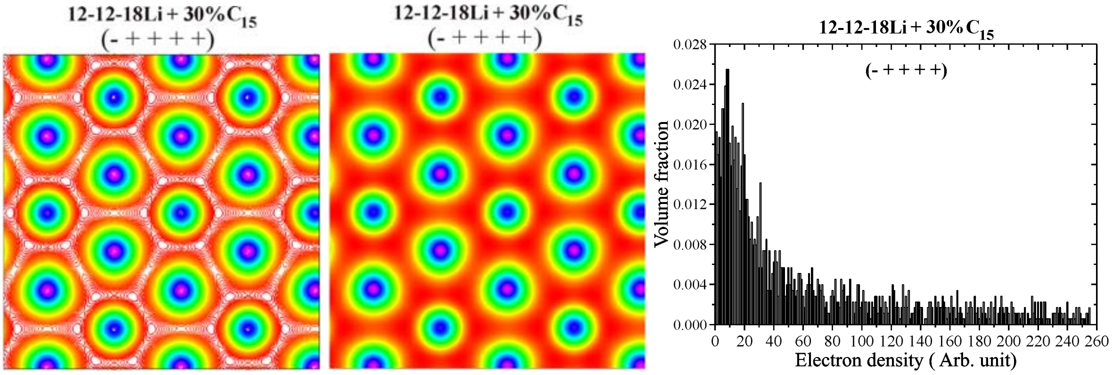

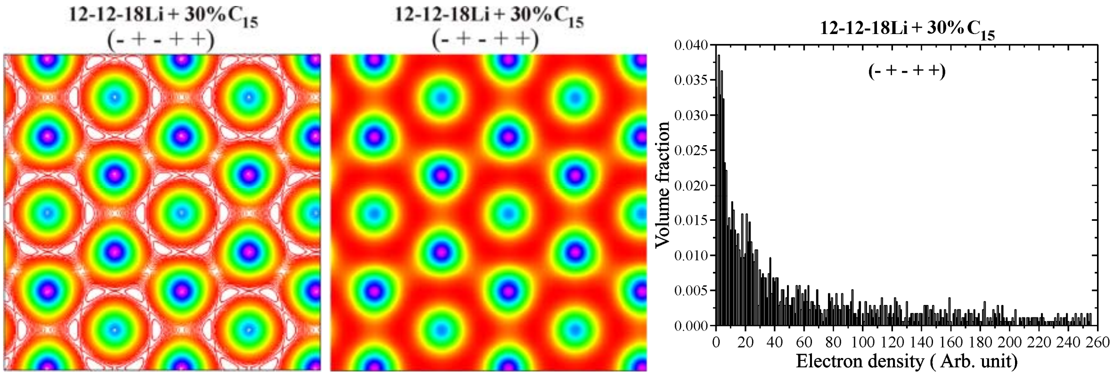

(b) 12-12-18Li+15%C_{17}

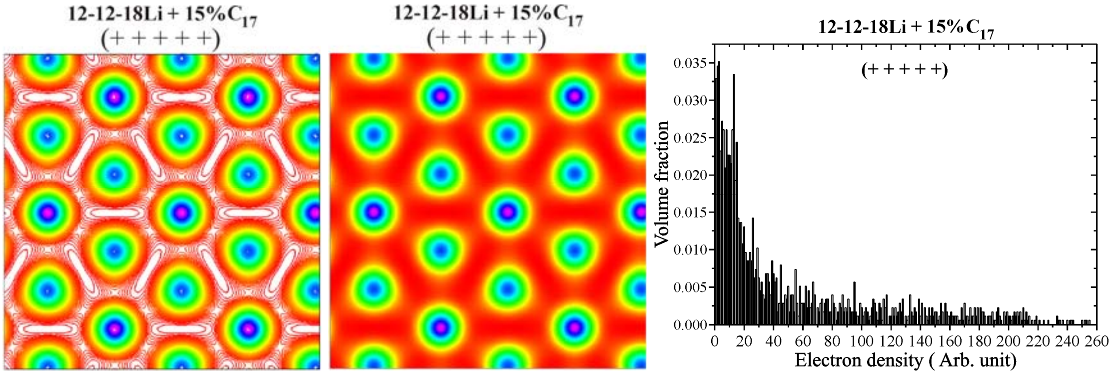

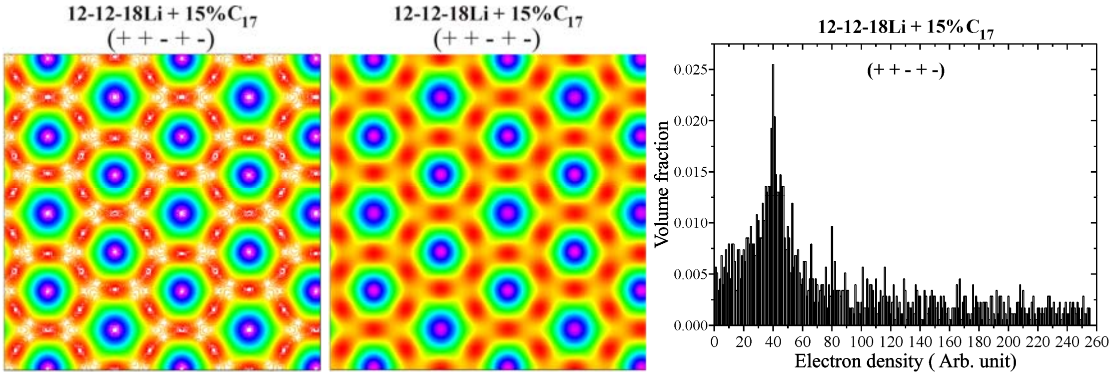

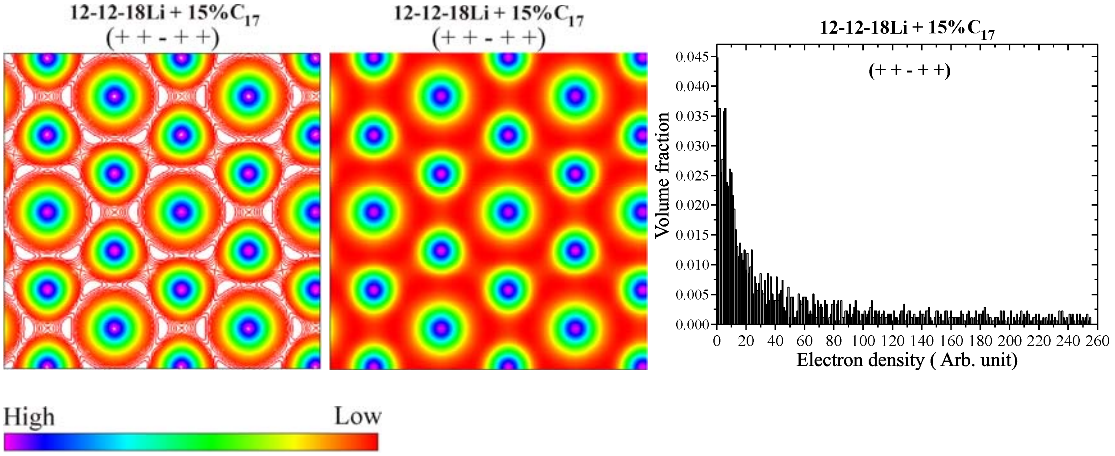

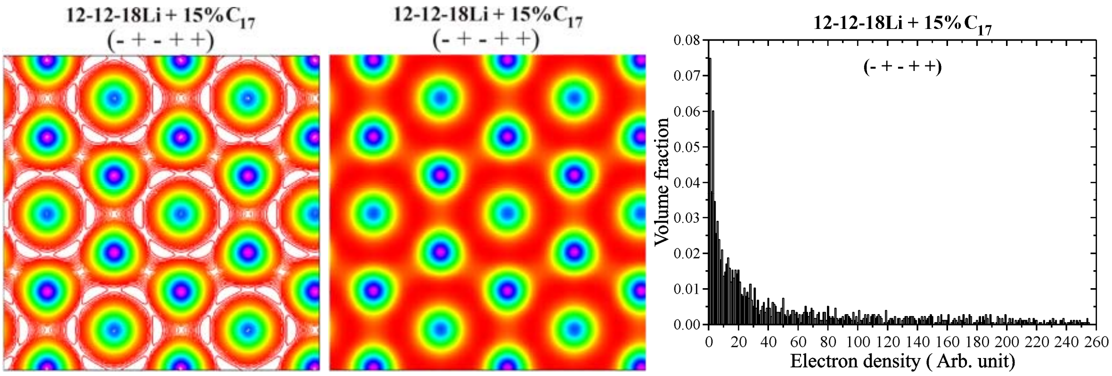
12-12-18Li + 15%C_{17} (- + - + +)

12-12-18Li + 15%C_{17} (- + - + +)

12-12-18Li + 15%C_{17}

(c) 12-12-18Li+30%C_{17}

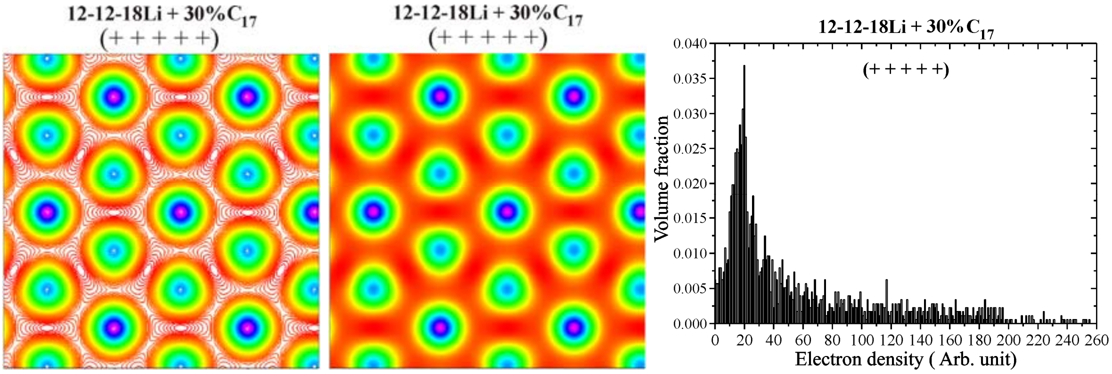
12-12-18Li + 30%C_{17} (+ + + + +)

12-12-18Li + 30%C_{17} (+ + + + +)

12-12-18Li + 30%C_{17}

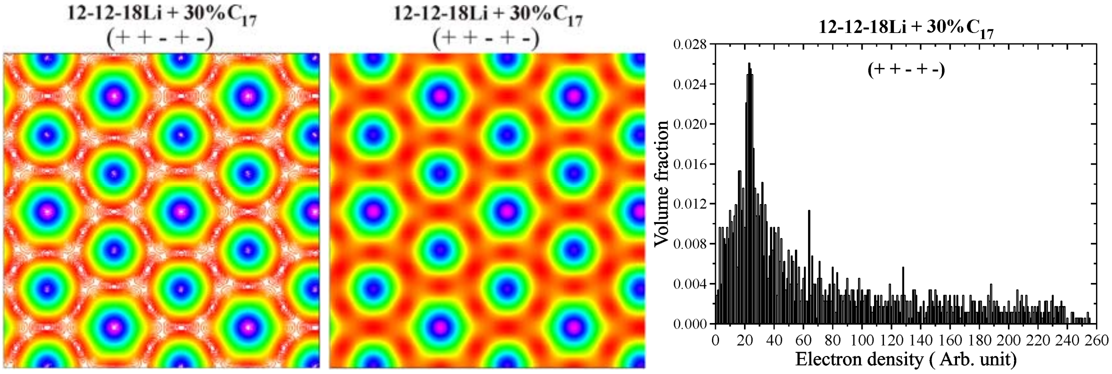
12-12-18Li + 30%C_{17} (+ + - + -)

12-12-18Li + 30%C_{17} (+ + - + -)

12-12-18Li + 30%C_{17}

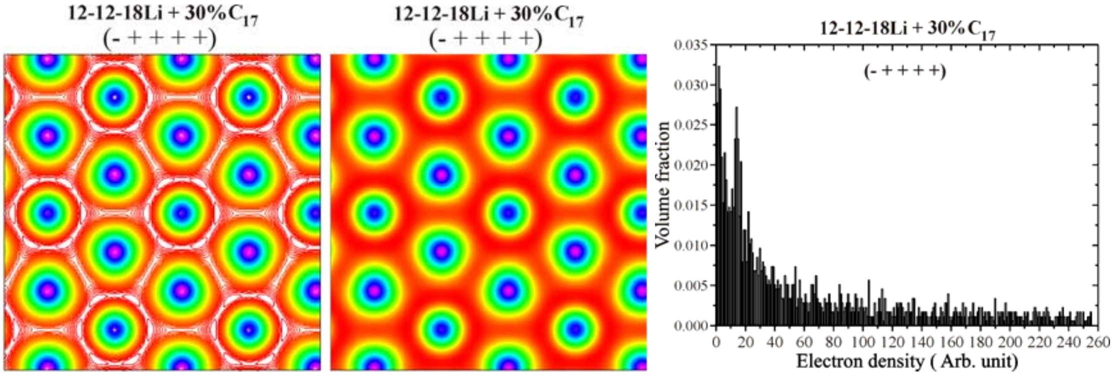
12-12-18Li + 30%C_{17} (- + + + +)

12-12-18Li + 30%C_{17} (- + + + +)

12-12-18Li + 30%C_{17}

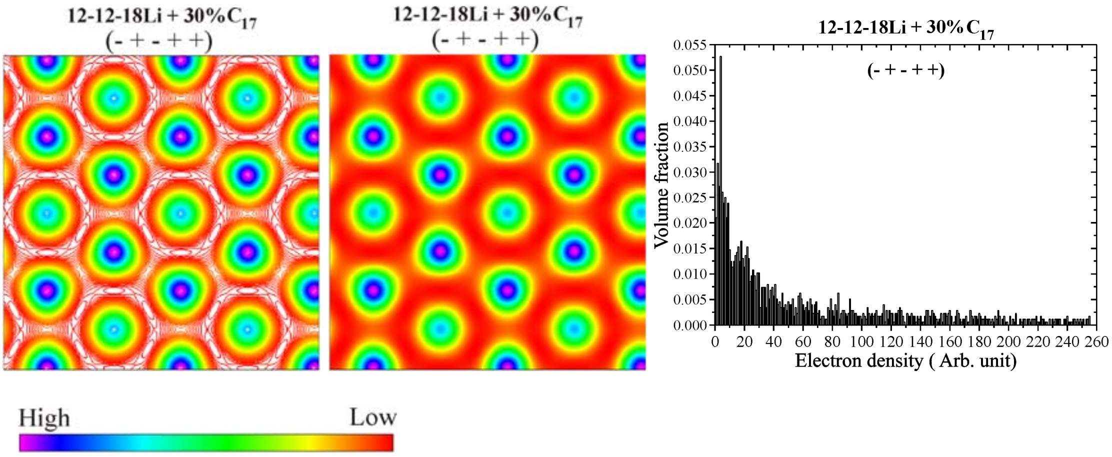
12-12-18Li + 30% C_{17}
(- + - + +)
12-12-18Li + 30% C_{17}
(- + - + +)
12-12-18Li + 30% C_{17}
(- + - + +)
Volume fraction
0.055
0.050
0.045
0.040
0.035
0.030
0.025
0.020
0.015
0.010
0.005
0.000
0
20
40
60
80
100
120
140
160
180
200
220
240
260
Electron density (Arb. unit)
High
Low

Appendix 7

Differential scanning calorimetry (DSC) data for Bn where n=12, 14, 16, 18.

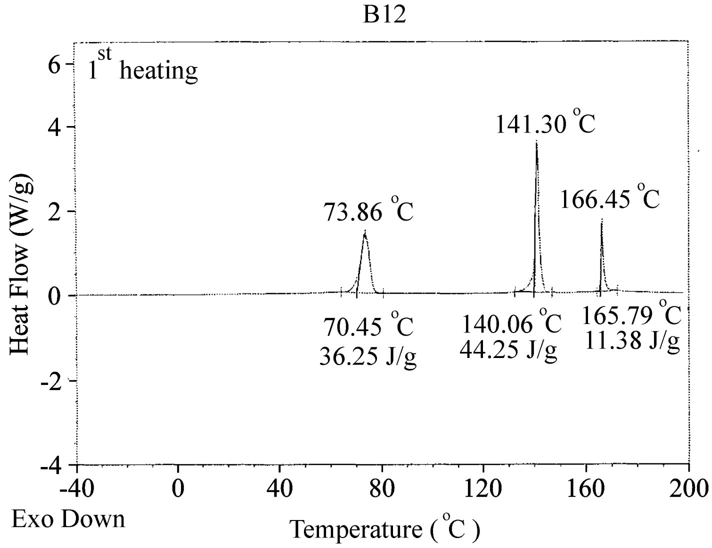

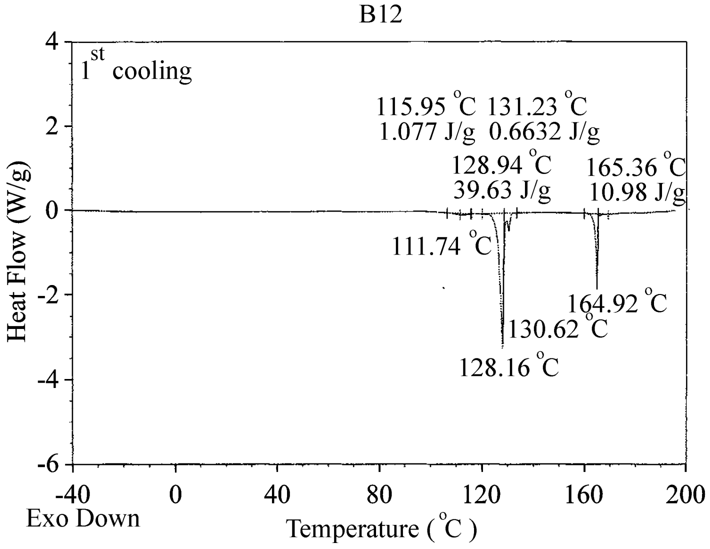

B12

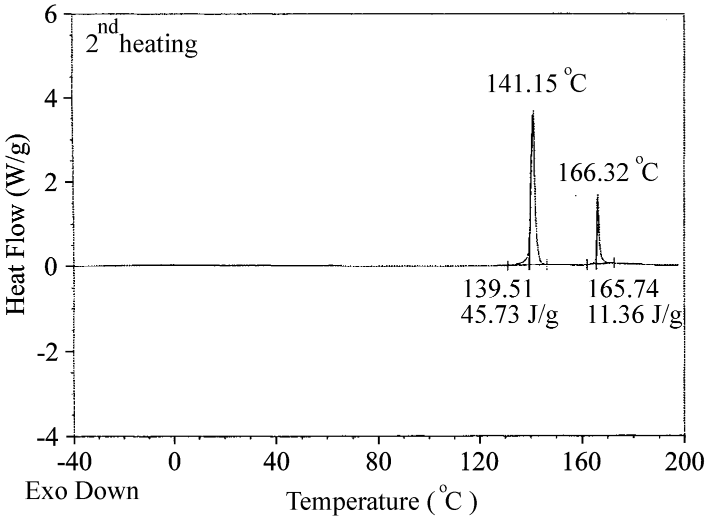
2nd heating
141.15 °C
166.32 °C
139.51
45.73 J/g
165.74
11.36 J/g
Heat Flow (W/g)
6
4
2
0
-2
-4
-40
0
40
80
120
160
200
Exo Down
Temperature (°C)

B14

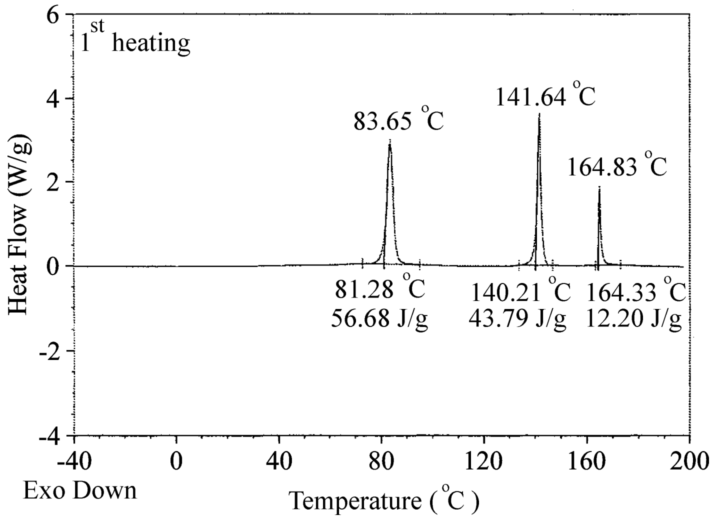
1st heating
83.65 °C
141.64 °C
164.83 °C
81.28 °C
56.68 J/g
140.21 °C
43.79 J/g
164.33 °C
12.20 J/g
Heat Flow (W/g)
6
4
2
0
-2
-4
-40
0
40
80
120
160
200
Exo Down
Temperature (°C)

B14

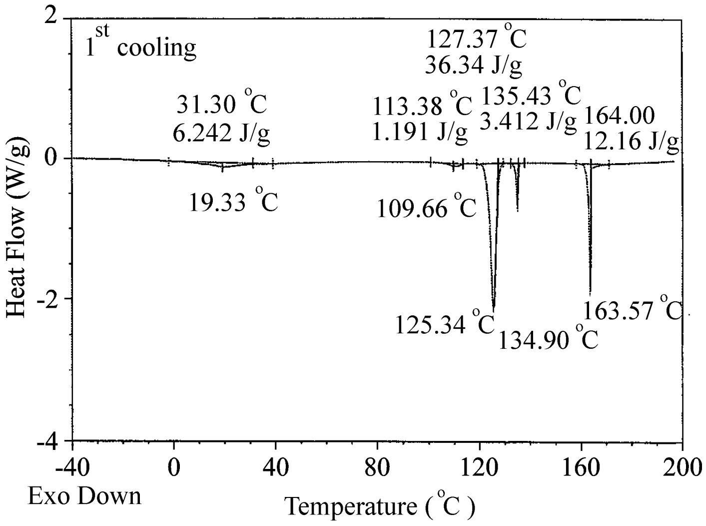
1st cooling
127.37 °C
36.34 J/g
31.30 °C
6.242 J/g
113.38 °C
1.191 J/g
135.43 °C
3.412 J/g
164.00
12.16 J/g
19.33 °C
109.66 °C
125.34 °C
134.90 °C
163.57 °C
Heat Flow (W/g)
2
0
-2
-4
-40
0
40
80
120
160
200
Exo Down
Temperature (°C)

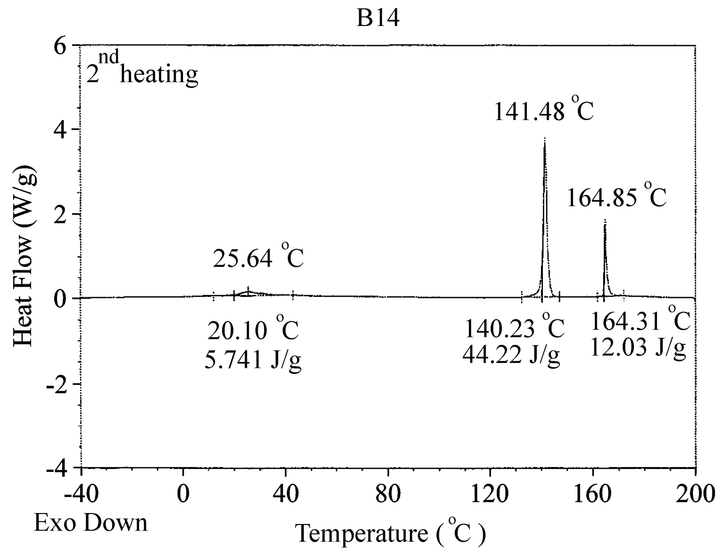
B14
2nd heating
141.48 °C
164.85 °C
25.64 °C
20.10 °C
5.741 J/g
140.23 °C
44.22 J/g
164.31 °C
12.03 J/g
Heat Flow (W/g)
6
4
2
0
-2
-4
-40
0
40
80
120
160
200
Exo Down
Temperature (°C)

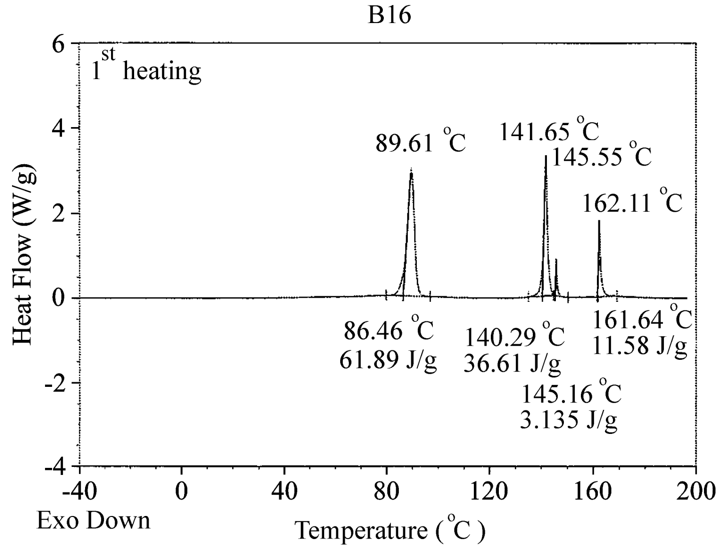
B16
1st heating
89.61 °C
141.65 °C
145.55 °C
162.11 °C
86.46 °C
61.89 J/g
140.29 °C
36.61 J/g
161.64 °C
11.58 J/g
145.16 °C
3.135 J/g
Heat Flow (W/g)
6
4
2
0
-2
-4
-40
0
40
80
120
160
200
Exo Down
Temperature (°C)

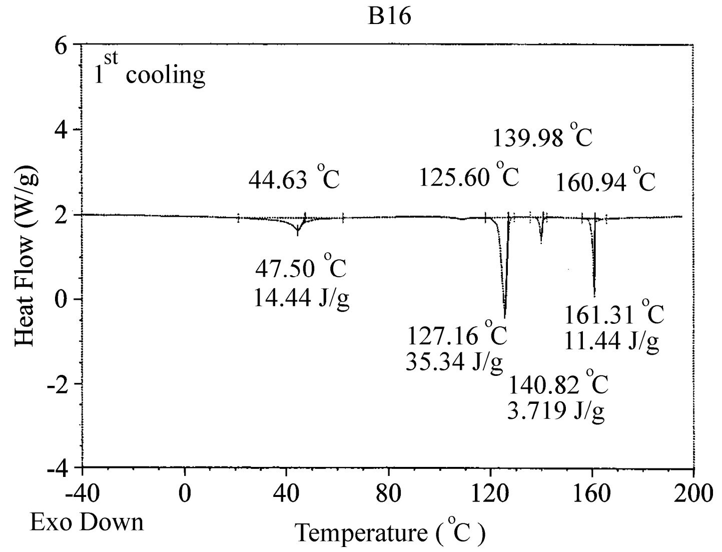
B16
1st cooling
139.98 °C
44.63 °C
125.60 °C
160.94 °C
47.50 °C
14.44 J/g
161.31 °C
11.44 J/g
127.16 °C
35.34 J/g
140.82 °C
3.719 J/g
Heat Flow (W/g)
6
4
2
0
-2
-4
-40
0
40
80
120
160
200
Exo Down
Temperature (°C)

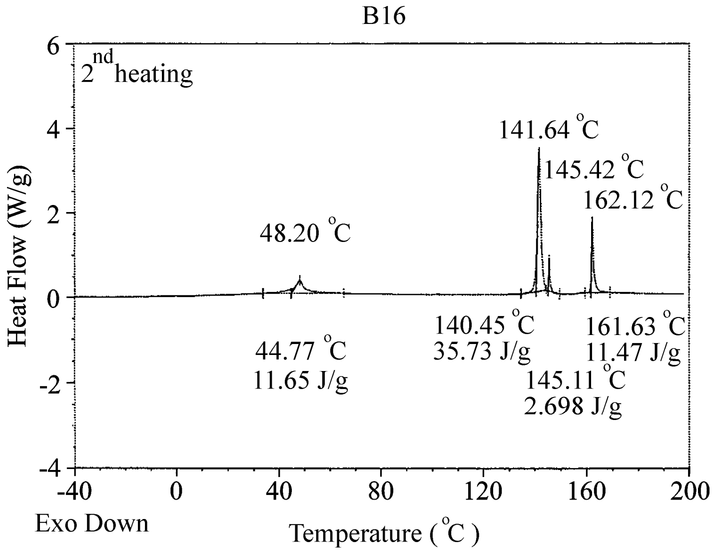
B16
2nd heating
141.64 °C
145.42 °C
162.12 °C
48.20 °C
140.45 °C
35.73 J/g
161.63 °C
11.47 J/g
44.77 °C
11.65 J/g
145.11 °C
2.698 J/g
Heat Flow (W/g)
6
4
2
0
-2
-4
-40
0
40
80
120
160
200
Exo Down
Temperature (°C)

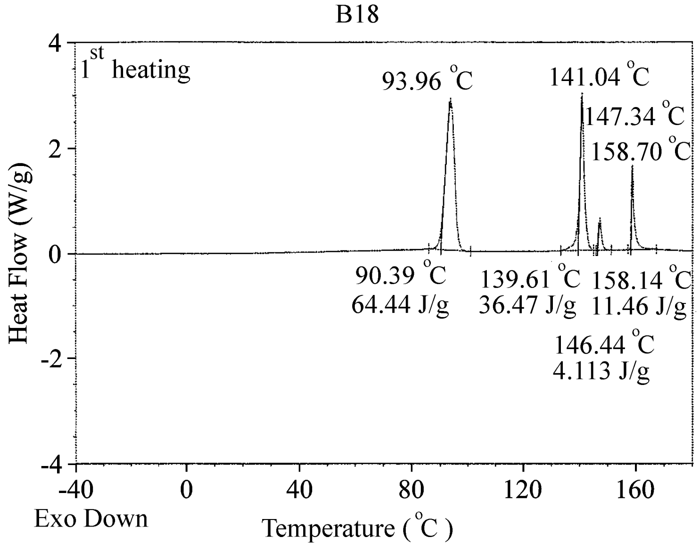
B18
1st heating
93.96 °C
141.04 °C
147.34 °C
158.70 °C
90.39 °C
64.44 J/g
139.61 °C
36.47 J/g
158.14 °C
11.46 J/g
146.44 °C
4.113 J/g
Heat Flow (W/g)
4
2
0
-2
-4
-40
0
40
80
120
160
Exo Down
Temperature (°C)

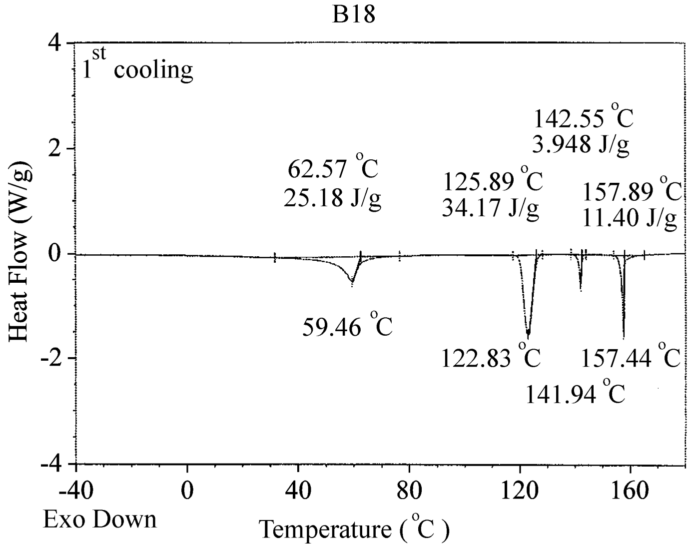
B18
1st cooling
142.55 °C
3.948 J/g
62.57 °C
25.18 J/g
125.89 °C
34.17 J/g
157.89 °C
11.40 J/g
59.46 °C
122.83 °C
157.44 °C
141.94 °C
Heat Flow (W/g)
4
2
0
-2
-4
-40
0
40
80
120
160
Exo Down
Temperature (°C)

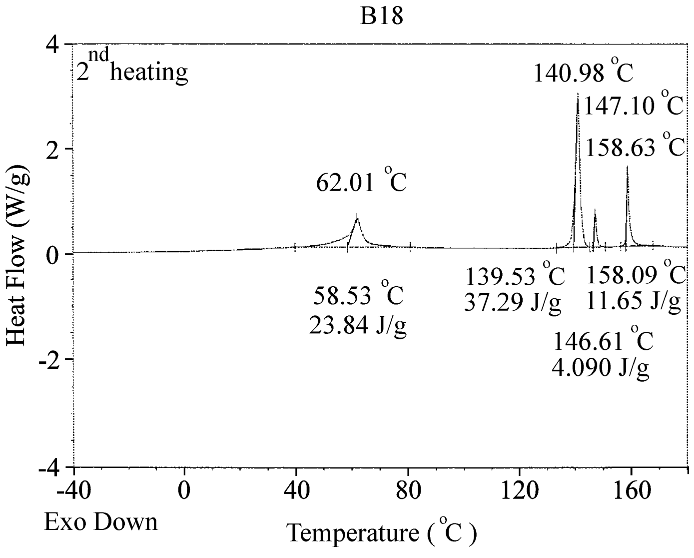
B18
2nd heating
140.98 °C
147.10 °C
158.63 °C
62.01 °C
58.53 °C
23.84 J/g
139.53 °C
37.29 J/g
158.09 °C
11.65 J/g
146.61 °C
4.090 J/g
Heat Flow (W/g)
4
2
0
-2
-4
-40
0
40
80
120
160
Exo Down
Temperature (°C)

Appendix 8

Measured interplanar d-spacings of diffraction peaks at different temperatures for the 2D hexagonal columnar (Col$_h$) and the wiggly lamellar (Lam$_w$) phases formed by Bn where n=12, 14, 16, 18.

Materials	**T (°C)**	**Lattice**	**(*hkl*)**	**d_{hk} (Å)**	**a_h, a_L (Å)**	**D_{cc}[a] (Å)**	**μ_{obj}^{cal} [b]**
B12	80	Col$_h$	(10)	61.5	72.0	72.0	15.1
			(11)	35.7			
			(20)	31.0			
			(21)	23.5			
			(30)	20.9			
			(22)	18.0			
			(31)	17.3			
			(40)	15.6			
			(32)	14.3			
	88	Col$_h$	(10)	61.7	72.3	72.3	15.2
			(11)	35.8			
			(20)	31.1			
			(21)	23.6			
			(30)	20.8			
			(22)	18.1			
			(31)	17.4			
			(40)	15.7			
			(32)	14.4			
	98	Col$_h$	(10)	62.1	72.7	72.7	15.4
			(11)	36.0			
			(20)	31.3			
			(21)	23.7			
			(30)	21.0			
			(22)	18.2			
			(31)	17.5			
			(40)	15.8			
			(32)	14.5			
			(52)	10.2			
			(61)	9.7			
	108	Col$_h$	(10)	62.4	73.2	73.2	15.6
			(11)	36.3			
			(20)	31.5			
			(21)	23.9			
			(30)	21.1			
			(22)	18.3			
			(31)	17.6			
			(40)	15.9			
			(32)	14.6			

Materials	**T (°C)**	**Lattice**	**(*hkl*)**	**d_{hk} (Å)**	**a (Å)**	**D_{cc} [a] (Å)**	**μ_{obj}^{cal} [b]**
B12	118	Col_h	(10)	62.7	73.5	73.5	15.8
			(11)	36.4			
			(20)	31.7			
			(21)	24.0			
			(30)	21.2			
			(22)	18.4			
			(31)	17.7			
			(40)	15.9			
			(32)	14.6			
	128	Col_h	(10)	63.0	73.9	73.9	15.9
			(11)	36.6			
			(20)	31.8			
			(21)	24.1			
			(30)	21.3			
			(22)	18.5			
			(31)	17.8			
			(40)	16.0			
			(32)	14.7			
	138	Col_h	(10)	63.4	74.5	74.5	16.2
			(11)	36.9			
			(20)	32.1			
			(21)	24.3			
			(30)	21.5			
			(22)	18.6			
			(31)	17.9			
			(40)	16.1			
			(32)	14.8			
	144	Lam_w	(10)	38.7	38.7	-	-
	150	Lam_w	(10)	38.6	38.6	-	-
	156	Lam_w	(10)	38.5	38.5	-	-
	162	Lam_w	(10)	38.5	38.5	-	-
B14	90	Col_h	(10)	64.4	75.4	75.4	15.6
			(11)	37.4			
			(20)	32.5			
			(21)	24.6			
			(30)	-			
			(22)	18.8			
			(31)	18.1			
			(40)	16.3			
			(32)	15.0			
	98	Col_h	(10)	64.6	75.7	75.7	15.7
			(11)	37.5			
			(20)	32.6			
			(21)	24.8			
			(30)	-			
			(22)	18.9			
			(31)	18.2			
			(40)	16.4			
			(32)	15.1			

Materials	**T (°C)**	**Lattice**	**(*hkl*)**	**d_{hk} (Å)**	**a (Å)**	**D_{cc}[a] (Å)**	μ_{obj}^{cal} [b]
B14	108	Col$_h$	(10)	64.9	76.1	76.1	15.9
			(11)	37.7			
			(20)	32.7			
			(21)	24.8			
			(30)	-			
			(22)	19.0			
			(31)	18.3			
			(40)	16.5			
			(32)	15.2			
	118	Col$_h$	(10)	65.1	76.3	76.3	15.9
			(11)	37.9			
			(20)	32.9			
			(21)	24.9			
			(30)	22.0			
			(22)	19.1			
			(31)	18.3			
			(40)	16.6			
			(32)	15.2			
	128	Col$_h$	(10)	65.4	76.8	76.8	16.2
			(11)	38.1			
			(20)	33.0			
			(21)	25.0			
			(30)	-			
			(22)	19.2			
			(31)	18.5			
			(40)	16.6			
			(32)	15.3			
	138	Col$_h$	(10)	65.9	77.2	77.2	16.3
			(11)	38.4			
			(20)	33.3			
			(21)	-			
			(30)	-			
			(22)	19.3			
			(31)	18.5			
			(40)	16.7			
			(32)	15.4			
	142	Lam$_w$	(10)	42.0	42.0	-	-
	146	Lam$_w$	(10)	41.9	41.9	-	-
B16	118	Col$_h$	(10)	64.4	74.7	74.7	14.4
			(11)	37.2			
			(20)	32.3			
			(21)	24.5			
			(30)	-			
			(22)	18.7			
			(31)	17.9			
			(40)	16.2			
			(32)	14.9			
			(52)	10.4			
			(61)	9.9			

Materials	**T (°C)**	**Lattice**	**(*hkl*)**	**d_{hk} (Å)**	**a (Å)**	**D_{cc}[a] (Å)**	μ_{obj}^{cal} [b]
B16	129	Col$_h$	(10)	64.6	75.1	75.1	14.6
			(11)	37.5			
			(20)	32.5			
			(21)	24.6			
			(30)	-			
			(22)	18.8			
			(31)	18.0			
			(40)	16.3			
			(32)	14.9			
			(52)	10.4			
			(61)	9.9			
	133	Col$_h$	(10)	64.8	75.3	75.3	14.6
			(11)	37.6			
			(20)	32.6			
			(21)	24.6			
			(30)	-			
			(22)	18.8			
			(31)	18.1			
			(40)	16.3			
			(32)	15.0			
			(52)	10.5			
			(61)	10.0			
	137	Col$_h$	(10)	65.1	75.6	75.6	14.8
			(11)	37.7			
			(20)	32.7			
			(21)	24.8			
			(30)	-			
			(22)	18.9			
			(31)	18.2			
			(40)	16.4			
			(32)	15.0			
			(52)	10.5			
			(61)	10.0			
	140	Lam$_w$	(10)	43.4	42.8	-	-
			(20)	21.3			
	145	Lam$_w$	(10)	43.2	42.6	-	-
			(20)	21.3			
	150	Lam$_w$	(10)	42.9	42.6	-	-
			(20)	21.3			
B18	99	Col$_h$	(10)	68.8	80.7	80.7	15.9
			(11)	39.9			
			(20)	34.7			
			(21)	26.4			
			(30)	-			
			(22)	-			
			(31)	19.6			
			(40)	17.5			
			(32)	16.0			

Materials	**T (°C)**	**Lattice**	**(*hkl*)**	**d_{hk} (Å)**	**a (Å)**	**D_{cc}[a] (Å)**	**μ_{obj}^{cal}** [b]
B18	103	Col$_h$	(10)	69.0	80.7	80.7	15.9
			(11)	40.0			
			(20)	34.8			
			(21)	26.4			
			(30)	-			
			(22)	20.1			
			(31)	19.4			
			(40)	17.5			
			(32)	16.1			
	108	Col$_h$	(10)	69.2	81.1	81.1	16.1
			(11)	40.2			
			(20)	34.9			
			(21)	26.5			
			(30)	-			
			(22)	20.3			
			(31)	19.5			
			(40)	17.6			
			(32)	16.2			
			(52)	11.3			
			(61)	10.8			
	113	Col$_h$	(10)	69.3	81.3	81.3	16.1
			(11)	40.3			
			(20)	35.0			
			(21)	26.5			
			(30)	-			
			(22)	20.3			
			(31)	19.5			
			(40)	17.6			
			(32)	16.2			
	118	Col$_h$	(10)	69.5	81.5	81.5	16.2
			(11)	40.4			
			(20)	35.1			
			(21)	26.6			
			(30)	-			
			(22)	20.4			
			(31)	19.6			
			(40)	17.7			
			(32)	16.2			
			(52)	-			
			(61)	10.8			
	123	Col$_h$	(10)	69.6	81.6	81.6	16.3
			(11)	40.5			
			(20)	35.1			
			(21)	26.6			
			(30)	-			
			(22)	20.4			
			(31)	19.6			
			(40)	17.7			
			(32)	16.3			

Materials	**T (°C)**	**Lattice**	**(*hkl*)**	**d_{hk} (Å)**	***a* (Å)**	**D_{cc}[a] (Å)**	**μ_{obj}^{cal} [b]**
B18	128	Col_h	(10)	69.7	81.7	81.7	16.3
			(11)	40.6			
			(20)	35.2			
			(21)	26.7			
			(30)	23.5			
			(22)	20.4			
			(31)	19.6			
			(40)	17.7			
			(32)	16.3			
			(52)	-			
			(61)	10.9			
	133	Col_h	(10)	69.8	81.9	81.9	16.4
			(11)	40.7			
			(20)	35.3			
			(21)	26.8			
			(30)	23.6			
			(22)	20.5			
			(31)	19.7			
			(40)	17.8			
			(32)	16.3			
			(52)	-			
			(61)	10.9			
	136	Col_h	(10)	69.9	82.1	82.1	16.5
			(11)	40.8			
			(20)	35.4			
			(21)	26.8			
			(30)	23.7			
			(22)	20.5			
			(31)	19.7			
			(40)	17.8			
			(32)	16.4			
			(52)	11.5			
			(61)	10.9			
	139	Lam_w	(10)	48.2	47.8	-	-
			(20)	23.9			
	145	Lam_w	(10)	47.7	47.7	-	-
			(20)	23.8			
	151	Lam_w	(10)	47.3	47.3	-	-
			(20)	23.6			
	156	Lam_w	(10)	47.0	47.0	-	-
			(20)	23.5			

[a] D_{cc} is the centre-to-centre distance between two nearest neighbour supramolecular objects. For the Col_h lattice, D_{cc} is equal to *a* parameter of the Col_h unit cell..

[b] For hexagonal columnar lattice, the number of molecules of Bn per column layer $= \mu_{obj}^{cal} = (\sqrt{3}/2)N_A a_h^2 l\rho/M_{Bn}$

(Avogadro’s number $N_{\mathrm{A}} = 6.022 \times 10^{23}$ mol^{-1}, a_h = a lattice parameter of the Col$_h$ unit cell, l= column layer thickness, $\rho =$the density of Bn compounds, $M_{Bn} =$molecular weight of Bn molecules. The density of B12 is 1.08g/cm^3, whereas the density of B14, B16, and B18 is assumed being equal to that of B12. The column layer thickness is assumed 4.5 Å, based on the assumption that columns are formed by non-tilting of Bn molecules.